Understanding the properties of biologically active glassy materials for tissue engineering through modelling and experiment

Submitted **November 2019**, in partial fulfillment of
the conditions for the award of the degree **Doctor of Philosophy.**

Adja B.R. Touré

Supervised by Dr. Elisa Mele, Dr. Jamieson K. Christie

School of Aeronautical, Automotive, Chemical and Materials Engineering
Loughborough University

Abstract

Bioactive glasses (BGs) are amorphous materials exhibiting biocompatibility properties, gaining great interest as biomaterials for regenerative medicine. This work comprises two parts. First, the bioactivity properties that fluoridated phosphate-based bioactive glasses (F-PBGs) exhibit once implanted, for dental repair applications, was studied. Second, the experimental design of cardiac patches, containing 45S5 bioactive glasses for cardiac tissue engineering, was undertaken.

Recently, the role played by fluoride ions on the bioactivity of F-PBGs has been debated in the literature and previous studies have concluded opposite results. Bioactivity and structure are closely related, so classical molecular dynamics (MD) simulations were used to accurately describe the atomistic structure of F-PBGs. To improve the modelling of F-containing bioactive phosphate, a conceptually advanced approach based on polarisation effects of both the oxygen and fluorine atoms was developed. The MD simulations were performed on the following systems $P_2O_{5(50-x)}$ $CaO_{(50-x)}CaF_{2(x)}$; x=0,2,5. In the composition with 2% and 5% of CaF2, no bonding between the phosphorus and fluorine atoms was observed and the atomistic visualisation highlighted the presence of Ca/F clusters. The main effect of fluoride addition was the bonding of the calcium with the fluorine. This bonding led to a re-polymerization of the network and the formation of F-rich and F-poor regions which, overall, decreased the bioactivity of the glass. Presence of clustering ultimately decreased the bioactivity of F-PBGs. Indeed, the ionic-rich regions dissolve at a higher rate than the network-rich regions leading to an uneven fluoro-apatite layer formation, which reduces F-PBGs's suitability for biomedical applications.

It would have been ideal to back up the computational data with experiments, but the synthesis of FPBGs was not feasible in the laboratory available. The experimental section was therefore orientated toward to study of commercially available 45S5 silicate-based bioactive glasses (Si-BGs).

Si-BGs are gaining more and more interest for soft tissue engineering applications. In particular, the use of Si-BGs/polymeric composite scaffold for cardiac tissue regeneration was shown to be promising but has not yet been addressed extensively. In this project, BGs-polymers composite cardiac patches for myocardial tissue regeneration exhibiting tunable degradation properties have been designed. Two techniques were combined: three-dimensional printing and electrospinning both using two highly biocompatible and

bioresorbable biopolymers: poly(glycerol sebacate) and poly(caprolactone). The designed scaffold was shown to be a promising device for cardiac tissue engineering. The manufactured cardiac patches are bioresorbable and biocompatible with a controllable degradation depending on the composition. The addition of BGs had beneficial effects on cell proliferation by helping to regulate the pH and hence, providing a suitable environment for their growth and proliferation. BGs degradation in the PCL-PGS scaffolds, also led to the formation of an open three-dimensional porosity network within the scaffold. This is beneficial for cell growth, flow transport of nutrients and metabolic waste. Finally, mechanical properties showed high values of more than 200% of the myocardium's which will be beneficial for a healthy recovery of the heart scarred tissue.

This project gathered modelling and experimental data that helped better understand the use of bioactive glasses for biomedical applications, including personalised treatments for patients.

Acknowledgements

I would like to thank my supervisors at the University of Loughborough, Dr. Jamieson Christie and Dr. Elisa Mele for giving me the opportunity to undertake a PhD under their supervision and for guiding and helping me grow as a researcher. Being able to lead research under your supervision was an exciting and rewarding experience. I thank the University Of Loughborough for funding my PhD and the Healthcare Research Theme Program for financing the experimental section of my project. I would also like to thank Bridie Catchpole for conducting the degradation study on the electrospun-free scaffolds and gaining some complementary data.

I would like thanks my french buddies, Romain and Berki, who made those three years in England felt a bit more like home. Romain thank you for being an interesting and challenging person. Berk Berk, you are the best and we have made a lot of great memories during those three years and I am not even thinking of our famous lunch time 'bain de soleil'.

I would also like to thank the great friends that I have made in Loughborough. Ollie thank you for all your help but most importantly for all of those great talks and dinners together. Sandra, you know you are my queen, don't ever change. Colum, Ciara, thank you for waiting for me to finish writing up before getting married - you may now proceed. Dan, thank you for bringing more drama into my life, you are my favourite drama queen. Tom, my Latex student and now prodigy, Jordan, the true northern man, thank you for being amazing and funny people.

Thank you, Justine, for all of your support, cat pictures and kindness, and Arthur for being this funny silly guy with great taste in music. Thank to all of my petits lous: Cécile, Caroline, Coraline, Johann! Also thank you to Fanny and all of our much-needed holidays away. Thank to the Dobson/Wood family for your support and the lovely Sunday dinners.

I would also like to thank my family for their love and support during those three years. Dad, thank you for inspiring me as a researcher and Mum, thank you for being patient with my studies. I would like to thank my AntaChou for listening to all the very detailed details of my life.

And finally, I would like to thank my dearest Will for all of your love and immense support. You are my favourite person, thank you for everything. Last but not least, thank you Floki McBh III, for being amazing and a source of constant instagram content.

Contents

List of Tables

List of Figures

Chapter 1

Introduction

1.1 Bioactive Glasses: a bus ride through history...

Before the invention of bioactive glasses, biomaterials, in the 1960s, were mostly composed of stainless steel hip implants pioneered by Dr. McKee[1,2] and the use of cement-based materials to afford better fixation[3]. During this time, the biomaterials community focused on researching inert materials for medical devices such as high-strength metallic implants or fixation materials such as cement or fasteners (e.g. pins and screws).[4,5]

Biocompatibility, at this point in time, was closely linked with low reactive materials and minimal interaction of the implant with the body and surrounding tissues.[6,7] However, significant failures for these implants were reported and attributed to the materials used and/or the mechanical design. Indeed, it was observed that such metallic implants are susceptible to corrosion, leading to implant failures and a limited lifetime in the body.[8]

It is in this context that, in 1967, a young professor made an encounter that would revolutionise the field of biomaterials. During a bus ride, Professor Larry Hench met a Colonel in the Medical Command who confided in him his frustration with the lack of technical advances in the medical field, while tremendous advances were witnessed in weapons and other areas of materials. The Colonel then raised the question of why couldn't amputee soldiers coming back from Vietnam be helped? Larry and the Colonel then discussed the composition of the bones made primarily of hydroxyapatite - a ceramic compound. The conversation awoke Hench's scientific mind and he began researching

more compatible materials. Metals and polymers were discarded as they were made of molecules and atoms not normally found in the body. Following this logic, L.Hench focused his research on calcium phosphate-based materials which are the main components of bones. The first bioactive glass was developed in 1969 by L.Hench[9] and composed of 46.1 SiO_2, 2.6 P_2O_5, 24.4 Na_2O, 26.9 CaO (in mol%). Studies showed that it could form a bond with bones so strong that it was impossible to be removed without damaging and breaking the bone[10] and it has been clinically used since 1985. Bioactive glasses were first referred to as 'Ceramic Prosthetic Materials' demonstrating that the concept of bioactive compounds was not yet fully adopted, and it was not until 1973 when the term 'bioactive glass' first appeared.

Nowadays, bioactive glasses are defined as inorganic biomedical material, and are often used for bone and teeth tissue engineering, as they have been shown to stimulate bone regeneration.[11–13] Alternatively they have recently gained more interest as a use for soft tissue engineering such as cardiac tissue and nerve regeneration, lung tissue repair and wound healing applications.[14–17] The term 'bioactive' defines any substances or materials that induce a beneficial biological response from the host body. Many of the bioactive glasses, used and studied, are derived from L.Hench's first bioactive glasses, as shown in Table 1.1.[9,18,19]

Bioactive glasses belong to a larger groups of materials triggering appropriate response from the body called biomaterials. Biomaterials are defined by the American National Institute of Health as "any substance or combination of substances, other than drugs, synthetic or natural in origin, which can be used for any period of time, which augments or replaces partially or totally any tissue, organ or function of the body, in order to maintain or improve the quality of life of the individual".[20] In other words, these materials are used to manufacture artificial organs, rehabilitation devices or implants replacing natural tissues in the body. Such materials can be implanted in the body to replace or repair failing tissue with the aim of bettering the quality of patients' lives by being placed in close or direct contact with the body. The definition of biomaterials also includes materials used in drug-delivery applications, biosensors and any external device that interacts with the

body e.g. artificial heart systems.[21,22]. To fulfil their role, biomaterials should exhibit the following properties: *in vivo* and *in vitro* biocompatibility, controllable biodegradability and biostability.[23] Biomaterials can be sub-divided into four main categories; (a) natural or synthetic polymers, (b) metals, (c) composites and (d) ceramics including bioactive glasses.

When a bioactive glass is put in contact with an aqueous solution it starts dissolving and releasing ions such as calcium, sodium and phosphate. The release of these ions leads to the formation of an apatite surface layer which plays a crucial role in the bioactivity. The mechanism through which a bioactive glass dissolves was first proposed by Hench (Figure 2.2)[24].

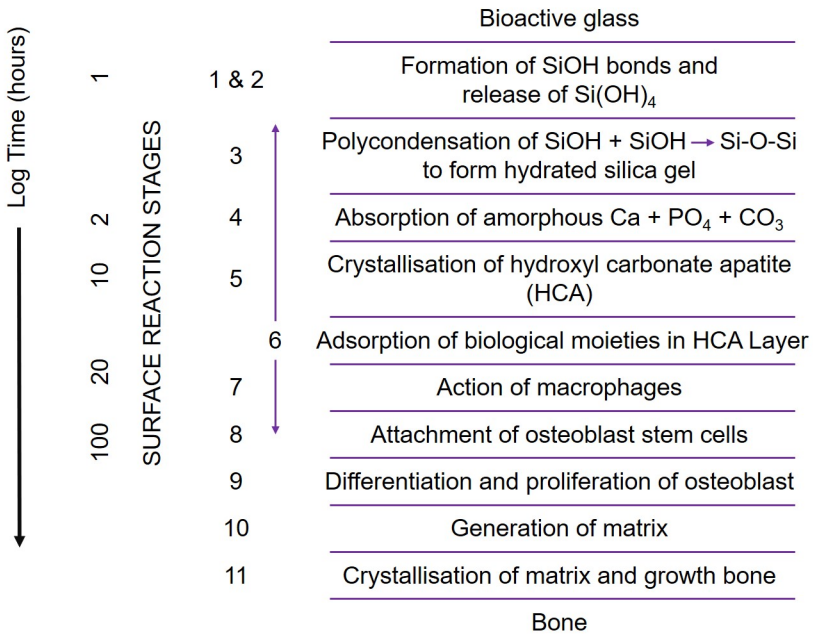

Figure 1.1: Sequence of interfacial reactions involved in forming a bond between bone and a bioactive glass.[24] (1998) Reproduced with permission of John Wiley and Sons.

Table 1.1: Selected bioactive glasses composition (mol%)[18]

Name	SiO_2	P_2O_5	Na_2O	CaO	CaF_2	K_2O	MgO	NC_{Si}
45S5	46.1	2.6	24.4	26.9	-	-	-	2.11
45S5F	46.1	2.6	24.4	13.45	13.4	-	-	2.70
S53P4	53..9	1.7	22.7	21.8	-	-	-	2.54
13-93	54.6	1.7	6	22.1	-	7.9	7.7	2.59[a]
6P61	61.0	2.5	10	13.5	-	2.4	10.7	3.05[a]
6P55	54.1	2.5	11.5	15.9	-	3.4	12.6	2.6[a]
6P50	49.4	2.5	14.9	16.6	-	3.5	13.2	2.36[a]
ICIE1	49.46	1.07	26.38	23.08	-	-	-	2.11
ICIE16	49.46	1.07	6.6	36.27	-	6.6	-	2.11

[a] the values were calculated assuming MgO acts as modifiers
NC represent the network connectivity which is defined in section 2.1.1 which is page 9.[18] (2015) Reproduced with permission of John Wiley and Sons.

1.2 Fluoridated-phosphate based glasses for hard tissue engineering

Phosphate-based bioglasses (PBGs) are mainly based on P_2O_5, Na_2O and CaO entities.[25] They are used in many different biomedical fields such as orthopaedic and dental surgery.[26,27] These type of glasses can be manufactured in various shapes such as discs[28], microtubes[29], microspheres[30,31] and fibres[32,33], hence the use of PBGs in various applications; fibres can be used as cell transportation device[32], nerve conduct[27] or muscle regeneration[34].

Glasses are not as dependent on a specific stoichiometry as crystals are, therefore they allow more flexibility in composition.[18] Over the last years, an increasing number of bioactive glasses have been developed, most of them with incorporated ions exhibiting potential therapeutic effects.[15,32,35–44]

Fluoride is a component of high interest for dental applications as it prevents caries.[45,46] Indeed, fluoride in dentistry presents three main benefits which are:

- The enhancement of tooth enamel remineralisation[47]
- The inhibition of enamel demineralisation[47]
- The inhibition of bacterial enzymes[48,49]

1.3 Silicate-based glasses for soft tissue engineering

Since the discovery of the first bioactive glass 45S5 by L. Hench in 1969[9], a significant amount of research has focused on hard tissue engineering applications such as bone tissue and enamel regeneration, as discussed in the previous section.[9–11,50–54] Recently BGs have attracted increasing interest for their interaction with soft tissues.[14,55] More studies are being published (Figure 1.2), focusing on using BGs in innovative approaches such as regeneration of soft tissues and for various clinical needs.[56] This is due to the enormous potential BGs exhibit in soft tissue repair. Indeed, promising results have been obtained in terms of angiogenesis (formation of blood vessel)[57–61] and wound healing[62–66] properties but also in nerve[67–70], gastro intestinal[71–74], laryngeal[14,75], lung tissue repair[76–79] and more interestingly, cardiac tissue repair[80–82].

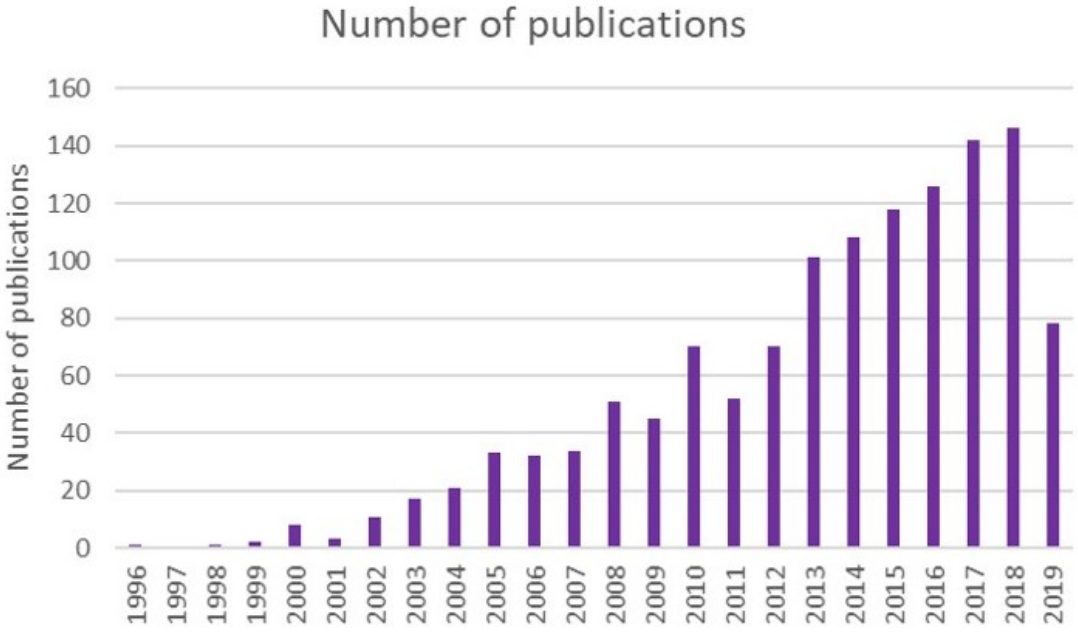

Figure 1.2: Number of papers published per year in the fields of 'bioactive glass' and 'tissue engineering' (according to Web of Science; literature search carried out in June 2019)

Cardiac tissue repair is necessary when the heart suffers what is known as myocardial infarction or heart attack. The latter occurs after a sudden blockage of blood vessels leads to the formation of scar tissue, which impairs the efficient functioning of the heart. To meet this challenge, cardiac tissue engineering has emerged as an highly promising field,

developing efficient and innovative treatments to target cardiac tissue repair.[83] Through this approach, the aim is to mimic the extracellular matrix (ECM) using natural or synthetic polymeric materials.[81] The ECM is an important component of all tissues and organs within the body, as this non-cellular constituent ensures the initiation of crucial biochemical and biomechanical cues needed in various tissue processes e.g morphogenesis, differentiation and homeostasis. Additionally, the ECM acts as a vital physical scaffold for cells and cells' constituents.[84]

1.4 Aims of the project

The research in this work is focused on the use of bioactive glasses as a biomaterial for soft and hard tissue engineering. To do so, both modelling and experimental methods are used in order to gain better understanding of their properties for tissue engineering applications. Bioactive glasses represent a promising class of amorphous materials whose wide range of compositions allows for use in many different fields.

The focus in this project is set on BGs for hard tissue engineering with fluoridated phosphate-based glasses for dentistry, and soft tissue engineering with silicate-based glasses for cardiac tissue engineering. To do so, modelling techniques, with the use of molecular dynamics, are used to better understand how the addition of fluorine affects the bioactivity of phosphate-based glasses through the development of a polarisable force field. The experimental part of the project was initially set to be focused on studying the chemical structure of synthesised fluoridated phosphate-based glasses. However, due to missing lab equipment such synthesis was not feasible during the project. To overcome this issue, it was decided to study commercially available bioactive glasses, 45S5 BGs, exhibiting promising interactions with soft tissues. Experimental techniques such as 3D printing and electrospinning are used to design cardiac patches presenting suitable mechanical properties and surface chemistry to support cardiac tissue regeneration. The following chapters present a detailed description on how such results and data were obtained.

Chapter 2

Literature Review

Every year increasing numbers of patients are seen suffering from tissue and organ failures, along with an increase of health care costs .[85] To face these current challenges, researchers' interests around the world have focused on the development of new, innovative, and/or improved treatments as there is a growing need for solutions.[21] To achieve such improvements, emphasis is being directed toward to development of materials able to assist or enhance the body's repairing processes.[86] Such materials can be synthetic (organic and inorganic), natural or a combination of both. Ultimately, they should exhibit *in vivo* and *in vitro* biocompatibility, controllable biodegradability and biostability. Such materials can be referred to as biomaterials.[23]

Biocompatibility refers to the ability of a material to perform its specific application with appropriate host response. In other words, exposure to a physiological environment should not prevent the material from performing its role.[87] A biodegradable material degrades and moves away from the site of action in the body but is not necessarily removed from the later. A bioresorbable material will completely eliminate itself and its degradation products from the body with no residual side effects.[88] Biostability refers to the chemical and physical stability of a biomaterial in a physiological environment as function of time. In others words, no physiological interactions change the material's property and trigger loss of function during the service life of the biomedical material.[89]

Since the first bioactive glass developed in 1969 by L.Hench[9], composed of 46.1 SiO_2, 2.6 P_2O_5, 24.4 Na_2O, 26.9 CaO (in mol%), many of the bioglasses[18,19] used and studied are

derived from this composition.[9] Inorganic biomedical materials have been used for hard and soft tissue engineering such as bone repair, cardiac tissue and nerve regeneration, lung tissue repair and wound healing applications.[14] Bioactive glasses belong to the third generation of biomedical materials.[90] The first generation of biomaterials is constituted of synthetic materials, manufactured to match the physical properties of the replaced tissue and to be biologically inert. The second generation of biomaterials was engineered to interact with the biological environment to enhance the biological response. They are resorbable materials with the ability to degrade whilst regenerating new tissues. The third generation of biomaterials simultaneously aims at having bioresorbable and bioactive actions, so they help the body heal when implanted, along with the ability to activate genes that stimulate the regeneration of tissue.[91,92]

2.1 General structural properties on bioactive glasses

2.1.1 Glass Composition and structure

Unlike crystalline solids[18] (Figure 2.1 a), bioactive glasses are amorphous materials without any long range periodic structure (Figure 2.1 b-d). The atomistic structure of bioglasses is based on a tetrahedron formed of network formers (phosphorus, silica or borate) linked to oxygen atoms. The oxygen atoms present can have two different roles.[18,93] They can be referred to as bridging oxygen when they link two building units in the network forming, for instance, a Si-O-Si or P-O-P bond. They can also be referred to as non-bridging oxygen when they do not participate in building the network.
The glass structure can be described by three main components[94]:

- The **network formers** are the backbone of the glass. They form a network with no need of additional components. Typical network formers are P_2O_5, SiO_2 or B_2O_3.[95]

- The **network modifiers**, as opposed to the network formers, alter the glass structure by linking to the non-terminal or bridging oxygen atom, and thereby turning them into terminal or non-bridging ones, by creating a predominantly ionic linkage.

Typical examples are the calcium or sodium ions.[96]

- The **intermediate oxides** can act as network modifiers or network formers and can be aluminium, titanium, carbon, tungsten, gallium or vanadium.

These PO_4 tetrahedral building units are commonly referred to as Q_n units, where n is the number of bridging oxygen atoms linked to the tetrahedron.[18] The network connectivity (NC)[97] represents the mean value of the number of bridging oxygen atoms per network former e.g Si for silicate-based glass or P for phosphate based-glasses. The network connectivity affects the solubility and degradation rates of the glass. The NC reflects the structural properties beyond the short range distances and shows interesting correlation with the glass bioactivity. It gives a notion of the average polymerisation of the network and is the main structural parameter affecting the bioactivity of the PBGs.[98,99] The NC represents a precious tool for predicting glass properties such as crystallisation tendency, bioactivity and glass transition temperature.[100]

Bioactive glasses are also characterised by their thermal behaviour[101] which is described by a glass transition range (T_g). This range marks the temperature interval within which the system goes from supercooled liquid to a solid glass. Furthermore, when heated, bioactive glasses show a slow decrease of viscosity over several orders of magnitude, which allows them to be processed into various shapes.

Bioactive glasses can be produced through two common methods. One consists of melting the precursors (inorganic oxides, carbonates, fluorides and others) at a temperature going up to 1500°C depending on the composition of the glasses. The subsequent cooling should be rapid enough so that no crystallization occurs. The other synthesis method is a poly-condensation reaction from organic precursors (alkoides such as tetraethyl orthosilicate): the produced glasses are referred to as sol-gel derived glasses.[102–104]

2.1.2 What makes glasses bioactiçve?

When immersed in an aqueous solution, bioactive glasses start dissolving and releasing calcium, sodium and phosphate ions leading to the formation of an apatite surface layer.

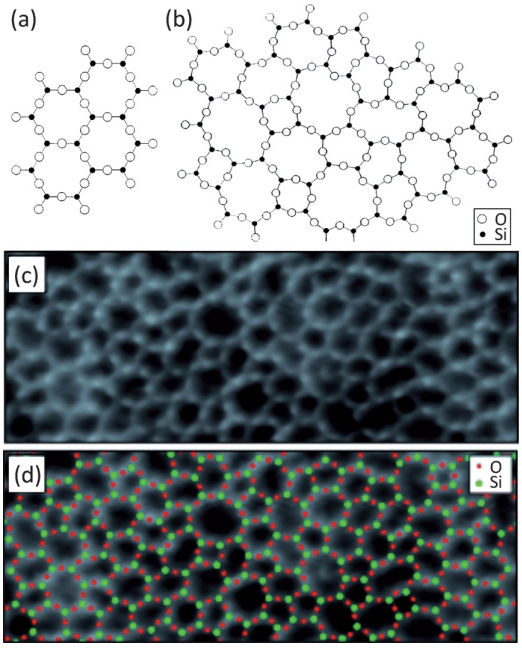

Figure 2.1: Structure of a) crystalline and b) vitreous silica (only three oxygen atoms are shown per SiO_4 tetrahedron, with the fourth lying above or below the image plane), c) atomic-resolution scanning tunnelling microscopy image of a vitreous SiO_2 film, and d) the same image superimposed with a schematic representation of oxygen and silicon .[18,95,105] (1932 and 2015) Reproduced with permission of John Wiley and Sons and the American Chemical Society.

As L.Hench showed in proposed dissolution mechanism[24], this apatite layer plays a crucial role in the bioactivity. Bioactive glasses are typically referred to as second generation biomaterials; however, the use of BGs in medical implants, developed for tissue engineering applications (e.g. cardiac patches), belongs to the third generation of biomaterials.[106,107]

2.1.2.1 Link between glass structure and solubility

The open network of bioactive glasses allows the water molecules to penetrate the glass network easily.[18] The mechanism through which a bioactive glass dissolves was first proposed by Hench (Figure 2.2)[24] and then illustrated with Molecular Dynamics (MD) simulations.[108,109] Those simulations highlighted not only the importance of an open network for water penetration, but also some important surface features such as the modifier cations or non-bridging oxygen atoms. Indeed, when a bioglass is put in contact with water, an ion exchange occurs between the glass surface and the water: modifier ions such as Na^+ are exchanged with some protons from the solution. MD simulations showed

that modifier cations act as Lewis acids, activating the dissociation of H_2O and steadying the HO^- ions.[108] Therefore, these sites allow a strong interaction between the glass and the water. Regarding the bridging oxygen atoms, MD simulations showed that they tend to exhibit hydrophobic properties and no significant interactions with the aqueous environment.

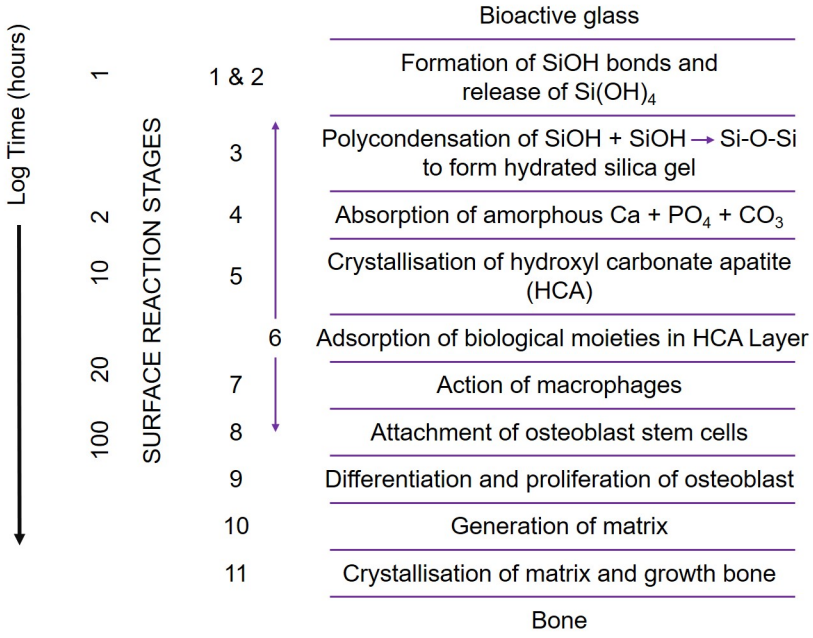

Figure 2.2: Sequence of interfacial reactions involved in forming a bond between bone and a bioactive glass.[24] (1998) Reproduced with permission of John Wiley and Sons.

The immersion of a bioglass in an aqueous environment is also accompanied by the formation of an apatite layer at the surface of the glass.[110] The apatite surface layer is key to the bioactivity of the glasses. Apatite is a term used to classify groups of calcium orthophosphate (e.g. hydroxyapatite $Ca_5(PO_4)_3OH$)[111,112]) and is one the main components of mineralized human tissues such as dentine, enamel and bones. Since the composition of apatite is similar to mineral tissues, it interacts with them. For instance, hydroxyapatite is said to interact with collagen fibrils to bond with the host bone.[113]

Diffraction methods experiments[114] showed that this apatite formation starts with the

development of an octacalcium phosphate layer, which thereafter endures various recrystallizations. This is due to the nucleation rates of octacalcium phosphate being higher at physiological pH values than hydroxyapatite, which is more stable at pH values between 5 and 10.[111]

The formation of apatite depends on the network connectivity: a more polymerised glass will have a slower apatite formation due to a smaller release of ions from the glass.[97] The limit point for the formation of an apatite layer is a network connectivity of 2.4.[97] At this value, the network is too rigid to allow any glass dissolution or significant ion release. These glasses are therefore classified as not bioactive enough. However, some exceptions exist; indeed some glasses with a network connectivity higher than 2.4 exhibit bioactive properties in vitro (e.g. 13-93[115] and S53P4[116]), albeit at a very slow rate. To understand that, it should be borne in mind that the network connectivity represents a mere average value. The sites which show a lower local connectivity network (referred to as floppy regions) allow the water to penetrate and ions to be released, leading to an apatite surface layer formation. This process happens until there are no floppy regions left. At this point, apatite is no longer formed and bioactivity goes down to zero.

The rate at which the apatite layer is formed has been shown to depend on many factors. If the network connectivity is maintained, the apatite layer formation can be accelerated by an increase of the phosphate content.[117,118] The substitution of calcium by strontium also increases apatite formation through the formation of a strontium-substituted apatite.[119,120] Studies also show that the presence of alkali metal ions such as Na^+, K^+, does not necessarily enhance bioactivity, since alkali-free bioactive glasses have been shown to form apatite at a similar rate to bioactive glasses containing them.[118,121] Indeed, the high amount of calcium present in the glass is enough to precipitate the apatite.

How the glass structure and the release of ions affect the apatite formation are important factors when studying the dissolution behaviour of a glass that will exhibit slow apatite

formation (e.g. non mineralising glasses for cartilage repair) or a fast one (e.g. for dental application). Several types of bioactive glasses have been engineered depending on their targeted applications: the 'conventional' silicates such as Bioglass 45S5, phosphate-based and borate-based glasses.

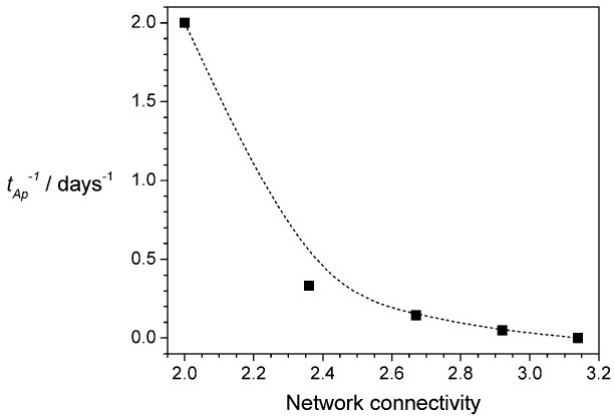

Figure 2.3: Rate of apatite formation of silicate based-glasses (t_{Ap}^{-1}, where t_{Ap} is the time of first apatite formation in a simulated body fluid.[18,122]) (1990 and 2015) Reproduced with permission of John Wiley and Sons.

2.1.2.2 Biological response induced by the dissolution of a bioactive glass

Once implanted in the body, bioactive glasses show osteoconductive properties; they are able to bond to both soft and hard tissues, along with angiogenesis properties (*in vivo* and *in vitro*), antibacterial and anti-inflammatory properties. This is summarised in Figure 2.4.[46,60,123–125]

Angiogenesis

Silicate and phosphate-based glasses Silicate-based glasses induce angiogenic differentiation of different types of mesenchymal stem cells by influencing genes up-regulating the angiogenesis such as genes encoding for vascular endothelial growth factor (VEGF) and fibroblast growth factor.[60,123]

Concerning phosphate-based glasses, a high concentration of phosphate ions triggers angiogenesis processes in the lungs in mice.[126] Indeed, phosphate ions induce an over expression of a type IV collagenase enzyme (matrix metalloproteinase-2; MMP2) which plays an

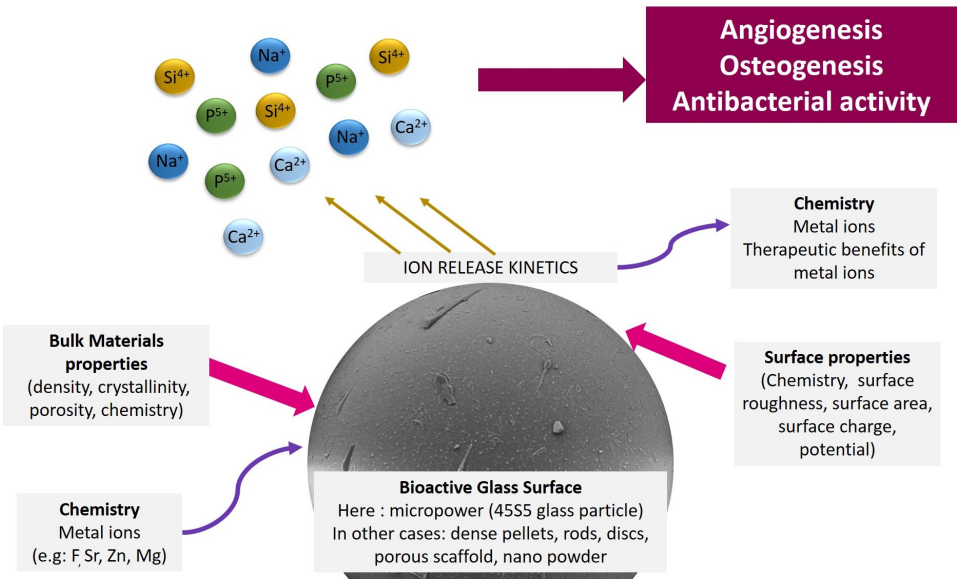

Figure 2.4: Summary of the biological responses induced by the dissolution of a bioglass[46,60,123–125]

important role in the formation and growth of new blood vessels, the repair of damaged tissues and inflammation.[124] Finally, phosphate ions also induce an over expression of fibroblast growth factor.[126]

Doped Glasses Among additive ions used as dopant for bioactive glasses, copper and cobalt ions have been shown to have a positive effect on the angiogenesis properties of glasses. Copper influences various factors inducing angiogenesis[127,128] such as VEGF and collagenase, which are important in all stages of the development of new blood vessels and in the regulation of the blood vessel formation. Copper activates transcription factors responsible for the initiation of angiogenesis.[129]

1% Cu-doped 45S5 Bioglass increases the formation of new blood vessels when tested on rat arteries in comparison with Cu-free 45S5 composition.[130] Cu-doped borate-based BGs showed interesting results in terms of *in situ* healing of skin wounds in rats.[131]

Magnesium in bioglasses has been shown to stimulate the proliferation and migration of microvascular cells.[132–135] However, additional studies would be necessary to gain further understanding of the effect of magnesium over angiogenesis.

Cobalt-doped bioglasses induce the over expression of angiogenic factors VEGF and fi-

Table 2.1: Compositions (wt%) of 45S5, 13-93, 13-93-B1, and 13-93-B3 Bioactive Glasses as used in the work of Bi *et al.*[153,154], Gu *et al.*[155] and Wang *et al.*[156]

Name	SiO_2	P_2O_5	Na_2O	CaO	K_2O	MgO	B_2O_3
45S5	46.1	2.6	24.4	26.9	-	-	-
13-93	54.6	1.7	6	22.1	7.9	7.7	-
13-93B1	34.4	3.9	5.8	19.5	11.6	4.9	20.0
13-93B2	18.0	2.0	6	22.0	8.0	8.0	36.0
13-93B3	-	3.7	5.5	18.5	11.1	4.6	56.6

broblast growth factor.[136,137] The use of doped-glass represents an interesting tool for optimising the angiogenesis of a given glass or biomaterial.

Melt-derived silicate and phosphate-based glasses Studies, carried out to optimise the bone regeneration properties of 45S5 glasses, have revealed the importance of various factors such as the fabrication method, the inner microstructure, pore of the scaffold and their composition.[138]

Porous BG scaffolds exhibit osteoconductive properties with a degradation rate of the scaffold matching the bone formation rate.[139–142] To control the porosity of the scaffold, some studies used 3D printing manufacturing (indirect selective laser sintering) and developed bioactive glass-containing 3D scaffolds.[143–146] Those 3D scaffolds represent a promising solution for the treatment of large bone defects.

Many different types of melt-derived silicate glasses have been developed and studied for regeneration properties, using different manufacturing processes and have led to bioactive glass fibres with different dimensions.[147–151]

Phosphate-based glasses are an interesting group of materials as their dissolution behaviour can be tailored by their composition and the addition of metal oxide such as TiO_2, CuO, NiO, MnO, and Fe_2O_3.[54,152] Calcium phosphate-based glasses can therefore be tailored so that their composition matches that of the bones.[152]

Antibacterial Properties

Bioactive glasses and body fluids When bioactive glasses are immersed into a physiological environment, they start dissolving following various dissolution stages summarized by L. Hench[24] as shown in Figure 2.2. This dissolution is accompanied by the release of various ions such as Na^+, K^+, Ca^{2+} which are exchanged with ions present in the body (H^+ or H_3O^+). This exchange of ions leads to an increase in the local pH from 7 up to 10 rendering the local environment alkaline. Additionally, the release of ions from the BG surface increases the salt concentration and hence the osmotic pressure.[157] These two mechanisms ensure the inhibition of bacterial growth and their potential subsequent adhesion and contamination of implants.[158] The sudden increase of pH induces a lot of stress for a bacteria, which tries to survive by changing its morphology and structure, triggering a modification of numerous genes and proteins patterns.[159]
Following the dissolution of the glass, the pH increases due to the observed liberation of sodium ions.[160] In parallel, a decrease of bacterial activity is observed until the pH reaches a neutral value. This suggests the importance of the dissolution mechanism in the control of bacteria development.[161] However, the effect is diminished *in vivo* because of the buffering media used. Various bioactive glasses (in composition, size and shapes) have been tested against many bacteria. They have shown efficiency in killing bacteria and inhibiting biofilm growth.[162–170]

Doped glasses Several ions have been shown to exhibit antibacterial properties such as copper (Cu), phosphate (P), strontium (Sr), zinc (Zn) and have been incorporated into the structure of glasses. They have been shown to enhance antimicrobial effect in glasses.[171,172]

2.2 Bioactive fluoridated phosphate-based glasses for hard tissue engineering

Phosphate-based bioglasses (PBGs) are used in many different biomedical fields such as orthopaedic and dental surgery.[26,27] It has been shown that depending on the formulation

of the glass, they are able to enhance bone cell growth and antigen expression.[46] This type of glasses is mainly based on P_2O_5, Na_2O and CaO entities.[25] Modifying oxides can be added depending on the targeted applications: CuO for antibacterial properties[35], TiO_2 and SrO to improve degradation properties[36,37], Ag_2O to enhance antibacterial properties[38], Fe_2O_3 to increase the chemical durability and enhance cell attachment and differentiation[32], and TiO_2 to enhance cell viability[41].

PBGs can be manufactured in various shapes such as discs[28], microtubes[29], microspheres[30,31] and fibres[32,33]. Hence the use of PBGs in various applications: fibres can be used as cell transportation device[32], nerve conduct[27] or muscle regeneration[34]. Microtubes can easily be incorporated in bio-polymers and used for soft and hard tissue regeneration. The morphology of microsphere represents an ideal environment for cells to attach and proliferate.[36] This feature also helps to prevent tissue damage and haemorrhage hence the use of the latter in radiotherapy application.[173]

2.2.1 Phosphate-based glasses

PBGs present many properties[27,94], the most interesting of which would be the complete dissolution of phosphate glasses in an aqueous environment. This feature is of high interest in the biomedical field. Additionally, the dissolution behaviour can easily be controlled by the glass composition and chemistry. Interestingly, these glasses can be synthesised with ions that can usually be found in the body. PBGs represent a unique group of materials that differ greatly from the silicate-based ones.

The chemistry of phosphate compounds leads to interesting structural differences in glass formation compared to silica starting network forming oxide, as illustrated in Figure 2.5.[174] In vitreous P_2O_5, the tetrahedral network is not fully polymerised unlike in the silica network. This property is due to the non-bridging and terminal oxygen atoms (double bonded) found in the vitreous P_2O_5.

The most commonly used oxides in phosphate bioactive glasses are the sodium oxide

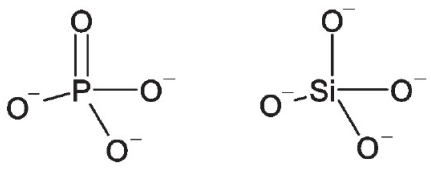

Figure 2.5: Illustration of the basic silicate and phosphate tetrahedra.

(Na_2O) and the calcium oxide (CaO). These oxides have different effects on the glass structure, as shown in Figure 2.6[174], where the calcium ions adopt a chelating structure, as they have the potential to bond with the oxygen atoms of two different chains of the phosphate glass and therefore render the glass more resistant to dissolution. This is due to the calcium ions' higher field strength which leads calcium ions to bond preferably to non-bridging oxygen at the expense of Na.[174] According to the Dietzel definition, the field strength F can be defined as $F = Z/a^2$, where Z represents the charge of the modifier ion and a the length of the modifier oxygen bond in a tetrahedron.[175] Figure 2.7 spotlights the three main building blocks which can be found in phosphate based glasses with the Q^1 or end unit, the Q^2 or middle unit and the Q^3 or branching unit. The structure of phosphate glasses still needs to be better understood and it generally depends on the [O]/[P] ratio. However, previous works[176–178] have helped gain understanding on their complex structure. In the work of Hoppe[176] it was found that a binary system, only constituted with P_2O_5 as network formers, initially presents a substantial excess of terminal oxygen atoms in comparison with bridging oxygen atoms. As the metal (M) is added, it will first occupy positions with a high coordination number which are the terminal oxygen atoms forming an M-O-P link. When all of these sites are occupied and if the content of M is further increased, a modified random network is developed. This point is reached when the content of metal oxide exceeds 30 mol%.

Concerning the glass composition (Na_2 O)0.55-x(CaO)-x(P_2O_5)0.45, the basic dissolution characteristics were investigated.[18,94,179,180] The work of Knowles *et al.*[94] does not present an exhaustive analysis of the dissolution-composition relationship but the main relationships have been studied. As shown in Figure 2.8, the weight loss per unit area against

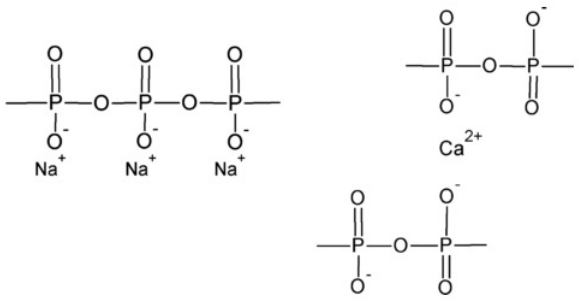

Figure 2.6: Schematic representation of difference between the bonding of Na and Ca in phosphate glasses. The work of Christie *et al.*[174] shows that this schematic is an oversimplification. (2013) Reproduced with permission of the American Chemical Society.

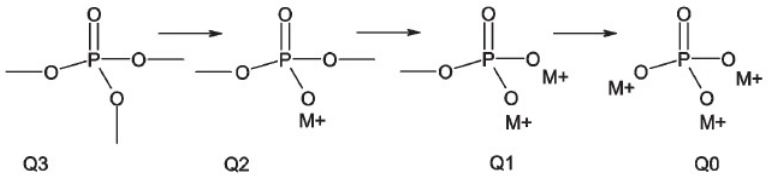

Figure 2.7: Main building blocks[94] (2003) Reproduced with permission of the American Chemical Society.

both time and CaO content was studied at a constant amount of P_2O_5 of 45%.

Generally, the more the CaO content is increased, the lower the dissolution rate.[94,179,180] The dissolution rate also appears linear in comparison to time. This property of phosphate-based glasses is very important as silicate-based glasses do not exhibit it. Indeed they have different dissolution mechanisms. For this reason, the linear dissolution rate in PBGs is a real advantage when the release of therapeutic elements must be controlled.

However, between a CaO content of 32 and 40 mol%, the non-linear dissolution rate indicates a two-staged degradation process.[94] Initially, a high dissolution rate is observed, the latter decreasing significantly after 10-20 hours. This two-staged degradation process is due to the ion release's profile.

Analysis of the ion release showed that sodium ions are released at a very high concentration, in the case of high dissolution rate glasses, and during the early stage of the dissolution as shown in Figure 2.9. This is also observed for glasses with a high level of Na_2O (which tend to exhibit the highest dissolution rate). These observations suggest a preferential release mechanism during the early stage of degradation. These values were supported by pH measurements which presented a rapid increase for all compositions.

This suggests that Na^+ release leads to a migration of H^+ back into the glass to ensure charge balancing and leaving an excess of OH^- anions. Concerning calcium ions, the opposite is observed, with glasses containing the lowest amount of calcium (the highest dissolution rate glasses) exhibiting the highest release of Ca^{2+} (Figure 2.10).

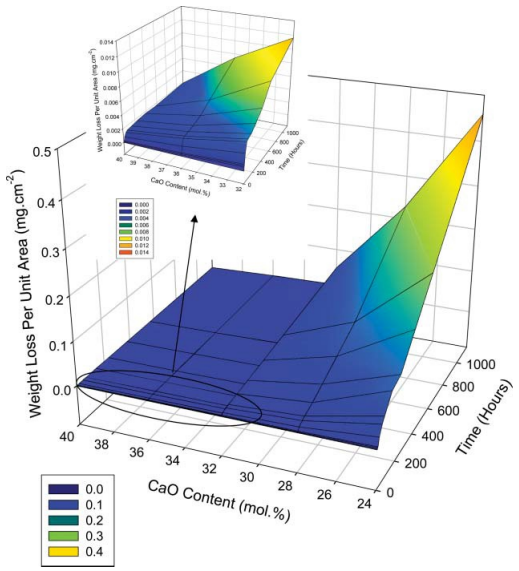

Figure 2.8: Effect of CaO content on the weight loss per unit area against time between CaO content of 24 and 40 mol% and inset an enlargement of the region from 32 to 40 mol%.[27,94,180]Reproduced with permission of the American Chemical Society.

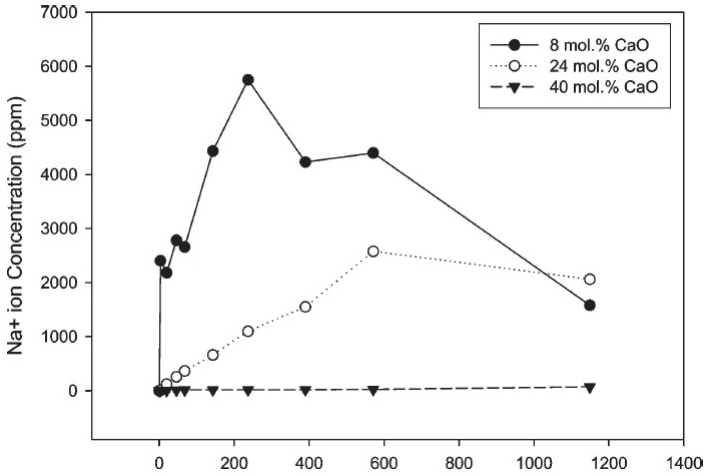

Figure 2.9: Change in sodium ion concentration in distilled water with time for glasses with 8, 24 and 40 mol% CaO (45 mol% P_2O_5 and the balance is Na_2O)[94]Reproduced with permission of the American Chemical Society.

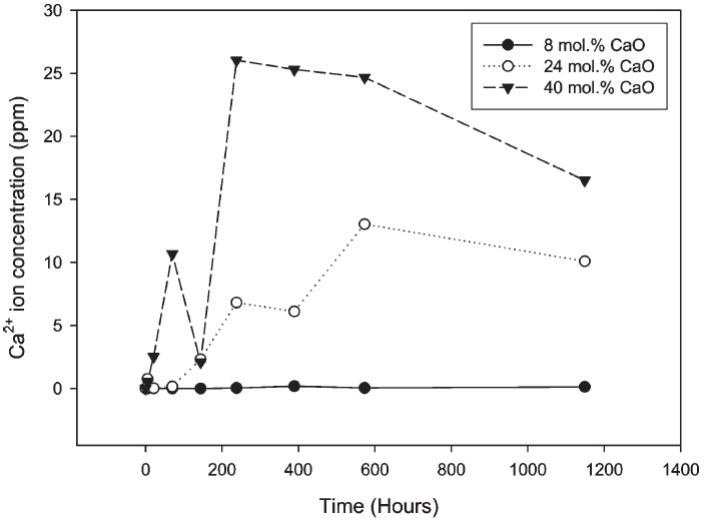

Figure 2.10: Change in calcium ion concentration in distilled water with time for glasses with 8, 24 and 40 mol% CaO (45 mol% P_2O_5 and the balance is Na_2O)[94]Reproduced with permission of the American Chemical Society.

2.2.1.1 Fluoridated phosphate-based glasses

Over the last few years, an increasing number of bioactive glasses have been developed, most of them with incorporated ions exhibiting potential therapeutic effects. Examples are calcium ions which favour osteoblast differentiation and apatite precipitation[42], strontium ions which stimulate bone forming cells[43] and silver ions which exhibit antibacterial properties[39,40]. Zinc ions are known to be bactericidal and essential for wound healing at the right concentration[15] and also stimulate bone formation[44], and fluoride ions are of high interest for dental applications[18,46].

Glasses are not as dependent on a specific stoichiometry as crystals are, therefore they allow more flexibility in composition.[18] A various concentration of ions, with physiological activity and/or therapeutic properties, can therefore be incorporated.

Therapeutic ion release According to *in vitro* cell culture studies, it has been shown that ionic dissolution products from bioactive glasses affect cell proliferation, mineralisation and gene expression.[18,46] These ions are released during the dissolution process to perform their therapeutic action in the human body. The great advantage of ions released locally and from an implant (rather than administrated medication) is that they have a targeted action on the desired site. The therapeutic effect is therefore optimised

and the side effects are minimised. Furthermore, the continuous glass degradation gives the opportunity for the ions to be released continuously and the therapeutic effect to be sustained. As mentioned in the section 2.1.2.1, the released rate can be adjusted, studied through variation of the glass network and type of modifiers or intermediate ions, and with the accurate study of the structure of these bioglasses using molecular dynamics simulations.

Interest of fluoridated bioactive glasses in biomedical applications Fluoride is a component of high interest in dental application as it prevents caries.[45,46] Indeed, fluoride in dentistry presents three main benefits:

- The enhancement of tooth enamel remineralisation[47]
- The inhibition of enamel demineralisation[47]
- The inhibition of bacterial enzymes[48,49]

CaF_2 has been shown to inhibit the formation of alveolar cavities.[181] Moreover, it has been shown that fluoride-containing bioactive glasses form fluoroapatite in physiological solutions.[47,118,121] This fluoridated form of hydroxyapatite, which is the main component of the tooth, is more stable against acid attacks than hydroxyapatite.[182] Additionally, the composition of phosphate-based bioglass which is similar to tooth's composition helps reduce hypersensitivity by filling the microtubule of the teeth.[183] A toothpaste containing very fine Bioglass 45S5 particulates is commercialised. The latter is a fluoride-containing toothpaste where the common abrasive additive in toothpaste, alumina particles, is replaced by Bioglass 45S5 which is a silicate-based glass. Clinical studies show that the Bioglass 45S5 particles adhere to the dentine and form an hydroxycarbonate apatite (HCA) layer that is similar in composition to tooth enamel and blocks the tubules, which are approximately l μm in diameter, relieving the pain for longer periods. Figure 2.11 shows the results obtained with Sensodyne Repair and Protect toothpaste®.[184]
Furthermore, studies have shown the efficiency of fluoride in promoting bone formation and, with the right concentration, in preventing osteoporosis-related fractures.[185,186]

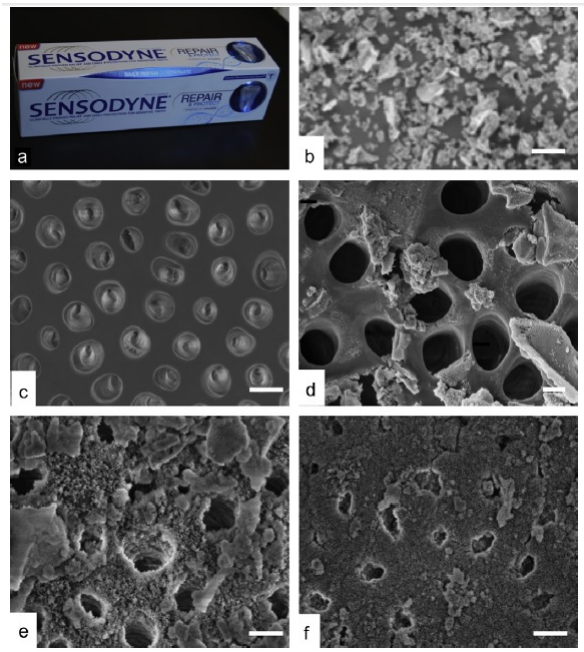

Figure 2.11: (a) Photograph of Sensodyne Repair and Protect toothpaste®, which contains NovaMin®, a fine particulate of Bioglass 45S5®. (b) SEM image of NovaMin®particles (bar = 20 lm). (c–f) SEM micrographs of human dentine (bar = 1 lm): (c) untreated, (d) immediately after application of NovaMin in artificial saliva (AS); (e) 24 h after application of NovaMin®in AS; (f) 5 days after application. SEM images modified from Earl et al.[184] (2002) Reproduced with permission of John Wiley and Sons.

Fluoride-releasing bioglasses have therefore been used in bone-regeneration applications as well as for dentistry.

2.2.1.2 Unsuitability of silicate-based glasses

Fluoride-containing silicate-based bioactive glasses have been synthesised and used in toothpaste to treat dentine hypersensitivity as shown in Figure 2.11.[18,184] In the past, fluoride atoms were assumed to replace oxygen atoms in silicate glass by forming a Si-F bond.[105] However, recent studies show that in reality, clusters of fluoride/modifiers cations are formed, with no Si-F bond detectable. This was determined by ^{19}F MAS-Nuclear Magnetic resonance (NMR) and Molecular Dynamics simulations.[93,187–189] As shown in Figure 2.12, fluoridated silicate-based glasses show a very small amount of Si-F bonding. The conclusion was that the incorporation of fluoride leads to the formation of modifier cations, and fluoride rich regions which are highly soluble, and silicate rich regions which are poorly soluble in a physiological environment. This ion clustering reduces bioactivity.

It was concluded that the addition of fluoride in silicate BGs decreased bioactivity and the resulted fluoridated BGs are unsuitable for a use as biomaterials, as the ion clustering will lead to a discontinuous hydroxyapatite layer formation on the surface of the bioglass in contact with water.[190]

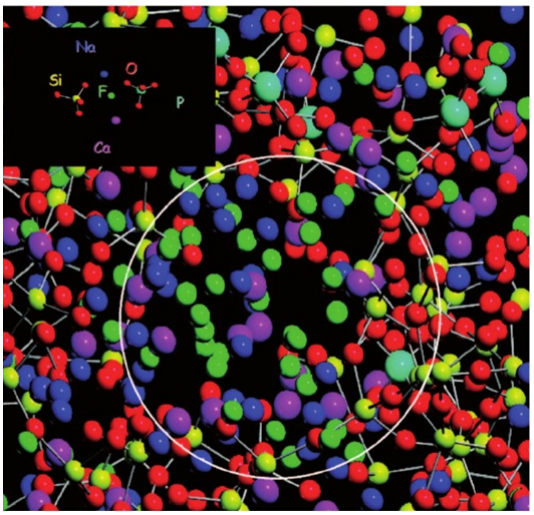

Figure 2.12: Fluoride environment in a bioactive glass (45S5 with 15% of CaO replaced by CaF_2) obtained by MD simulation: the area in the white circle is enriched in fluoride ions (green), charge-balanced by calcium (pink) and sodium (blue) cations.[190] (2008) Reproduced with permission of the American Chemical Society.

2.2.2 Study of the bioactivity of phosphate-based glasses through experimental data and its limitations

As shown in the example above (Section 2.2.1.2), bioactivity and structure are closely related. Therefore, to study the bioactivity of a given glass, it is essential to study its chemical structure. Many different techniques can be used to help analyse the structure of glasses[36], such as X-ray, Fourier Transform Infrared (FTIR), Raman spectroscopy or Nuclear Magnetic Resonance(NMR).

Probing the structure of phosphate-based glasses: Analytical techniques X-Ray diffraction analysis provides information on the disordered and amorphous global structure.[36,191,192] It is a useful and important tool to help prove the absence of any crystal structures within the glasses.[192,193] The amorphous nature of a glass is an important

feature that is critically linked to its biological behaviour and degradation.[194–196] Additionally, bioactive glasses have by definition an amorphous structure, whereas glass-ceramics have partial crystalline structures[197], hence the necessity to characterise the structure using XRD, where a crystal structure would be signalled by the presence of one or more sharp peaks.

FTIR provides information on the type of atom bonds and local coordination.[198] This high energy diffraction method can be used in complement with Raman spectroscopy.[199] These techniques help analyse the structure on the length scale of the nearest neighbour and have been frequently used to probe the structure of glasses.[69,117,192,193,200–203] They are based on both absorption and scattering of electromagnetic radiations. These radiations obtained have different wave-numbers which are corresponding to the vibration of different chemical groups of a molecule.

NMR is also a commonly used method as it is element specific.[204,205] More particularly, solid state NMR can provide a lot of information on glass structure, as ^{31}P is one of the most receptive nucleus due to its large magnetic moment.[206] NMR is usually used in conjunction with magic angle spinning (MAS)[207] with solid power being rotated rapidly at 54.7° to the main magnetic field, which cancels the effect of anisotropy and greatly improves the resolution. Under these conditions, the Q_n species can be observed due to the differing isotropic chemical shifts.[16,121,177,187,208–211] MAS NMR has been used on binary, ternary and more complex systems.[94,189,212–214] Other methods such as absorption spectroscopy (XAS)[215] and neutron scattering can be used in more specific cases to obtain accurate structure analysis.

Experimental study of fluoridated phosphate-based glasses Fluoridated phosphate-based glasses have been experimentally studied and more specially, the role of fluoride has been underlined in phospho-silicate (glasses containing both silicate and phosphorus as network formers)[216], alkali phosphate[217] and tin phosphate glasses[218]. Concerning phospho-silicate glasses[216], ^{19}F and ^{29}Si MAS NMR have helped to show that the addition of CaF_2 leads to the formation of calcium sodium fluoride species and no Si-F bonding was observed. ^{23}Na MAS NMR highlighted the presence of sites where the coordination num-

ber between Na and F augments with the increase of CaF_2. ^{31}P MAS NMR demonstrated the presence of orthophosphate with no Si-O-P bond present. Finally, it was observed that the glass transition decreases with the addition of CaF_2 and this can be explained by the hypothetical presence of CaF^+ as no Si-F bonding was observed.

In alkali-phosphate glass, ^{19}F, ^{27}Al and ^{31}P MAS NMR have been used to study the influence of fluoride in the Na-P-O and Na-Al-P-O bondings.[217] In sodium phosphate-based glasses, this study observed the formation of a P-F bonding where F replaces the oxygen in the phosphate tetrahedra. However, in aluminium glass, MAS NMR revealed the formation of F-Al bonding.[217]

High resolution X-ray photoelectrons spectroscopy and Raman microscopies have been used to investigate the structure of $50SnF_2$-20SnO-$30P_2O_5$ glass.[218] The results showed a high non-bridging oxygen amount. However, to complement these experimental results, theoretical calculations have been implemented. Indeed, experimental study has its limitation that can be complemented by computational calculations.

Limits of the experimental data Computational simulation methods such as molecular dynamics[219–223], ab-initio[93,93,224–228] or density functional theory (DFT) [189,218,226] can be used as a complement to experimental data. Indeed, experimental data often lacks precise information with regards to the atomistic and microscopic structure within the glass, and how network modifiers affect its structure.[218] Molecular dynamics simulations have often been used as a complement to experimental data by showing different effects[109,222,223,225,229–231] which are linkable to the bioactivity, such as the tendency of modifiers to form clusters, the coordination environment of network formers, inhomogeneities and the existence of chain and ring nano-structures. Additionally, in some cases the acquisition of experimental measurements has proven to be complicated, time consuming or even unattainable.[226,227] Therefore, simulations appeared an efficient and reliable way to map out relevant structural features and link the composition of PBGs to their structure and solubility. Some bonds are not visible through MAS NMR, an example would be the Si-F bond in fluoridated silicate-based glasses.[189]

2.2.3 Study of the bioactivity through computational simulations : computational techniques and previous works

Atomistic computational models are powerful tools that aim to mimic the behaviour of a large and complex system. To do so, these models are programmed to explicitly take into account the smallest constituent of the system. In materials science and chemistry, an atomistic model is based on precise calculations that model of the atomistic structure of larger systems e.g molecules and crystals.

2.2.3.1 Polarisable force field development and potential models

The use of polarisable force fields is crucial to obtain a correct description of medium range structure and hence the bioactivity of a bioactive glass.[227] The role of the force field is to model accurately the atomistic structure of a studied system. The potential model represents the most important part of a simulation. Indeed, the reliability and accuracy of the calculated structures and energies rely on the quality and accuracy of the potential model used. The potential model aims to describe the interactions between the atoms within the systems. The energy of a system is sometimes written as an expansion of interatomic potential, as shown in the equation 2.1. In principle the internal energy of a solid is a many-body quantity. The later depends on the position and momenta of all electrons and nuclei. This makes the problem impossible to solve, and therefore some approximations must be made to simplify the calculations. For this reason, the energy of the electron is presumed to be mostly embedded into its corresponding atom, and the energy can be decomposed into an expansion in terms of interactions between different subsets of the total number of atoms, N:

$$V = \sum_{i=1}^{N} V_i + \frac{1}{2}\sum_{i=1}^{N}\sum_{j=1}^{N} V_{ij} + \frac{1}{6}\sum_{i=1}^{N}\sum_{j=1}^{N}\sum_{k=1}^{N} V_{ijk} \tag{2.1}$$

where i, j and k are atoms. The first term represents the self-energy of the atoms, the second the two-body interaction, etc. In order to keep this decomposition as accurate as possible, it has to be performed at a high enough order, bearing in mind that the contri-

bution from higher order terms is smaller for most systems. In that sense, when reaching a certain order, terms above it are neglected. To compensate, a degree of parametrisation for the remaining terms is introduced. Since the further apart two atoms are, the weaker the interactions, a cut-off distance can be introduced to simplify the computational task. The interactions between the atoms can be expressed by many different potential functions, the form of which are usually chosen based on the physical insight of the nature of the forces between the particles.

Long range energy contribution

Coulomb summation In ionic material, the Coulomb forces can represent up to 90% of the total energy depending on the type of material. It is therefore by far the most dominant term, expressed by the following Coulomb's law:

$$U_{ij}^{Coulomb} = \frac{q_i q_j}{4\pi\epsilon_o r_{ij}} \tag{2.2}$$

where q is the charge of the ions i or j, ϵ_o is the vacuum permittivity and r_{ij} is the distance between the ions. To sum the interactions between the numerous ions , a summation technique which is called the 'Ewald summation' was used.[232]

Ewald summation The Ewald summation enables the computation of long range interactions within a periodic system. Since the coulombic part is a long range interaction, the summation is non-convergent when carried out in real space. Additionally, the convergence depends on the number of atoms in the summation. The Ewald summation[232] provides a solution to this problem. To do so, in small to moderate-sized systems, the electrostatic energy is evaluated through the Ewald summation: the inverse distance is rewritten using Laplace transform technique and then split into two rapidly convergent series: one is summed in real space and the other in reciprocal space. A reciprocal lattice is a Fourier transformation of another space. The first lattice is a periodic spatial function in real space. The electrostatic potential of an ion can be resolved into two parts.

Therefore, the resulting energy can be expressed using the expressions:

$$E_{recip} = \frac{1}{2} \cdot \frac{4\pi}{V} \sum_{G} \frac{exp(-G^2/4\eta)}{G^2} \cdot \sum_{i} \sum_{j} q_i q_j exp(-iGr_{ij})$$
$$E_{real} = \frac{1}{2} \cdot \sum_{i} \sum_{j} \frac{q_i q_j erfc(\eta^{1/2} r_{ij})}{r_{ij}} \tag{2.3}$$

where η is the parameter controlling the distribution of the summation between real and reciprocal-space, q is the ion charge, G is the reciprocal lattice vector and V is the unit cell volume. The optimal value for η is described as follows[233]:

$$\eta_{opt} = \left(\frac{nw\pi^3}{V^2} \right)^{1/3} \tag{2.4}$$

where w is the relative computational expense for the operations involved, n is the number of species in the unit cell, including shells, and V is the unit cell volume.[234] Values for w have been studied in order to obtain the optimal value.[233,235].

Representation of the ion charges

Rigid Ion Model The rigid ion model was proposed by Kellerman in 1940[236] for the calculation of lattice dynamics of NaCl. Later on, a modified rigid ion model (M.R.I) was developed. In this model, fixed partial charges are used and the ionic polarisability is neglected.[237] Nowadays, some more realistic approximations are used such as the deformation model[238], the breathing shell model[239] and the shell model[240]. The shell model has been proven to provide more accurate representation of medium range structure compared to rigid ion model.[227] In this work, only the latter will be discussed.

Electronic polarisability of ions: Shell Model The shell model was first developed by Dick and Overhauser.[240] This model takes into account the electronic polarisation of the atoms. An atom is polarisable if it develops a dipole moment when placed in an

electric field. This dipole moment is commonly expressed by the equation:

$$\mu = \alpha E \tag{2.5}$$

where μ is the induced dipole, E is the electric field and α is the polarisability.

In a static shell model, the ion is split into a core and a massless shell, hereafter called the core-shell unit. In this simple mechanical description, the core can be represented by the nucleus of the atom. The core contains the mass of the ion and a charge Q. The shell approximately represents the valence electrons and is also attributed a charge q. The total charge of the sum $(Q + q)$ is always equal to the total charge of the atoms. Figure 2.13 shows a schematic representation of this shell model. There is no electrostatic interaction (i.e self interaction) between the core and the shell of the same atom. Non-coulombic interactions arise from the shell alone. Finally, the core and shell are connected by a

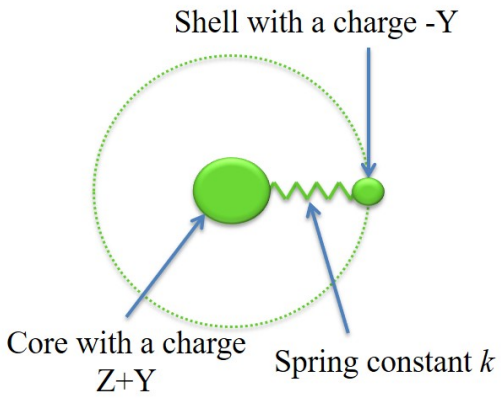

Figure 2.13: Schematic representation of the shell model

harmonic spring with a constant k, hence the following interaction energy :

$$U(r_i) = \frac{1}{2} k_i r_i^2 \tag{2.6}$$

where k represents the force constant of the harmonic spring, and r the distance between the core and the shell. The position of the core is important as it gives the exact ion position in the lattice, unlike the shell position which has no physical meaning. At the beginning of the simulation, core and shell are usually given the same position. The

electric field aims at separating the core and the shell, giving rise to a polarisation dipole. The short-range forces affect the polarisability which becomes environment-dependent. When a static equilibrium is reached, the polarisability can be expressed through the equation:

$$\alpha = (2q_s^2 - q_c^2)/k \tag{2.7}$$

where q_s and q_c are the shell and core charges and k is the force constant of the harmonic spring.

In an adiabatic method, the shell is attributed a fraction of the atomic mass, in order to have a dynamical description. This fraction of mass m is chosen according to the frequency of vibration of the harmonic spring (equation 2.8), which has to be much larger than the frequency of vibration of the whole atom in the bulk system. This condition should be respected in order to avoid any exchange of kinetic energy between the core-shell unit and the rest of the system. Indeed, two core-shell units are linked with a harmonic bond. Therefore, the core-shell units should have a negligible internal vibrational energy, compared to the vibrational energy of the bond linking the two atoms. This should remain throughout the whole simulation in order to maintain a net polarisation. However, during the simulation, there is a slow leakage of kinetic energy into the core-shell units, but this represent a negligible amount of the total kinetic energy and can be corrected by a frictional term. The polarisation of the ion is described in terms of displacement of its shell with respect to the core.

$$\mu = \frac{1}{2\pi}\left(\frac{k}{x(1-x)}m\right)^{1/2} \tag{2.8}$$

where x is the displacement. In DL_POLY (the code used to run the simulation), the adiabatic method is used.

Short range two-bodied potential functions To run an accurate molecular dynamics simulation, an exact potential function must be defined. A potential function describes the energy with which the particles will interact. Indeed, the functional form and parameter sets are used to describe the potential energy of the system. This potential function

can also be referred to as an interatomic potential or a force field. For an interatomic potential, the functional term includes a bonded term, for covalently linked atoms, and a non-bonded (or not covalent) term, comprising long-ranged electrostatic and Van Der Waals forces:

$$V_{TOTAL} = V_{BONDED} + V_{NON-BONDED} \tag{2.9}$$

Bond Stretching term

$$V_{BONDED} = \sum_{BONDED} \frac{1}{2} k_B (r - r_{eq})^2 \tag{2.10}$$

Where k_B is the force constant of the bond, r the bond length and r_{eq} the equilibrium bond length. However, in the case of this project, only ionic solid ionic solids are discussed, therefore this term was neglected.

Van der Waals The Van Der Waals forces describe the residual attractive and repulsive forces between the atoms. Depending on the type of bond between the two atoms, the Van Der Waals terms can be expressed by different equations: Lennard-Jones potential[241],Born Mayer potential[242], Morse Potential[243], Buckingham potential[244], Born-Huggins-Meyer potential[245], Hydrogen-bond (12 - 10) potential[246], Shifted force n - m potential[247] and others. Those of relevance to this study which are the Buckingham, Morse and Lennard-Jones potentials and will be discussed here.

Lennard-Jones potential For large systems, the Lennard-Jones potential[241] provides an accurate description of the interactions between non-bonded ions. The potential function, shown below, can be decomposed into an attractive term, usually $-\frac{1}{r^6}$ which predominates at a long distance r and a repulsive term which usually is $\frac{1}{r^{12}}$ which predominates at a short distance r.

$$V(u_{ij}) = \frac{A}{r_{ij}^{12}} - \frac{B}{rij^6} \tag{2.11}$$

where $A = 4\epsilon\sigma^{12}$ and $B = 4\epsilon\sigma^6$ with ϵ being the depth of the potential well or more practically representing the attraction strength of two particles, σ, the finite distance

where the two-body potential is equal to zero and r being the distance between the particle.

Buckingham potential The Buckingham potential[244] is one of the most commonly used potential for two body non-bonded interactions in ionic solids. The potential is expressed as follows:

$$V(r_{ij}) = A_{ij}e^{\frac{-r_{ij}}{\rho_{ij}}} - \frac{C_{ij}}{r_{ij}^6} \tag{2.12}$$

where A_{ij}, ρ_{ij} and C_{ij} are the Buckingham potential parameters for interactions between the atoms i and j. The short-range repulsion is represented by the first term and the long range attraction, which dominates at larger separation, is represented by the second term. The inclusion of the exponential term makes the use of this potential more computationally expensive. However, this exponential function is a more accurate estimate of the repulsive term.

Morse potential The Morse potential[243] is a function which accurately describes the interactions between two atoms where a dissociation is possible. Thie potential is useful in the case where interactions at bond distance display a non-harmonic oscillator, such as OH bond in hydroxy group or for the P-O interaction in the PO_4 tetrahedron group. The Morse potential realistically takes into account that dissociation can occur unlike the Harmonic potential, and can be expressed by the following expression:

$$V(r_{ij}) = D(1 - e^{[-\alpha(r_{ij}-r_o)]})^2 - D \tag{2.13}$$

where D is the bond energy, r_o is the equilibrium separation and α is a variable that can be determined by spectroscopic data and represents the slope of the potential energy well. The Morse potential can also include a subtraction of the Coulomb interaction as follows:

$$V(r_{ij}) = D(1 - e^{[-\alpha(r_{ij}-r_o)]})^2 - D - \frac{Cq_iq_j}{r} \tag{2.14}$$

where q_i and q_j are the charges of the ions i and j respectively, C is the fraction of the Coulombic subtraction, and the value of 1.0 means that no Coulombic interactions exists between the atoms. For a value of $C = 0$, the equation reduces to the original Morse potential with full Coulombic interaction.

Three body potential function The three body potential is used to describe the interactions between three atoms , as shown in Figure 2.14, where j and k are linked in the middle by a third atom i. The energy of the system is proportional to the deviation of the angle from the equilibrium angle, θ_{ijk}. This three body potential also known as the 'bond bending term' introduces an energy penalty for any deviation from the equilibrium bond angle θ_0, and is written as follows:

$$V = \frac{1}{2} k_{ijk} (\theta_{ijk} - \theta_0)^2 \tag{2.15}$$

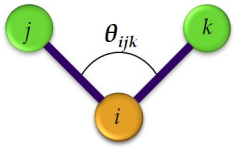

Figure 2.14: Schematic representation of the three body interaction.

where k_{ijk} is the bond bending force constant between the bond ij and ik.

Potential Derivation The potential functions, shown above, are used to accurately describe the energy of a system. However, they all require some parameters to be set. These parameters can be evaluated by two different methods : an empirical derivation fitting or a direct calculation method. These methods are detailed in the following sections.

Empirical fitting Empirical fitting is a way to determine the potential parameters of a given potential function.[248] To do this, the structural and lattice properties of bulk crystals of interest are used. The aim of empirical fitting is to allow the potential parameters to vary one or more at a time, and to calculate crystals properties such as elastic and

dielectric constants, phonon dispersion curves, vibrational frequencies, and structural and lattice properties. The aim is to reproduce as closely as possible the data from the crystals. To evaluate the accuracy of the fit, the sum of squares is often calculated (Equation 2.16). The parameters are considered satisfactory when the sum of squares is at its lowest value, which means that the parameters set lead to the calculated properties closest to the initial data.

$$F = \sum_{all-observables} w(f_{calc} - f_{obs})^2 \tag{2.16}$$

where f_{calc} and f_{obs} are respectively the calculated and observed quantities used for the fitting, and w is the weighting factor. This weighting factor depends on different parameters, such as the relative magnitude of the quantities and reliability of the data. For instance, the lattice parameters are generally given a higher weighting factor as they can be measured more accurately than other properties. As an infinite number of possible fits exist, depending of the weighting factors, there are multiple fits possible. It is important to use sufficient experimental data when fitting a potential function by using multiple structures.[233]

Direct calculation method The direct calculation method of deriving potential parameters is based on quantum mechanical calculation, either by electron gas methods or ab initio calculation[249], local density approximation methods or with embedded atoms methods (EAM).

The interaction energy between a periodic array of atoms can be calculated for a range of distances, and resulting potential energy curve is fitted to a suitable functional form. This method can calculate potentials for any interaction, but it may be dependent on the availability of suitable basis sets.

Such a method would not be adequate for the type of study conducted here. Indeed, the size of the system studied would require a colossal amount of computer time to be able to apply any quantum mechanical calculations.

2.2.3.2 Classical molecular dynamics simulations

Classical molecular dynamics[219,220] (MD) is a computational simulation technique. This method was originally developed for the field of theoretical physics in the late 1950s.[250,251] In this model, the ions in the crystal interact via long-range and short-range electrostatic forces, including the repulsions and the Van der Waals attractions between neighbouring electron charge clouds. The time evolution of a set of interacting particles can be calculated by integrating Newton's second law. If we consider the example of one particle in movement and under the influence of a force $\vec{F}(\vec{r})$:

$$m\frac{d^2\vec{r}}{dt^2} = \vec{F}(\vec{r}) \tag{2.17}$$

where for N interacting particles the classical equation of motion is

$$m\frac{d^2\vec{r}}{dt^2} = F_i(r_1, r_2, ..., r_i, ..., r_N), i = 1, N \tag{2.18}$$

Verlet scheme This algorithm[252] is the most commonly used to integrate the equations of motion. This algorithm was initially adopted by Verlet and relies on a direct solution of a second-order equation:

$$m_i\ddot{r}_i = f_i \tag{2.19}$$

where m_i is the mass of the atom, i, r_i is the Cartesian coordinate, and f_i is the force on the atom i. This method is based on the position $r(t)$, the accelerations $a(t)$, and the positions $r(t - \delta t)$ for each particle form the previous step. The equation for advancing the position is:

$$r(t + \delta t) = 2r(t) - r(t - \delta t) + \delta t^2 a(t) \tag{2.20}$$

In this equation the velocities do not appear. They have been eliminated by the addition of the equations obtained by Taylor expansion about $r(t)$

$$r(t + \delta t) = r(t) + \delta t v(t) + (1/2)\delta t^2 a(t) + ... \tag{2.21}$$

$$r(t-\delta t) = r(t) - \delta t v(t) + (1/2)\delta t^2 a(t) - ...$$

They are useful to estimate the kinetic energy and hence the total energy of the system. This can be obtained through the formula:

$$v(t) = \frac{r(t+\delta t) - r(t-\delta t)}{2\delta t} \tag{2.22}$$

where the error of velocities in the equation 2.22 is of the order of δt^2 and the error of the equation is of error of δt^4.

Calculation step In molecular dynamics, the simulation period is divided into a set of calculations, each occurring over very short time steps Δt, which are typically between $10^{-16} - 10^{-15}$ sec. During these time steps, the forces of each atom are computed, and the accelerations are calculated to generate a new set of positions for the atoms and initial velocities for the next step. Then the atoms are moves to new positions and the pattern is repeated again. Small time intervals are usually selected, so that the forces can be considered as constant.

At the end of the simulation, a dynamical trajectory is generated. These data describe the time evolution of the dynamic variable $\vec{p_i}$ and $\vec{r_i}$ for each particle and over the simulation time. The microscopic dynamical behaviour of the system is described by a set of trajectories constituted of each particle in the system.

Born Model of solids In this model[242,253], it is presumed that the energy and its derivatives can be calculated by summing all the interactions between the atoms in the system. This summation results in the development of a total interaction and total net force acting on each atom towards each other. This method relies on the calculation of the total energy of the lattice. The energy interaction of each atom to the others is expressed as follows:

$$U_i = \frac{1}{2}\sum_j \left(\frac{q_i q_j}{4\pi\epsilon_0(r_{ij})} + \phi_{ij} r_{ij}\right) + \frac{1}{3}\sum_{jk} \phi_{ijk}(r_{ijk}) + \frac{1}{4}\sum_{jkl} \phi_{ijkl}(r_{ijkl}) + ... \tag{2.23}$$

The first term represents the long range Coulomb energy and the short range interaction between two atoms. The second and third characterise the interaction between three or four atoms, referred to as three or four body interactions. ϕ_{ij} is the short-range energy between the ions i and j, r_{ij} is the distance between the atoms i and j respectively and q_i and q_j represent the charges on them. As for the lattice energy of the system, it can be calculated with the following expression:

$$U_{latt} = \sum_{Lij}(\frac{q_i q_j}{4\pi\epsilon_0}(r_{ijL}) + \phi_{ijL}r_{ijL}) + \sum_{Lijk}\phi_{Lijk}(r_i r_j r_k) + \sum_{Ljkl}\phi_{Lijk}(r_i r_j r_k r_l) + ... \quad (2.24)$$

where L is a set of lattice vectors representing the periodicity of the lattice itself in three dimensions. For instance, this changes r_{ij} to $r_{ij} + L$ and similarly for r_{ijk}.

Statistical mechanics

Boundaries and ensemble In computer simulations, the studied material can be represented by a model. This model should ideally be as large as possible; however, the size of the model is limited by the computational expenses. The more atoms the model contains, the more expensive the simulation is. To tackle this issue, hundreds up to thousands of atoms are put in a bo, known as a simulation box. All the structure calculations are carried out within this box. Thereafter, the box is duplicated in every direction to give an infinite lattice, as shown in Figure 2.15. As a particle moves during the simulation which is due to the influence of interatomic forces from the neighbouring atoms, the replica of this particle undergoes the same interatomic forces and therefore the same movement. This applies even if the particle happens to leave the initial simulation box; its image will enter the box through the opposite side so that the number of particles within the box is conserved. Periodic boundaries conditions are introduced to avoid modelling too many atoms on a surface at any one time, which would be computationally expensive, and also to avoid the appearance of any surface atoms.

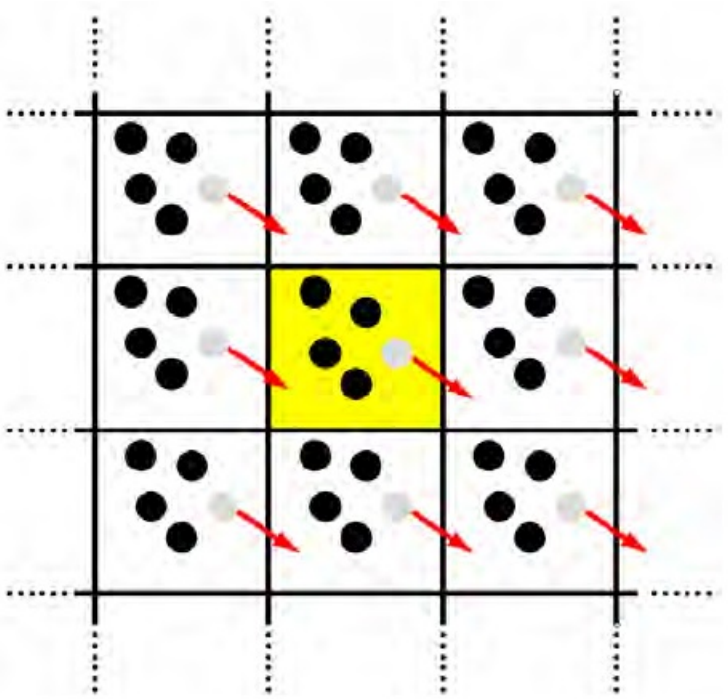

Figure 2.15: Schematic representation of the simulation boxes in 2D. Particle trajectories shown in the central simulation box (yellow) are replicated in every directions.[254]

Ensembles There are different thermodynamic conditions, under which a simulation box can be run; these are known as ensembles.[255] The common ensembles under which simulations are run ar as follows:

- Micro-canonical ensemble (NVE): in this thermodynamic state the number of atoms N, the volume V and the total energy of the system E are fixed.

- Canonical ensemble (NVT): in this ensemble, the number of atoms N, the volume V and the temperature T, and therefore the kinetic energy, are fixed.

- Isothermal-isobaric ensemble (NPT): this thermodynamic state is characterised by a fixed number of atoms N, pressure P and temperature T.

- Grand-canonical ensemble (μVT): this thermodynamic state is characterised by a fixed chemical potential μ , a fixed volume V and a fixed temperature T.

The choice of the ensemble is based on the simulated systems and on the targeted computed properties.

2.2.3.3 Ab initio Molecular Dynamics

Ab-initio Molecular Dynamics[224](AIMD) can be presented as a combination of quantum mechanical electronic structure calculation and classical molecular dynamics calculation. Ab-initio Molecular Dynamics does not rely on the development of an accurate potential force field, but combines electronic structure calculation with finite temperature dynamics to describe events involved in chemical transformations. This method is more expensive but provides more accurate results.

There are three ab-initio molecular dynamics approaches which all rely on the Born Oppenheimer approximation: Ehrenfest MD, Born-Oppenheimer MD and Car-Parrinello MD.

The Born-Oppenheimer MD is based on the Born Oppenheimer approximation, which assumes that the position of the atoms is a function of the propagated forces.[256]

Ab-initio has not been used in this research due to the size of the model studied. Simulating such a large model would lead to significant computational expenses and time.

2.2.3.4 Previous works: the debated role of fluoride ions in PBGs

Both ab-initio and molecular dynamics have been used to model the atomistic structure of fluoridated phosphate-based glasses. The two methods led to opposite results casting ambiguity over the influence of the addition of fluoride to PBGs.

Ab-initio MD of structural changes associated with the incorporation of fluoride in BGs Christie *et al.*[225] used first-principles Born Oppenheimer Molecular Dynamics (MD) simulation to create accurate models of two phosphate glass compositions with different fluoride contents (Table 2.2). The atomic forces were computed from a quantum mechanical representation of the electronic structure. This expensive method is limited to small models, but provides highly accurate results that do not rely on the generation of an empirical force field. The aim of this work was to characterise the atomic

Table 2.2: Simulated Compositions, their densities and size. The fluoride-free F0 composition is included as reference[225]

Composition	P_2O_5 mol %	Na_2O mol %	CaO mol %	CaF_2 mol %	Density (g.cm^{-3})	Number of atoms	Cell size (Å)
F0	50.0	20.0	30.0	0.0	2.585	Not simulated	
F2	49.0	19.6	29.4	2.0	2.593	363	17.0718
F6	47.0	18.8	28.2	6.0	2.610	167	13.9227

structure of fluoridated phosphate-based glasses and the effect of the addition of fluoride on the bioactivity of the glass. The underlying purpose of this study was to verify if as in silicate-BGs, clusters were formed.

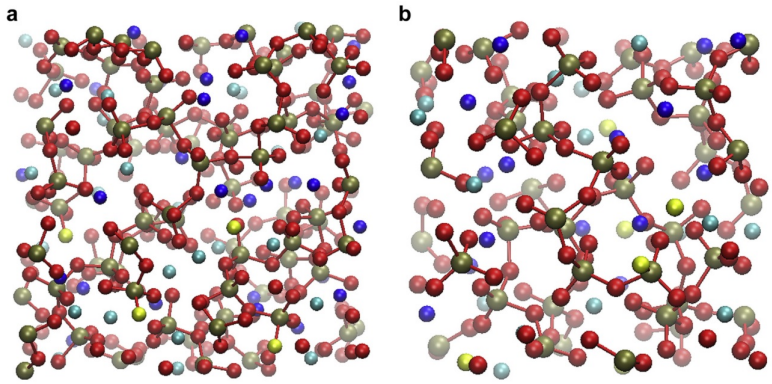

Figure 2.16: Views of the (a) F2 and (b) F6 compositions. The colours are: phosphorus (brown), oxygen (red), sodium (dark blue), calcium (light blue), fluoride (yellow).[225]

Figure 2.16 shows the resulted simulations for the two compositions F2 and F6 (Table 2.2). The incorporation of fluoride has two effects on the bioactivity of the phosphate glasses. The first is the replacement of an oxygen atom in the PO_4 tetrahedron by a non-bridging fluoride atom (Figure 2.17). Indeed, there is a significant P-F bonding, and the tetrahedral structure around the phosphorus is therefore preserved. The change in the structure leads to a decrease in the network connectivity. This is due to the fact that bridging oxygen of the network is replaced by non-bridging fluoride ions, as shown in the schematic Figure 2.18. In other terms, the network chain lengths are reduced with the incorporation of fluoride. A decrease of the network connectivity leads to an increase of the bioactivity of the glass, since the network is more fragmented and therefore more soluble.

The second effect observed with the incorporation of fluoride is the formation of a significant number of clusters in the glass of modifier rich regions and network rich regions. A moderate amount of fluoride tends to bond to modifiers atoms (sodium and calcium), which would tend to create highly soluble regions (modifiers rich region) and poorly soluble ones (network rich regions). However, it has also been observed that this effect is insignificant, since an equal amount of fluoride bonds to the phosphorus.

This study concluded that the addition of fluoride in phosphate-based glasses does not lead to a decrease of bioactivity which is not the case with silicate-based glasses. For this reason, fluoridated phosphate-based glasses were deemed suitable for use as biomaterials based on the results published in this paper.[225]

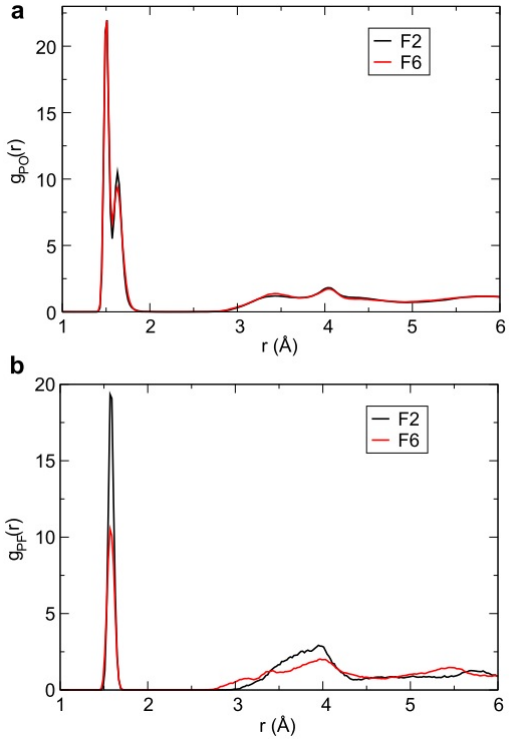

Figure 2.17: Partial pair-correlation functions (a)$g_{PO}(r)$ and (b) $g_{PF}(r)$ for the F2 (black) and F6 (red) compositions.[225]

Classical MD simulation of the structure of fluoridated phosphate bioactive glasses In the work of Shaharyar *et al.*[210], MD simulations with the DL_POLY code[257] are used to obtain atomic-scale models of the glasses. The force field developed and used is based on existing works, and the shell model theory[227,240,258], which is explained in section 2.2.3.1. Oxygen atoms are represented as core-shell units (Os), connected by

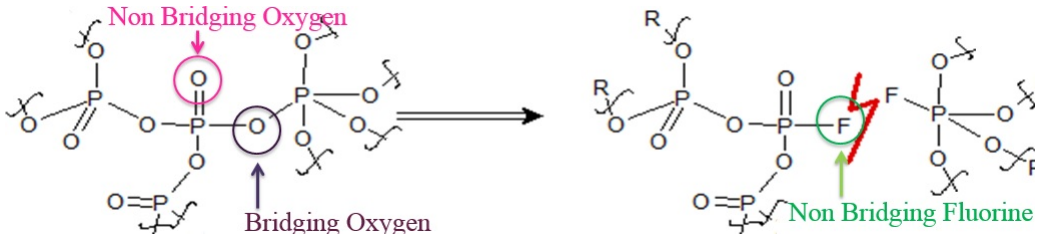

Figure 2.18: Schematic representation of an bridging oxygen replaced by a non-bridging fluoride.[225]

Table 2.3: Simulated Compositions.[210]

x	P_2O_5 mol %	Na_2O mol %	CaO mol %	CaF_2 mol %
0	45	10.0	45.0	0.0
5	45	10.0	40.0	5.0
10	45	10.0	35.0	10.0

a harmonic spring. The interactions between the oxygen atoms and the others such as P, Na and Ca[259] are described using the Buckingham potential, as explained in section 2.2.3.1. The interactions between fluoride atoms and Os, P, Na and Ca are fitted to the crystalline structure of fluoroapatite, difluorophosdphoric acid anhydride, sodium fluoride and calcium difluoride. A three-body harmonic potential is used to control the tetrahedral angle Os-P-Os in the phosphate group but no arbitrary constraints are placed in the inter-tetrahedral structure.

Two compositions are modelled in this study; $(45-x)CaO-10Na_2O-45P_2O_5-xCaF_2)$ where is $x = 5$ and $x = 10$. For each composition (Table 2.3), the simulation is started with a random atom configuration containing approximately 3000 atoms. For $x = 5$ the simulation contains 68 fluoride atoms and 136 for $x = 10$. A reference without fluoride is also included in this study.

The radial distribution function (Figure 2.19) and the Table 2.4 show that the fluoride tends to predominantly bond with the modifiers ions. Only a relatively small amount of fluoride bonds to phosphorus atoms, with a tendency that increases with the amount of CaF_2 incorporated, and this bonding to P does not affect the tetrahedral structure around the phosphorus. It should also be noted that this amount of P-F bonding is initially higher

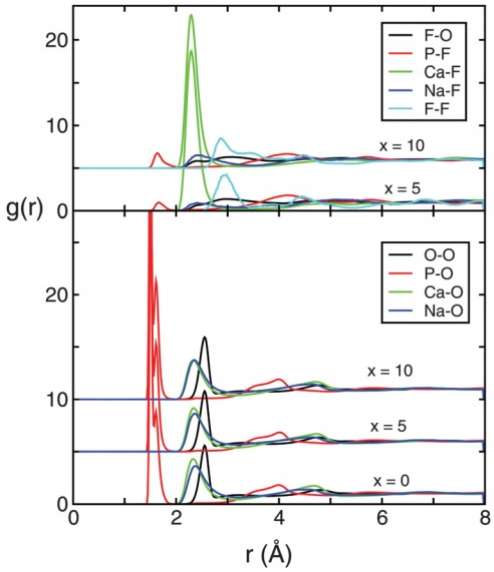

Figure 2.19: Radial Distribution function of the interaction between the oxygen, phosphorus, calcium, sodium and fluoride atoms.[210]

Table 2.4: Q^n distribution function with the corresponding NC.[210]

x	Q^0	Q^1	Q^2	Q^3	Q^4	NC
0	0.08	26.6	68.9	4.4	0	1.78
5	0.58	19.25	73.25	6.9	0	1.87
10	0.61	13.5	77.8	8.0	0.05	1.93

(at higher temperature) which suggests that the system slowly converges to an equilibrium. A much higher amount of fluoride is found coordinated with calcium and sodium, as shown by the sharp peaks in the Ca-F rdfs in Figure 2.19 and the smaller in the Na-F rdfs.

The incorporation of fluoride ions leads to a re-polymerisation of the network by removing the cations from the glass network. Indeed, fluoride tends to associate with the network modifier cations to form alkali/alkine aggregates. The chemical dissolution of the glass is in that sense slowed for a time: until the glass network is broken down by the attack of hydroxy ions and water molecules. At this stage, phosphate-based glasses degrade continuously and the fluoride content no longer has an impact on the chemical durability any more. This work presents very different results from the ab-initio study[225]: they suggest this difference is due to the cooling rate used. However, this observation appears unlikely

since similar cooling rates were used to do ab-initio MD of fluoridated silicate[227] and phosphate[225] glass, and reliable results have been obtained with similar cooling rate.[219–223] One can therefore assume that if results are satisfactory for fluoridated silicate, it should be no different for fluoridated phosphate. Additionally, the article does not mention the potential and parameters used to develop the MD model described in the work of Shaharyar *et al.*.[210]

2.2.3.5 The role of fluoride ions in bioactive glasses

Preliminary modelling experiments using both molecular dynamics and ab-initio have concluded with opposite results , and there is therefore some uncertainty about the behaviour of fluorine in bioactive phosphate glasses. Such ambiguity should be eliminated as fluoridated PBGs are promising materials for dentistry, as they prevent tooth decay, enhance tooth enamel remineralisation and inhibit bacterial infections. It is, therefore, crucial to provide a clear answer on the influence of fluoride ions in PBGs using modelling techniques.

2.3 Bioactivity of silicate-based glasses for cardiac tissue engineering

Since the discovery of the first bioactive glass 45S5 by L. Hench[9], BGs have gained interest for their interaction with soft tissues.[14,55] due to the significant potential BGs exhibit in soft tissue repair.[57–70,80–82]

2.3.1 Silicate based-glasses for biomaterial applications

Since 1969, extensive improvements of the glass composition have been led to the procurement of highly viable materials for the human body; materials performing without forming any scar tissue and enhancing their bonding properties.[50] From those studies, a Na_2O-CaO-SiO_2 ternary state diagram emerged, as shown in Figure 2.20.

45S5 BGs have often been used in built up composite structures, which aim to mimic the

extracellular matrix of the targeted tissue.[9] To do this, various materials can be used such as natural, elastomeric or synthetic polymers. 45S5 glasses composition sits within the range of suitable composition for soft tissue bonding. They, therefore demonstrate potential applications in soft tissue repair and more specifically, in cardiac tissue engineering, , a field of application that has not yet been addressed extensively.

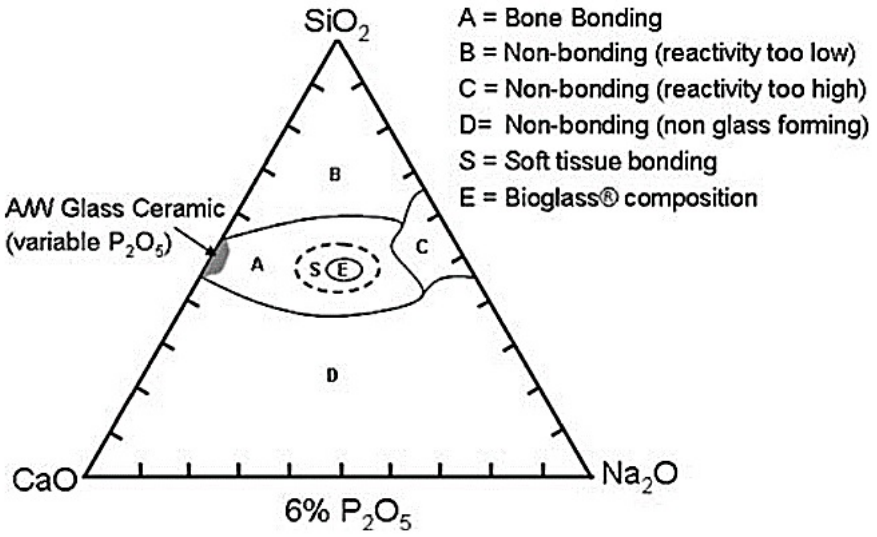

Figure 2.20: Compositional diagram representing the type of tissue bonding properties of bioactive glasses.[9] The name Bioglass® referred to the inital 45S5 glass. (2006) Reproduced with permission of Springer Nature.

2.3.2 Myocardial infarction and cardiac tissue engineering

2.3.2.1 Myocardial infarction

Heart disease is the main cause of death in the Western world.[260] There is therefore here lies a growing need for innovative therapies.

A healthy heart works like a pump and beats at an average of 100,000 times a day. The heart is divided into two sides, separated by an inner wall called the septum. Each side is subdivided into two chambers. The right side of the heart pumps blood to the lungs to collect the oxygen. The left side of the heart receives the oxygen-rich blood from the lungs and pumps it into the body.

A heart attack, also called myocardial infarction (MI), follows a sudden blockage of one or more of the blood vessels supplying the heart or coronary arteries. The blockage leaves

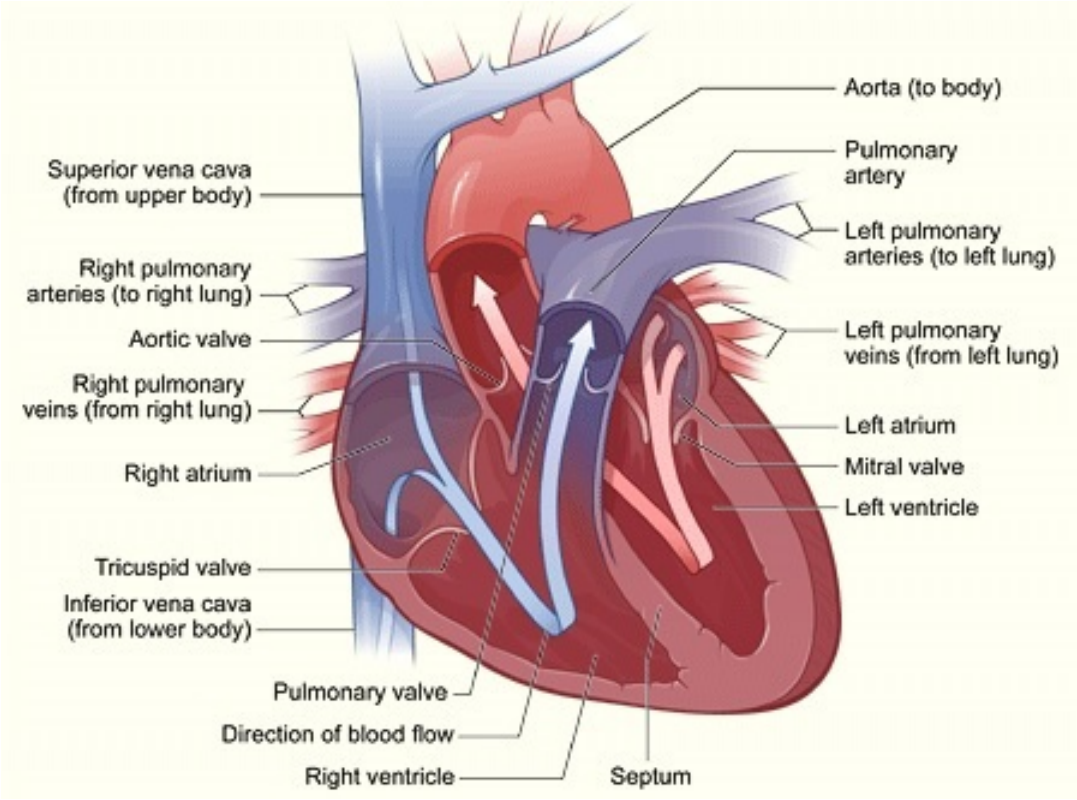

Figure 2.21: The illustration shows a cross-section of a healthy heart and its inside structures.[261]

damaged tissues on the heart which the body does not repair naturally. Instead, a scar is formed as the mature contracting cardiac cells (cardiomyocytes) have a limited capacity to multiply.[262] Moreover, permanent cell death can occur if the blood flow is not rapidly restored within the affected area of the heart muscle. This is due to the abrupt decrease of nutrients and oxygen supply to the heart muscle.

A very alarming condition arises from the presence of these scarred tissues around the heart, as they are unable to conduct electrical or mechanical stimuli, and this leads to a reduction of the pumping efficiency of the heart's main chambers, the ventricles.[83] Faced with this decrease in cardiac pumping efficiency, the heart tries to compensate through several mechanisms such as vasoconstriction (constriction of blood vessels) in order to pump more blood into the heart and provide better pumping force. Vasoconstriction leads to an increase in the blood pressure and heart rate, together with a hypertrophy (enlargement) of the heart muscle and left ventricles dilation.

Initially, this observed vasoconstriction helps the heart to stabilise. However, in the long

term, the constriction of blood vessels can lead to further complications and incremental deteriorations of the heart as they weaken the latter. This subsequent deterioration can ultimately trigger heart failure.[83] More dangerously, if the heart fails to keep blood pressure at the right level throughout the whole body, body function failure can be a result. Unfortunately for patients, the only therapeutic treatment, at this stage is heart transplant, which often involves a tedious and difficult waiting list. They can also be treated with mechanical Ventricular Assist Devices (VADs). In this case, they may face possible complications (bleeding, thrombotic events, infections or failure of the electrical motor). In the face of these difficulties, one can therefore understand the growing need to find a way to regenerate damaged tissues. An interesting and promising method involves the use of cardiac tissue engineered treatments.

2.3.2.2 Cardiac tissue engineering for myocardial infarction

What is cardiac tissue engineering? Cardiac tissue engineering is a highly promising approach to develop efficient and innovative treatments for heart disease.[83] Through this approach, the aim is to mimic the extracellular matrix (ECM) using natural or synthetic polymeric materials.[81] The ECM is an important component of all tissues and organs within the body, as this non-cellular constituent ensures the initiation of crucial biochemical and biomechanical cues needed in various tissue processes e.g morphogenesis, differentiation and homeostasis. Additionally, the ECM acts as an vital physical scaffold for cells and cells' constituents.[84]

The cardiac extracellular matrix is a complex architectural network formed of proteins which give the heart its strength and elasticity, along with glycoproteins, proteoglycans and glycosaminoglycans, which are key to the elasticity of the heart.[263]

Biomimetic materials should resemble the ECM by mimicking its fibrillar architecture and providing the necessary contact guidance for specific cardiac cells to function.[81] The biomimetic material should also exhibit elastic properties to match the systolic pressure of the heart. Degradation characteristics are an additional important parameter to consider. Indeed, degradable materials represent a better alternative to surgery, if the substrate can

be physiologically removed and eliminated by the body system. Finally, tissue engineered materials should respond positively to the cardiac cell environment and exhibit angiogenic properties in order that can stimulate the myocardial regeneration. Ultimately, the aim of these engineered constructs is to support or replace the heart muscle function.

Myocardial tissue properties Myocardial tissue presents a highly hierarchical structure with aligned fibrous cells embedded into 3D honeycomb-like micro-patterns.[264] This 3D pattern represents the extracellular matrix and comprises collagen fibres and other proteins. The use of a scaffold with a fibrous or porous structure therefore appears as a sensible structure for organization, survival and function of the cardiac cells.
Regarding the mechanical properties, an effective cardiac patch should have a Young's modulus ranging from tens of kPa and 1 MPa, as it has been reported that the left ventricular stiffness is around 10-20 kPa at the beginning of the diastole, and in the range of 0.2-0.5 MPa at the end of the diastole.[265] In other studies, it has been reported that the native heart tissue has a Young's modulus ranging from 10-15 kPa.[266] In the case of ischemic tissues (restriction in blood supply to tissues, causing a shortage of oxygen and glucose needed for cellular metabolism) associated with fibrosis (formation of excess fibrous connective tissue in an organ or tissue in a reparative or reactive process), the Young's modulus increases up to 30-50 kPa.[267]

2.3.2.3 Current trends and challenges in cardiovascular tissue engineering

The need for cardiac tissue regeneration has emerged following the discovery that myocytes have a limited regenerative capacity, around 1% of the cells per year at 20 years of age, decreasing to 0.3% by the age of 75.[268] Two main challenges emerge when considering cardiovascular tissue engineering devices: opting for the right type of human cells, and providing a matrix that resembles the cardiac tissues with suitable mechanical properties.[269]

Cellular therapy and engineered constructs Different general approaches have been investigated to regenerate the functional myocardium (Figure 2.22).[270]

- Ventricular restrain (Figure 2.22 bottom-right)
- Cell suspension (Figure 2.22 left)
- Natural or synthetic scaffolds with and without cells (Figure 2.22 top-right)

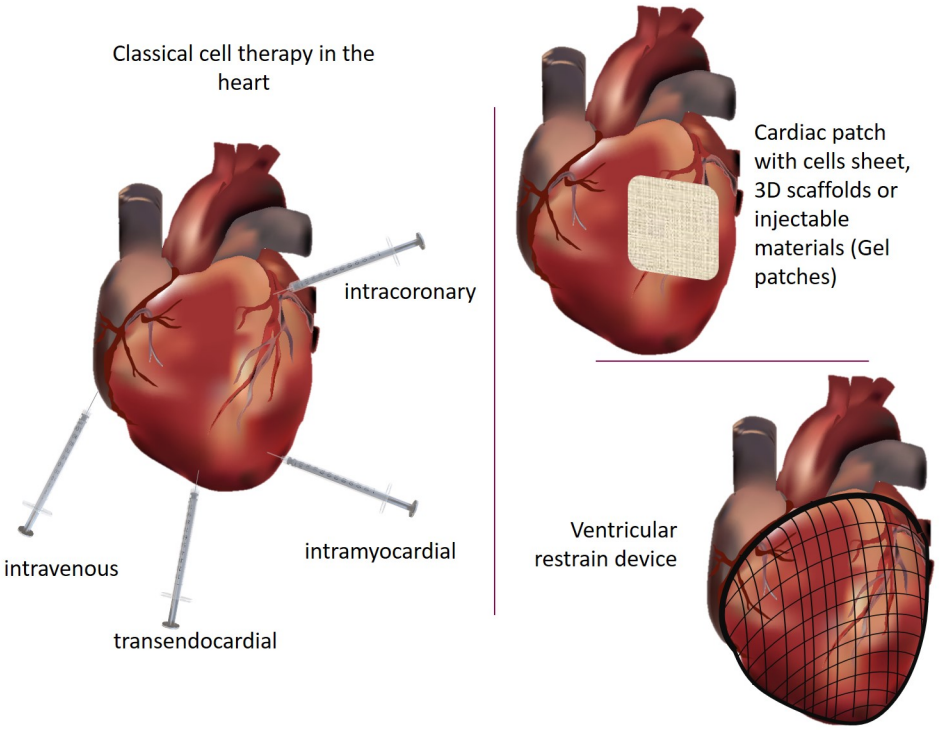

Figure 2.22: Various approaches to treat myocardial infarction.[271]

Ventricular restrain has been considered in many studies to evaluate its use to constrain the left ventricle (LV). This non-transplant surgical therapy involves the use of a prosthetic material to envelop the failing heart and mechanically constrain the latter, and more precisely the left ventricle, at the end-diastole. This constraint prevents further remodelling and helps improve the ventricular function.[272] However, in recent years, fewer and fewer studies have focused on using this kind of device as an efficient treatment for scarred myocardial tissue.[273–275] One study has recently been trialling a ventricular support system, and this has shown promising results in canine models.[274] The very few studies on ventricular restraints demonstrate a decreasing interest, which can be at-

tributed to the invasive procedure required for this approach, and the availability of less invasive and more efficient treatments.[260]

Cell suspensions are used in cardiac cell therapy to heal the scarred tissue. To do this, cells are implanted into or onto the damaged myocardium using different techniques (intracoronary, intravenous, transendocardial and intramyocardial injections).[271] In terms of cells used, studies carried out on animals and humans using a variety of cell types have showed promising results, demonstrating that implanted cells can incorporate themselves into the heart.[63,276] However, this method does not provide long lasting effects as cell tend to migrate away from the site of injection.

Finally, **natural or synthetic scaffolds, possibly combined with cells** and **biodegradable scaffolds** with a structural support to manage the tissue regeneration can be used (Figure 2.22 (top-right)). To engineer these scaffolds, different cell sources and bioreactors have been studied in order to obtain viable and functional tissue.[269] To ensure cardiac cells to repair or regenerate, a matrix providing similar composition, structure and suitable mechanical properties as the cardiac ECM is necessary. This matrix can then be used to seed cells and create a cardiac tissue construct *in vivo*. Similarly, the matrix can be used as an inducer for the cells to grow their own matrix.[277] Synthetic or natural biocompatible constructs design to mimic the hierarchical structure and mechanical properties of the heart matrix can be used for this purpose.[269] New emerging technologies aim to combine degradable scaffolds with bioactive particles, which will help the scarred tissue to regenerate. It is believed that this acellular therapy can support cellular differentiation and organisation with an adequate micro-environment and architecture. Indeed, cells respond to their environment and one of the key components affecting cell behaviour is the ECM.[269]

These different trends reflect two main features that should be considered when designing a cardiovascular tissue regeneration solution: the importance of considering the ECM (its molecular composition, hierarchical structure and biomechanics) and considering how the cells need to remodel the initial matrix and progressively replace the damaged cells.

Hereafter, challenges lie in the choice of the material (natural, synthetic or a combination of both, with or without pre-seeded cells) and the type 3D structure of the construct to support cell viability, vascularisation and matching mechanical properties of myocardium.

Current challenges arising from the mechanical properties The stiffness of the infarcted myocardial tissue changes shortly after an infarction and becomes stiffer when a scar is formed; this is also referred to as cardiac remodelling.[269,278–280] The design of cardiac scaffolds should consider variations of mechanical properties with time. Currently, biomaterial scaffolds for cardiac tissue engineering are designed in many different forms.[260,281] Porous and fibrous scaffolds are often manufactured to provide macroscopic voids for the migration and infiltration of cells, and to mimic the hierarchy of the native ECM allowing control over the cellular alignment.[260,281,282] Additionally, the fabrication techniques play an important role in the mechanical properties, as additive manufacturing or electrospinning can produce various structure exhibiting a certain range of mechanical properties (stiffness and elastic moduli).[269]

Natural and synthetic materials for cardiac tissue engineering An additional important factor is the choice of the material used for the scaffold.[283] Natural materials such as collagen, fibrinogen, chitosan, gelatin, elastin and silk, can trigger signalling pathways affecting cells using surface receptor interactions, uptake, and degradation by cell-instructive enzymes mechanisms.[264,269] One of the disadvantages of working with natural materials are the difficulties encountered when trying to process them without disrupting potentially important hierarchical features.[269] Hydrogels formed from natural materials have been considered as a potential solution, but they tend to exhibit poor mechanical properties.[284] On the other hand, synthetic materials offer a wide range of tunable properties in terms of mechanics, chemistry and degradation. However, their biocompatibility and cellular interaction behaviour should be closely monitored.[270,285–290]

2.3.3 Silicate-based bioactive glasses for cardiac tissue engineering patches

Bioactive glasses have been considered as a use in cardiac patches in combination with poly(glycerol sebacate)(PGS).[291] In this work, PGS was chosen to provide the necessary mechanical flexible support, while the BGs improve the mechanical properties of the patch and provide a foothold for the cells to develop and differentiate. Those elastomeric patches were firstly developed by Chen et al.[292], with ranging concentration of BGs from 0% to 10%wt, and the study of their degradation behaviour has shown that the addition of BGs does indeed counteract the acidity caused by the degradation of PGS. Indeed, the degradation products of PGS lead to an acidic environment and cellular toxicity, especially when the polymer contains a high amount of unreacted carboxylic acid groups.[293] It has been reported that the acidic degradation products of the polyesters lead to an inflammatory response and therefore limit their ability to be used as a scaffold for cardiac tissue engineering.[292] To tackle this issue, the use of slightly alkaline nano-fillers such as 45S5 Bioglass have been investigated as a solution.

In terms of mechanical properties, the Young's modulus (describing the tensile elasticity, or the tendency of the patches to deform) and strain at break of the samples increased along with the percentage of BGs particles incorporated. Those results confirmed the positive effects of the addition of BGs into PGS scaffolds.[294] Concerning the biocompatibility, the *in vitro* proliferation of mouse fibroblasts was investigated and it was observed that the nanocomposite/PGS samples provided a greater proliferation of the fibroblasts than on the pure PGS. In the same way, it was concluded that the addition of BG particles led to the decrease of the cytotoxicity on human embryonic stem cell-derived cardiomyocytes in comparison to pure PGS. In that sense, the addition of bioglasses which degrade slowly *in vivo* could be used as a degradation kinetics regulator to meet the clinical requirements in terms of tissue regeneration. Those promising results show the potential of the PGS-BGs scaffold for a use in cardiac tissue engineering with suitable mechanical properties and better biocompatibility.

2.3.4 Technology for cardiac regeneration and repair

The various requirements for functional cardiac tissue scaffolds have led to the development of different fabrication approaches and material utilisations for cardiac tissue repair.[295] Indeed, national statistics show quite dramatic results, with around a million people affected by heart failure in the UK each year resulting in 36,000 deaths each year. Additionally, heart disease is nowadays the leading cause of death and disability in the world, with an estimated 15 million people dying from strokes and heart attack in 2016 according to the World Health Organisation[260], with the most common cause of heart disease being myocardial infarction.[265,296] Various approaches have been developed to regenerate the functional myocardium[270], such as cell suspension[63,276], natural or synthetic scaffolds with and without cells[269] and ventricular restrains.[273–275] Biomaterial scaffold architecture plays a key role in most tissue engineering strategy. Indeed, biomimetic materials should mimic the extracellular matrix of the tissue of interest in order to have the desired effect on tissue regeneration. The main idea in engineered cardiac tissue is to reconstruct a structurally similar and functional replica from damaged tissue. The manufactured constructs should exhibit sufficient elastic properties, suitable biocompatibility and enhance cell regeneration.[297] Different manufacturing techniques have been developed in order to obtain satisfactory scaffolds, such as electrospinning[298], three dimensional printing[299] or cell sheet technologies.[300] In this project, the focus was on fast, efficient and reliable techniques to manufacture cardiac patches such as electrospinning and three-dimensional printing. Electrospinning allows the manufacture of a matrix mimicking the extra cellular matrix of the cardiac cells in order to provide a much needed interface for cardiac cells to attach and grow. Three-dimensional printing is a useful tool to obtain repeatable mechanical properties over a large number of patches.

2.3.4.1 Electrospinning

Electrospinning has emerged, in the recent years, as an inexpensive, efficient and leading method to fabricate fibres with diameters down to tens of nanometers.[298] With this

method, fibres, from a rich variety of materials including polymers, composites, and ceramics, are fabricated. This strategy involves the formation of bioresorbable and biocompatible materials into 2D scaffolds, that mimic native tissues or organs. An electrospun scaffold can therefore endorse numerous important roles in tissue engineering, such as mimicking the extra cellular matrix (ECM), modulating cell proliferation and differentiation (depending on the structure) and being a carrier of bioactive signalling molecules. Electrospun scaffolds provide a framework for tissue engineering and help to stabilise cells and protect infiltration from surrounding tissue.[297]

Overview of the technique The basic electrospinning set-up[298] consists of three major components: a high-voltage power supply, a spinneret (a metallic needle), and a collector (a grounded conductor)(figure 2.23).The metallic needle is connected to a syringe in which the polymer solution (or melt) is put. A syringe pump is used to push the solution through the needle at a constant and selected rate. When a high voltage is applied, the drop of polymer solution present at the tip of the needle becomes highly electrified. At this point, the drop experiences two major types of electrostatic forces: the electrostatic repulsion between the surface charges and the Coulomb force applied by the external electric field.[298] As a result, the liquid drop is distorted into a conical object, commonly known as the Taylor cone. When the strength of electric field becomes greater that a threshold value, the electrostatic forces overcome the surface tension of the polymer solution and thus trigger the ejection of a liquid jet from the nozzle. This highly electrified jet then goes through a stretching and whipping process, which forms a long and thin thread. As this liquid jet is continuously elongated and the solvent evaporates, its diameter can be reduced from hundreds of micrometers to as little as tens of nanometres The charged fibres are attracted by the grounded collector and settle as a randomly oriented, non-woven mat. The main parameters which are set and greatly influence the shape and size of the fibres are: the voltage applied, the speed at which the liquid is pushed out of the needle, the distance between the collector and the metallic needle, and the type of solution electrospun.

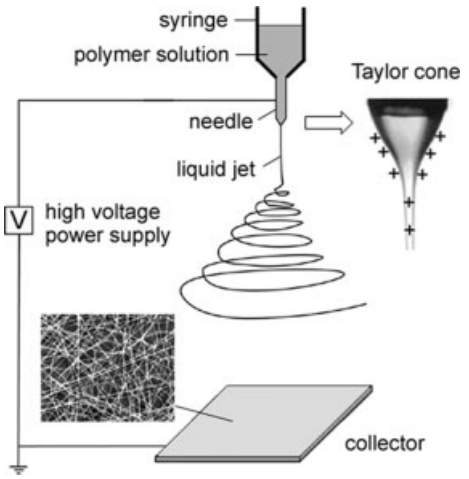

Figure 2.23: Schematic illustration of the basic set-up for electrospinning.[298] (2004) Reproduced with permission of John Wiley and Sons.

Control of the morphology and diameter The morphology and diameter of electrospun fibres can be controlled by a number of processing parameters such as[298]:

- the intrinsic properties of the solution such as the type of polymer, the conformation of polymer chain, viscosity (or concentration), elasticity, electrical conductivity, and the polarity and surface tension of the solvent;

- the operational conditions such as the applied electric field, the distance between the collector and the metallic needle, the speed at which the liquid is pushed out of the needle;

- other variables such as the humidity and temperature of the surroundings.

The presence of beads, constituted of a heap of non-fibrous polymeric material, in electrospun fibres is a very common problem.[301] This problem was investigated by looking at the influence of solution properties on the density of beads contained in the electrospun fibres. It was found that the viscosity, surface tension, and the density of net charges carried by the liquid jet all influenced the morphology of resultant fibres. However, the formation of beads could be attributed to the action of three main forces:

- the surface tension tends to convert the liquid jet into one or many spherical droplets due to the minimization of surface area[302];

- the electrostatic repulsion between charges on the jet surface tends to increase the surface area, which favours the formation of a thin jet rather than beads;

- viscoelastic force also resists rapid changes in shape and supports the formation of fibres with smooth surfaces.

To summarize, the formation of beads can be eliminated if the influence of surface tension is offset by the effects of the last two forces. Indeed, the more viscous the solution, the less often beads are observed. The addition of salts to increase the net charge density, or the use of solvents with lower surface tensions could also lead to the effective elimination of beads.

Electrospinning represents a highly promising technique; however, it presents one major drawback, namely that porous scaffolds fabricated by random processes cannot be produced with complete control of the geometrical parameters, such as pore size, pore interconnection size and porosity.[303] However, this issue has been addressed in this project, as scaffolds with controlled pore and geometrical parameters were fabricated.

Electrospinning for cardiac tissue engineering Electrospinning finds its adequacy for cardiac tissue engineering because electrospun nano-fibres morphologically mimic the natural extracellular matrix of the heart, constituted of continuous fibres ranging from nano to micro scale with high porosity and variable pore size distribution.[264]

Beyond the morphological similarities between electrospinning and the ECM of the heart, electrospinning is a versatile method that manufactures a variety of nano-fibrous structures using a plethora of available materials. Electrospinning is a simple low-cost technique, and is adaptable to both a biological laboratory and also for industrial applications. Additionally, advances within the field enable the development of reproducible and varied constructs. For instance, aligned nano-fibres can be produced using high speed rotating drums and mandrel collectors and could be used in the repair of myocardial infarctions.[304] Collectors can also be designed with a specific structure depending on the targeted applications e.g valves or blood vessels. For example, a honeycomb micro-frame was used to electrospin a layer of natural polymeric fibres, which was then cross-linked into a mesh

with controllable pore size.[305,306]

2.3.4.2 Three-dimensional Printing

Three-dimensional printing (3DP), also referred to as layered manufacturing, rapid prototyping or additive manufacturing, is an innovative development in the field of manufacturing.[299] 3DP is a technology developed in the early 1990s at Massachusetts Institute of Technology (MIT, Cambridge, MA).[307] Three-dimensional printing builds the solid volume from a model by successively adding material layer by layer. 3D printing technology has recently gained greater interest due to the potential applications in tissue engineering, and the ability to create a 3D object of virtually any shape from a computer assisted designed (CAD) model.[303] There is now increasing interest in 3D-printed biopolymers. Indeed, combining 3D printing and biopolymers has been shown to have great potential in tissue engineering applications. The aim of 3D-printed scaffolds for tissue engineering is to construct a biomimetic structural environment that facilitates the repair and regeneration of soft and hard tissues.

Overview of the technique Modelling is the first step of 3DP. To do this, virtual models CAD or animation modelling software and "slices" are designed and computed into digital cross-sections, so that the printer can successively use them as a guideline to print.[303] A binding material is then deposited on the build bed or platform, until the material/binder layering is complete and the final 3D model has been printed. During this step, the machine reads the design and lays down the successive layers of liquid, powder, or other materials to build the model from a series of cross-sections until the 3D printed object is finished. Many different ways of 3D printing techniques exist[303]:

- selective laser sintering (SLS): the slices are written by a carbon dioxide (CO_2) laser beam;
- stereolithography (SLA): thin successive layers are photocrosslinked by ultraviolet or visible light which induces photopolymerisation of a reactive system according to a sliced CAD model[308];

- fused deposition modelling (FDM): small temperature-controlled extruder forces out a thermoplastic filament material and deposits the semi-molten polymer onto a platform in a layer by layer process. The monofilament is moved by two rollers and acts as a piston to drive the semi-molten extrusion. At the end of each finished layer, the base platform is lowered and the next layer is deposited[309],

- direct metal laser sintering (DMLS).[303]

They differ with regard to the materials which can be used and in the way the layers are deposited to create parts. For bio-polymers, the most commonly used processes are SLS, SLA, and FDM.[303,310]

Three-dimensional printing for cardiac tissue engineering Three-dimensional printing represents a promising technique to overcome the usual limitations of the fabrication of 3D constructs for myocardial tissue engineering. Indeed, one of the main limitations is the availability of oxygen necessary to the survival of cells.[311] 3D printing is a technique that allows the manufacture of scaffolds, integrating open pores or channels that allow oxygen to easily reach the middle region of the construct, and to allow larger constructs to be built *in vitro*.[312] Another solution investigated was how to increase the cell density within the construct.[313] However, this has proved to be a difficult task. Indeed, current methods providing proper vascularisation have not reached the metabolic high-density requirements of these cardiac tissues. This will result in significant cell death, as cardiomyocytes do not proliferate. To overcome these issues, 3D printing has been considered for many applications, such as cardiac valve, coronary vasculature and myocardial tissue printing.[314]

The biomaterials used to produce scaffold for cardiac tissue engineering can be natural polymers including collagen, synthetic thermoplastics, such as poly(glycolic acid) or poly(lactic acid), or elastomers such as poly(glycerol sebacate).[82]

2.3.5 Natural materials for cardiac tissue engineering

Natural polymers have intrinsically the necessary biochemical properties for cells attachment and proliferation.[264] Additionally, their degradation products are non-toxic and have a low immune response. The common natural polymers used in cardiac tissue engineering include collagen, fibrinogen, chitosan, gelatin, elastin and silk.

Among the many materials investigated for the making of cardiac patches, collagen, the predominant protein in the extracellular matrix[260] has been regularly used, both alone and with cells. For cardiovascular engineering, the collagen forms of interest are the types I and III which are the main components of myocardial tissue ECM. Collagen has a long-standing safety record in terms of biological applications.[315]

Collagen used as 3D printed scaffold was shown to increase angiogenesis.[276] The application of a 3D printed collagen scaffold, seeded with human mesenchymal stem cells, led to positive results with a reduction in left ventricle interior diameter in the contraction phase (systole), an increased anterior wall thickness, and a 30% increase in fractional shortening (the fraction of any diastolic dimension that is lost in systole). The authors concluded that pluripotent human mesenchymal stem cells (hMSCs) can be efficiently delivered to a site of myocardial injury using a collagen cardiac patch, and such delivery results in improved myocardial remodelling after infarction. Giraud et al.[316] showed that the use of cardiac patches made of a combination of collagen type I and rat skeletal muscle cells, improves fractional shortening within 4 weeks.

Dvir et al.[317] designed cardiac patches with an alginate based scaffold, seeded in neonatal cardiomyocytes (cardiac muscle cells) and insulin-like growth factor-1 (IGF-1), stromal-cell derived factor 1 (SDF-1), and vascular endothelial growth factor (VEGF) (figure 2.24). After 28 days, having been vascularized on the omentum (a fold of peritoneum connecting the stomach with other abdominal organs) and transplanted onto infarcted rat hearts, the cardiac patches showed structural and electrical integration into the host myocardium. Additionally, thicker scars were observed which would prevent further dilation of the chamber and ventricular dysfunction.

Collagen, on its own and as part of a blend, has also been electrospun and used to pro-

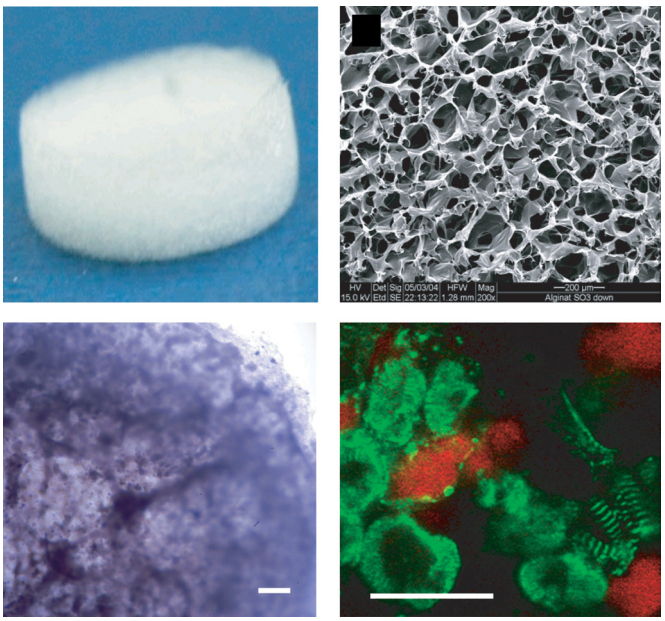

Figure 2.24: Construction of a cardiac patch in an alginate-sulphate/alginate scaffold capable of binding and releasing mixture factors.[317] (2009) Reproduced with permission of The Proceedings of the National Academy of Sciences.

duce a nearly ideal scaffold for tissue engineering.[318,319] Collagen electrospun fibres have been used as supports for cardiomyoblasts culture and for the delivery of human induced pluripotent stem cells in a mouse mode.

The use of natural polymers presents many advantages and would appear a natural choice for tissue engineering. However, there are also some major drawbacks: poor mechanical performances have been reported.[265] Most of these polymers require an extra crosslinking step to become insoluble in aqueous solutions such as culture media. This crosslinking step may affect not only their 3D structure and porosity, but also their biocompatibility, due to the introduction of non-biocompatible chemical agents.[266]

2.3.6 Synthetic polymers of interest for cardiac tissue engineering

There has been considerable investigation of synthetic polymers as they enable better control over mechanical and degradation properties of the scaffold. Two types of polymers can be used as graft for cardiac tissue engineering: polyesters, such as poly(caprolactone),

poly(lactic acid) and poly(glycolic acid), or elastomers such as polyurethane, poly(ethylene glycol) and poly(glycerol sebacate). Biocompatible and biodegradable polyesters with controllable mechanical and morphological properties[270,285] are easy to manufacture, providing structural support to the heart and improving cardiac function of the latter[286] by supporting cell growth[287–290].

A biodegradable polymer degrades and is transported away from the site of action in the body, but is not necessarily removed from the body. The degradation products of a bioresorbable polymer are completely eliminated from the body with no residual side effects.[88]

Elastomers are more flexible and therefore exhibit mechanical properties which are closer to that of the heart.[320] They can exhibit high elasticity to endure strong deformation forces, prevent the cells from detaching[82,321] and can be synthesised with thermoresponsive properties.[322] Like polyesters, they are biocompatible and biodegradable and can provide structural support to cells.[323–325]

2.3.6.1 Poly(Glycerol Sebacate)

PGS is a biodegradable polymer increasingly used in biomedical applications.[326] This crosslinked elastomer is relatively inexpensive to synthesise and exhibits bioresorbable properties, as it can degrade and the degradation products are eliminated through natural pathways.[327,328] Additionally, the degradation and mechanical properties of PGS can be customised by the synthesis parameters.[329] This semi crystalline polymer has a crystallisation temperature of -18.50°C and a melting temperature 9.6°C.[330] PGS has shown potential application in nerve[331], cartilage[329], retinal[332] and vascular tissue engineering[333] along with repair of tympanic membrane perforation[334] and drug delivery.[335] Recently, due to its potential and low price, it has been investigated for cardiac tissue engineering.[305,336] Indeed, polymeric heart patches have been developed with elastomer polymers to provide the necessary mechanical support to the left ventricle of the heart. In this project, PGS was, therefore, used to manufacture cardiac patches to provide the mechanical properties needed for cardiac tissue engineering.

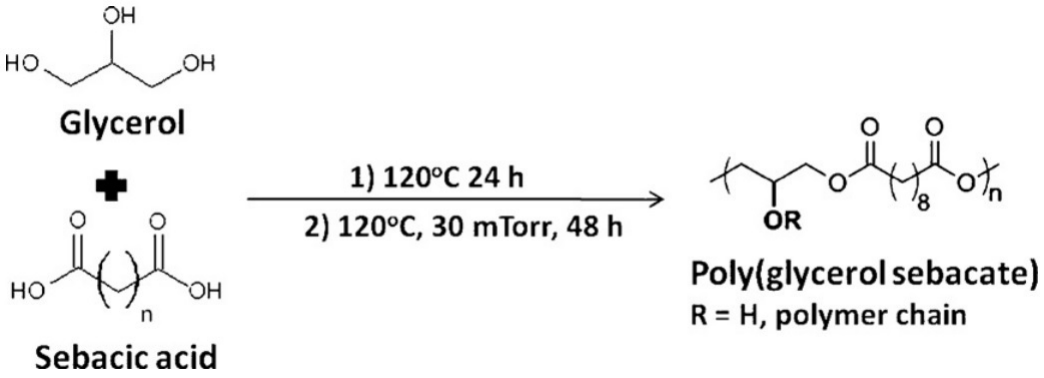

Figure 2.25: Reaction scheme for the chemical synthesis of poly(glycerol sebacate).[336] (2012) Reproduced with permission of The Proceedings of Elsevier.

Synthesis Poly(glycerol sebacate) is commonly synthesized from glycerol and sebacic acid[336] as shown in figure 2.25. The first synthesis of PGS was performed by Wang et al..[326] The synthesis of PGS can be divided into two main steps: poly-condensation and crosslinking. In the poly-condensation step, an equimolar mixture of glycerol and sebacic acid is reacted at 120°C and under argon for 24 hours, before reducing the pressure from 1Torr to 40mTorr over 5h. During the crosslinking step, the mixture is kept under vacuum (40 mTorr) and 120°C for 48 hours. The method is the most commonly used for synthesising PGS. Studies have been conducted to modify the properties of PGS by changing parameters such as the molar concentration of the reactants[329] and the synthesis temperature[337]. However, the synthesis method was kept as shown above.

Visually, PGS is a see-through slightly yellow polyester. Figure 2.25 shows its chemical structure. PGS can be analysed by FTIR and NMR. The level of cross-linking due to the amount of ester linkage formed during the second step can be controlled (increase with the curing and temperature) and followed by FTIR. When the curing time increases, the FTIR spectrum shows a reduction in the carboxylic acid O-H bend at 1418cm^{-}1.[338] Additionally, FTIR results show the reduction of the O-H stretch bands at 3300 cm^{-}1, demonstrating that the acid groups reacted with the alcohol group to form an ester bond.

Mechanical properties The strain-stress of PGS can be measured through tensile tests; PGS exhibits non-linear stress-strain behaviour which is characteristic of elas-

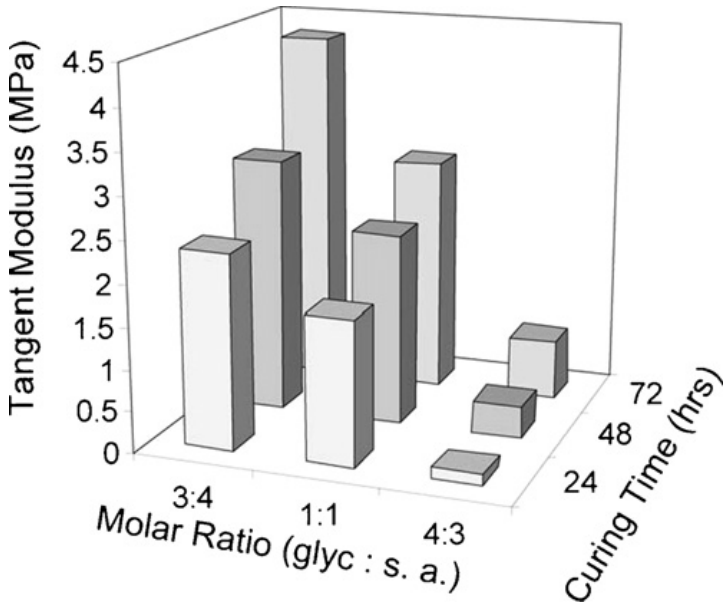

Figure 2.26: Tangent modulus (at 10% strain) values for PGS cylinders with various processing parameters.[329] (2010) Reproduced with permission of John Wiley and Sons.

tomeric material.[265,339] This elastic characteristic is due to the covalently cross-linked, three-dimensional network of random coils, with hydroxyl groups attached to its backbone; both the cross-linking and the hydrogen bonding interactions between the hydroxyl groups contribute to its elastomeric properties.[340]

The mechanical properties of PGS depend on three processing parameters:

- curing temperature: the influence of curing temperature on the mechanical properties of PGS was studied and Young's modulus values were of 0.056 MPa, 0.22 MPa and 1.2 MPa, were recorded for curing temperatures of 110°C, 120°C and 130°C, respectively.[265]

- molar ratio of glycerol to sebacic acid; as shown in figure 2.26 increasing the glycerol molar ratio decreases the tangent modulus and vice versa.[329]

- curing time: as shown in figure 2.26, the tangent modulus increases with increasing curing time.[329]

When synthesised in a 1:1 ratio at 120°C and cured for 48 hours, PGS materials have average tensile Young's modulus in the range 0.0250 to 1.2 MPa, the ultimate tensile strength is 0.5 MPa and strain to failure greater than 330%.[265,331,339] The Young's modulus of PGS is between that of ligaments (kPa range)[336,341] and the myocardium of the

human heart, which ranges between 0.02 and 0.5 MPa, and its maximum elongation is similar to that of arteries and veins, which is up to 260%.

Physiochemical and biodegradation properties Polymer degradation is defined as "the chemical reaction resulting in a cleavage of main-chain bonds producing shorter oligomers, monomers, and/or other low molecular weight degradation products." [342]

Many studies have been carried out to understand the degradation behaviour of PGS *in vivo* and *in vitro* [339,343] and it was established that PGS undergoes surface degradation; the main mechanism of degradation being the cleavage of the ester linkages. This surface degradation process is responsible for a slow loss of mechanical strength (tensile properties), relative to mass loss (per unit original area). Additionally, while the mass loss changes linearly with time, some detectable swelling and better retention of geometry occur. As explained in Part 2.3.7.1, there is a degradation behaviour discrepancy between *in vivo* and *in vitro* experiments due to the action of some enzymes.

One very interesting property concerning PGS is that its degradation kinetics can be controlled by diverse processing parameters such as the curing time and temperature. [265] These parameters were studied in order to match the characteristic of the heart tissue recovery kinetics and it has been concluded that the degradation kinetics of PGS synthesized at 110°C was faster than that of PGS synthesized at 120°C, while PGS synthesized at 130°C showed no evidence of degradation. [336] Therefore, in this project, PGS was synthesised at 120°C to obtain an adequate degradations kinetics.

The degradation properties of the polymers have also been studied *in vitro* and *in vivo* and it has been observed that PGS degrades in the body quite rapidly, with a complete absorption *in vivo* within 6 weeks, while the injured heart is still in the process of recovering. [331] *In vitro* tests shown that the same sized PGS samples remained without any degradations for longer than three months. [293] This difference between *in vivo* and *in vitro* degradations of PGS was caused by the hydrolysis of the ester links in the polymer chains, similar to the decomposition of fats in the body. It was concluded that the rapid degradation of PGS *in vivo* is due to the catalytic function of enzyme esterases, which

are specialised in catalysing the hydrolysis of fats in the body.[82]

Biocompatibility The biocompatibility properties of PGS originate from the starting reactant used in its synthesis. Indeed, glycerol is a basic building block for lipids, while sebacic acid is a natural metabolic intermediate in the oxidation of medium to long fatty acid.[337,339,344,345] It should be noted that glycerol and all of its copolymers have been approved by the Food and Drug Administration (FDA).[339,346] The degradation products are therefore metabolised by the body naturally. The synthesis itself is also biocompatible as no additives, solvents or catalysts are used during the process.[336,347,348] However, the biocompatibility properties of any material are not only dependent on its chemical products, but also on factors such as density, surface porosity, surface hydrophilicity, surface energy, the environment where it is implanted and the material degradation products.[349,350]

To assess how the cellular behaviour is affected by the degradation products Schwann cells were exposed to PGS and Poly Lactic-co-Glycolic Acid (PLGA) extracts. PGS is often compared to PLGA, as the synthetic polymer is often used in tissue engineering applications and exhibits a resorption time similar to that of PGS. Results showed that cells cultured in both PGS and PLGA samples had comparable metabolic rates, attachment, or proliferation and both polymers showed no cytotoxic effects in contact with the cells as no apoptosis was witnessed.[351] PGS showed positive tissue response in comparison to PLGA as significantly less inflammation and fibrosis, and no detectable swelling was observed with PGS extract during degradation. This study was performed to demonstrate the good performance of PGS for neural applications.

In vitro tests shown that fibroblast cells in contact with PGS (and PGLA as control) exhibit a normal morphology and higher cell growth rate.[339]

In vivo biocompatibility tests were conducted with Sprague-Dawley rats. The study revealed that the inflammatory response of PGS was similar to that of PLGA. Indeed, PGS induced insignificant fibrous capsule formation.[339] A fibrous capsule is a layer of connective tissue that is formed due to a biological response to an implanted foreign material.[351]

In terms of cardiac tissue engineering, the focus is on polymers exhibiting adequate bio-

compatibility with cardiac tissue and extra cellular matrix.

The native myocardium is composed of cardiomyocytes, cardiac fibroblasts (CFs) and endothelial cells.[352] *In vitro* and *in vivo* biocompatibility of PGS with cardiomyocytes and CFs was assessed.[352,353] The ability of PGS to provide desired attachment of the seeded cardiomyocytes and retain healthy beating cells *in vitro* without any detachment of the cells was assessed.[352] This is a necessary property for cardiac tissue engineering.

The behaviour of CFs in contact with PGS has also been studied.[353] This study demonstrated the biocompatibility that PGS exhibits with CFs, making this material more suitable for use as cardiac biomaterial. *In vivo* study was also carried out in rats on infarcted myocardium. After 2 weeks of implantation, the scaffold was vascularised, assessing furthermore the excellent biocompatibility of PGS and cardiomyocyte tissues.

In order to enhance PGS biocompatibility properties and mechanical properties, numerous approaches have been studied[354] whether chemical (grafting of hydrophilic groups[355]), physical (surface treatment with sodium hydroxide[356]) or biological modifications (enzyme treatment, coating with biocompatible molecules such as laminin, fibronectin, fibrin, collagen or elastin.[357]). Through these different approaches, material-cell interactions can be improved and this will ultimately broaden the range of applications for PGS-based scaffolds.

2.3.6.2 Poly(caprolactone)

Poly(caprolactone) (PCL) is a functional polymer that has been studied extensively.[358] This polymer is an aliphatic polyester composed of hexanoate repeat units (Figure 2.27). The physical, thermal and mechanical properties of PCL are functions of its molecular weight and its degree of crystallinity. PCL can reach a 69% degree of crystallinity.[359] PCL exhibits a slow degradation through the hydrolysis of its ester linkages and the subsequent elimination of the resulting fragment by macrophages and cells.[360]

PCL exhibits biocompatibility properties, as its degradation by-products are non-toxic and usually metabolised and eliminated by organisms in the body.[359] Additionally, its slow degradation ensures that its mechanical properties are maintained over a long period

of time. PCL has a low glass transition temperature of -60°C and is therefore in a constant viscous state at room temperature.[297] Consequently, PCL and its copolymer were extensively used in numerous drug-delivery devices during what has been referred to as the 'resorbable-polymer-boom' of the 1970s and 1980s.[361]

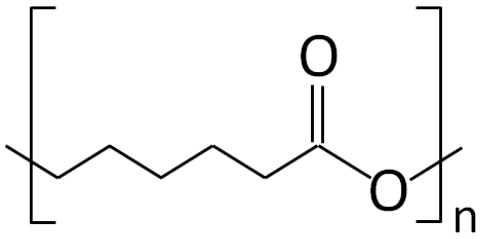

Figure 2.27: PCL structure

Two methods can be used to prepare PCL[362]:

- The condensation of 6-hydroxycaproic (6-hydroxyhexanoic) acid
- The ring-opening polymerisation (ROP) of ϵ-caprolactone.

Physiochemical and biodegradation properties PCL can be degraded by outdoor living organisms (bacteria and fungi). However, it is not biodegradable in animal and human bodies due to the lack of necessary enzymes.[363] Nonetheless, it does not mean that PCL is not bioresorbable but rather that the process takes a great amount of time. The degradation of PCL varies from 2 to 4 years depending on the starting molecular weight.[364] From the *in vivo* and *in vitro* studies, it can be concluded that despite PCL being hydrophobic it endures a slow two-stage degradation process, triggered by the susceptibility of its ester linkage to hydrolysis.[358,359,361,365] The first stage is therefore the non-enzymatic hydrolytic cleavage of ester groups, followed by the intracellular degradation when the polymer is more crystalline and of lower molecular weight (less than 3000 Da/dalton). During the second stage, the polymer is fragmented and degraded by phagosomes of macrophages and giant cells.[366]

The degradation of PCL first starts with the hydrolytic degradation of its poly(α-hydroxy) esters via surface degradation pathways. The latter is determined by a diffusion reaction phenomenon. This surface degradation or erosion begins with the hydrolytic cleavage of the polymer backbone, but only on its surface.[88] The phenomenon occurs when the

amount of water intrusion into the polymer is smaller than the rate of hydrolytic breakage and the production of oligomers and monomers. Following this event, a thinning of the polymer is observed over time, with no impact of the molecular weight on the internal bulk part of the polymer. This process gives PCL a great advantage when it comes to drug delivery applications.[367,368]

Bulk degradation is witnessed when the water diffuses within the entire bulk of the polymer which triggers hydrolysis throughout the entire matrices of the polymer. This phenomenon will lead to the reduction of the average molecular weight due to the scission of hydrolytic chain.[365] An equilibrium for this diffusion-reaction phenomenon is then achieved. However, if this equilibrium is disrupted, the degradation mechanism could produce an acidic gradient, via the carboxyl and hydroxyl end group by-products. Indeed, in the case of bulk degradation, the newly generated carboxyl end group formed during ester bond cleavage could accumulate. Subsequently, the internal degradation accelerates in comparison to the surface, leaving an outer layer of higher molecular weight skin with a lower molecular weight, degraded interior. The degradation mechanism then relies on two molecular weight distributions. When the inner polymer is small enough, it diffuses expeditiously through the outer layer. An onset weight loss and a decrease of chain scission is then observed. An inflammatory reaction resulting from the rapid release of oligomers and acid-by products can then be witnessed.[369] Additionally, the physical shape of PCL has been shown to have no direct effect on the degradation rate, suggesting the a homogeneous degradation dominates the process.[361,370]

A long term *in vivo* (in rats) degradation study of PCL was conducted for 3 years.[371] Using radioactive tritium labelling, the distribution, absorption and excretion of PCL was traced. Results revealed that PCL capsules with an initial Mn of 66,000 g/mol stayed intact in shape for up to two years after implantation, and ruptured down to low Mw (8000 g/mol) pieces after 30 months. The Mw of PCL was shown to decease in a linear way with time (66,000 g/mol at 0 month, 24,000 g/mol at around 16 months, 15,000 g/mol at 24 months and 8,000 at 30 months).

To investigate the absorption and excretion of PCL (Mw 3000 g/mol), tritium-labelled

PCL was implanted subcutaneously in rats. The radioactive tracer and excreta were first detected 15 days post-implantation in both plasma and faeces. After 135 days, the plasma radioactivity dropped back to null values while 92% of the implanted radioactive tracer was detected in feces and urine. No significant radioactivity was found in the organs. Those data shed light on the behaviour of PCL over an extended period of time proving its bioresorbability and biocompatibility. Most of the polymer was eliminated naturally and no traces were found in the organs. The degradation properties of PCL match the requirements for use in cardiac tissue engineering.

Compression tests performed on 3D printing scaffolds (4x4x8 mm, Figure 2.28) showed that PCL scaffolds have a mechanical behaviour similar to flexible foam.[372,373] The stiffness of PCL scaffolds was measured *in vitro* and *in vivo*, and it was observed that the stiffness increased after 3 months and subsequently remained almost unchanged subsequently. This was probably due to the simultaneous rise in its crystallinity, around 3-5%, over the same period. A higher crystallinity and more crystalline regions would enable the polymeric material to better resist deformation. Depending on the molecular weight and initial crystallinity, increases in mechanical properties along with crystallinity are common. The mechanical properties, particularly the stiffness trend of the *in vitro* and *in vivo* PCL scaffolds after 6 months, were very similar.

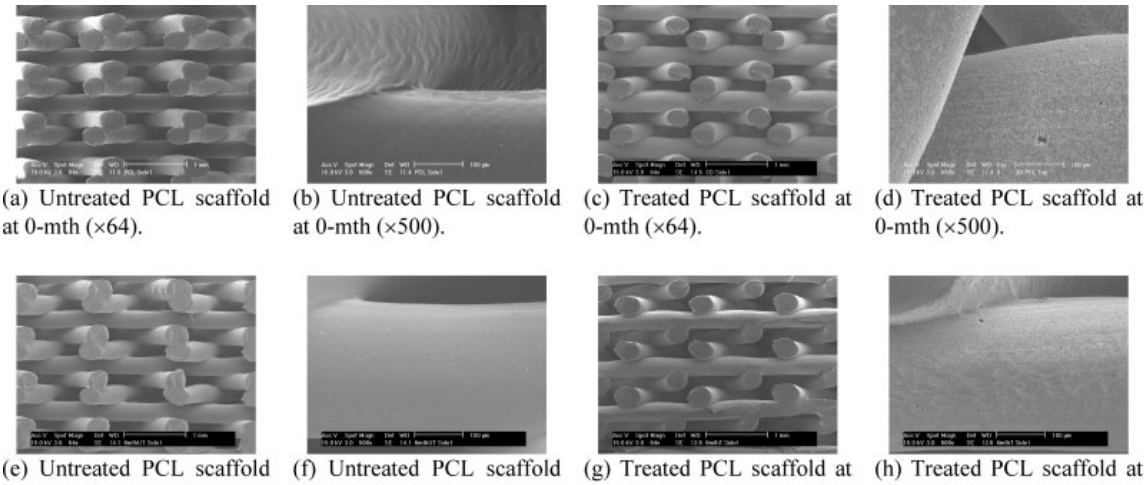

(a) Untreated PCL scaffold at 0-mth (×64). (b) Untreated PCL scaffold at 0-mth (×500). (c) Treated PCL scaffold at 0-mth (×64). (d) Treated PCL scaffold at 0-mth (×500).

(e) Untreated PCL scaffold at 6-mths (×64). (f) Untreated PCL scaffold at 6-mths (×500). (g) Treated PCL scaffold at 6-mths (×64). (h) Treated PCL scaffold at 6-mths (×500).

Figure 2.28: Gross morphology of *in vitro* degraded PCL scaffolds observed by SEM.[359] (2009) Reproduced with permission of John Wiley and Sons.

Biocompatibility Generally, bioresorbable polymers exhibit favourable biocompatibility with living tissue.[361,374] Inflammation is mostly triggered by the release of low molecular mass molecules through degradation or due to impurities. These released molecules can be acidic and therefore lead to secondary inflammatory reactions. Another important factor in the development of inflammation is the site of implementation and its ability to eliminate by-products. It is therefore crucial to study the degradation rate of the polymer and the local tissue clearance mechanism.[366]

Concerning PCL, the short and long term biocompatibility of PCL scaffolds using different animal models has been studied *in vivo* and *in vitro*.[375–380] These studies demonstrated the beneficial biocompatibility properties of PCL and PCL-composites. Biocompatibility PCL composites for cardiac tissue engineering will be further discussed below.

Surface functionalisation Surface modifications of PCL have been considered in order to increase biocompatibility of the implants, by improving the hydrophilicity and cellular compatibility.[381] The idea is to control and manipulate the surface properties of the scaffold without altering the main properties of the latter.[368,382] PCL shows poor cell attachment as it is a hydrophobic polymer demonstrating inadequate wettability. Various surface modifications can therefore be of interest to improve *in vivo* integration of PCL-based scaffolds[383]such as

- physical modifications: encouraging cell attachment by coating the surface with various materials, such as extracellular matrix proteins, collagen and laminin using physical adsorption.[384];
- chemical modifications: plasma treatment represents an effective way of increasing the hydrophilicity of PCL. PCL/ hydroxyapatite scaffolds were modified by air or argon plasma, leading to an improved cell adhesion and proliferation.[385,386] In another study, PCL electrospun nanofibres were modified by immobilisation of type-I collagen scaffolds using plasma treatment. Collagen immobilization enhanced the human dermal fibroblasts' adherence, spreading and proliferation.[387];
- surface-initiated atom transfer radical polymerisation (ATPR) to allow the making

of polymer brushes on different kinds of substrate. It has been shown that gelatin grafting on to plasma treated PCL nanofibres improves endothelial cell spreading, proliferation and orientation.[388] Additionally, Poly (glycidyl methacrylate) brushes were used to immobilize the collagen via surface-initiated ATRP on the PCL film surface. The new functionalised PCL film surfaces showed excellent cell adhesion features[389];

- biological modification: immobilisation of biomolecules such as growth factor to enhance cell attachment and proliferation. A study revealed that the immobilization of laminin-derived sequences onto the surface of PCL scaffolds increased the attachment of adipose-derived stem cells.[390] Additionally, bone marrow stromal cells adhesion was quantitatively increased using surface functionalisation of PCL scaffolds with RGD peptides.[160]

2.3.7 Biomimetic approach with PGS and PCL-based scaffolds for cardiac tissue engineering

Biomimetic scaffolds represent a promising solution for myocardial tissue engineering.[349,353] Indeed, cardiomyocytes have high oxygen demand, as healthy ones are physiologically embedded in a network of capillaries providing unobstructed oxygen supply.[391] Additionally, these biomimetic scaffolds should aim at replicating the complex structure of the cardiac muscle, made of highly branched and hierarchically fibres embedded in a 3D collagen network that resembles a honeycomb network.[392]

As described above, PGS and PCL are two remarkable polymers presenting highly interesting properties for cardiac tissue regeneration. The following section gives a by no means exhaustive list of PCL, PGS and 3D manufacturing techniques which can produce biomimetic scaffolds for cardiac tissue engineering.

2.3.7.1 Poly(glycerol sebacate)-based scaffolds

Micro-fabrication techniques were used to develop an innovative accordion-like honeycomb microstructure using poly(glycerol sebacate) to yield porous, elastomeric 3-D scaffolds

with controllable stiffness and anisotropy.[349]

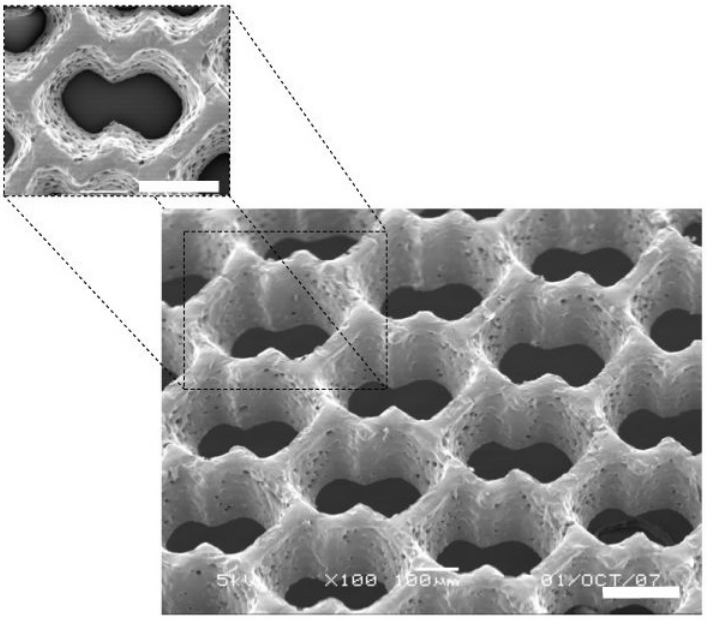

Figure 2.29: Scanning electron micrographs of PGS accordion-like honeycomb scaffolds fabricated using laser microablation. Scale bars = 200 μm.[349] (2008) Reproduced with permission of Springer Nature.

These micro-fabrication techniques involved the overlapping of two 200 x 200 μm square pores oriented at 45 degrees in a pattern to leave a planar network of undulated, 50 μm wide struts. The pores were fabricated using lasers. Cultured neonatal rat heart cells were seeded on these scaffolds, and they demonstrated interesting properties such as closely matched mechanical properties compared to native adult rat right ventricular myocardium, with stiffness controlled by polymer curing time. Additionally, the heart cell contractility was achieved by inducing an electric field stimulation (with directionally-dependent electrical excitation thresholds). Finally, greater heart cell alignment than isotropic control scaffolds was obtained. Accordion-like honeycombs therefore represent a solution to overcome principal structural-mechanical limitations of previous scaffolds, promoting the formation of grafts with aligned heart cells and mechanical properties which are similar to the myocardium.This study provided satisfactory scaffolds with excellent biocompatibility and ability to promote cardiac tissue regeneration. However, it is debatable if the use of such a difficult micro-fabrication technique is suitable for the targeted purpose: this multi-staged technique does not easily allow the rapid and repeatable man-

ufacture of the patches, and using only PGS which is viscous at room temperature, the in-theatre application of the patches might represent a real challenge.

In terms of electrospinning scaffolds, core/shell PGS/gelatin blends[393] were electrospun (Figure 2.30), where PGS was used as a core polymer to impart the mechanical properties and gelatin as a shell material, in order to achieve favourable cell adhesion and proliferation. The cardiogenic differentiation of mesenchymal stem cells MSCs was confirmed by employing specific markers. It is acknowledged that the co-culture of mesenchymal stem cells and cardiomyocytes with a suitable elastomeric biomaterial combination such as PGS/gelatin has synergistic effects and is more effective than mesenchymal stem cells and cardiomyocytes alone.

In the work of Kharaziha *et al.*, PGS and gelatin were blended before being electrospun, resulting in the fabrication of scaffolds that can mimic the left ventricular myocardium architecture.[394] From the *in vitro* studies using neonatal rat cardiac fibroblast cells (CFs) and cardiomyocytes, it was found that aligned fibrous scaffold, consisting of 33 wt% PGS, induced optimal synchronous contractions of cardiomyocytes while significantly enhancing cellular alignment.

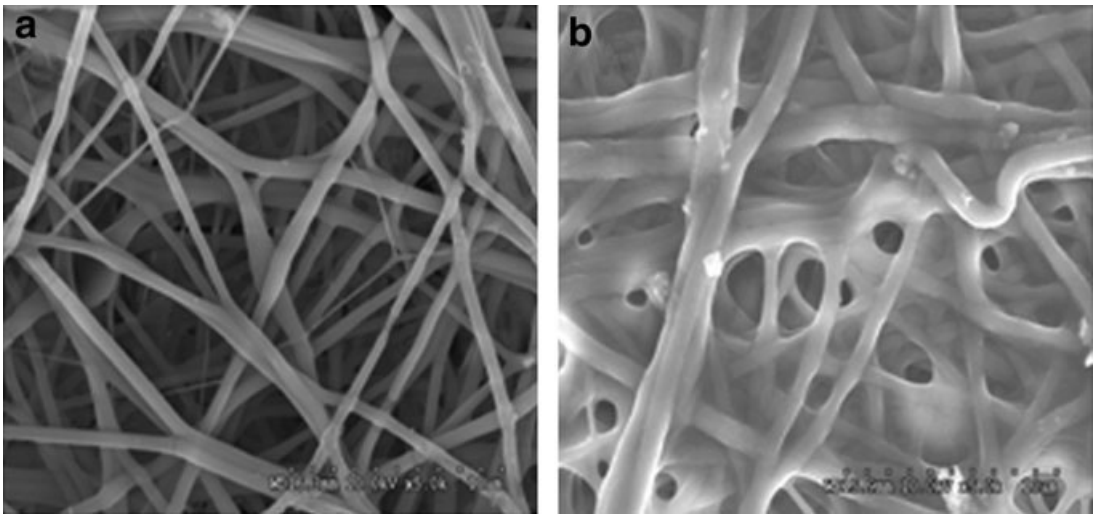

Figure 2.30: Scanning electron microscopy (SEM) images showing the fibre morphology of (a) gelatin fibres and (b) poly(glycerol sebacate) (PGS)/gelatin core/shell fibres at 5000 x magnification.[393] (2011) Reproduced with permission of John Wiley and Sons.

In order to provide better mechanical properties, PGS can also be blended with other

synthetic polymers. A polyester blend consisted of PGS, poly(3- hydroxybutyrate-co-3-hydroxyvalerate) (PHBV) and poly(lactic acid)[304] was shown to enhance cell viability, uniform cell distribution and alignment, due to nutrient provision from inside the 3D structure. Non-linearly elastic biomaterials were fabricated from PGS and poly(lactic acid) using the core/shell electrospinning technique[293] and showed tensile strength, rupture elongation, and stiffness constants comparable to muscle tissue properties. *In vitro* evaluations also showed that PGS/PLLA fibrous biomaterials possessed excellent biocompatibility.

Similarly, a micro-structured electrospun fibrous blend of PGS and poly(butylene succinate-butylene dilinoleate) (PBS-DLA)[395] of different compositions was examined for its suitability for heart patches. The use of PBS-DLA led not only to an increase of the average fibre diameter but also to an increase of the elastic modulus as well as the hydrophobicity of the blended scaffolds. Once tested *in vitro*, these micro-structured PGS/PBS-DLA scaffolds provided suitable mechanical strength, flexibility, and guidance for both mouse myoblast cell line and cardiomyocytes.

2.3.7.2 Poly(caprolactone)-based scaffolds

Electrospun PCL fibres of a 250 nm average diameter have been suspended on a wire ring, and have been shown to support the attachment and contraction of neonatal rat cardiomyocytes *in vitro*(Figure 2.31).[270] Indeed after 3 days, cardiomyocytes start to contract weakly and in an unsynchronized trend. These contractions become stronger and synchronize as time progresses. Cardiomyocytes have been shown to adhere, to populate the entire scaffold mesh, and stain positively for cardio-specific proteins.[396] This scaffold was used as a temporary ECM, enabling the cells to adhere, spread, proliferate and establish electrical communications between layers creating synchronized beating. It was also reported that this scaffold did not restrict the contractile functions of the cardiomyocytes.[81]

With regard to 3D printing, constructs of arbitrary complexity with uniformly dispersed

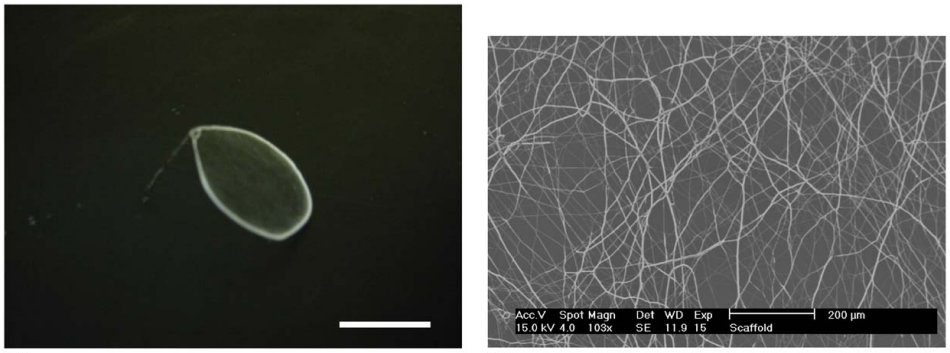

Figure 2.31: (a) Gross view of culture system. A thin, non-woven fibrous mesh is suspended across a wire ring. The thickness of the mesh is 10 mm. The wire ring acts as a passive load to condition cardiomyocytes during *in vitro* culture. Scale bar=15mm. (b) SEM micrograph of mesh. The electrospun fibres have an average diameter of 250 nm, and observed fibre diameters range from 100nm to 5 mm. The pores are interconnected and are much larger than the fibres. The topography of the non-woven mesh resembles that of an ECM and facilitates cell attachment. Scale bar=200 mm.[270] (2004) Reproduced with permission of Elsevier.

cells have been studied. For instance, SLS was used to produce structures that were porous on both the micron and millimetre scale, ensuring efficient mass transport throughout the structure.[312,397] These scaffolds were manufactured using poly(caprolactone) (PCL) which gave sintered structures with 48% porosity, 34 μm surface roughness, a tensile stiffness of 0.43 MPa, and a yield strain of 89%. As for biocompatibility, specific viable cells were maintained for three weeks in culture, and formed muscle fibres in the form of multinucleated myotubes after 11 days. Unfortunately, no further studies were conducted on the therapeutic performance of those constructs.

PCL fibre scaffolds present a high stiffness and hydrophobicity, which lead to insufficient cell attachment and proliferation in cardiac tissue engineering.[381] Many studies have targeted the improvement of PCL characteristics. For instance, blends of polymers have been investigated to improve biocompatibility and mechanical properties. A blend of PCL and collagen types I have been reported to exhibit appropriate mechanical properties (tensile modulus of 18 MPa and tensile strength of 7.79 MPa) for a blood vessel conduct.[398] PCL/gelatin scaffolds were shown to have a higher tensile strength in comparison to other hydride scaffolds.[399] The effect of pore size on cell attachment and migration

was also studied *in vitro* and it has been observed that cell migration was predominant in PCL/gelatin scaffolds. Random and aligned PCL/gelatin nano-fibrous scaffolds were electrospun[393] and results indicated that PCL/gelatin nanofibrous scaffolds presented smaller fibre diameters (239 ± 37 nm for random fibres and 269 ± 33 nm for aligned fibres), increased hydrophilicity, and lower stiffness compared to electrospun PCL nanofibres. The aligned PCL/gelatin nanofibres presented anisotropic wetting characteristics and mechanical properties, which closely match the requirements of native cardiac anisotropy. *In vivo* tests showed that rabbit cardiomyocytes were cultured on electrospun random and aligned nanofibres. It was concluded that an aligned PCL/gelatin scaffold greatly promoted cell attachment and alignment because of the biological components and ordered topography of the scaffolds.

PCL has also been electrospun in a blend with an oligomer hydrogel (bisphenol A ethoxylated dimethacrylate [BPAEDMA]). The elastic modulus of PCL/BPAEDMA nanofibrous scaffolds was found to decrease with the increase of the oligomer hydrogel. These scaffolds were shown to exhibit flexibility and allow adhesion of cells and tunable mechanical strength. In addition, these elements are both non-toxic and non-immunogenic.

2.3.7.3 Poly(caprolactone) and poly(glycerol sebacate)-based scaffolds

To obtain more efficient cardiac patches in term of biocompatibility and mechanical properties, both PCL and PGS have been used to manufacture electrospun scaffolds. The idea here is to balance out each others disadvantages. Indeed, despite the PGS elastomer being of great interest, its use in tissue engineering application is limited by the challenge of casting it into micro- and nanofibrous structure. Additionally, PGS mechanical properties change quite rapidly once implanted in the body. On the other hand, PCL exhibits steady mechanical properties and does not represent any difficulties in manufacturing as it has a low melting point and is soluble in many solvents. However, it is quite hydrophobic. By combining these two polymers, the aim is to obtain a polymer blend that has tunable and lasting mechanical properties, is easy to process into micro and nano-structures, and

has sufficient biocompatibility and hydrophilic properties.

Such scaffolds using PGS pre-polymer/PCL blend have been fabricated using the electrospinning technique.[305,400] It was shown that the higher the concentration of PGS pre-polymer, the higher the diameter of fibres in the scaffold and that the fibre diameter decreased down to a certain threshold of 17.5 kV(Figure 2.32).[305] Similarly, it was shown that a higher PGS pre-polymer concentration led to more suitable mechanical properties (elastic modulus (EM), ultimate tensile strength (UTS) and ultimate elongation (UE) explained in Chapter 5) of electrospun PGS(pre-polymer): PCL scaffolds in comparison with PCL-composite scaffolds. Finally, in terms of biological evaluation, these scaffolds significantly improved Human Umbilical Vein Endothelial Cell (HUVEC) attachment and proliferation compared to PCL-only scaffolds.[305,400] The work of Rai *et al.*[400] lays down promising results for the use of these polymer blends. However, this work studies the pre-polymer PGS (non cross-linked polymer) in the polymer blend and does not seek to clarify how the use of such non cross-linked polymer influences the mechanical degradation properties and if it has negative effects once biologically degraded.

A fibrous scaffold of a blend system of PGS and PCL functionalised using chemical

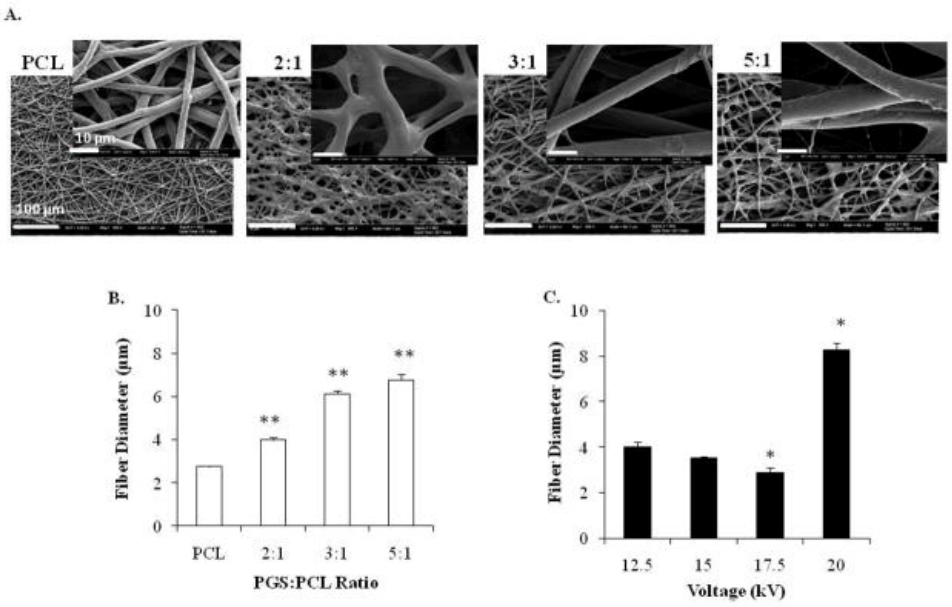

Figure 2.32: Effect of PGS:PCL ratio and voltage on fibre morphology and diameter.[305] (2011) Reproduced with permission of John Wiley and Sons.

immobilization of vascular endothelial growth factor (VEGF) was fabricated for cardiac

patch application.[400] The electrospun fibres were shown to support the attachment and growth of seeded myogenic and vasculogenic cell lines. This fabrication technique showed promising results, as this approach provided a uniform immobilization of VEGF on the fibres.

2.3.8 Research opportunities to improve cardiac tissue repair treatments

Bioactive glasses have been reported to have promising interactions with cardiac tissue and regeneration properties. However, their use for such applications has not been studied intensively with the aim of improving existing cardiac engineering treatments.

Cardiac patches containing BGs in a PGS polymeric matrix have been fabricated. Unfortunately, no study has yet been performed on the degradation processes which are believed to affect the mechanical properties of the scaffolds and cell behaviour. To what extent do BGs provide a damping effect on the pH and how does the scaffold behave once the BGs are fully dissolved? Additionally, it is worth considering if the use of a fast degrading polymer like PGS could be the most sensible option for cardiac patches.

Various studies used PGS in combination with a slow degrading polymer (PCL). Many of them used the PGS as a pre-polymer without commenting on any post-crosslinking procedures, and how crosslinking would affect the mechanical and biological properties.

In terms of manufacturing techniques, 3D printing and electrospinning are two promising tools, that are both reliable and scalable. 3D printing provides controllable and repeatable mechanical properties, while electrospinning assists the manufacture of ECM-like scaffolds. However, no studies have reported the simultaneous use of both techniques, in order to combine the advantages of them both.

To treat myocardial scarred tissue, there is is a need to find efficient and promising treatments, using reliable and scalable technologies and easily produced biocompatible materials. Here lie the research opportunities to fabricate a new, innovative treatment for cardiac tissue repair

Chapter 3

Aims and Objectives

Bioactive glasses have demonstrated their considerable suitability for applications in hard and soft tissue repair.

Fluoridated PBGs are promising materials for dentistry, as they prevent tooth decay, enhance tooth enamel remineralisation and inhibit bacterial infections. However, preliminary modelling experiments, studying the influence of fluoride ions, have generated much debate in the litterature. This thesis aims to provide a clear answer regarding the role played by fluorine in PBGs. In order to achieve this, classical molecular dynamics simulations have been selected to describe accurately the atomistic structure of F-PBGs, containing different amounts of fluorine. Additionally, modelling experiments aim to consider, for the first time, the polarisability of both oxygen and fluorine atoms.

Ideally, such computational models should be backed up with experimental data. However, due to the lack of suitable laboratory equipment, the synthesis of fluoridated phosphate-based glasses was impossible. Therefore, for the experimental section, the research was focused on the use of silicate-based glasses for soft tissue engineering. This commercially available biomaterial has shown promising interactions with soft tissues such scarred cardiac myocardium. In the field of tissue engineering, multi-material scaffolds combined with engineering fabrication approaches are of high interest, as they are able to fulfil numerous requirements for the targeted applications. The use of 45S5 silicate-based glasses, within a polymeric matrix, has been reported in cardiac tissue applications, but it has yet to be addressed extensively.[291,294,305,400]

The aim of this research is therefore to apply modelling techniques considering the polarisability of oxygen and fluorine atoms, in order to resolve current debates in the literature. Additionally, the experimental section aims to investigate polymer-bioactive glass composites using different manufacturing methods to determine their potential application in cardiac regenerative medicine. The specific objectives are:

- to improve the modelling of F-containing bioactive phosphate glasses, developing a novel force field including the polarisability of the oxygen and fluorine atoms, and to analyse the chemical structure of F-containing PBGs using molecular dynamics to conclude on the bioactivity of FPBGs;
- to provide new experimental insights and understanding of how a multi-material strategy (biocompatible polymers and bioactive glass-based scaffolds) used in combination with multi-manufacturing techniques, 3D printing and electrospinning, can be used to design effective and innovative scaffolds for tissue engineering.

Chapter 4

Atomistic structure of phosphate-based glasses containing fluoride

4.1 Introduction:

Bioactivity of fluoridated phosphate-based glasses

In this chapter, bioactive glasses containing fluoride which are beneficial in dentistry are studied.[18,45,46] Fluoride induces the enhancement of tooth enamel remineralisation, the inhibition of enamel demineralisation and bacterial infections. Fluoride ions cause fluoroapatite to form in physiological solutions.[118,121] This fluoridated form of hydroxyapatite, which is the main component of the tooth, is more stable against acid attacks than hydroxyapatite.[182] Fluoridated PBGs are promising materials for dentistry, as they prevent tooth decay, enhance tooth enamel remineralisation and inhibit bacterial infections.

Through this study is shown how the addition of fluoride influences the bioactivity of PBGs.[401] To obtain the most accurate and detailed representation of its structural organisation, the structure of F-PBGs was studied using computer simulations. Recently, the role played by fluoride ions on the bioactivity of F-PBGs has been debated in the literature and previous studies have concluded opposite results. In order to provide a

clear answer, classical molecular dynamics simulations was used to describe accurately the atomistic structure of F-PBGs containing different amounts of fluorine. This work provides a new insight into the physical chemistry of fluorinated phosphate-based glasses (F-PBGs). In this study and for the first time, the polarisability of both the oxygen and fluorine has been taken into account in order to obtain a detailed atomistic description of the system along with the Q_n distribution which is vital to understand the bioactivity of the glasses.

4.2 Materials and methods: Computational procedure

The use of polarisable force fields is crucial to obtain a correct description of medium range structure and hence the bioactivity.[227] The role of the force field is to model accurately the atomistic structure of $P_2O_{5(50-x/2)}$-$CaO_{(50-x/2)}$-$CaF_{2(x)}$ with $x = 0,2,5$ using the molecular dynamics code[219,220] DL_POLY Classic.[257] The amount of CaF_2 is increased, while the network connectivity is kept constant to remove any effect of changing the NC on bioactivity. The extent of any fluoride clustering and its effect on the bioactivity of fluoridated PBGs is discussed in this chapter.

4.2.1 Polarisable force field development: Potential models

In this work, the force field developed was based on the Born-Mayer ionic model[402], which is based on the assumption that the ions, in the glass, interact via long-range Coulombic internal forces, short-range two- and three-body interactions. The short-range interactions between ions i and j are expressed through the Buckingham potential, which accurately describe the interaction. The Coulombic energy is expressed as

$$U_{ij}^{Coulomb} = \frac{q_i q_j}{4\pi\epsilon_o r_{ij}} \tag{4.1}$$

where q_i is the charge of ion i and ϵ_0 is the permittivity of free space. Finally, the three-body interactions are included through a harmonic potential:

$$V = \frac{1}{2}k_{ijk}(\theta_{ijk} - \theta_0)^2 \tag{4.2}$$

where k_{ijk} and θ_{ijk} respectively represent the strength of the bond-bending term, and the bond angle between the three ions i, j and k.

4.2.2 Implementation of the core shell model

The force field developed takes into consideration the polarisation of the oxygen and fluoride atoms, using the shell model.[240] In the shell model, the polarisabilty is included by splitting the atom's total charge into a core of charge (Z+Y) and a shell of charge (-Y). Atoms such as the oxygen are usually represented through the shell model to take into account the high polarisability of the oxygen atoms. The shell model was also applied to fluoride ions to represent their polarisability. The polarisability of fluoride ions sits in between that of the oxygen and the sodium (Table 4.1). Applying the core-shell model to the fluoride ions could therefore be of interest to develop a more accurate force field.

The next step was to determine which values for F_{core} and F_{shell} to select. The gulp program provides a option which is called "Split" which varies specified core-shell charge split during fitting. However, the GULP manual does not give clear enough information on the way to use this option and no examples were found. Therefore, it was decided to write the input file using data reported in the literature.

The Database of Published Interatomic Potential Parameters provided many different potential and values for F_{core} and F_{shell} shown in Table 4.2.

The values for the core and shell charges for the oxygen were kept at the values derived by

Table 4.1: Electronic Polarisability in Units of $10^{-24}cm^3$

Name	O^{2-}	F^-	Na^+
Electronic Polarisability in Units of $10^{-24}cm^3$	3.88	1.04	0.179

Table 4.2: F_{core}, F_{shell} and spring values

Reference	F_{core} (e)	F_{shell} (e)	Spring (eV Å^{-2})
Atwood 1978[403,404]	0.6810	-1.6810	41.76
Binks 1994[405]	0.378	-1.378	24.36
Diller 1979[406]	.339	-1.339	37.98
Jackson 2000[407]	0.59	-1.59	20.77
Catlow 1977[408]	1.380	-2.380	101.200

Catlow et al.[408] (Table 4.3) for transferability of the potential and since these potentials were used to described one of the crystal (CaF_2) that was chosen, among other to fit the force field describing F-PBGs. Ionic charges were used to represent the calcium and phosphorus ions. The adiabatic shell model is used in this work to avoid significant exchange of kinetic energy between the core-shell unit and the rest of the system.

Table 4.3: Ion charges used in this work

Ion	Core (e)	Shell (e)	Core-shell Interaction (eV Å^{-2})
Ca	+2.000		
P	+5.000		
O[222]	+0.8482	-2.8482	74.92
F[408]	+1.380	-2.380	101.200

4.2.3 Empirical Fitting

4.2.3.1 Crystal Data and creation of the Gulp files

The potential, for every atoms composing the crystal structure, were empirically fitted. To do so, crystal data, from various crystals of interest, were selected. The crystals used for the empirical fitting are: the phosphorus pentafluoride PF_5, the phosphorus oxide triofluoride POF_3, the calcium fluoride CaF_2, the disodium fluorotrioxophosphate Na_2PO_3F, the calcium fluorooxophosphate $Ca_5FO_{12}P_3$. The crystal data were found on the Physical Sciences Data-science Service data base. The GULP input files were created using these crystal data.

4.2.3.2 Methodology

During the fitting, one or two parameters are varied at a time. Following that, the simulation was ran using GULP and an Output file was generated. Results were judged satisfactory when the sum of squares values, based on parameters such as the lattice parameters, was the closest to 0 and some lattice vector recalculated within 2-3 % of the experimental values. This value was set as there are no set values for what can be an acceptable error. A 2 to 3 % error will not necessarily affect the results since the glass itself has a density error when it is produced, and the MD simulation also introduce an error itself (error in trajectory averages on both truncation and sampling errors).[409] The accuracy of the potential fitting is determined by the percentage of errors between the optimised lattice structure and the experimental data, summed over all lattice parameters, corresponding to minimising F in the equation 2.16. Therefore, this percentage of error that was set should be used with cautions as a 2-3 % was judged acceptable but a 3 % error on each lattice parameter and in the same direction would be unacceptable as it would lead to an too large error overall.

4.2.4 Already existing Fluoroapatite Potential

Mkhonto *et al*[410] derived a potential model for fluoroapatite $Ca_{10}(PO_4)_6F_2$ fitted to structure, elastic constant and vibrational frequencies of the phosphate groups. They also used existing calcite and fluorite potential models.[411] The aim of this study was to model the effect of water on the surface structure and morphology of fluoroapatite by introducing a novel model. The derived potentials were calculated in compatibility with existing potentials for calcite and fluorite. The Ca-F and Ca-O parameters in the fluoroapatite, the oxygen and fluoride core-shell charges and interactions were taken from the literature.[412,412,413] The other potentials such as the interaction between oxygen and fluoride ions and between the oxygen and phosphorus within the phosphate group were empirically fitted using the GULP program to a variety of experimental parameters such as the elastic constant, bond dissociation energy, vibrational data and crystal structure of the phosphate group. Some interaction were described by the Morse potential or the Buck-

ingham potential.

Initially, the Buckingham potential was selected to describe the two-body interactions as it is a fairly adequate potential to describe interactions within ionic solid. The values presented differed largely for the ones initially selected.[221,222,414] However, the fit of the potential, using those data which seemed thorough, was attempted. The Morse potential is interesting to work with as it takes into account physical and concrete properties such as the dissociation energy D or the equilibrium separation.

Unfortunately, the study did not fit any parameters for the phosphorus fluoride interaction. The idea was therefore to simultaneously fit a Morse potential for the P-F bond using GULP and to run an MD simulations with DL_POLY without any fluoride in order to compare the results to already existing ones.[225]

4.2.4.1 Morse potential for the P-F bond

In order to fit a Morse potential to a diatomic bond, three parameters are required to be set :

- The dissociation energy D in eV is $439kj/mol = 4.55eV$;[415]
- The equilibrium separation r_0 is equal to 158-153 pm[416] so the mean as the value which is 155.2 pm was used;
- The last parameters is called α and is variable which can be determined by spectroscopic data. After conducting some research we decided to fit this last potential empirically using GULP due to the lack of data on this parameter.

4.2.4.2 DL_POLY simulation without fluoride-Phosphate interaction

A simulation was ran using the potential from the work of Mkhonto *et al*[410], in order to determine the accuracy of those potential the idea was to compare the results to already existing ones.[225] It then came to attention that, in the potential parameters used in this work, the value used as charge for the phosphorus was equal to 1.180 instead of 5.00. This false value for the phosphorus core is not explained in the review. However, due to the

absence of response after contacting the author, it was decided to not to use this value for the phosphorus as the charge was wrong and carry on fitting them from bulk crystals.

4.2.5 Potential fitting using already existing potentials

4.2.5.1 Phosphate potential

The fitting the potential was first attempted using existing phosphate potentials[222] which were developed for the study of phosphate-based bioglasses. The idea behind the use of those potentials was to obtain a fairly transferable force field. The Buckingham potential parameters was fitted for the following interactions:

- Ca_{core}-F_{shell}
- F_{shell}-F_{shell}
- P_{core}-F_{shell}
- O_{shell}-F_{shell}

They were fitted empirically to the structures and elastic constants of relevant crystals using the energy minimization code GULP[233]:phosphorus pentafluoride PF_5, phosphorus oxide triofluoride POF_3, calcium fluoride CaF_2, disodium fluorotrioxophosphate Na_2PO_3F, and calcium fluorooxophosphate $Ca_5FO_{12}P_3$.

4.2.5.2 Phosphate and fluoride potentials

To gain a better transferability of the force field, already existing potentials, developed for phosphate glasses[221,222,414] and fluoroapatite[408,410], were used. The P-F_s, P-F_s-P, F_s-P-F_s and F_s-P-O_s interactions (where e.g., F_s is the shell on the fluoride atom) were fitted empirically to the structures and elastic constants of relevant crystals ($Ca_5FO_{12}P_3$, PF_5, POF_3 and CaF_2).

Table 4.4: Two-body potential fitting results using existing fluoride potential and phosphate glass potential.[222,410,412,413]

Interactions	A_ij(eV)	ρ_ij	C_{ij}(eV.A^{-6})
O_s-F_s	583833.70	0.2116	7.68
F_s-F_s	99731834.0	0.1201	17.02
Na-F_s	1254.0	0.2745	0.00
Ca-F_s	1272.80	0.29971	0.00
P-O_s	1020.00	0.34322	0.030
O_s-O_s	22764.30	0.14900	27.88
Na-O_s	56465.3453	0.193931	0.00
Ca-O_s	2152.3566	0.309227	0.099440

Table 4.5: Three-body potential fitting results using existing fluoride potential and phosphate glass potential.[222,410,412,413]

Interactions	k (eV.$rad^{-}2$)	θ (deg)
O_s-P-O_s	3.3588	109.470
P-O_s-P	7.6346	141.179333

4.2.6 Classical molecular dynamics simulations

Once the potential was derived and gave satisfactory results, the classical molecular dynamics simulations were performed using the DL_POLY code.[257] Three different compositions (Table 4.6) in the $(P_2O_5)_{(50-x/2)}(CaO)_{50-x/2}(CaF_2)_x$ system were modelled: one with 0 mol% of CaF_2 (referred to as F0), one with 2 mol% of CaF_2 (F2) and one with 5 mol% of CaF_2 (F5). The amount of CaF_2 was increased while the ratio of the number of oxygen atoms to the number of phosphorus atoms, and hence the network connectivity, were kept constant. The densities of the compositions of fluoridated phosphate glasses modelled (Table 4.6) were not available in the literature, glass properties databases or experimentally achievable. We have therefore estimated the densities using already exiting density data on calcium phosphate bioglasses.[225,417–420]

At the start, the configuration for the various compositions consisted of quasi-randomly placed atoms in a cubic box positioned so that two atoms would not be found within 80-90 % of their expected interatomic separation. The molecular dynamics runs were

Table 4.6: Simulated compositions with the corresponding densities and cell sizes.

	P_2O_5 mol%	CaO mol%	CaF_2 mol%	Density (g cm^{-3})	Number of atoms	Cell size (Å)
F0	50.0	50.0	0.0	2.589	2000	30.96
F2	49.0	49.0	2.0	2.592	1800	29.90
F5	47.5	47.5	5.0	2.597	1700	29.34

then performed in a constant volume and temperature canonical (NVT) ensemble. The different simulations were run using a well-established and reliable methodology to model glasses[174,210,214,221,222,229]. For each composition the initial configuration was run at 2500K until the system reaches an equilibrium. Following that, the system was gradually cooled down from 2500K to 300K ensuring that the system reached thermal equilibrium for each of the temperatures (2500K, 2000K, 1500K, 1000K, 650K and 300K). Each step was run for 40ps which corresponds to an overall cooling rate of 9-10K/ps. This cooling rate has been shown to give reliable results in terms of medium-range structure.[229] In this work all data are taken from averages of five independent simulations for each composition.

4.3 Results and discussion

4.3.1 Polarisable force field development

4.3.1.1 Fitting potential results using existing phosphate potentials

The optimised potentials, using existing phosphate potentials[222] and lattice parameters of the recalculated structures, are shown in Tables 4.7 and 4.8. The results obtained on the crystal structure for the POF_3, shows a high percentage of error on the z direction. This could be explained by the layered structure of the crystal on the z direction. The results obtained for the CaF_2 crystals, were highly unsatisfactory with a mean error percentage of 31.17 %. As shown in Figure 4, the conjecture was that the structure probably requires a Ca-Ca interaction to correctly reproduce the structure, however this interaction is not consistent with the potential used in phosphate glasses as there are very weak Ca-Ca

Table 4.7: Two-body potential fitting results using existing phosphate glass potential.[222]

Interactions	A_{ij}(eV)	$\rho_i j$	$C_i j$(eV.A^{-}6)
P_c-F_s	488.18	0.3483	1.05
O_s-F_s	0.000003	0.3362	22.10
F_s-F_s	1127.70	0.2753	11.19
Na_c-F_s	1594.2	0.2555	0.00
Ca_c-F_s	3141.93	0.0058	0.00
P_c-O_s	1020.00	0.34322	0.030
O_s-O_s	22764.30	0.14900	27.88
Na_c-O_s	56465.3453	0.193931	0.00
Ca_c-O_s	2152.3566	0.309227	0.099440

Table 4.8: Three-body potential fitting results using existing phosphate glass potential.[222]

Interactions	k (eV.rad^{-}2)	θ (deg)
O_s-P-O_s	3.3588	109.470
P-O_s-P	7.6346	141.179333
P-F_s-P	7.6346	141.179333
F_s-P-O_s	27.853756	109.470
F_s-P-F_s	0.652140	109.470
P-F_s-P	7.6346	141.179333

interactions in PBG. It was therefore decided to discarded the crystal. Na_2POF_3 (Figure 4.1)was a crystal investigated in a first place, however fitting with other crystals led to a crash of the program. The rest of the crystal gave unsatisfactory results, with mean percentages of error of 2.26, 3.89 and 6.53 for respectively Ca_5FO_{12}, NaF and PF_5. Those results were not satisfactory and therefore, were not kept for the following steps. In a new attempt, already existing fluoride potential, and phosphate potentials were used as a starting point to fit the Buckingham parameters.

Table 4.9: Percentage of difference between the recalculated structure and data along with the mean % values.

Crystal	a(Å)	b(Å)	c(Å)	Mean % of error
PF_5	-4,74	-4,74	10.11	6.53
POF_3	3.95	3.95	6.42	4.77
CaF_2	-31.17	-31.17	-31.17	-31.17
$Ca_5FO_{12}P_3$	2.30	2.30	2.17	2.26
NaF	-3.89	-3.89	-3.89	-3.89

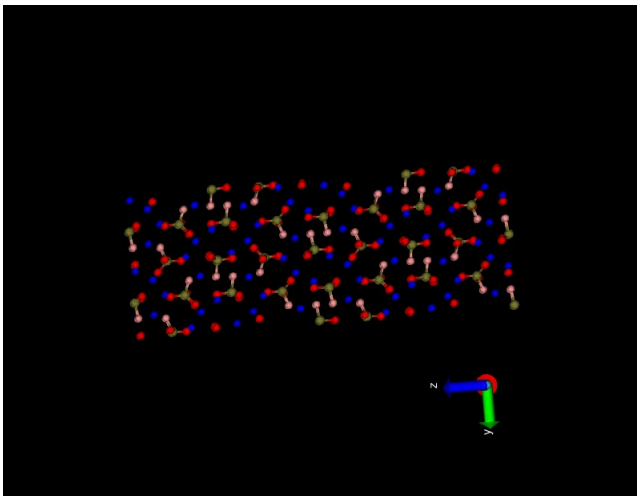

Figure 4.1: View of the crystal structure of Na_2POF_3

4.3.1.2 Fitting results Using existing phosphate and fluoride potentials

The optimised potentials are given in Tables 4.10 and 4.11, and the lattice parameters of the corresponding crystal structures, optimised with the potentials, are presented in Table 4.12. The results obtained on the optimised structures of $Ca_5FO_{12}P_3$, POF_3 and CaF_2 were in good agreement with the experimental lattice parameters, with an average error of 2.67, 1.28 and 0.51 % respectively. PF_5 showed a higher percentage of error between the optimised structure and the experimental data. However, when the small amount of fluoride put in our models (with a maximum of 5 mol%) is taken into account, a configuration where five fluoride atoms are bonded to one phosphorus atom is very unlikely, hence this error was deemed unimportant and the use of such potentials was chosen for the subsequent molecular dynamics simulations.

Table 4.10: Two-body Buckingham potential terms

Interactions	A_{ij}(eV)	ρ_{ij}(Å)	C_{ij}(eV Å^{-6})
P-F_s	1089.25	0.2568	7.28
O_s-F_s [410]	583833.70	0.2116	7.68
F_s-F_s [410]	99731834.0	0.1201	17.02
Ca-F_s [410]	1272.80	0.29971	0.00
P-O_s [222]	1020.00	0.34322	0.030
O_s-O_s [222]	22764.30	0.14900	27.88
Ca-O_s [222]	2152.3566	0.309227	0.099440

Table 4.11: Three-body harmonic potential terms

Interactions	k (eV rad^{-2})	θ (deg)
O_s-P-O_s [222]	3.3588	109.470
P-O_s-P [222]	7.6346	141.179333
P-F_s-P	7.6346	141.179333
F_s-P-O_s	27.853756	109.470
F_s-P-F_s	0.652140	109.470

Table 4.12: Percentage difference in lattice parameters between the optimised structure and experimental data

Crystal	a(Å)	b(Å)	c(Å)	Average
POF_3	1.90	1.90	0.50	1.28
CaF_2	-0.51	-0.51	-0.51	-0.51
$Ca_5FO_{12}P_3$	3.94	3.94	0.13	2.67
PF_5	-15.59	-15.59	5.95	12.38

4.3.2 Analysis of the structure of F-PBGS through molecular dynamics simulations

The potential developed in part 4.3.1.2 gave the most satisfactory results in terms of the lattice parameters of the corresponding crystal structures optimised with the potential. The molecular dynamics simulations was therefore carried out using this values. Through this project, the aim was to gain further understanding of the atomic structure of fluoridated phosphate-based glasses and on how the addition of fluoride will effect the

bioactivity. Figure 4.2 shows a picture of the F0 composition. All results shown in the following sections were calculated from the average of 5 simulations, for each compositions.

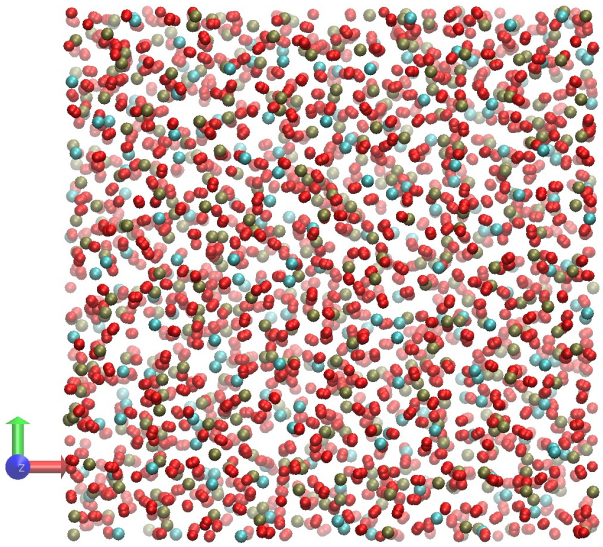

Figure 4.2: View of the F0 composition. The colours are: phosphorus (green), oxygen (red) and calcium (blue).

4.3.2.1 Short-range structure of the bioglasses

For all the compositions, the partial pair-correlation function $g_{P-O}(r)$ (Figure 4.3) showed the presence of two kinds of phosphorus bonding with bond lengths around 1.47 Å and 1.61 Å. Those bond lengths respectively correspond to the double and single bond between the phosphorus and the oxygen atoms. The pair-correlation functions (Figure 4.3 (top)) overlap for the F0, F2 and F5 compositions, which proves that the P-O bonding does not depend on composition, and those results are in agreement with previous simulations of fluoride-free phosphate glasses.[222] Neutron diffraction experiments[421] indicated that the P-O distance depends on the ratio $y = n(M_{2/\mu})/n(P_2O_5)$ where $n(x)$ is defined by the molar amount of the species x and μ represents the charge of the modifier M. For $y = 1.04$ (our composition) the corresponding P-NBO and P-BO bond lengths should be around 1.51 Å and 1.62 Å respectively, with which we are in good agreement.

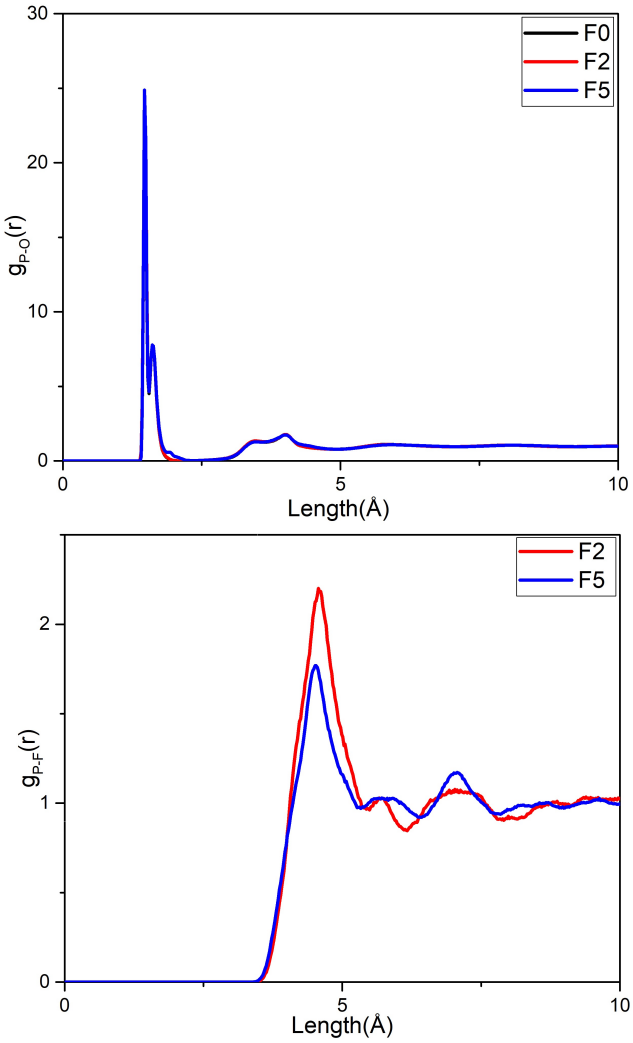

Figure 4.3: Partial pair-correlation functions $g_{P-O}(r)$ (top) and $g_{P-F}(r)$ (bottom) for the F0 (black), F2 (red) and F5 (blue) compositions

4.3.2.2 Fluoride interaction with the phosphorus

In the F2 and F5 compositions, the partial pair-correlation functions $g_{P-F}(r)$(Figure 4.3) show its first peak at a distance of 4.5-4.6 Å. Typical P-F chemical bonds, in crystals such as PF_5, are usually around 1.5 Å. No fluoride atoms bonding to the phosphorus atoms were observed. The only atoms coordinated to the phosphorus were the oxygen atoms. 99.6 % of the phosphorus atoms are coordinated to four oxygen atoms for all the different compositions. (The remaining 0.4 % are coordinated to three or five oxygen atoms).

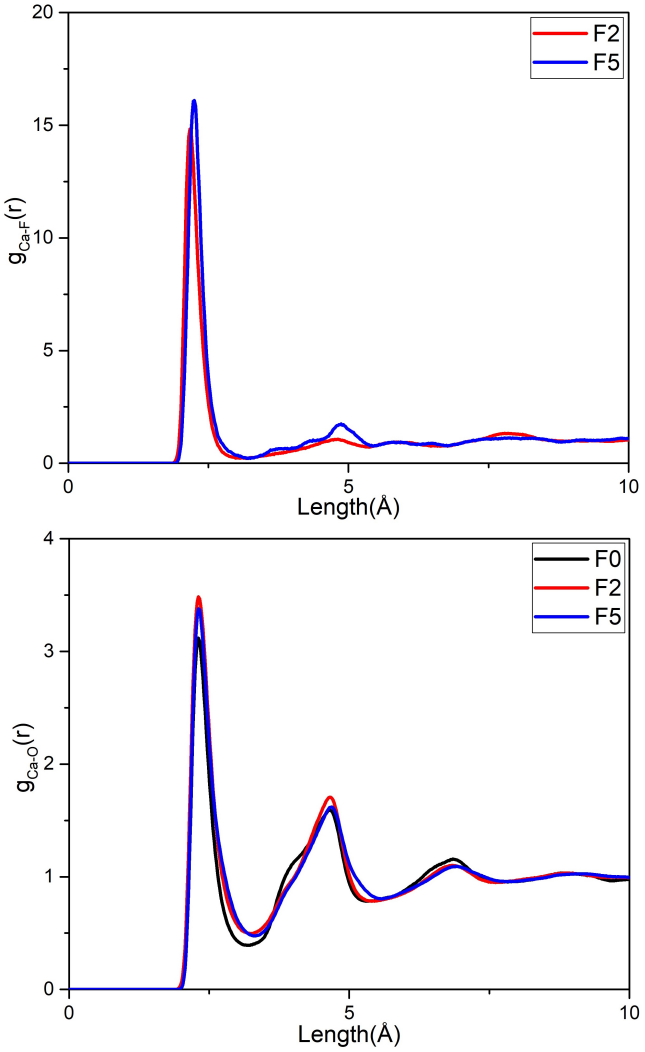

Figure 4.4: Partial pair-correlation functions $g_{Ca-O}(r)$ (top) and $g_{Ca-F}(r)$ (bottom) for the F0 (black), F2 (red) and F5 (blue) compositions

4.3.2.3 Calcium association with the oxygen and the fluoride

The partial pair correlation functions $g_{Ca-O}(r)$ and $g_{Ca-F}(r)$ (Figure 4.4) were analysed and showed that the Ca-O and Ca-F bond lengths are 2.31 Å and 2.21 Å respectively. Those values represented were characteristic Ca-O and Ca-F distances for F-PBGs.[225] It was therefore concluded that the calcium atom bonded chemically to both fluoride and oxygen atoms. To determine which of the latter calcium atom predominantly binds, the Ca-F and Ca-O coordination numbers were calculated. For Ca-F they were respectively 0.19 and 0.56 for the F2 and F5 compositions and the Ca-O. CNs were 6.763 ± 0.002, 6.57 ± 0.01, 6.05 ± 0.01 respectively for F0, F2 and F5. Additionally, the Ca-O coordination number decreased with increasing CaF_2 content while the coordination number of Ca-

F increases. The fluoride atom replaced the oxygen atom in the calcium atom's first coordination shell and the phosphate's coordination shell was not affected .

4.3.2.4 Clustering

Visualisation of the F2 and F5 composition showed clustering formed of fluoride and calcium atoms (Figure 4.5). These clusters led to the segregation of the glass network into modifier-rich (soluble in an aqueous environment) and network-rich regions (poorly soluble in an aqueous environment). As observed in silicate glasses[422], these clusters could lead to the formation of a discontinuous apatite layer on the surface of the bioactive glasses once implanted in the body. A decrease of the bioactivity of the glasses will result from this uneven apatite layer.

The clustering ratio of the different models can be defined as the ratio R_{X-Y} of the observed total number of atoms of species Y found within a coordination sphere of an atom of species X ($N_{X-Y,MD}$) compared to that expected if the atoms were homogeneously dispersed ($N_{X-Y,hom}$). It can be calculated using the following formulas[423–426]

$$R_{X-Y} = \frac{N_{X-Y,MD}}{N_{X-Y,hom}} = \frac{\mathrm{CN}_{X-Y} + \delta_{(X-Y)}}{\frac{4}{3}\pi r_c^3 \frac{N_X}{V_{box}}} \tag{4.3}$$

where $\delta_{(X-Y)}$ is 1 if $X = Y$ and 0 otherwise and r_c is a cut-off distance at which the X-Y coordination number of interest CN_{X-Y} is calculated. N_X represents the total number of X atoms contained in the whole simulation box of volume V_{box}. The clustering ratios for the fluoridated phosphate glasses were calculated with r_c=4 Å which correlated with the first coordination shell of the central atom of species X since it is where the nanoscale aggregation would appear (Table 4.13). For each composition, clustering of Ca, F, P, and O were calculated at the beginning (2500K) and at the end (300K) of the simulation.

Clear evidence of substantial fluoride clustering throughout the simulation was observed (Figure 4.5). During the simulation, there was an increase of the clustering ratio for the F-F and Ca-F interactions and a small decrease for the P-F interactions. These results were in agreement with the pair-correlation functions and visualisation. They also showed that the high level of fluoride clustering observed at the end of the simulation is a result

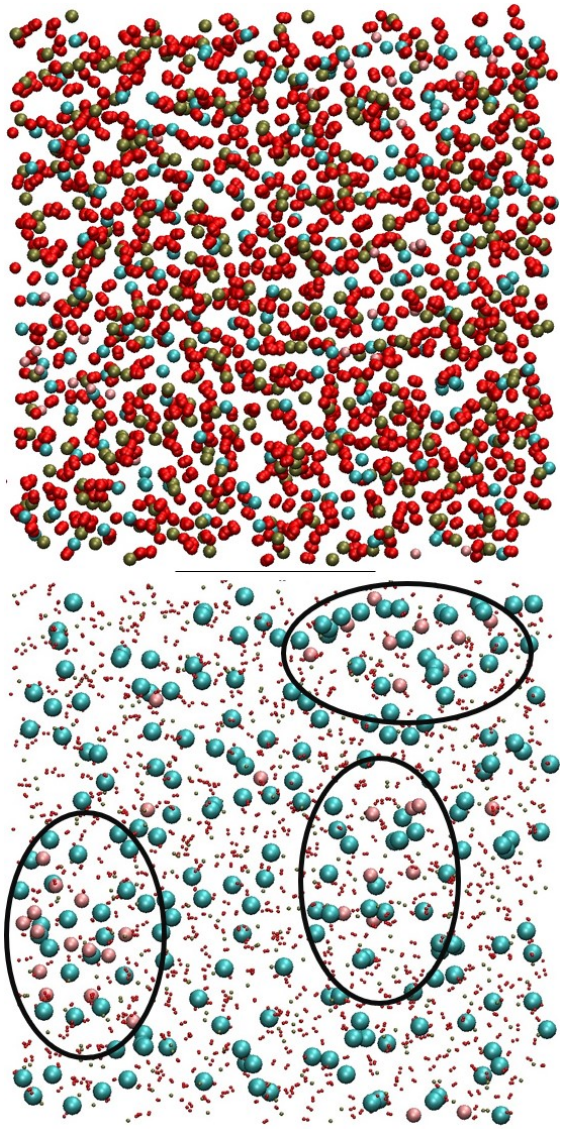

Figure 4.5: View of a representative F5 composition (top) with shrunk oxygen and phosphorus atoms and clusters highlighted (bottom) at 300K. The colours are: phosphorus (green), oxygen (red), calcium (blue) and fluoride (pink).

of the quench: that fluoride atoms form clusters during the cooling. Previous ab initio simulations[225] concluded different results in terms of phosphorus to fluoride bonding. The observed phosphorus to fluoride bonding in that study is probably due to the small size of the model (197 to 363 atoms) which might not be large enough to observe the fluoride-fluoride and fluoride-calcium interactions and the larger cooling rate necessary for ab initio simulations.

Table 4.13: F-F, Ca-F, Ca-Ca and P-F clustering ratios

	F2		F5	
	2500K	300K	2500K	300K
F-F	7.22 ± 0.09	10.64 ± 0.24	3.42 ± 0.02	6.98 ± 0.23
Ca-F	1.06 ± 0.01	1.12 ± 0.01	0.99 ± 0.01	1.28 ± 0.02
Ca-Ca	1.37 ± 0.01	1.201 ± 0.002	1.401 ± 0.002	1.209 ± 0.002
P-F	0.97 ± 0.01	0.874 ± 0.005	0.99 ± 0.01	0.69 ± 0.01

4.4 Conclusion

This study presents classical MD simulations of fluoride containing phosphate-based glasses in the system CaF_2-P_2O_5-CaO.[401] A novel empirical force field was developed with ionic charges and the use of a shell model for polarisation effects.

The empirical fitting was performed using relevant bulk crystals: $Ca_5FO_{12}P_3$, POF_3, NaF, CaF_2, Na_2PO_3F, PF_5 with the Buckingham potential. The potential fitting was performed using already existing phosphate and fluoride potential and gave transferability to the force field developed. The systems composed of $P_2O_{5(50-x)}$ $CaO_{(50-x)}CaF_{2(x)}$; x=0,2,5 were studied. The classical MD simulation results showed that the addition of fluoride led to the re-polymerization of the network into glass network modifier-rich (soluble) and network-rich (poorly soluble) regions, as it has also been reported for fluoride containing silicate glasses.[18] The analysis of the results indicated that the fluoride preferably bonded to the calcium and the oxygen was bonded to the phosphorus through single and double bonds. Additionally, no phosphorous to fluoride bonding was observed in the simulated systems and the phosphorus bonds with the oxygen creating single and double bond with the latter. Thereupon, the addition of fluoride in phosphate glasses was shown to lead to a decrease of the bioactivity. Despite studies showing that the rate at which the apatite layer is formed can be accelerated by a small addition of fluoride[13,118,185,213], the apatite layer will not be homogeneous due the variation of dissolution in the modifier-rich (soluble) and network-rich (poorly soluble) regions. This will ultimately have deleterious effect on the bioactivity of the glass once implanted. Previous ab-initio simulations[225] concluded on different results in terms of phosphorus to fluoride bonding. The observed phosphorus to fluoride bonding in this study is probably due to the small size model(197

to 363 atoms). Further studies could be undertake in order to determine the minimum energy pathway leading to the formation of fluoride/calcium rich cluster.

The minimum energy pathway (MEP) refers to the lowest energy path leading to the rearrangement of a group of atoms from one stable position to another[427]. The determination of the MEP constitutes a real challenge in theoretical and condensed matter chemistry. MEP can also be referred to as "reaction coordinates"[428] and refers to various chemical transitions such as reactions, changes in conformation of molecules, or diffusion processes in solids. For the atom to go from one stable position to another, the system goes up to what is called an energy barrier that has to be activated in order to overcome the saddle point energy or potential maximum energy along the MEP. This energy barrier is of high importance to estimate the transition rate.[429] Calculations had been started using already existing atomistic conformations.

The NEB method was developed to find a MEP between a pair of initial and final states, both of which are local minima on the potential energy surface. Through this method, all point on the path is at an energy minimum in all directions. The NEB is a chain-of-states method through which a string of images (geometric configurations of the system) is used to describe a reaction pathway[430].

Chapter 5

Multi-layered patches containing silicate-based glasses for cardiac tissue engineering

5.1 Introduction

The various requirements for functional cardiac tissue scaffolds have led to the development of different fabrication approaches and material utilisations for cardiac tissue repair.[295] Indeed, national statistics show quite dramatic results, with around a million people affected by heart failure in the UK each year resulting in 36,000 deaths each year. Additionally, heart disease is nowadays the leading cause of death and disability in the world with an estimated 15 millions people dying from strokes and heart attack in 2016 according to the World Health Organisation.[260] The most common cause leading to heart diseases being myocardial infarction.[265,296] Various approaches have been developed to regenerate the functional myocardium[270] such as cell suspension[63,276], natural or synthetic scaffolds with and without cells[269] and ventricular restrains.[273–275] Biomaterial scaffold architecture plays a key role in most tissue engineering strategy. Indeed, biomimetic materials should mimic the extracellular matrix of the tissue of interest in order to have the desired effect on tissue regeneration. The main idea in engineered cardiac tissue is

to reconstruct a structurally similar and functional replica from damaged tissue. The manufactured constructs should exhibit sufficient elastic properties, suitable biocompatibility and enhance cell regeneration.[297] Different manufacturing techniques have been developed in order to obtain satisfactory scaffolds such as electrospinning[298], three dimensional printing[299] or cell sheet technologies.[300] In this project, the focus was put onto fast efficient and reliable techniques to manufacture cardiac patches that are electrospinning and three-dimensional printing. Electrospinning allows the manufacture of a matrix mimicking the extra cellular matrix of the cardiac cells which is a much needed interface for cardiac cells to attach and grow. Three-dimensional printing is a useful tool to obtain repeatable mechanical properties over a large number of patches.

5.1.1 Native myocardium and cardiac structure

Native myocardium is made of cardiomyocytes, cardiac fibroblast (CFs) and endothelial cells. The myocardium is highly organised.[431] Cardiomyocytes are self-beating cells which contract more than three billion times in the average human lifespan, pumping over 7000 L of blood per day through 100,000 miles of blood vessels.[80] In terms of structural properties, cardiomyocytes are aligned parallel to the heart wall. They are cylindrical rod-shaped muscle cells which are typically around 100-150 μm by 20-35 μm and govern the function of the myocardium. Cardiomyocytes are interconnected by intercalated disks (constituted of different types of cells junction) which maintain the electromechanical integrity of the heart.

CFs constitute over 50% of the cells of the heart[432] and are key to regulating the myocardial function and structure. Their role is to contribute to the structural, biochemical, mechanical and electrical properties of the myocardium. Indeed, they help regulate the turnover of the ECM as well as controlling proliferation and interaction with myocytes. CFs therefore affect the cardiomyocytes behaviour.[339,432,433] CFs also play an important role in the remodelling of infarcted myocardium.[434]

After a cardiac infarction, several changes occur in the structure and function of the

heart, referred to as cardiac remodelling. This process happens at a genetic, cellular and intracellular level and has been shown to start shortly after the myocardial infarction and carries on years after.[278–280] To maintain cardiac output, the loss of contractile tissue is compensated by hypertrophy of myocytes and stabilisation of the infarct area through the development of scar tissue.[435] Cardiomyocytes undergo elongation or hypertrophy due to an increase in the left ventricular volume and stress in the cardiac wall.[436] This overstretch of the ventricle and cardiomyocytes further impairs contractable properties of the heart and contributes to the expansion of the scarred region.[437] The ECM also undergoes remodelling. Indeed, shortly after the infarction, a new ECM is formed with increased fibrillar collagen (type I and III). Vascular remodelling occurs to increase the blood flow reaching the ventricle.

5.1.2 Polymers-Bioactive glasses composites scaffolds

PGS and PCL are the two biodegradable polymers that were used to manufacture the cardiac patches along with water soluble 45S5 BGs. However, they tend to exhibit different degradation rates. Indeed, PGS degrades relatively faster than PCL as it can be resorbed within 60 days in the body while PCL undergoes slow degradation with implants remaining in the body for up to 2 years.[364,438] Additionally, the processing methods used to fabricate the scaffolds plays an important role in the degradation behaviour. Therefore the degradation process of the engineered cardiac patches had to be assessed. The pH, weight loss, water absorption should be measured as they are key features describing the efficiency of the patches. Indeed, the pH has to be adequate for the cells as an acidic environment leads to a decrease of the contractile capacity of the cardiac muscle.[439] Additionally, weight loss and water absorption give information on how the degradation mechanism of this polymer blend affects its physical properties. Finally, those information in combination with mechanical properties after degradation helped assessing how long the patch will ensure its role.

On top of degradation and mechanical properties, cardiac patches are required to provide suitable surface chemistry for cell attachment, proliferation and differentiation along

with a 3D porous open network to promote sufficient vascularisation for the transport of nutrients and metabolic waste in order to promote cell growth. *In vitro* biological study therefore assessed to which extent the manufactured cardiac patches fill in those requirements. Cardiomyocytes require high oxygen supply (27.6 nmol mg protein^{-1} min^{-1}). Engineering patches providing an high enough supply of oxygen and nutrients constitute therefore a real challenge and have to be tested.

5.1.3 Mechanical properties in cardiac tissue engineering

The aim of the engineered cardiac patches is to help the scarred tissue of the myocardium to regenerate. To achieve successful manufacturing of a cardiac patch for myocardial tissue regeneration, matching the properties of the scaffold and native myocardium is essential.[336] Cardiac muscle fibres are in highly vascularised and hierarchical systems, embedded within a 3D collagen network (made of different level of organisation) resembling a honeycomb.[440] This collagen organisation ensures sufficient cardiomyocyte contraction during systole whilst protecting the cells from over-extension during diastole. Therefore, maintenance of a robust, elastic material is necessary for the cardiac pump function.[441,442] This structural organisation leads to anisotropy in the electrical and mechanical properties of the heart.[349,392]

The Young's modulus (measure of stiffness) of the heart muscle ranges from 10 to 20 kPa at the beginning of diastole to 200 to 500 kPa at the end of diastole.[443–447] The tensile strength of the human myocardium varies between 30 to 70 kPa.[265,400,448] Many studies have tried and replicate similar experimental mechanical properties. Recently, the influence of the addition of a heart patch exhibiting a Young's modulus going up to 200% of the average myocardium's has been studied using theoretical simulations.[449] In these simulations, the use of such non-contractile patches has been shown to help reduce the wall stress proportionally along with the infarct expansion and global left ventricle remodelling. Those findings were also corroborated by recent studies which confirmed that the use of a stiffer and thicker materials lowered infarct expansion, left ventricle remodelling and bettered global left ventricle function.[265,400,450,451]

Myocardial infarction is followed by the development of scar tissue due the cardiac remodelling. This scar presents mechanical properties that affect the heart function. The evolution of the scar mechanics and structure along with the left ventricular structure has been studied in rat models.[452] The study revealed that over 1, 2, 3, and 6 weeks, the healing infarct in rats exhibited structural and mechanical isotropy and that the increasing amount of collagen played an important role in the mechanical properties as it influenced cardiac remodelling. Finite Element Modelling showed that the infarct region is stiffer (higher Young's modulus) than healthy myocardium tissue and that a re-orientation of the collagen fibres occurs within 1 week.[453,454]

5.1.4 Aims and objectives

This project targeted the design cardiac patches for myocardial tissue regeneration.[455] This cardiac patches aimed at being bioresorbable and biocompatible with a controllable degradation and resorption rate to match cell/tissue growth *in vitro*/*vivo*, and also provided suitable surface chemistry for cell attachment, proliferation, and differentiation. Additionally, these patches were manufactured into a three-dimensional and highly porous scaffold with an interconnected porous network for cell growth, flow transport of nutrients, and metabolic waste and have suitable mechanical properties to match the tissues at the site of implantation. To do so, two manufacturing techniques were combined: 3D printing and electrospinning with the use poly(glycerol sebacate) and poly(caprolactone). Those polymers have been used in combination with bioactive glass 45S5 which has gained more and more interest as a use in soft tissue regeneration. This innovative cardiac patches have been mechanically tested to match the properties of the cycling beating heart.

5.2 Material and methods

5.2.1 Instrumentation

5.2.1.1 Infrared

Infrared spectra were recorded on neat compounds using a Fourier Transform Infrared Spectrophotometer Shimadzu FTIR-8400S, equipped with an ATR diamond and irradiating between 7800cm^{-}1 and 350cm^{-}1. Only relevant absorbances are reported. The data were recorded through the software IRsolution.

5.2.1.2 NMR spectroscopy

^{1}H nuclear magnetic resonance (NMR) spectra were recorded, in commercial deuterated solvents, on a JEOL ECS-400 spectrometer (^{1}H at 399.782 MHz, ^{13}C at 100.525 MHz), a Bruker Advance Ultra-Shield 400 spectrometer (^{1}H at 400.134 MHz, ^{13}C at 100.624 MHz) at 293 K. Chemical shifts were expressed as δ in parts per million (ppm) and were adjusted to the chemical shift of the residual NMR solvent resonance peak ($CDCl_3$, ^{1}H: δ = 7.26 ppm). ^{1}H coupling constants (J) were reported in Hertz (Hz). Information about multiplicity are abbreviated as follows: s = singlet, d = doublet, t = triplet, q = quartet, quin = quintet, m = multiple

5.2.1.3 SEM characterisation

The surface micro-structure of samples was characterized in a field emission gun (FEG) scanning electron microscope (SEM) (model LEO 1530VP).The samples were Au/Pd-coated and observed at an accelerating voltage of 5 kV.

5.2.1.4 X-Ray Diffraction

Powder X-ray diffraction data were collected using the Bruker D8 Advance diffractometer in reflection geometry, Cu Kα (1.54060 Å) radiation (Chemistry Department, Loughborough University). The sample was prepared as substrate. A small amount of sample was ground in acetone. The suspension was dropped with a pestle onto a silicon sample

substrate to produce a thin smear. The data were collected over the 2θ range of 5 to 60° with a step size of 0.014 and a count time of 5.5 s per step. Therefore, the data were collected for a total measurement time of approximately 6 hours 11 min. t, app.m = apparent multiplet, dd = doublet of doublet, etc.

5.2.2 Polyglycerol sebacate synthesis

The polymer was synthesized according to the work of Wang *et al.*[326] in two steps and by polycondensation. A round-bottom flask equipped with a N_2 bubbler and a Dean-Stark trap was charged with a 1:1 molar ratio of anhydrous glycerol (Sigma Aldrich, purity 99%) and recrystallized sebacic acid (Sigma Aldrich, purity 99%). Bubbling N_2 was passed through the mixture for 10 min then it was heated up to 120°C and maintained at this exact temperature for 24h before the pressure was reduced from 1 torr to 40 mtorr over 5 h. The reaction mixture was kept at 40 mtorr and 120°C for 48 h. PGS was characterised using IR and NMR.

5.2.3 Silicate-based bioactive glasses characterisation

The bioglass 45S5® was purchased from XL Tech science and characterised using SEM and XRD. Analysis to determine if the BGs could be electrospun in a polymer blends or 3D printing were ran.

5.2.4 Electrospinning of the PCL/PGS solution

PCL with a molecular weight of 80 kDa (Aldrich,) and the synthesised PGS were dissolved in a 7:3 mixture of dichloromethane and methanol to obtain a 13 and 14 wt% solutions. The polymer solution was delivered with a syringe pump (NE-300 syringe pump from New Era Pump Systems) at a flow rate of 0.8 ml/min to a stainless steel needle (inner diameter=1 mm; 100 Sterican 21G) connected to a high voltage power supply (Linari Engineering). At a voltage of 8 kV, a fluid jet was ejected from the needle, and the resulting electrospun mesh was collected on aluminium sheet placed at 15cm from the needle. The scaffolds were stored at room temperature for several days.

5.2.5 3D printing of the PCL/PGS/BGs scaffolds

To determine the most suitable composition for cardiac tissue engineered patches, various polymeric compositions were manufactured to obtain adequate mechanical properties. The following compositions were prepared and investigated for the purpose of cardiac tissue regeneration:

- Composition 1 : Poly(caprolactone)
- Composition 2 : Poly(caprolactone), Bioglass (5 wt%)
- Composition 3 : Poly(caprolactone), Bioglass (10 wt%)
- Composition 4 : Poly(caprolactone) : Poly(glycerol sebacate) (1:1)
- Composition 5 : Poly(caprolactone) : Poly(glycerol sebacate) (1:1), Bioglass (5 wt%)
- Composition 6 : Poly(caprolactone) : Poly(glycerol sebacate) (1:1), Bioglass (10 wt%)
- Composition 7 : Poly(caprolactone) : Poly(glycerol sebacate) (2:1), Bioglass (10 wt%)
- Composition 8 : Poly(caprolactone) : Poly(glycerol sebacate) (1:2), Bioglass (5 wt%)

The aim was to understand the influence of all of the polymers, composites and compositions on the mechanical properties. For the preparation of solutions, various procedures were tested in order to obtain an homogeneous solution with no agglomerated particles and appropriate for 3D printing.

The initial idea consisted in 3D printing at a high temperature (above 200°C). Indeed, PCL is a polymer with a low melting point and the idea was to prepare an homogeneous solution at high temperature and 3D print it through an high temperature extrusion process and direct deposition. Three PCL polymers with various molecular weight (Mw) and degree of polymerisation (Mn) were investigated:

- PCL80000 : Mn= 80,000
- PCL45000 : Mn= 45,000
- PCL10000 : Mn= 10,000

PCL80000 had too high of a molecular weight to be melted and extruded through high temperature extrusion process. Even at a temperature of 260°C the polymer was too viscous to be extruded and also to be mixed with PGS and BGs. A lower molecular weighted PCL was then trialled. The PCL 45000 was 3D printable at high pressure and high temperature 220°C which could, however, lead to the degradation of the polymer. Additionally, an homogeneous solution with PGS and BGs was not obtainable. PCL10000 was easily 3D printable, however the scaffold obtained were excessively brittle to be used as cardiac patches.

Another idea was to use a filament made from PCL, PGS and BGs and 3D print it through fused deposition method (FDM). PGS is highly viscous but, unfortunately, liquid at room temperature which did not allow us to use this method.

Finally, the idea was set on using direct deposition method with a solution of dissolved polymers and suspended BGs particles. PCL and PGS are soluble in Chloroform and Dichloromethane. However, those solvents are highly dangerous in terms of toxicity and have supposed carcinogenic properties. Acetone, a benign solvent was then selected. PCL and PGS have a relatively good solubility in acetone. To increase their solubility the solution were prepared at temperature varying between 30 and 50°C.

Solutions for the various compositions were prepared as follow with the amount shown in Table 5.1: For the solutions containing bioglasses, BGs was dry ball milled using an agate ball mill and the desired amount was added to 5 g of acetone with 50 μL of Dimethyl Sulfoxide (DMSO). The solution was then left under vigorous agitation for 1 hour and then filtered with a 150 μm sieve. the rest of acetone was then used to rinse. The solution was then heated up to 40°C. The necessary amount of PGS was then added. Following the complete dissolution of PGS, PCL was added slowly before leaving on a stirrer at 40°C overnight.

Table 5.1: Composition of the solutions for 3D printing

Composition	PCL(g)	PGS(g)	BGs(g)	Acetone(g)	DMSO μL
1	2.5	-	-	7.5	-
2	2.5	-	0.132	8	50
3	2.5	-	0.278	8.5	50
4	2.5	2.5	-	10	
5	2.5	2.5	0.556	10	50
6	2.5	2.5	0.265	10	50
7	5.0	2.5	0.835	10	50
8	2.5	5.0	0.395	8.5	50

The solutions were placed in a syringe as shown in Figure 5.1. The samples were 3D printed at a temperature of 37°C.

Figure 5.1: Solution of composition 6 ready to be 3D printed

For repeatability and good comparison of the mechanical properties of all the composition, the inner structure properties of the scaffold were kept similar with the parameters shown in table 5.2.

The scaffolds were 3D printed on top of aluminium foil as shown is picture 5.2. In terms of 3D printing procedure, the pressure, speed time for pre flow and post flow were adjusted and optimised to obtain the desirable inner structure with no contact between two strands in the same layer as shown in figure 5.3.

Table 5.2: 3D printing parameters

Parameters	Layer 1	Layer 2
Hatch Type	Line	Line
Distance from contour (mm)	0.30	0.30
Angle (°)	0.0	90.0
Distance between strands (mm)	1.45	1.45
Strand Shift X axis (mm)	0.00	0.70
Strand Shift Z axis (mm)	0.00	0.00

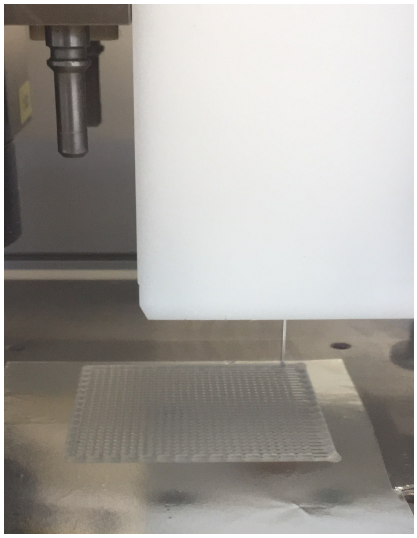

Figure 5.2: 3D printing on aluminium foil

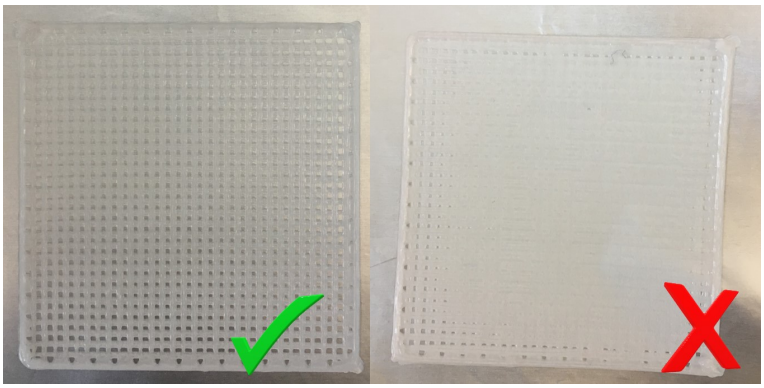

Figure 5.3: Final 3D printing on aluminium foil

5.2.6 Manufacturing of the hybrid cardiac patches

Once all the components of the cardiac patches were manufactured separately successfully, the focus was put on understanding how to best combined them. Two methods were investigated:

- 3D printing of the solution on top of the electrospun scaffold (order 1)
- Electrospinning on top of the already 3D printed and dried scaffolds (order 2)

Two samples following the protocol explained in Section 5.2.5 were manufactured and analysed through FEG-SEM where the cross-section and view from both sides was observed.

5.2.7 Characterisation of the thermal properties

A DSC Q200 V24 differential scanning calorimeter was used for this study. Polymeric samples were put in DSC aluminium pans. Following this the pan was hermetically sealed and placed to the sample holder of the instrument

To determine the precise weight of polymer used for the experiment, the pans and seals were weighed before the addition of the polymer. The polymer was then placed in the pans which were subsequently sealed and weighed again. Assuming no weight loss occurred during this process, the exact weight was then recalculated. Thus 6.7 mg of PCL-PGS, 4.9 mg of PGS and 10.1 mg of PCL were used as samples with an empty DSC pan used as control. The latter was weighted, sealed, and of similar weight. The experience was performed under nitrogen.

To determine both exothermic and endothermic changes the heat/cool/heat program was used. Through this procedure, the sample was initially heated up to 160°C at a ramp of 10°C/min and kept at 160°C for 1.00 min in order to obtain a amorphous dispersion of the polymer chains at a liquid state. The samples were then cooled down to -70°C at a pace of 20°C/min which allowed the observation of the endothermic peak corresponding to the crystallisation of the polymer chains. Once the temperature reached -70°C, this

temperature was ensured for 1min then followed by an increase of temperature up to 160°C at a ramp of 10°C/min to observe the exothermic peak representing the fusion

5.2.8 Mechanical testing

Mechanical properties of the samples were determined using tensile techniques. The material's mechanical strength was measured, along with its ability to resist loads without failure due to excessive stress or deformation. Typical point of interests to determine a material strength are:

- Ultimate Tensile Strength (UTS) or peak stress, which describes the strength at the maximum load.
- Young's modulus (E), representing the elastic strength of the material
- Elongation, which is the maximum extension a material can take without breaking.

To determine the mechanical properties of polymeric materials, the strain (ϵ) as a function of the stress (δ) applied to a specific sample is measured. At low strain, most solids materials exhibit an elastic deformation. In this zone, the stress (δ) is proportional to the strain (ϵ):

$$\delta = E \cdot \epsilon \tag{5.1}$$

where E refers to the Young's modulus of the plastic and measures the stiffness of the material. This equation is known as Hooke's law which implies a proportionality between the applied stress (or load) and the resulting observed strain (or elongation) up to a certain limits called the proportional limit.[456] Beyond this elasticity limit, the material will not return to its original shape and size once the strain is removed and will endure permanent deformations. If the yield is increased pass this point, the material will reach the yielding point, where an increase in strain occurs without an increase in stress. This point marks the begin of plastic deformation of the material. Following this the material will reach its breaking point.

Some polymers exhibit an orientation and alignment of their chains in the direction of

the load, leading to an increase in the material's strength and stiffness. This phenomenon is referred to as "strain hardening" and "stress induced crystallization".[457] On the other hand, amorphous polymers, after reaching this stage, can exhibit true strain softening, where a brittle fracture is characterised by no observed yielding point.[458]
Temperature greatly affects the mechanical properties of polymers, indeed, above the glass transition temperature a sudden change of mechanical behaviour can be witnessed and the polymeric materials can change from brittle to ductile.[458] PGS and PCL are both above their Tg at room temperature (and subsequently at body temperature), it has been reported, using simulations and experimental measurements, that increasing the temperature of an amorphous polymer induces a decrease in elastic moduli.[459,460]

During this project, uniaxial tensile tests were performed on the multi-layered scaffold. 20x40 mm rectangular strips were cut from each scaffold. The thickness of the scaffold was measured using a Digital Vernier Caliper. Each scaffold was strained to the breaking point at a constant speed of 10 mm/min using a microtensile tester (Instron 5944). Samples were mounted in tensile grips 13 mm from each sample end, leaving an approximate gauge of 16 mm. The stress and strain were analysed using a Instron Bluehill Inc software. The Young's modulus was calculated from the slope of the stress-strain curve.

5.2.9 *In vitro* degradation tests

The *in vivo* degradation behaviour of the multi-layered scaffolds was evaluated in phosphate-buffered saline (PBS) solution under static conditions at 40 °C for 5 months. Multi-layered scaffold containing no BGs were used as controls for the study. The pH, water absorption, weight loss were measured. To determine initial dry weight, the samples were weighed with a 0.1 mg resolution balance (Sartoruis, CP3245). Each sample was then placed in the well of a 24-well cell culture plate (Fisher Scientific, 10380932). Following this, 2.5 mL of phosphate buffered saline (PBS), pH 7.4 (ThermoFisher Scientific, 10380932) was added to each well, ensuring that the scaffolds were fully immersed in the solution. The plates were then sealed with para-film (Heathrow Scientific Moisture Proof Sealing) and

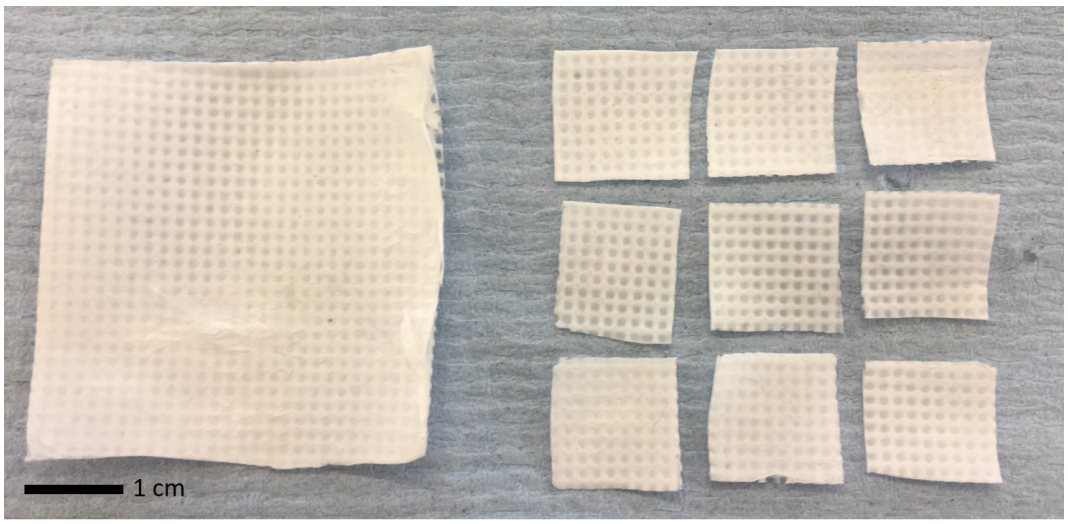

Figure 5.4: Preparation of the scaffold for the degradation tests

incubated (Gallenkamp) at 40°C for the duration of the experiment. At multiple time points, samples (n=5) were removed from solution and sponged gently to remove excess water. Each sample was then weighed to determine the wet weight. The samples were then washed with deionised water, and left to dry overnight, before weighing again to determine the degraded dry weight. The percentage water absorption (WA) of each sample was calculated using the following formula:

$$\text{Water absorption}(\%) = \frac{(\text{Wet weight - Degraded dry weight})}{\text{Degraded dry weight}} \cdot 100. \tag{5.2}$$

The percentage weight loss of each sample was calculated using the formula:

$$\text{Weight loss}(\%) = \frac{(\text{Initial dry weight – Degraded dry weight})}{\text{Initial dry weight}} \cdot 100. \tag{5.3}$$

where degraded dry weight refers to the weight of the sample after being removed from the PBS solution and dried. At each of the time points and for each samples (n=5), the pH of the PBS solution was measured following the removal of the samples from the wells.(Hanna instruments, H198103).

5.2.9.1 Mechanical tests

The variation of the mechanical properties was also measured. To do so, 20x40 mm rectangular samples (n=8) were cut from the 3D printed scaffolds. The samples were placed in Petri dishes, and immersed in PBS to ensure coverage of the samples as shown in Figure 5.5. The samples were put in the oven for 1 and 2 months at 40°C. Following this incubating period the mechanical tests were performed. A microtensile tester (Instron 5944) was used to measure tensile strain; following the same experimental parameters as shown in section 5.2.8.

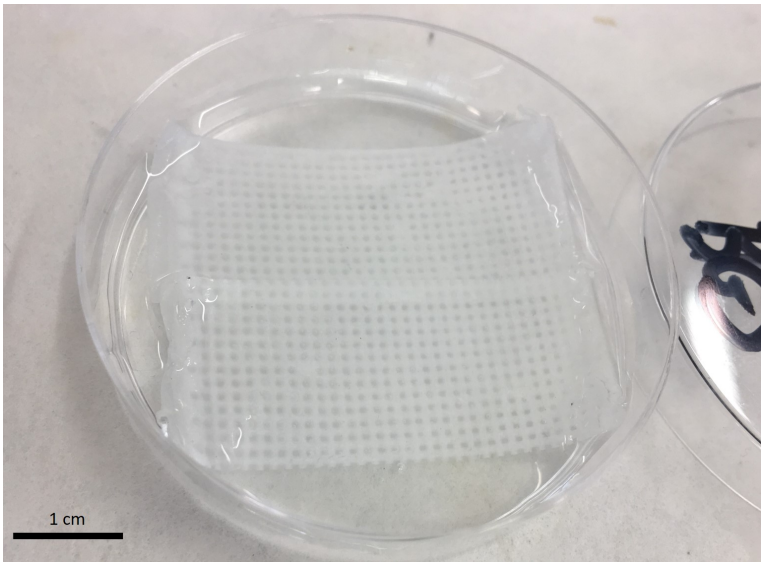

Figure 5.5: Preparation of the scaffold for the mechanical degradation tests

5.2.9.2 Thermal characterisation : DSC

Five-month degraded scaffolds of composition C4-EM, C5-EM and C9-EM were removed from the PBS solution and then thoroughly rinsed with deionised water before being dried over night. Once those samples were dried, DSC thermal testing were conducted on them to try and determine any shifts in polymer composition during the degradation process. The same protocol as described in section 5.2.7 page 112 was used and 5.9mg, 7.1mg and 8.2 mg of samples of composition C4-EM, C5-EM and C9-EM respectively were tested.

5.2.10 *In vitro* viability and toxicity cell studies

5.2.10.1 3T3 cell cultures

3T3 fibroblast were harvested and cultured from mice. After thawing, the 3T3 cells were grown in Alpha MEM Medium (BioWhittaker® Reagents, Lonza Walkerville Inc, United States). Cell culture media was complemented with 10% foetal bovine serum (Sigma Aldrich; UK), 1% antibiotic and antimycotic (100 μg/ml penicillin, 100 mg/ml streptomycin, and 0.25μg/ml amphotericin B; Sigma Aldrich; Uk) and 1% of L-Glutamine (Sigma Aldrich; Uk). Cell cultures were maintained in T75cm^2 flasks (Costar, Corning Inc., Corning, NY, USA) in standard culture conditions of 37°C and 5% CO_2, cells were passaged every 2 days after harvesting them by trypsinization using 0.05% Trypsin-EDTA solution (Gibco®, Fisher Scientific UK) at 80–90% culture confluence and further sub cultivated into culture flasks.

5.2.10.2 Preparation of 96-well plates for cell culture

3T3 cells were counted using the Trypan blue (Sigma-Aldrich®, UK) and a hemocytometer. The cells were seeded in 96 well flat bottom plates using a pipette. To do so, a solution of 1 million cell per mL of media was prepared after cell counting and 0.01mL of this solution (containing 10 000 cells) was deposited in 36 wells of the 96 well plate and completed with 0.190 mL of media.

5.2.10.3 Indirect *In Vitro* toxicity and cell viability assay

To determine the viability and cytotoxicity of the 3D printed samples, three 1 cm square scaffolds were cut from three different 3D printed scaffolds for each of the following compositions: C4-EM, C9-EM and C10-EM. Scaffolds were sterilised using UV and EtOH as this has been reported to have an important effect on cell viability.[461–463] The scaffolds were covered with 2.5 mL of media and placed in an incubator under standard culture conditions of 37°C and 5% CO_2. 2.5 mL of only media without scaffold or cells were incubated alongside. After 1, 3 and 7 days, the 0.2 mL of media covering the scaffold was taken using a pipettes and placed on top of the cells in the 96 well plates. Negative con-

trol cells were incubated in culture media Alpha MEM, the second negative control cells were incubated with cell culture media placed alongside the incubated immersed scaffolds. Positive control cells were killed just 20 min before testing the viability using Industrial Methylated Spirit (IMS). Following this step the cells were incubated for 24 hours and viability was measured using the PrestoBlue Cell Viability Reagent Protocol and assessed using fluorescence measurements. All of the conditions were tested in triplicate wells.
After being incubated for 24 hours, media and IMS were slowly aspirated using a aspirating pipette linked to an aspirator. 0.1 ml of an 1/10 presto in media solution was deposited in each well plate containing cells and on 3 wells containing no cells to measure the background fluorescence of the presto blue. The well plate was covered in aluminium foil and placed in an incubator for 30 min. Following that, fluorescence/viability was assessed using a plate reader. The following parameters were used during the reading, the 96 well plate was agitated for 5s, measurements of fluorescence were done at an excitation of 560 nm and a emission of 590 nm. Measurements obtain for NC1 were assimilated with 100% viability. Viability values for other samples were normalised from this value.

5.3 Results and discussion

5.3.1 Poly(glycerol sebacate) characterisation

The structure of PGS was characterised by NMR and IR. FTIR analysis (Figure 5.6) confirmed the formation of ester bonds in the PGS, shown by the intense peak at 1732 cm^{-1}. The two absorption maxima around 2928 cm^{-1} and 2854 cm^{-1} were attributable to the methylene group, and the broad peak observed around 3600 cm^{-1} was due to hydrogen bonded hydroxyl groups or can also be due to the humidity in the room.[400] IR spectrum showed that the PGS was successfully synthesized.
IR (νmax/$cm^{-}1$, neat):2928, 2854, 1732, 1257, 1232, 1161, 1126, 1093, 1047 1H NMR (400 MHz, $CDCl_3$) δ (ppm):1.246–1.297 (s, 20 H) 1.62–1.16 (m, 10 H) 2.29–2.356 (m, 10 H) 3.69–3.73 (m, 2 H) 4.11–4.31 (m, 6 H); Impurities 2.17 due do traces of acetone from cleaning the glass.

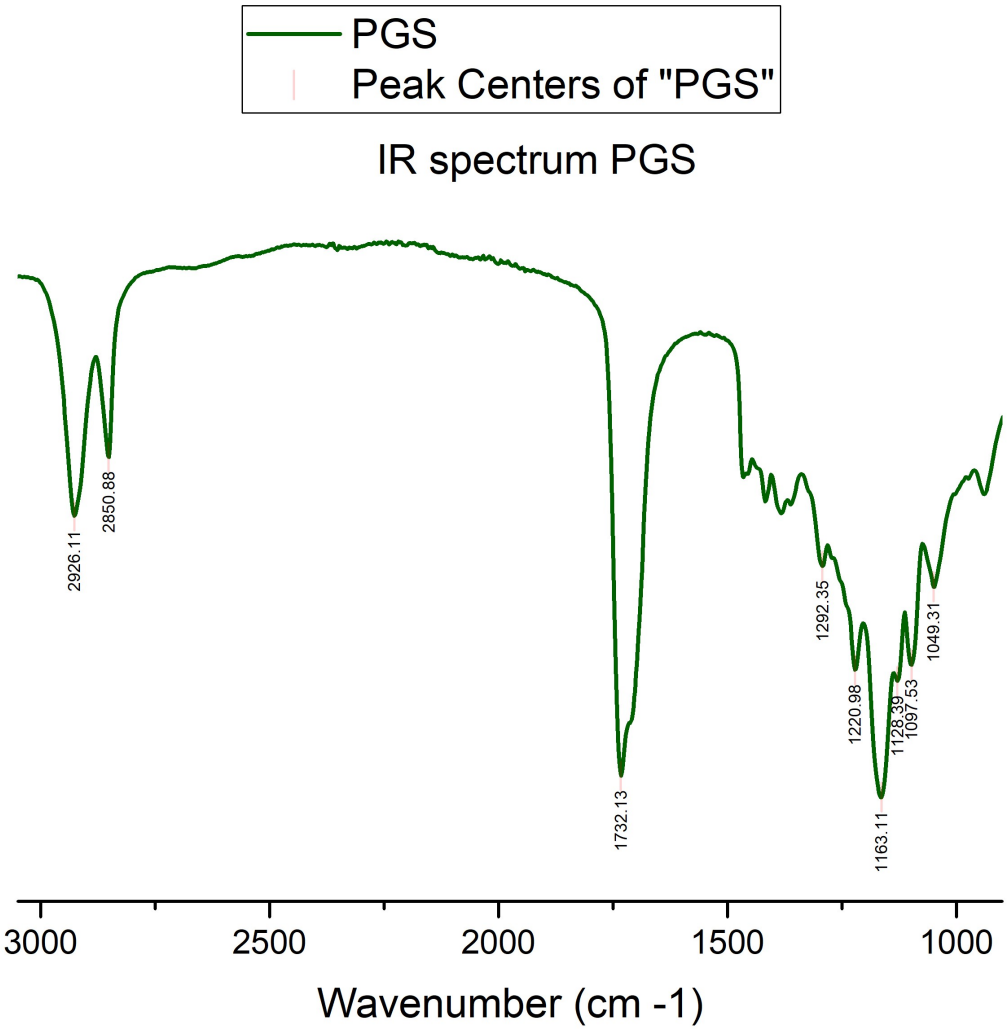

Figure 5.6: FTIR poly(glycerol sebacate)

The full spectrum of ^{1}H NMR spectrum in shown in figure 5.7 was analysed using already existing data from the literature.[347,464] As we could expect three signals belonging to the sebacic unit between 1.2 and 2.5 ppm; signals for the methylene protons of glycerol between 3.5 and 4.4 ppm; and signal for the methylene protons of the three glycerides between 4.8 and 5.5 ppm, as shown in Figure 5.7. The small peaks present at $\delta = 5.088$ ppm and 5.255 ppm correspond to some traces of non cross-linked polymer chains.

5.3.2 Silicate-based bioactive glasses characterisation

The particles used in the manufacturing of the cardiac patches should exhibit the following requirements:

- Amorphous structure throughout all of the particles

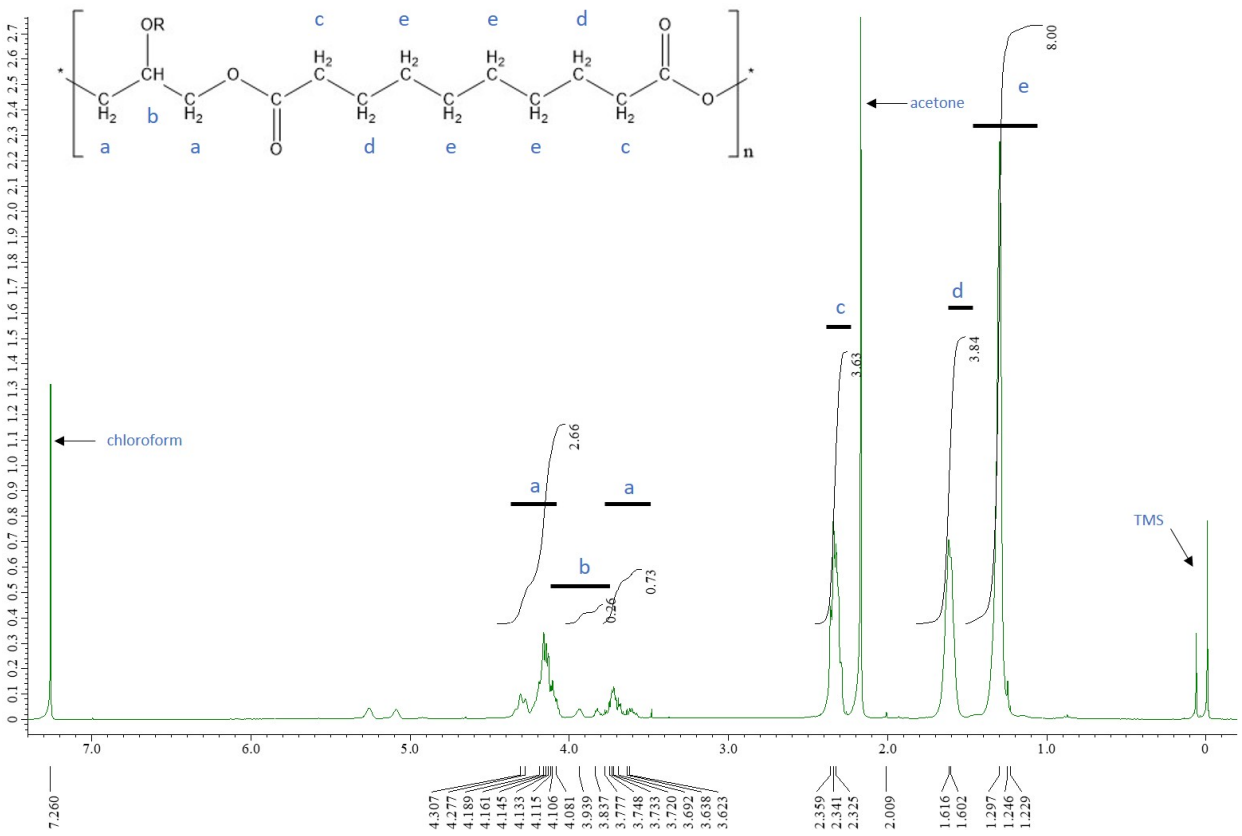

Figure 5.7: ^{1}H-NMR spectra with attributed signals

- Particle size smaller than needle size used in 3D printing or electrospinning (Syringe nominal inside diameter of 0.514mm)

- Avoid any agglomeration of the particles within the solution to obtain homogeneous and repeatable 3D printed scaffolds

The XRD spectrum (Figure 5.8) performed on the bioglasses showed the presence of a crystalline phase materialised by a sharp peak. In 45S5 bioglasses, formation of sodium calcium silicate crystals such as $Na_2CaSi_2O_6$ or $Na_2Ca_2Si_3O_9$) is highly common.[465] Unfortunately, the percentage of crystalline phase present within the glass could not be assessed and quantified with certainty. However, data in the literature revealed that this crystalline phase in bioglass is a very common problem which can be due to various factors such as the presence of water or during the sintering process.[465,466] Crystallisation occurring within the amorphous phase of bioactive glasses decreases the formation of the hydroxyapatite layer.[465] Additionally, it is argued that this crystalline phase can decrease the bioactivity of the glass.[465,467–469]

However, in the case of this project, using bioactive glasses containing an unmeasured and controllable level of crystalline phase would have negative effects on the data recorded as it would influence them in an unpredictable and unrepeatable way. The company providing the bioglass was then contacted to obtain another batch. However, obtaining a replacement batch was a long process. Therefore, preliminary work was undergone with this batch while waiting for a replacement.

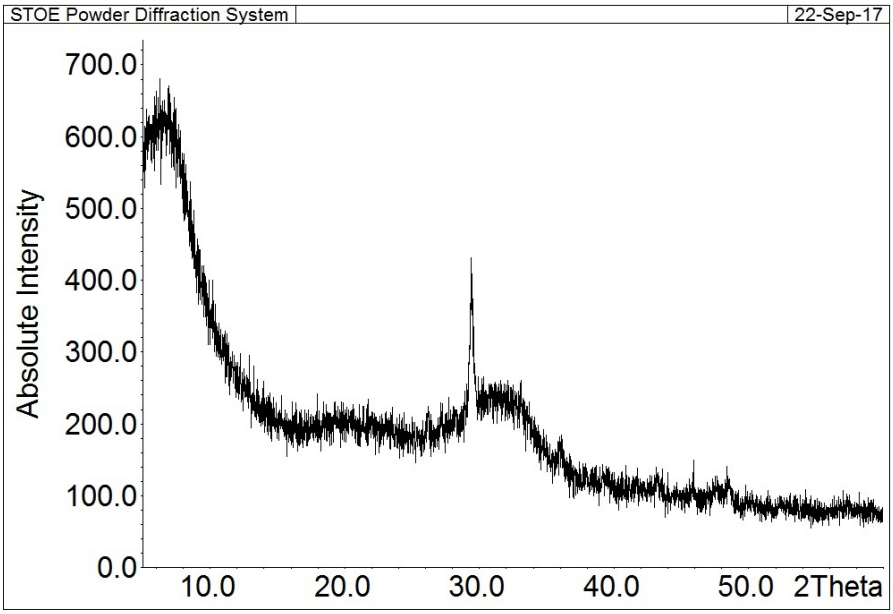

Figure 5.8: XRD 45S5®X-Ray Diffraction

The SEM picture (Figure 5.9) shows no sign of agglomeration of the particles but put in evidence the size dispersion of the particle which can go from 30 μm to 150 μm. The dispersion can cause problem in terms of 3D printing as they can block the nozzle preventing the 3D printing of defect-less scaffolds. The particle were deemed to large to be used with an electrospinning technique. The particles sizes were reduced and homogenized by ball milling. Following that the size dispersion was observed once more using FEG-SEM. The purchased bioglass were milled with 10 wt.% of acetylene acetate by a planetary high-energy ball-milling (Fritsch, pulverisette 7). Zirconia balls and a zirconia vial were used in the wet ball milling process. The rotating speed and ball-milling time were fixed at 450 rpm and 23 repetitions of 15min. The samples were then separated from the Zirconia balls and washed with Ethyl Acetate. The solutions was then centrifuged for 15 min at an rpm of 800. The supernatant solvent was removed and the wet bioglass were dried in

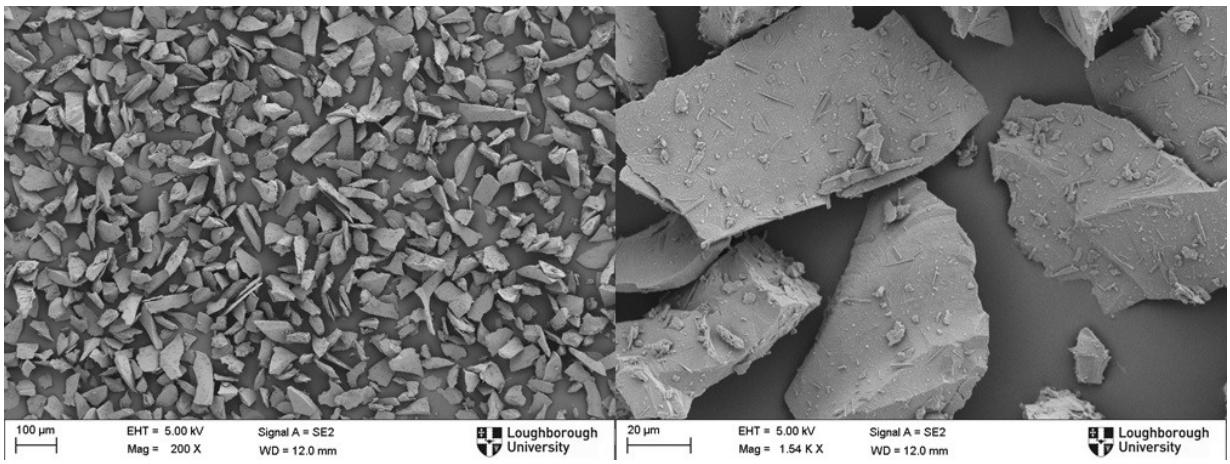

Figure 5.9: FEG-SEM Bioglass 45S5®

an oven at 50° over night.

Analysis of the particles Once dried the particle were analysed by SEM and XRD.

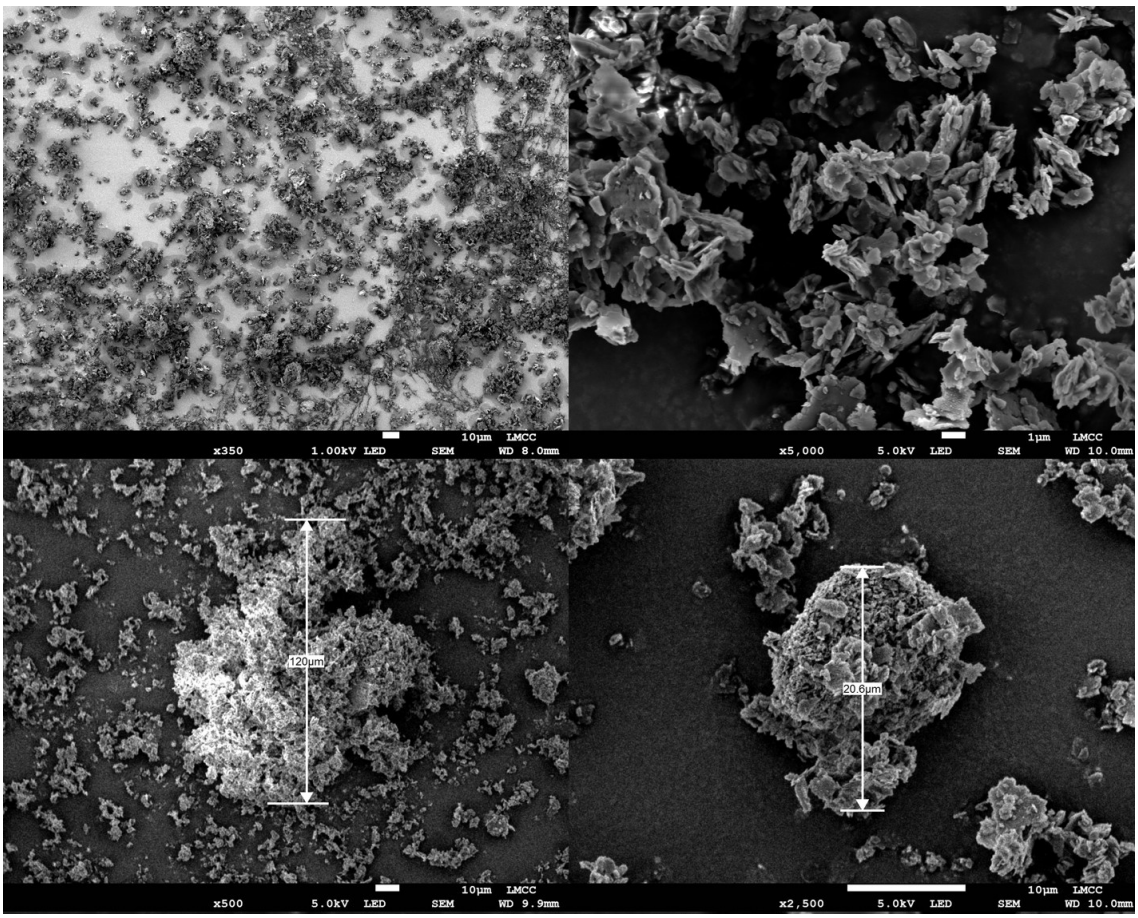

Figure 5.10: FEG-SEM Bioglass 45S5®after Wet Ball milling and drying

SEM images showed a significant decease of particle size however, they tended to agglomerates. Forming entities of diameter varying between 10 and 120 μm. This decrease of particle size insured the possibility to 3D print using an 23 Ga needle (230 μm in diameter). However, due to the small size, the particle led to the formation of more aggregates which would ultimately lead to anisotropy in the 3D printed scaffold. This feature would then decrease the repeatability and efficiency of the experiment. To assert the good repeatability of the experiment, a small amount of Dimethyl Sulfoxide (DMSO) was used to help prevent the particle from agglomerating. Indeed, DMSO has often been used as a functional solvent to stabilise and disperse particles.[470,471] DMSO is as a polar, aprotic solvent, with good solvating strength.[472] This green solvent with low toxicity can help nanoparticle solvating and stabilization.

The XRD results showed a reduction of the crystalline phase which was due to the decrease of the crystalline material within the particle. This is a result of the milling procedure

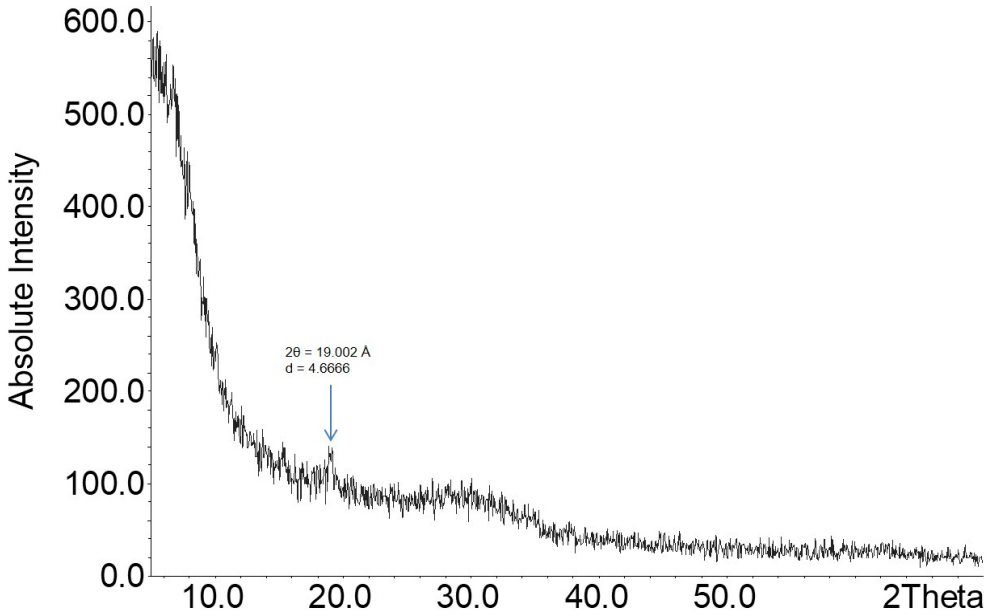

Figure 5.11: FEG-SEM Bioglass 45S5®after Wet Ball milling and drying

indeed, wet milling has the ability to decrease the crystallinity of a material.[473–475]

5.3.3 Electrospinning of the PCL/PGS solution

The morphological assessment of the scaffolds done through FEG scanning electron microscopy (SEM) (Figures 5.12 and 5.13) demonstrated that the fibres obtained had continuous morphology without any observed beads. FEG-SEM images showed scaffolds made of 3D meshes interconnected fibres. The average diameter was 5.50 $\pm$ 0.4 μm and 6.57 $\pm$ 0.65 μm respectively for fibres electrospun from solution with 14 and 13 wt% concentration.

PGS/PCL fibres glued together at some intersections and formed a physical link. This was attributed to the presence of PGS which is a highly viscous polymer at room temperature. This property was deemed of great interest for the multi-layered cardiac patches as it ensured a perfect contact between the 3D printed layer and the electrospun one and prevent the separation of the two scaffolds in simulated body fluids and once implanted in the body.

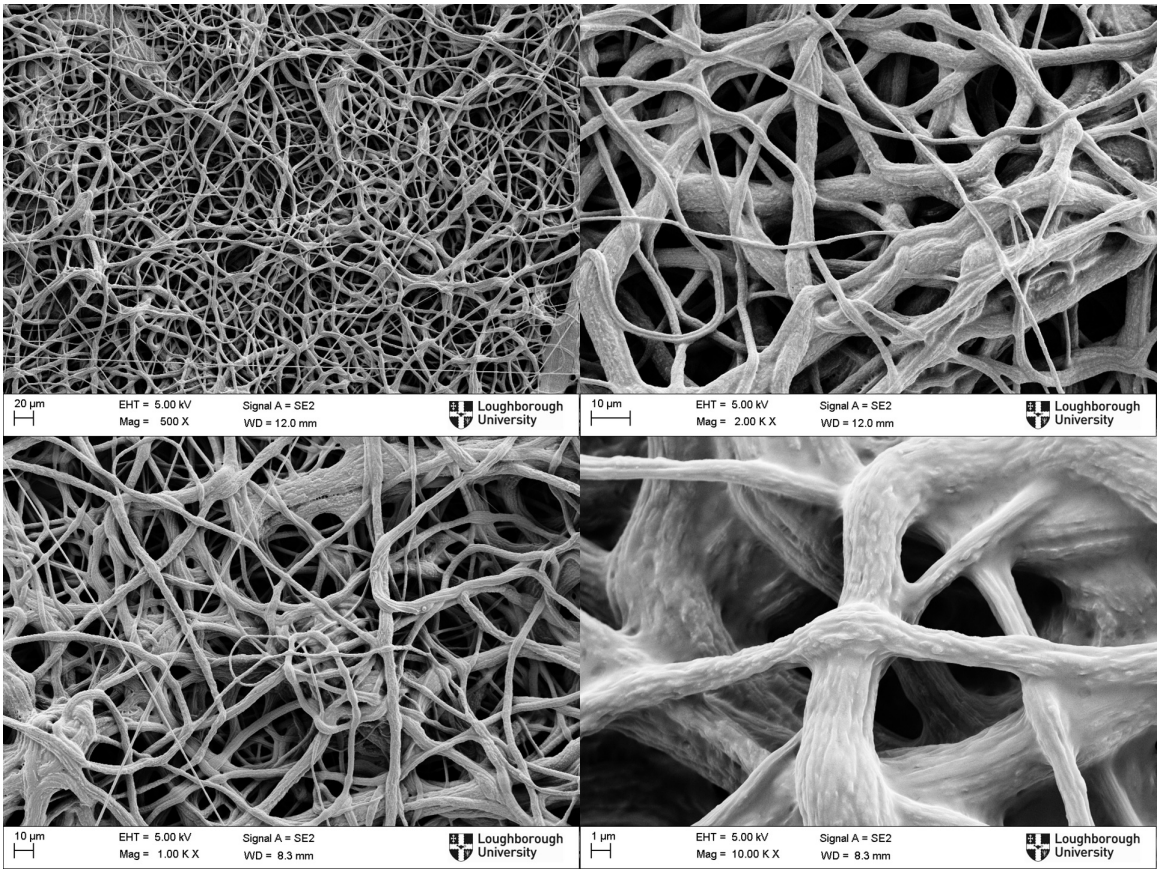

Figure 5.12: FEG-SEM 13%wt of polymer (1:1 PGS/PCL) in DCM/MeOH (7:3)

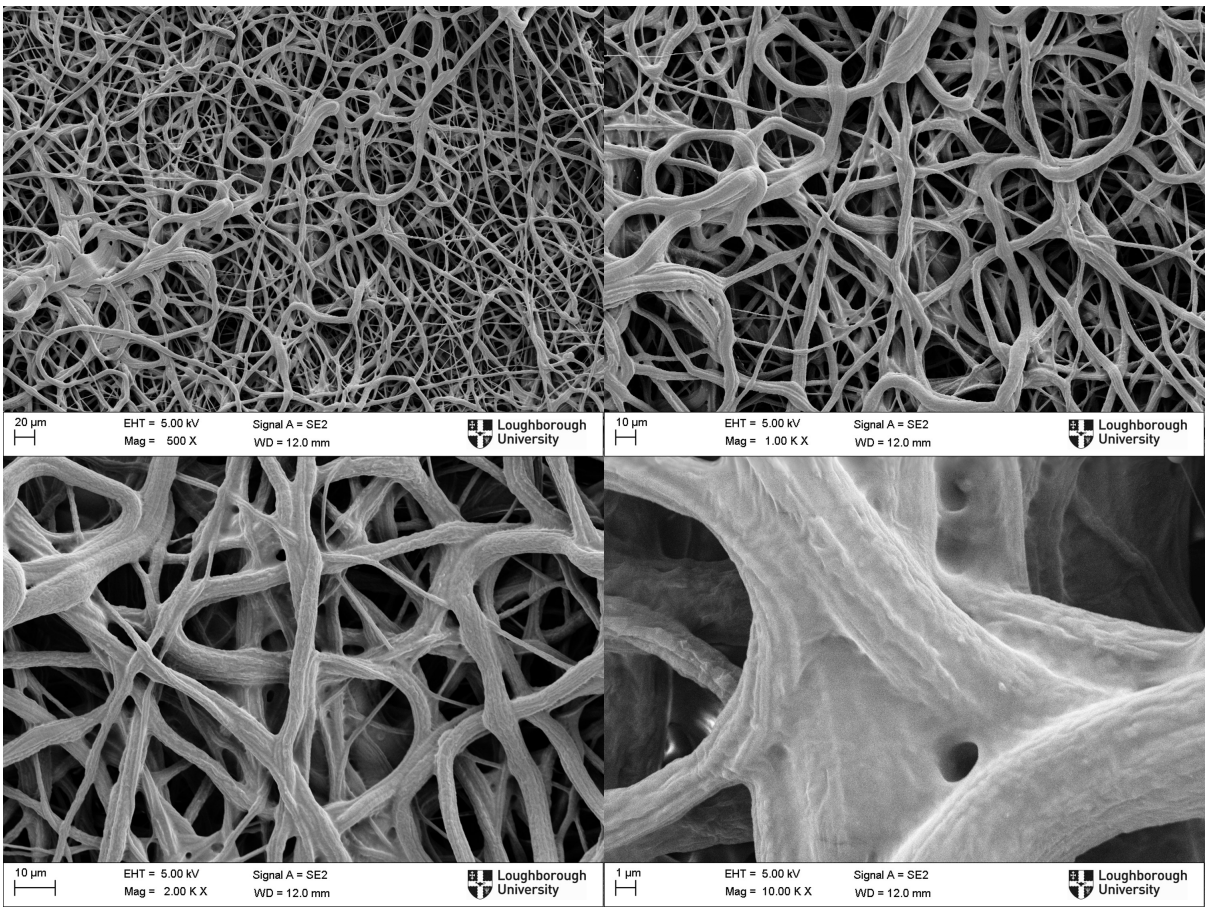

Figure 5.13: FEG-SEM 14%wt of polymer (1:1 PGS/PCL) in DCM/MeOH (7:3)

5.3.4 3D printing of the PCL/PGS/BGs scaffolds

3D printed scaffolds made of two bio-polymers and bioactive glasses 45S5 for cardiac tissue engineering were manufactured. An homogeneous solution of the polymers, with good particle dispersion to prevent any uneven scaffold distribution and any blockage during the 3D deposition, was successfully obtained. The 3D scaffolds present satisfactory structures following the set geometrical dimensions form the CAD file with adequate repeatability over multiple scaffold which were visually assessed. The next step was to determine how to assemble the two-layered scaffolds.

5.3.5 Manufacturing of the hybrid cardiac patches

Figure 5.15 shows the cross section and view from both sides of the samples prepared following "order 1". The addition of the liquid solution of solvent/polymer mixture on top of the electrospun scaffold (Figure 5.14) led to the loss of 3D mesh architectural

structure of the underlying scaffold. Indeed, the viscous but liquid 3D printed solution infiltrated and filled in the open-structure of the pores as clearly illustrated in figure 5.15 in the view from the electrospun side and from the cross-section where two intertwined scaffolds were clearly demonstrated. The view from the 3D printed side showed a good satisfactory structure in the manufactured layers. The two scaffolds appeared to be in perfect contact. However, the infiltration of the 3D printed layer within the electrospun scaffold would lead to the annihilation the mesh open structure of the electrospun scaffold which aimed at mimicking the ECM of the cardiac cells. This would therefore alter the role of the electrospun scaffold. Additionally, this intertwined scaffolds could lead to an uneven and non repeatable porosity in the combined scaffolds and also alter the mechanical properties of the scaffold. This manufacturing method was therefore deemed inadequate.

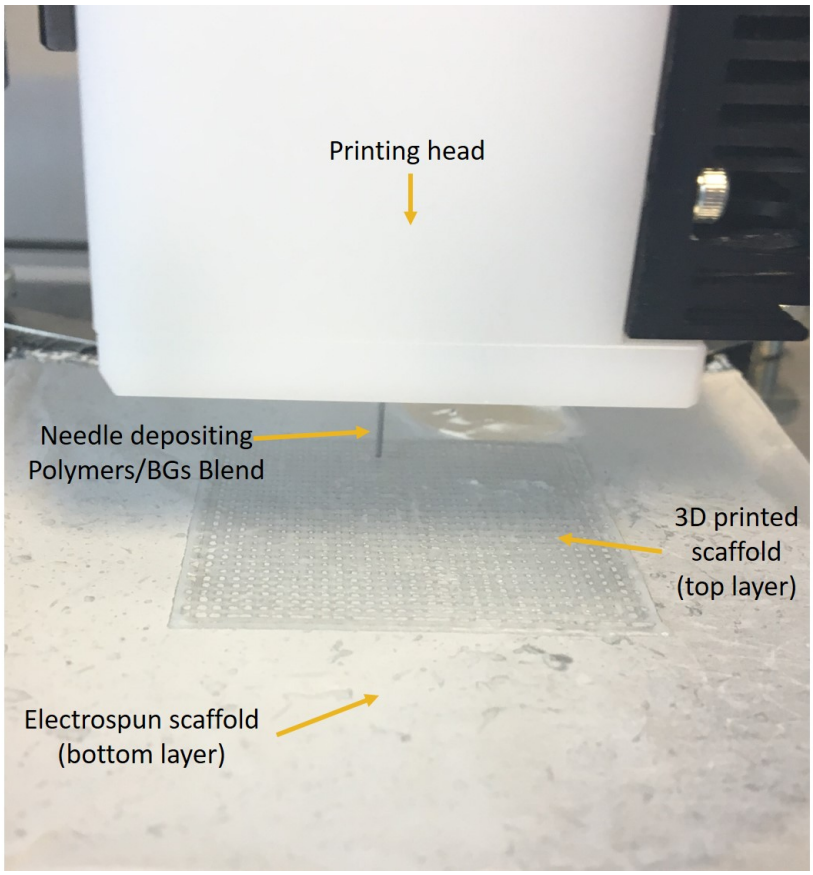

Figure 5.14: Order 1: Experimental set-up

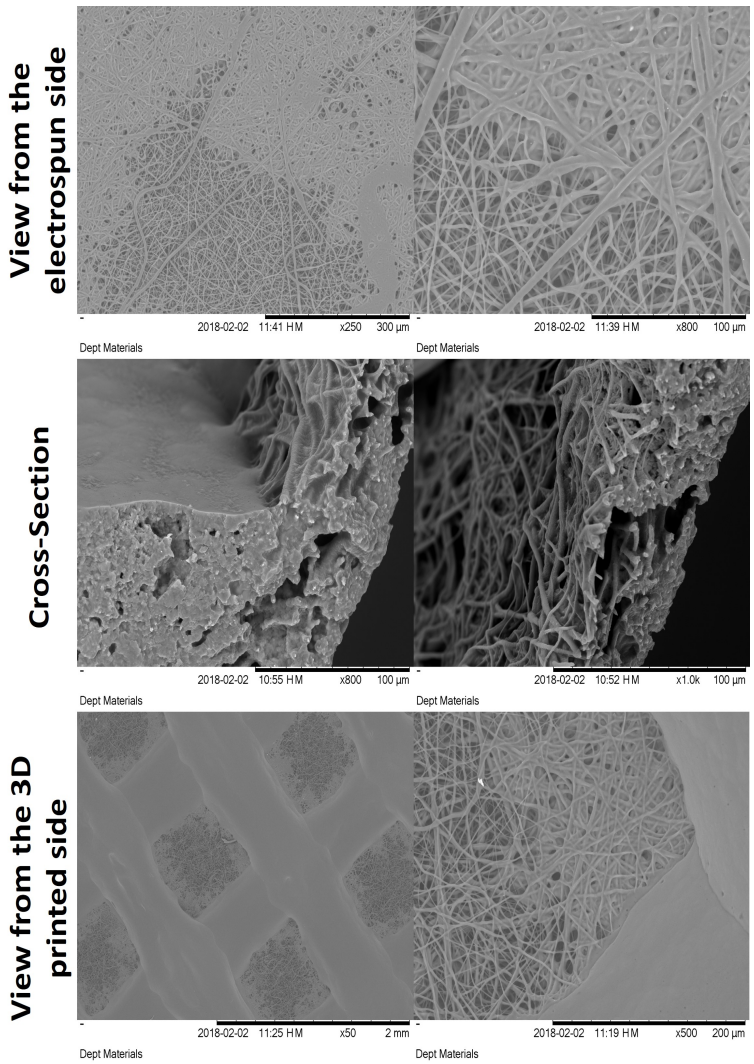

Figure 5.15: Order 1: View form the electrospun side, cross-section and view from the printing side using FEG-SEM of scaffold made of PGS/PCL(1:1) electrospun mat and PCL/PGS(1:1)BGs(5 wt%) 3D printed layers

In the case where the mixture of PGS/PCL was electrospun on top of the 3D printed scaffold (Figure 5.16), surface analysis showed that both of the scaffold presented no alterations after being combined (Figure 5.17). This was a necessary property to ensure good interaction with the cells once implanted and even mechanical properties. The 3D printed scaffolds exhibited a good satisfactory structure. When looking at the cross-section it appeared from the SEM that the two scaffolds may not have been in sufficient contact to prevent a separation of the layers once implanted. Indeed, it appeared that the contact was only ensured by a few fibres stuck to the 3D printed scaffold. To gain an initial idea on the scaffold behaviour in an aqueous environment and of a separation of the layers would occur, samples were placed in deionised water at room temperature and

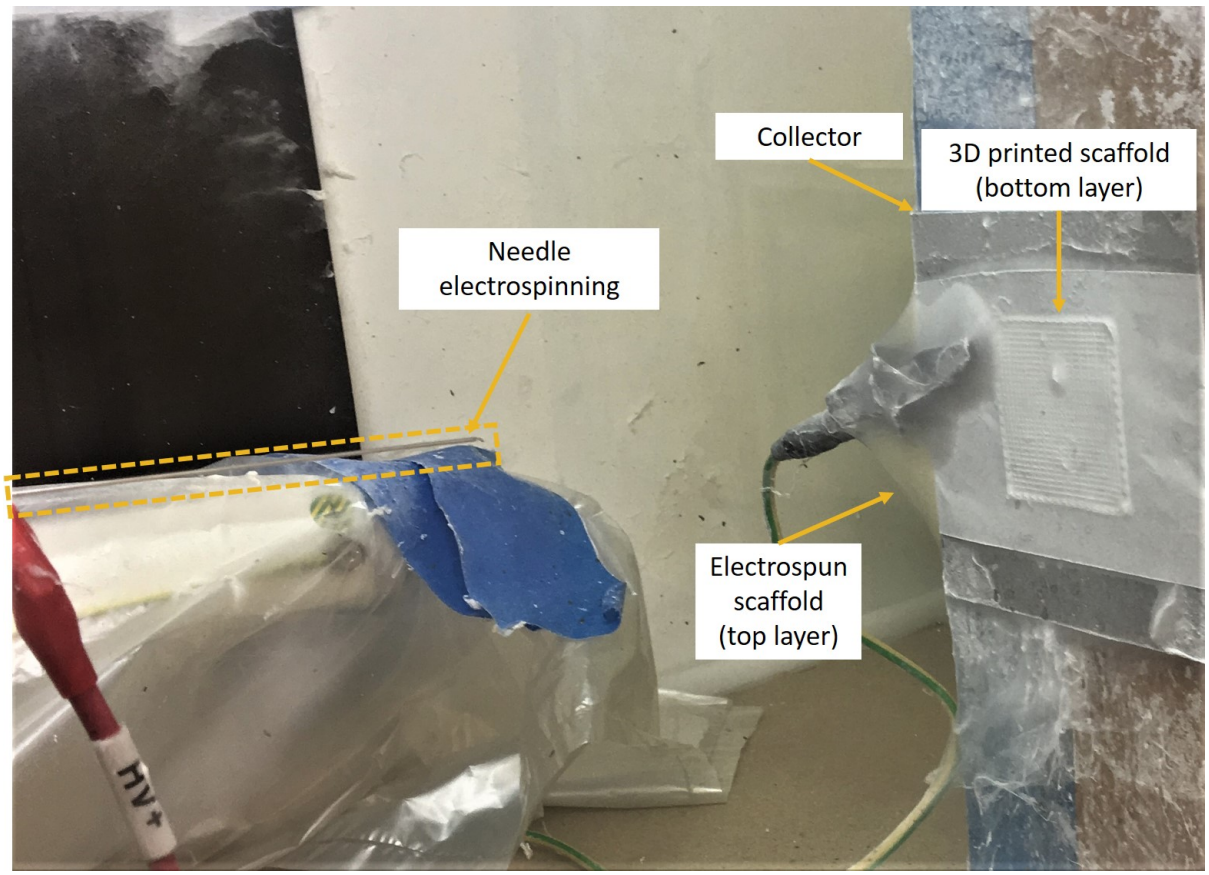

Figure 5.16: Order 2: Experimental set-up

at 37° under agitation for a week. The sample showed no separation of the two layers which led to the selection of this manufacturing technique for the following tests and optimisation.

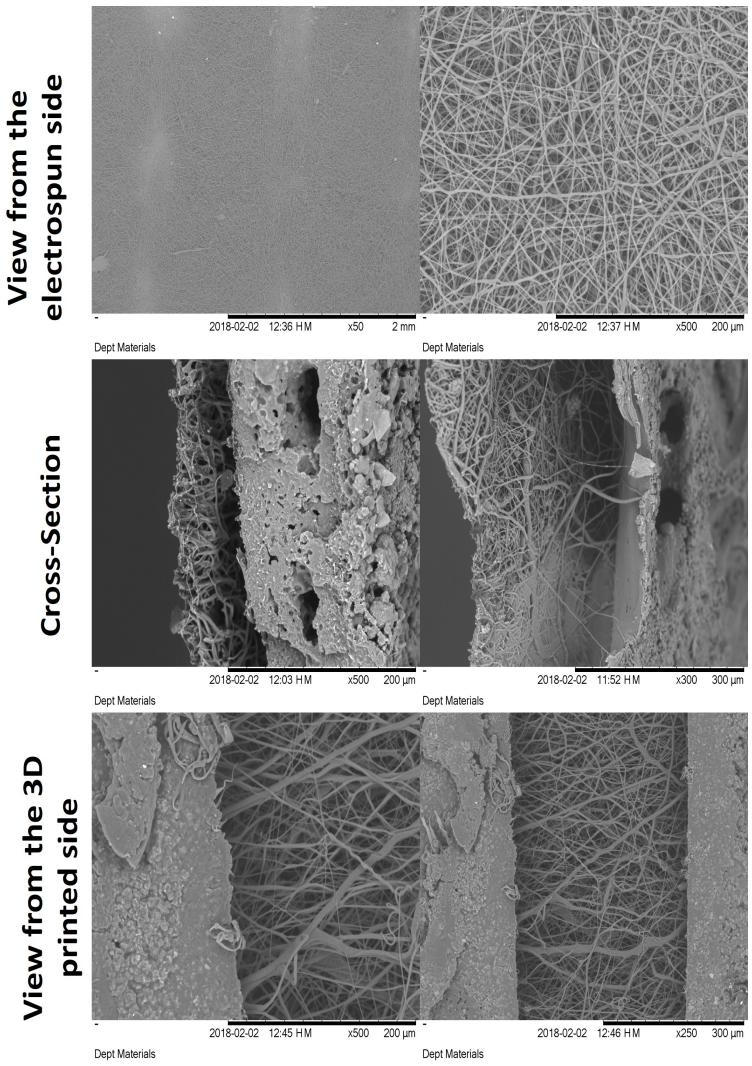

Figure 5.17: Order 2: View form the electrospun side, cross-section and view from the printing side using FEG-SEM of scaffold made of PGS/PCL(1:1) electrospun mat and PCL/PGS(1:1)BGs(5 wt%) 3D printed layers

The fabrication and analysis of the scaffolds led us to select the second order as manufacturing approach. The first technique led to the formation of intertwine layers with infiltrated solution within the electrospun scaffold that would ultimately alter the porosity, interaction with the cells and also the mechanical properties. The second approach gave good intact layers and the ability of the two layers to remain in contact has been tested. The cohesion of the layers on a longer time scale and the separation of the scaffolds during the degradation tests in simulated body fluid was also tested and is discussed below.

5.3.6 Optimisation of the scaffolds: use of different bioglasses

The 45/70 μm particle batch was analysed through SEM. Analysis (Figure 5.18) showed no sign of agglomeration of the particles and demonstrated the highly satisfactory size dispersion of the particle which ranged from 45 μm to 75 μm with perfectly round-shaped spheres. The observed dispersion and particle shapes were of great interest for the 3D printing step as no blockage of the nozzle was observed during 3D printing and ensured defect-less scaffolds. The particle sizes measured were small enough to be electrospun through a 21G needle. The electrospinning of a solution of the polymer mixture containing various amounts of bioglasses was therefore attempted. The electrospun scaffold morphology was assessed using FEG-SEM. Particle analysis performed using the software

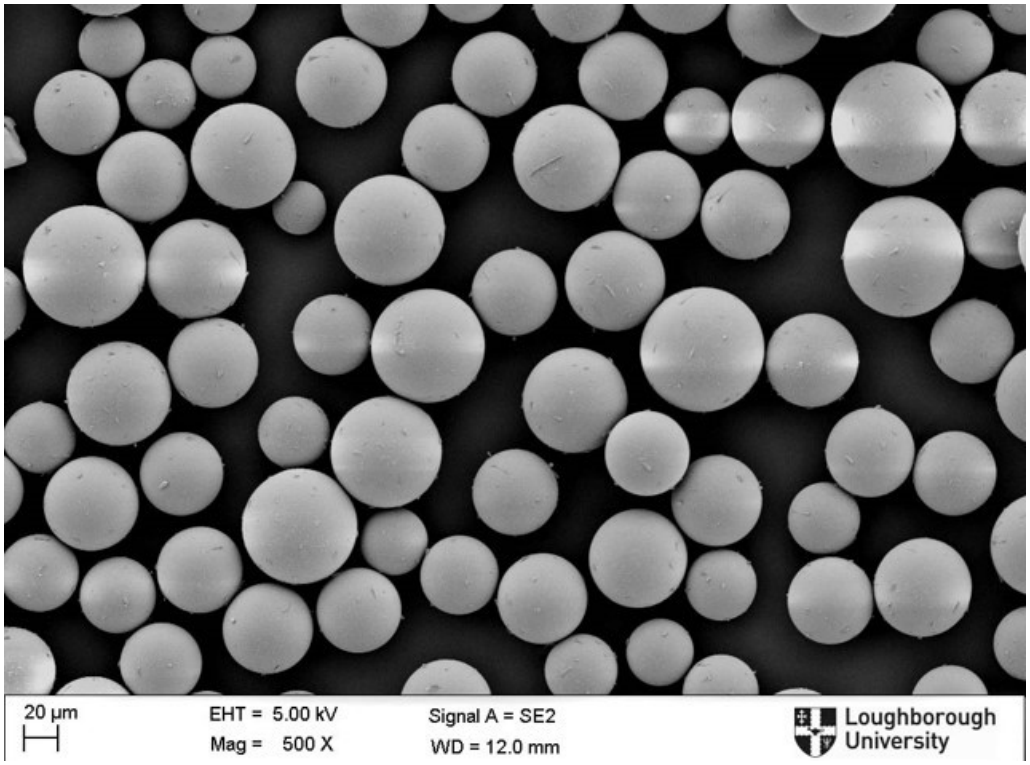

Figure 5.18: FEG-SEM Bioglass 45S5®45/70 μm

ImageJ (Figure 5.19) showed a recalculated particle size of an average of 55.2 $\pm$ 30 μm (Figure 5.20).

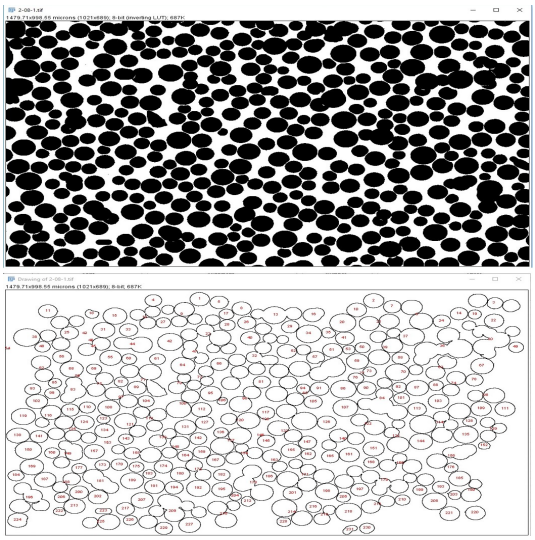

Figure 5.19: Particle Size Analysis (ImageJ), the particle are recognised using a threshold (top) and associated with a diameter (bottom)

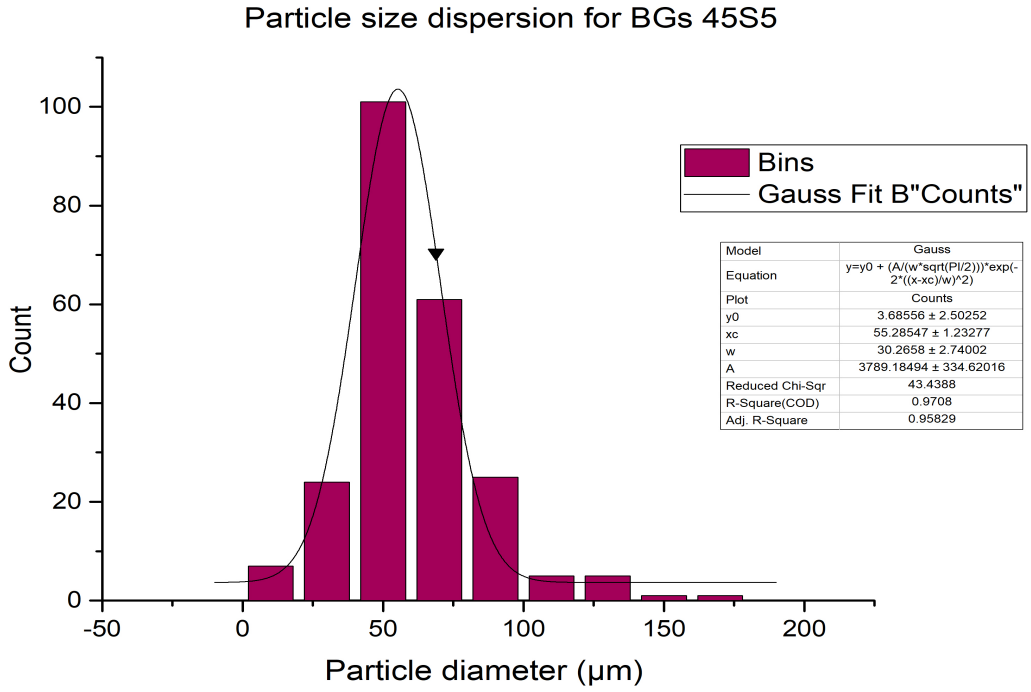

Figure 5.20: Particle size distribution

The XRD measurements (Figure 5.21) performed on the bioglasses showed the absence of a crystalline phase. This 45/70 μm particle batch showed highly satisfactory properties. Indeed, the sample presented an amorphous structure within the glasses.

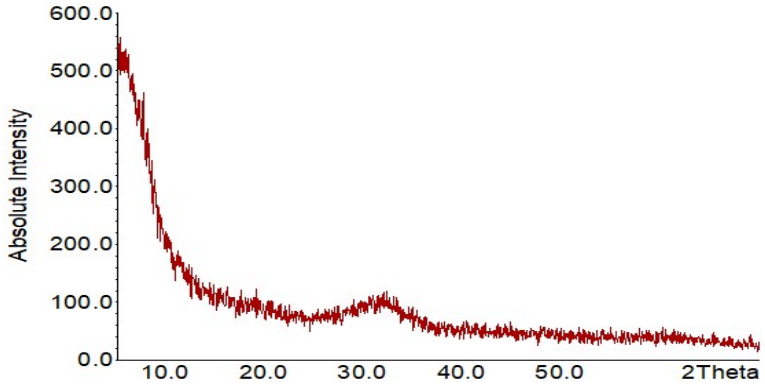

Figure 5.21: XRD 45S5®with size:45-75/*micro*m X-Ray Diffraction

5.3.6.1 Preparation of the scaffolds

Electrospun The samples were prepared as described above: 2 compositions were studied one with 5% of BGs and one with 10%. Both electrospun samples were morphologically assessed using FEG-SEM. The images are presented in Figures 5.22 and 5.23. The scaffolds showed satisfactory electrospun fibres with no beads. Diameter of the fibres was calculated using the software ImageJ. The average diameter of the fibres was 2.05 $\pm$ 0.17 μm and 1.32 $\pm$ 0.10 μm respectively for the solution containing 5 and 10 wt%. However, despite covering a large portion of the samples no particles of BGs was observed.This absence of particle in the scaffold could either be due to the needle getting blocked by too large agglomerates or the particles being to heavy to fly the short distance between the needle and the collector.

In order to determine which mechanism was preventing the BGs to reach the scaffold the experience was performed again. This time, a piece of foil was placed right under the needle and the collector distance was shorten from 15 cm down to 8cm. The experiment was run for 30 minutes and the samples were analysed using an optical microscope. Once again, no particle of BGs was observed in the electrospun sample and the foil placed under the needle showed droplets of dry polymers containing what appeared to be bright

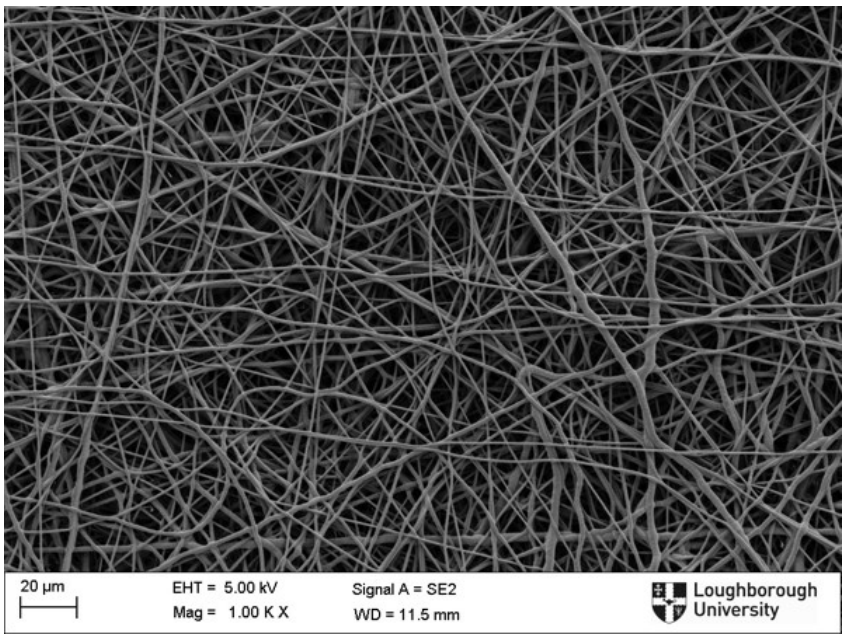

Figure 5.22: FEG-SEM 14%wt of polymer (1:1 PGS/PCL) in DCM/MeOH (7:3) and with added Bioglass 45S5®45/70 μm (5 wt%)

white bubbles. To determine if those bright spots could be particles observed using a optical microscope, a droplet of the mixture contained in the syringe was placed on a foil sheet and also observed under the light of the microscope. The observed image also picture droplets of see-through polymer circling what appears to be bright white droplets. The assumption that the BGs were to big to reach the collector and therefore falling on the floor was selected. The sample was then observed trough SEM and it confirmed our hypothesis that the particles were too large and heavy to reach the collector and therefore fell off somewhere between the syringe and collector as shown in Figure 5.24.

3D printed Solution for 3D printing were prepared as follow: the solution for the various compositions were prepared as shown in Table 5.3: The desired amount of BGs was suspended in 10g of acetone with 50 μL of Dimethyl Sulfoxide (DMSO). The solution was then left under vigorous agitation for 1 hour. The solution was then heated up to 40°C. The necessary amount of PGS was then added. Following the complete dissolution of PGS, PCL was added slowly before leaving on a stirrer at 40°C overnight.
The solutions were placed in a syringe and 3D printed at a temperature of 37°C following the inner structure properties shown in table 5.2. Figure 5.25 shows a microscopic image

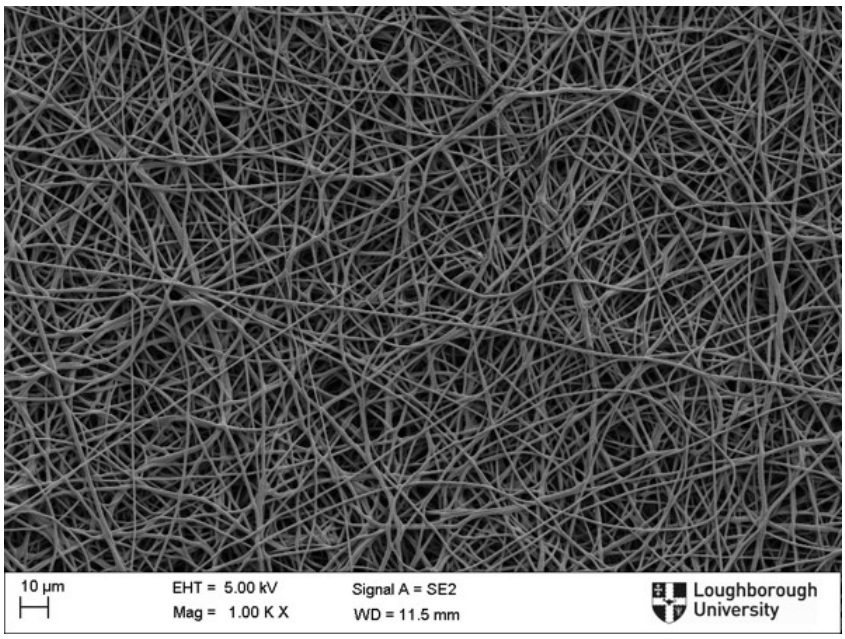

Figure 5.23: FEG-SEM 14%wt of polymer (1:1 PGS/PCL) in DCM/MeOH (7:3) and with added Bioglass 45S5®45/70 μm (10 wt%)

Table 5.3: Composition of the solutions for 3D printing

Composition	PCL	PGS (g)	BGs (g)	Acetone (g)	DMSO μL
Optimisation 1 (Opt1)	2.5	2.5	0.265	8	50
Optimisation 2 (Opt2)	2.5	2.5	0.556	8	50

of the multi-layered scaffold demonstrating highly symmetrical structure manufactured. FEG-SEM was used to characterise the samples and demonstrated the great regularity of the 3D scaffolds. The presence of particle was also observable when their amount equals 10 wt% as shown in figure 5.26.

Figure 5.24: Droplets collected under the syringe during the electrospinning of the solution containing 14%wt of polymer (1:1 PGS/PCL) in DCM/MeOH (7:3) and with added Bioglass 45S5®45/70 μm (10 wt%)

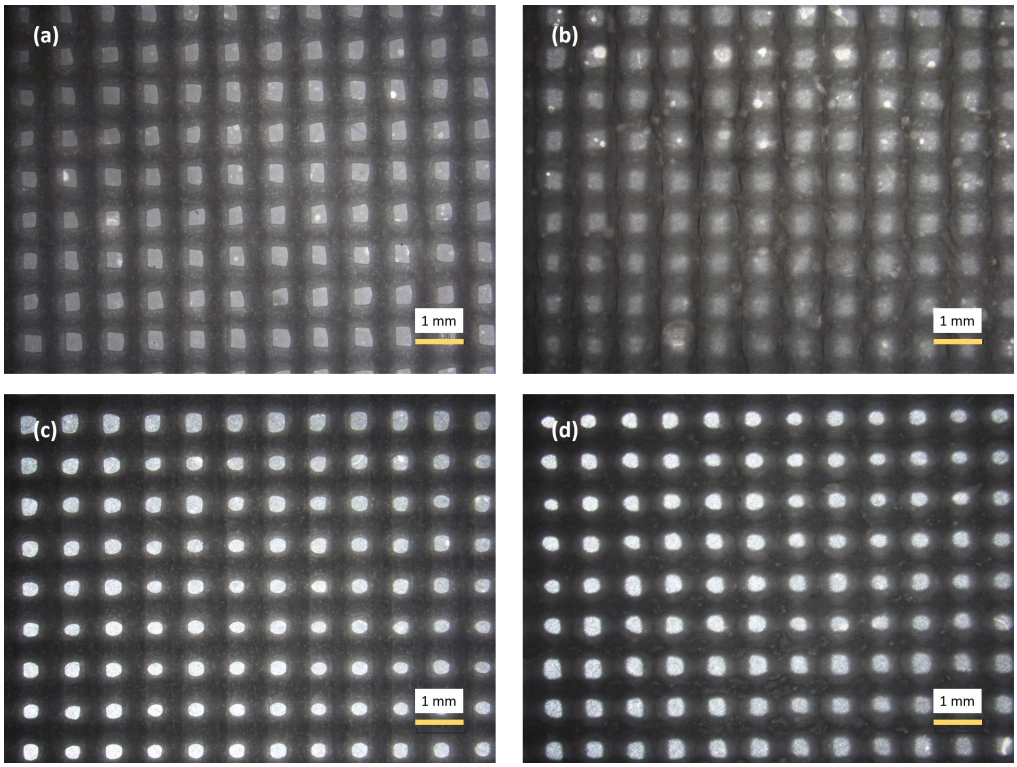

Figure 5.25: Microcopy images of the multi-layered scaffol: (a) and (b) are of composition C9 and (c) and (d) are of composition C10 with the view from the printed side (left) and from the electrospun side (right)

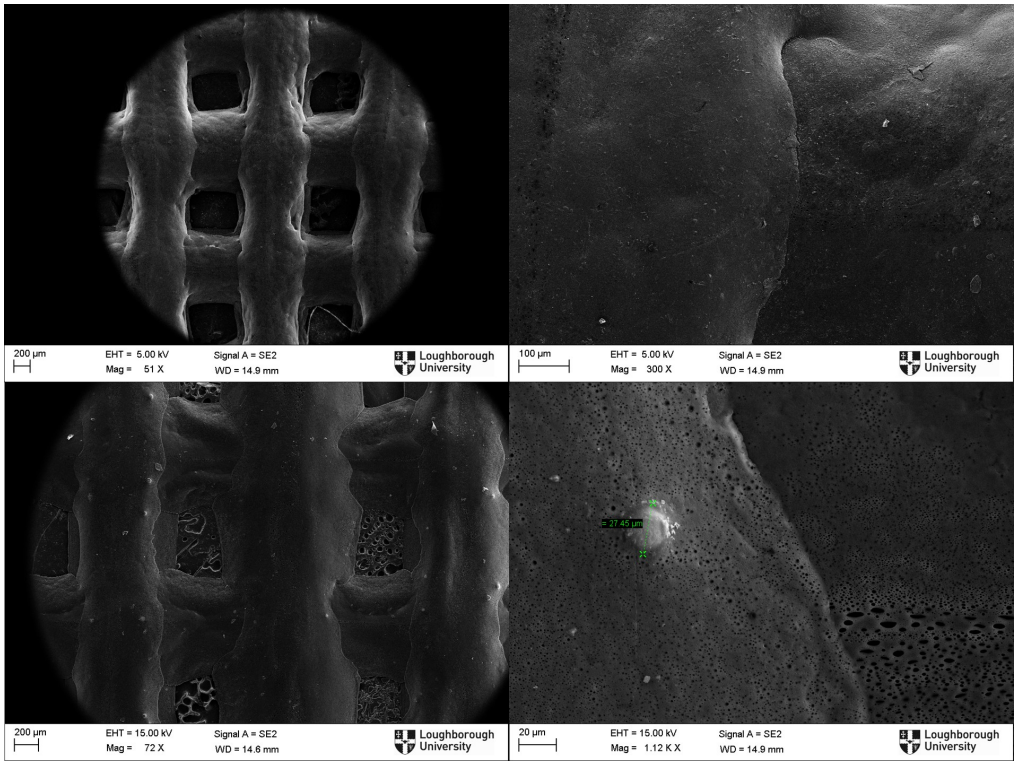

Figure 5.26: FEG-SEM of the 3D printed scaffolds with 5 wt% of BGs (top) and 10 wt% of BGs(bottom)

The use of the 45/75 μm 45S5 Bioglass® allowed the improvement of the printing process. Firstly, the use of spherical non aggregated particle ensured a better dispersion of the latter in solvents which subsequently provided geometrically repeatable scaffolds. To obtain an adequate dispersion of the fine particles, a smaller amount of acetone was used which maintained a high enough viscosity for the particles to stay dispersed throughout the entire 3D printing process. Additionally, less 3D printing related problems such blocked nozzle occurred. So far, the use of the 45/75 μm 45S5 Bioglass® constituted a real optimisation in comparison with the first BGs used as they are amorphous with small variation in sizes and they allowed the development of a simpler procedure for the manufacturing of the 3D printing scaffolds.

The composition containing the 45/75 μm 45S5 Bioglass was refereed to as Composition 9 (C9) for the one containing 5 wt% of BGs and Composition 10 (C10) for the one containing 10 wt% of BGs.

5.3.7 Characterisation of the thermal properties

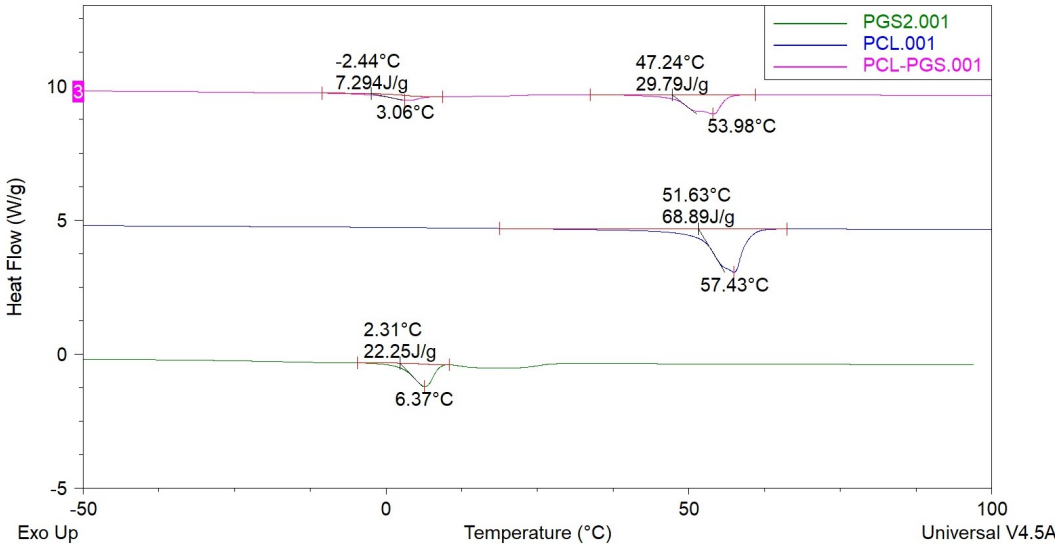

Figure 5.27: Endothermic values on the PCL, PGS and, PCL-PGS compositions

Figure 5.27 shows the calculated endothermic values for the PCL, PGS and, PCL-PGS compositions. Thermal analysis demonstrated the absence of chemical interactions between the polymers once blended. Indeed, the results show no significant variations in the glass-transition temperature (Tg) and melting temperature(Tm). FTIR used in com-

bination with DSC has been shown to be a powerful analytical tool.[476] Those results are in agreement with IR spectrum measurements as shown in Figure 5.28.

FTIR analysis (Figure 5.28) of the different composition confirmed the absence of interaction between the different component. Comparison with the literature enabled the attribution of the intense peaks around 1700 cm^{-1} to the ester bonds. While, two absorption maxima around 2900 cm^{-1} and 2850 cm^{-1} were attributable to the methylene group, and the broad peak observed around 3600 cm^{-1} was due to hydrogen bonded hydroxyl groups or can also be due to the humidity in the room.[400,461,477] PGS and PCL being two polymer exhibiting very similar chemical functions (ester bonds, ester bonds and hydroxyl group, the absence of any new absorption peak in both multi-layer and electrospun scaffold along with the DSC data. The small adsorption peak observed around 2340 cm^{-1} was due to the presence of CO_2 during the sample acquisition.[478]

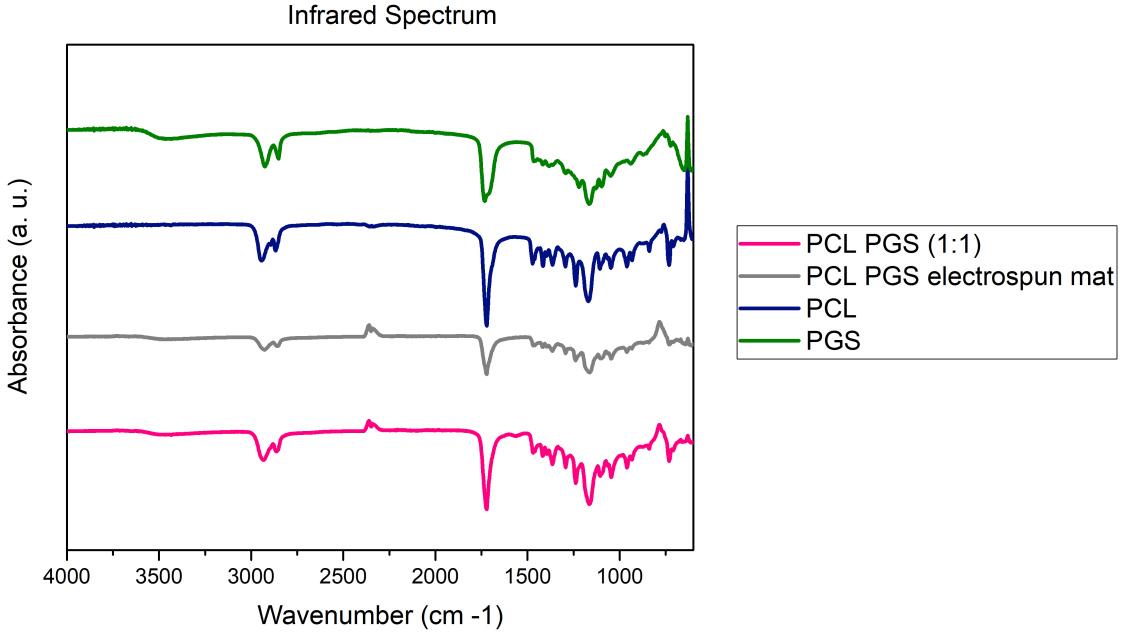

Figure 5.28: IR spectrum of the PCL, PGS and, PCL-PGS compositions

Table 5.4: Selected Compositions for the 3D printed layer

Composition	PCL/PGS Ratio	Bioglass Percentage (wt%)
C1	(1:0)	0
C2	(1:0)	5
C3	(1:0)	10
C4	(1:1)	0
C5	(1:1)	5
C6	(1:1)	10
C7	(2:1)	10
C8	(1:2)	5
C9*	(1:1)	5
C10*	(1:1)	10

* Compositions C9 and C10 were prepared using 45-75 μm Bioglass

5.3.8 Mechanical characterisation

The aim was to produce a patch with satisfactory mechanical properties in order to provide a suitable treatment for scarred myocardial infarction. Therefore, selection of the material composition was firstly made. Testing the mechanical properties of several compositions helped better understand the effect of each component on the mechanical properties. Mechanical properties served as a first selection as the myocardium's properties have been intensively studied and mechanical requirements of a scaffold play a crucial role in cardiac tissue regeneration.[265,400,443–448] Additionally, it is a efficient and straight forward screening method.

The tested compositions are detailed in Table 5.4

All compositions were tested with and without electrospun mat, which was made of PCL and PGS in a 1:1 ratio. For better clarity, the samples were tested with electrospun mat of composition X, referred to as CX-EM, where EM stands for electrospun mat and the ones without any electrospun mat referred to as CX where X is the composition as detailed above. Using tensile testing, the effects of polymer content, the electrospun mat and amount and size of BGs were assessed.

5.3.8.1 Influence polymer content

To study the influence of the polymer used, the compositions C1, C4, C5, C7 and C8 showed interesting data. Figure 5.29 shows the results obtained for the measure of the Young's modulus(E), Failure at strain (FS) and UTS when the amount of PGS is varied with the polymer blend.

The addition of PGS led to a decrease of all three measurements. For the compositions

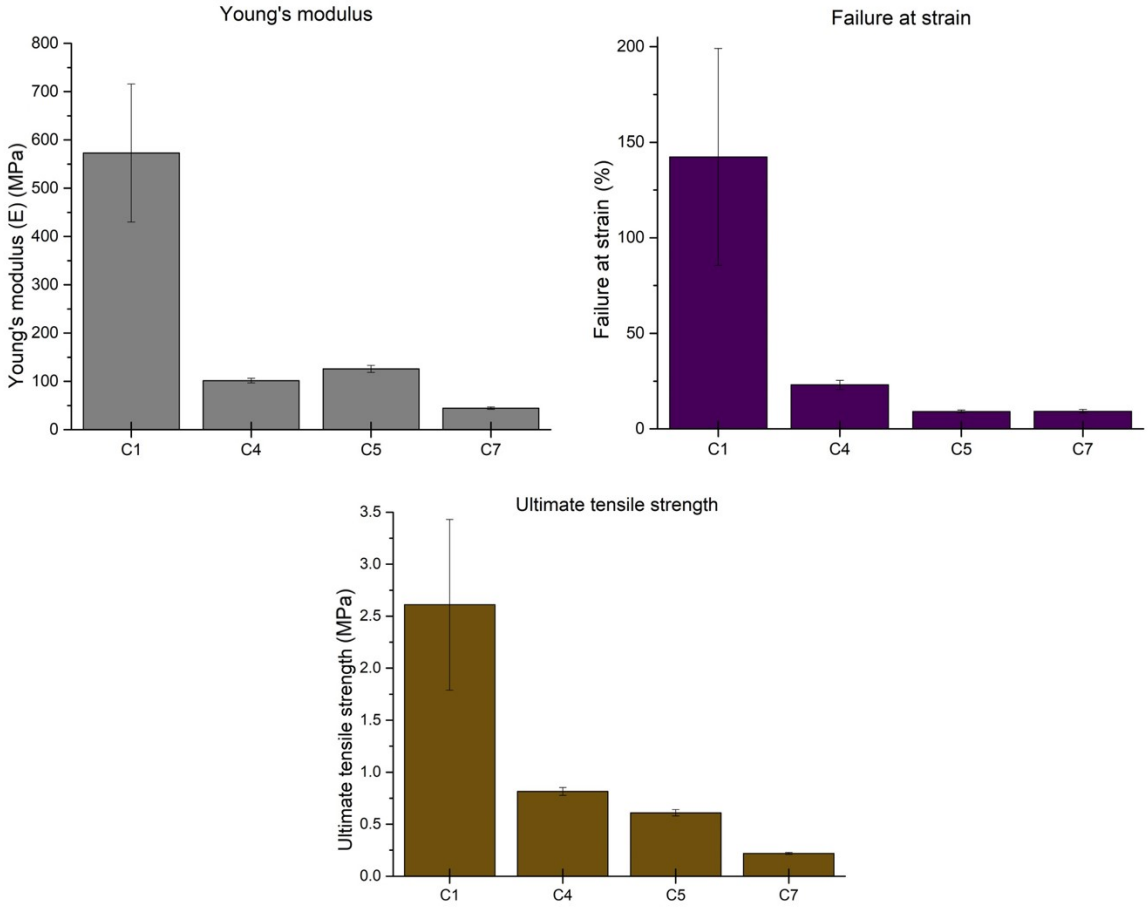

Figure 5.29: Influence of polymer on the mechanical properties with the study of compositions **C1** (PCL), **C4**(PCL-PGS(1:1)), **C5** (PCL-PGS(1:1)-5wt%BGs), and **C7** (PCL-PGS(1:2)-5wt%BGs)

C1, and C4 containing no BGs, the largest drop in the mechanical properties was witnessed with an decrease from 573 ± 143 MPa to 102 ± 4 MPa for the Young's modulus, from 142 ± 57 % to 23 ± 2% for the failure at strain and from 2.61 ± 0.82 MPa to 0.82 ± 0.04 MPa for the UTS respectively for C1 and C4. This trend was further present in the composition C7 where the polymer blend contains twice as much PGS with a E going

down to 44 ± 2 MPa, a FS to 9.2 ± 1.0 % and an UTS to 0.22 ± 0.01 MPa.

The addition of PGS led to a more flexible cardiac patch that also tend to break at shorter elongation. PGS being a elastomer, more flexible patches were obtained. However, the addition of PGS did not enable the patch to sustain more elongation before breaking. This was attributed to the polymer blend and the absence of chemistry bonds between PGS and PCL as shown in the DSC measurements (Figure 5.27). Indeed, a mixture of two polymers composed of large macro molecular chains is obtained (chains which are cross-linked for PGS) that possibly do not mix at a macro level and therefore the mix appears to be non miscible at a macro level and would explain why the PCL scaffold (C1) could sustain a larger elongation as shown in Figure 5.30 and not the composition C4, C5, C7 and C8.

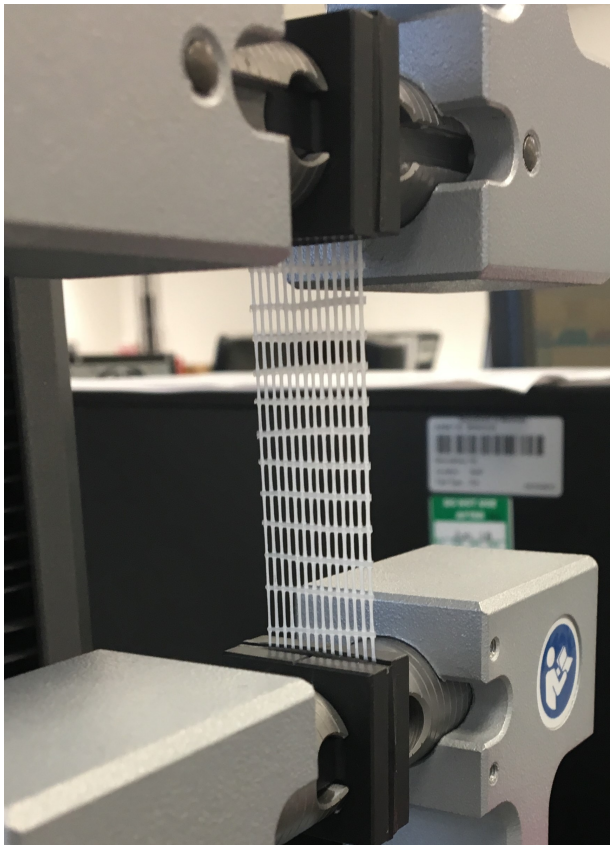

Figure 5.30: Scaffold of composition C1 being elongated under tensile stress

Additionally, PGS sheets (cross-linked at 120° as was the PGS used in this study) have been shown to exhibit lower E (0.22 ± 0.03 MPa), FS (2.56 ± 0.26%) and UTS (0.39 ± 0.03

MPa), while PGS pre-polymer films demonstrated the following mechanical properties E (1.2 ± 0.3 MPa), FS (45 ± 8 %) and UTS (0.32 ± 0.04 MPa).[400] In this study, they produced blends of PGS ans PCL through electrospinning that demonstrated an increase in stiffness and elongation. Indeed, the E went up from 6 ± 2 MPa to 8 ± 2 MPa respectively for the PCL fibres to the PCL-PGS fibres along with the E that went from 116 ± 30 % to 142 ± 29% and the UTS from 2.0 ± 0.7 MPa to 3.0 ± 0.5 MPa. These results could be explained by the use of the pre-polymer which is not cross-linked and therefore constituted of smaller polymer chains. The study does not present any thermal analysis which could help understand if chemical bonds are created between the two polymers.

5.3.8.2 Influence electrospun mat (EM)

Following the study of the influence of the polymer content (see section 5.3.8.1), the effect of the addition of the electrospun mat (EM) on the mechanical properties was investigated. Firstly, the mechanical properties of the EM on its own were tested. It should be noted that these results have to be taken with caution, as during the realisation of the tests, the samples used were extremely thin (a few mm) and their thickness and width were altered whilst being removed from the aluminium foil and mounted on the tensile machine. However, results showed that PCL-PGS(1:1) electrospun mat exhibited a E of 66 ± 16 MPa and demonstrated a high FS of 72 ± 6 % and UTS of 4.5 ± 1.1 MPa. These results appear quite surprising considering this sample exhibits a very narrow thickness (a few mm) but could be elongated up to 73 ± 6 % and required a high UTS to break. At this point the material was beyond its elasticity limits. The hypothesis here is that the EM experienced strain hardening or stress induced crystallisation where the polymer undergoes a re-orientation and alignment of their chains in the direction of the loading increasing their strength and stiffness, which could explain the high values of FS and UTS.

The mechanical properties of PGS/PCL EM were investigated on the work of Rai *et al.*[400] were a 15 wt% polymer solution (PGS pre-polymer/PCL (2:1 weight ratio)) in

DCM/MeOH (7:3 volume ratio) was electrospun at a flow rate of 1.6 ml.h^{-1} at a distance of 15 cm and voltage of 15kV. This samples showed a Young's modulus of 0.02–0.5 MPa and tensile strength = 3–15 kPa. In the work of Vogt *et al.*[461], 1:1 blends of PCL and PGS (using PGS prepolymer and mildly crosslinked PGS) in acetic acid with a concentration of 27.6 wt%. The electrospun scaffold were obtained at flow rate of 1.1 ml.h^{-1} at a distance of 11 cm and voltage of 15kV. Mechanical characterisation of the EM for the composition using mildly crosslinked PGS showed an E of 7.1 ± 0.8 MPa, an UTS of 5 ± 1 MPa and a FS of 333 ± 48 %.

With regards to this data, the obtained values were significantly higher (for E and UTS) and were explained by the use of a fully polymerised PGS. Additionally, the FS values obtained were smaller than the one in the work of Vogt *et al.*[461] which was once again explained by the use of cross-linked PGS leading to a more difficult dissolution.

When the EM was added to the 3D printed scaffolds, all of the compositions showed an increase of the E; as shown in Figure 5.31. This increase in stiffness could be explained by the presence of the thicker scaffold combined of two layers which then presented a higher stiffness. An increase in the ultimate tensile strength with the addition of the EM was also observed with a 36 % increase for C4, 80 % for C5 and 38 % for C9. This was a subsequent effect of the hardening the EM experienced toward the end of the test. Figure 5.32 shows how the multi-layered scaffold behave under elongation. In most cases the 3D printed layer was the first one to break, followed by the breaking of the EM showed in the stress-strain measurements with a sudden drop in stress. The failure at strain did not seem to show any correlates with the addition of the EM; going from 23 ± 2 down to 6.0 ± 0.2 % for C4, from 9.0 ± 0.7 up to 11.3 ± 0.5 % for C5 and from 9.0 ± 1.O down to 4.6 ± 0.4 % for C9. The FS was therefore not influenced by the addition of the EM.

The electrospun fibres acted as a reinforcement for the assembled patches due to the excellent fibre–fibre bonding and strong interfacial adhesion between the electrospun layer and the 3D-printed one. Similar mechanical behaviour, even though for a different scaffold architecture, has been recorded for three-layer systems made of porous PGS tubes wrapped with PCL electrospun fibres and reinforced by PCL rings (tensile load at break

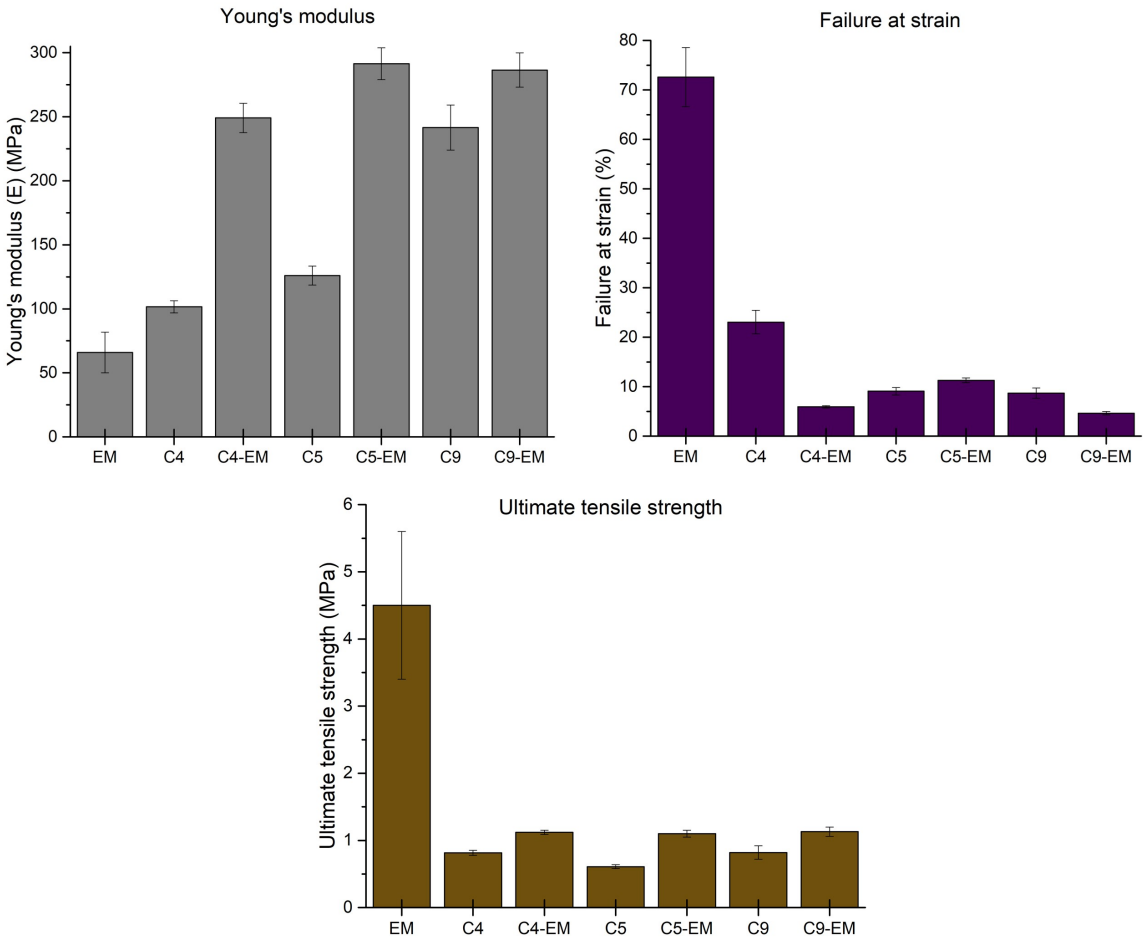

Figure 5.31: Influence of the electrospun on the mechanical properties with the study of compositions **EM** (Electrospun Mat), **C4** and **C4-EM**(PCL-PGS(1:1)), **C5** and **C5-EM** (PCL-PGS(1:1)-5wt%BGs), **C9** and **C9-EM** (PCL-PGS(1:1)-5wt% [45-75μm]-BGs) and **C8** (PCL-PGS(1:2)-5wt%BGs)

of around 5.5 N), where PGS significantly contributed to the elastomeric response.[479] The use of electrospun sheets to increase tensile strength in composites has been described in the literature for microfibre-based netting materials.[480–482]

5.3.8.3 Influence of bioactive glasses

Finally, the influence of the addition of BGs on the mechanical properties was then assessed. Scaffolds with various types and amounts of BGs were manufactured. Two types of BGs were used; Type 1 refers to the first BGs used and wet ball milled as detailed in section 5.3.2 page 122 and type 2 the [45-75 μm]-BGs used as optimisations.

In terms of the amount of BGs, Figure 5.33 shows that increasing of the amount of BGs

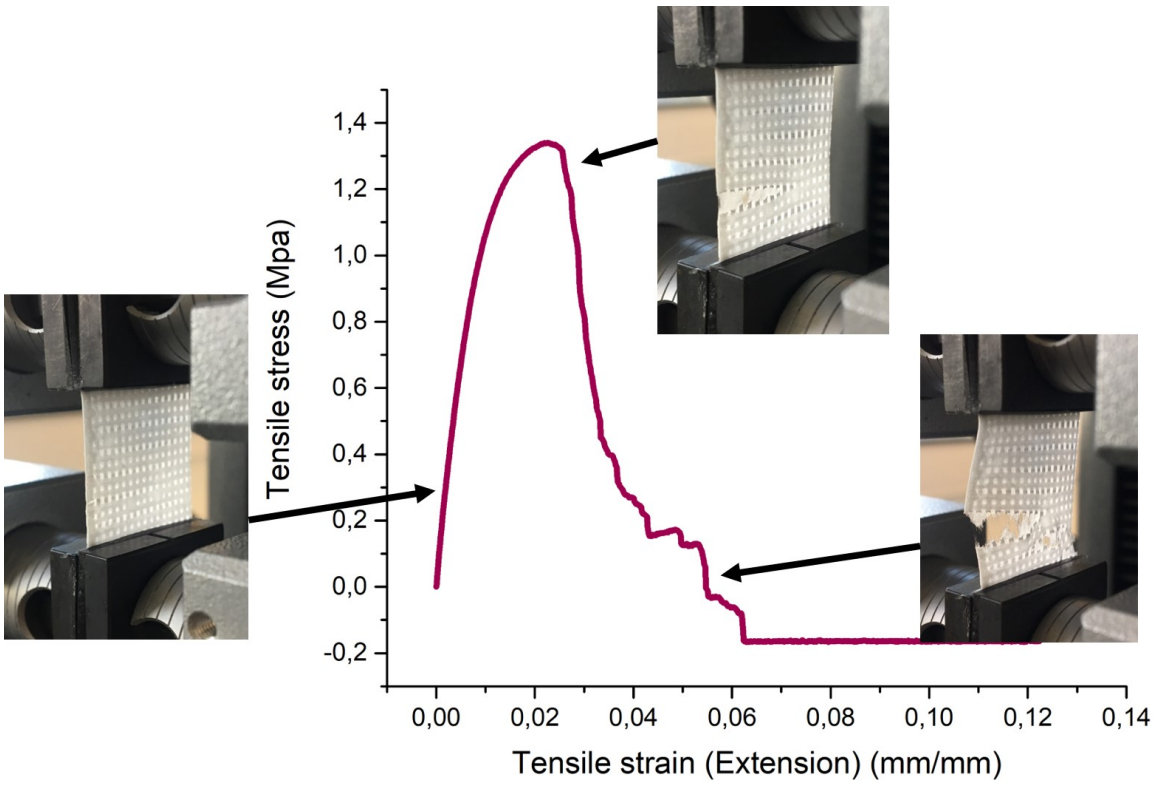

Figure 5.32: Schematic: Multi-layered scaffold behaviour under elongation

led to an statistically significant increase in the E for most compositions. Indeed, for the patches made solely out of PCL, E gradually increased from 572 ± 143, 1030 ± 113 to 1128 ± 42 MPa respectively for the compositions containing 0, 5 and 10 wt% of BGs. The same observation was made for the PCL-PGS compositions containing type 1 and 2 BGs. Indeed, E gradually increased with the addition of BGs (101 ± 4, 126 ± 7 and 279 ± 34 MPa respectively for the C4, C5 and C6 compositions and 241 ± 17 and 311 ± 39 MPa respectively for the C9 and C10 compositions). The addition of BGs led to a stiffer and thicker scaffold. However, this increase in stiffness was accompanied by an important decrease in the FS(120 ± 44 down to 4.0 ± 1.3 MPa respectively for C2 and C3; 23 ± 2, 9.1 ± 0.7 and 2.7 ± 0.5% respectively for C4, C5 and C6; 9.0 ± 1.0 and 4.1 ± 1.1 MPa for C9 and C10). Increasing the amount of BGs made the scaffolds less elastic as it introduced inhomogeneities within the structure. Indeed, a mixture of polymers is obtained containing highly brittle micro particles of solid inorganic material. In terms of UTS, the data presented no significant changes. In other terms, the incorporation of 5wt% of bioactive glass microspheres in the PCL–PGS matrix gave a significant reduc-

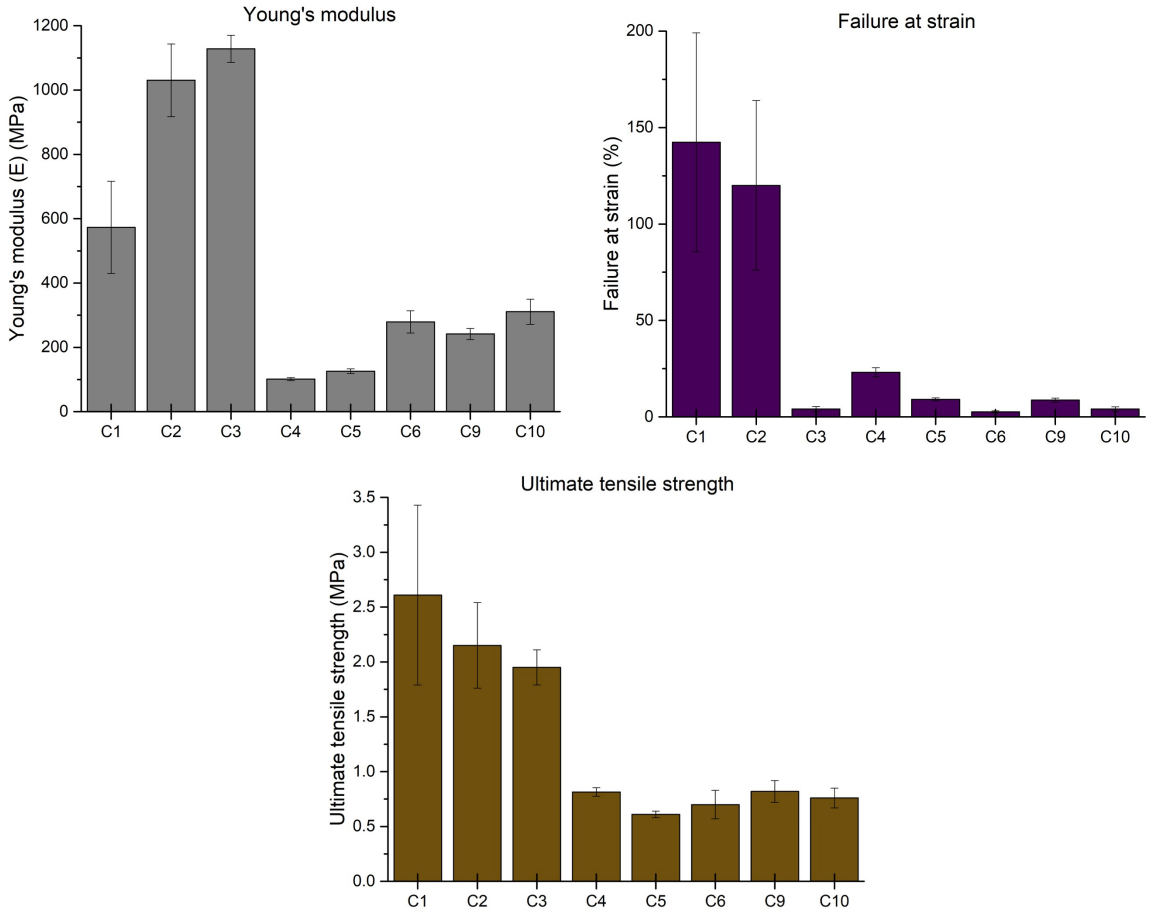

Figure 5.33: Influence of the bioactive glasses on the mechanical properties with the study of compositions **C1** (PCL), **C2** (PCL-5wt%BGs), **C3** (PCL-10wt%BGs), **C4** (PCL-PGS(1:1)), **C5** (PCL-PGS(1:1)-5wt%BGs), **C6** (PCL-PGS(1:1)-10wt%BGs), **C9** (PCL-PGS(1:1)-5wt% [45-75μm]-BGs) and **C10** (PCL-PGS(1:1)-10wt% [45-75μm]-BGs)

tion in the sample extension before failure, with no statistically significant changes in the maximum load.

The main structural differences between type 1 and type 2 BGs, as they have been shown using SEM in section 5.3.2 and section 5.3.6, were the morphology and size dispersion. Type 1 after being ball-milled presented agglomerated particle of a few micrometers shaped-like flakes; Type 2 presented sphere like particles with size varying between 45 and 75 μm.

An increase, by a factor 2, from type 1 to type 2 in E was observed for composition C5 and C9. C6 and C10 showed no statistical differences in term of E values. No significant statistical variations were observed for FS while the UTS increased by a 0.2 MPa for C5

and C9. Once again, no statistical differences were observed for C6 and C10 for the UTS values.

5.3.8.4 Conclusion on the mechanical properties

When the fibres were deposited onto the 3D printed PCL-PGS scaffolds, a significant rise in the Young's modulus of the composite scaffolds was observed: from 102 ± 5 MPa for C4 samples to 250 ± 12 MPa for C4-EM ones. The increase in stiffness can be associated with the excellent adhesion between the 3D-printed layer and the electrospun one, and makes the electrospun/3D-printed samples of potential interest as engineered scaffolds for soft tissue engineering. The effect of the electrospun fibres on the mechanical properties of the scaffolds was evident also for samples containing BG microspheres. 3D-printed scaffolds with 5 and 10 wt% of BGs had E values of 126 ± 7 MPa and 280 ± 20 MPa, respectively; the deposition of the electrospun mats determined an increase in Young's modulus up to 241 ± 17 MPa for C9-EM and 311 ± 20 MPa for C10-EM. A comparison between composite 3D-EM samples shows that 5 wt% of BGs had no significant impact on the stiffness, differently from 10 wt% BGs that induced a 30% increase in the Young's modulus. Similar values of elastic modulus in tension have been reported for polymer-BGs scaffolds for bone tissue engineering, including: 60 μm-thick PCL films containing 50 wt% of 45S5 bio-glasses (approx.200 MPa)[483], electrospun mats (80 μm thick) of polyvinyl alcohol and 45S5 BGs (approx. 250 MPa)[484], and polydimethylsiloxane-BGs-PCL monoliths (230–330 MPa)[485].

5.3.8.5 Comparison with the mechanical properties of the heart: Pre-selection of the compositions

Engineered heart patches should sustain systolic (contractive) forces and also withstand diastolic (expansive) loads. The stress-strain profile obtained are reflecting elastomeric materials as they exhibit no discontinuity in the curve. In overall, the scaffolds made of both PCL and PGS were found to be less stiff and tough that the PCL based scaffolds and the addition of BGs was found to increase this stiffness.

The following compositions were selected following the mechanical tests:

- Composition 4 (C4-EM): Poly(caprolactone) : Poly(glycerol sebacate) (1:1)
- Composition 5 (C5-EM): Poly(caprolactone) : Poly(glycerol sebacate) (1:1), Bioglass (5 wt%)
- Composition 9 (C9-EM): Poly(caprolactone) : Poly(glycerol sebacate) (1:1), 45-75 μm-Bioglass (5 wt%)
- Composition 10 (C10-EM): Poly(caprolactone) : Poly(glycerol sebacate) (1:1), 45-75 μm-Bioglass (10 wt%)

Composition 4 was used as reference. All of the other compositions exhibited E ranging from 126 to 310 MPa and tensile strength ranging from 610 to 820 kPa. Those values were relatively high for the purpose of cardiac patches. However, understanding how the mechanical properties could change once implanted in the body is crucial data. As those samples were composed of 5 to 10 wt% of BGs which exhibit rapid dissolution once exposed to an aqueous environment and therefore their dissolution could drastically influence the mechanical properties. The latter should also decrease along with the recovery of the heart. Additionally, it should be noted that those mechanical tests were performed at room temperature and not at 37°C as the tensile test equipment used could not ensure a controlled temperature on the samples. Mechanical strength and E have been shown to decrease with the increase of temperature for polymers.[486] Indeed, it has been reported that, an increase in temperature of an amorphous polymer leads to a decrease in elastic moduli.[459,460]

5.3.9 *In vitro* degradation tests: hybrid patches with and without BGs

5.3.9.1 pH, weight loss and water absorption

Measurements of pH, weight, loss and water absorption are shown in Figure 5.34. During degradation, several physical and chemical interactions such as swelling of the polymers and decrease in cross-linking density occured.

In terms of pH measurement, the highest pH drop was observed for the composition C4 which did not contain any BGs as it decreased down to 5.9 after 6 hours. PGS undergoes degradation through the hydrolysis of the ester bonds which produces an carboxylic group.[343,487] This in addition with the presence of unreacted carboxylic acid group on the backbone of PGS contributes to the pH drop observed for all samples. The conjuncture was thereafter that the presence of BGs helped regulating the acidity and pH of the media. It appeared that the type 1 BGs helped damping the pH drop in a better way. This observation can be attributed to their size as they were only a few micrometers and agglomerated, they therefore exhibited a higher surface exposition and were dissolved more rapidly. Releasing the alkaline entities which are, according to the model developed by Hench, $Si(OH)_4$[24] and forming an alkaline hydroxyapatite layer. This is an important results as BGs will therefore help counteract the acidic degraded by products and be doing so increase the beneficial effect of the patches for the purpose of cardiac tissue engineering.

The patches containing 5 wt% of type 2 BGs showed a largest drop in pH amongst the BGs-containing scaffolds with a pH of 6.06 after 6 hours. The values of the pH of C9 were inferior to that of C10 suggesting that increasing the amount of BGs helped counteract the acidity of the degradation by product of PGS. For composition C10, latency period was observed where the pH drops down to 6.24 after 1 hour before gradually going back to 7.0 after 1 day suggesting that the gradual dissolution of the BGs, started after 1 hour of immersion of PBS was enough to counteract the acidity.

Over 60 days, the pH of composition C4 was observed to exhibit an non-linear profile

constituted of sudden increase and drops in values. This was attributed to the types BGs used which were formed of micro-particles that tended to agglomerate forming a large diversity in size measurements. This contributed to an uneven 3D printed scaffolds and dissolution of the glass. This other composition shows a more linear decrease of pH over time reflecting a better controlled dissolution over the engineering scaffolds. This was due to the use of spherical BGs leading to a better distribution with the scaffolds.

Weight Loss exhibited higher values for the compositions containing BGs at 60 days. This results were explained by the dissolution of the BGs leaving a suspected porosity (confirmed by following SEM analysis in section 5.3.9.2, page 153) within the scaffold that provided a greater surface of contact between the polymers and aqueous solution. However, the weight loss for the composition C5 was smaller than C4 for the first 6 hours; the peak in weight loss (8.53 ± 0.02 %) simultaneously corresponds to a sudden increase in pH (7.06 ± 0.08) and water absorption(43.5 ± 0.03 %). This underlines the following mechanism: the particle dissolution was followed by an increase of pH leading to more weight loss and water absorption.

The weight loss and water absorption profile of composition C9 and 10 followed a same pattern with a highest peak at 6 hours with a subsequent linear decrease over 60 days.

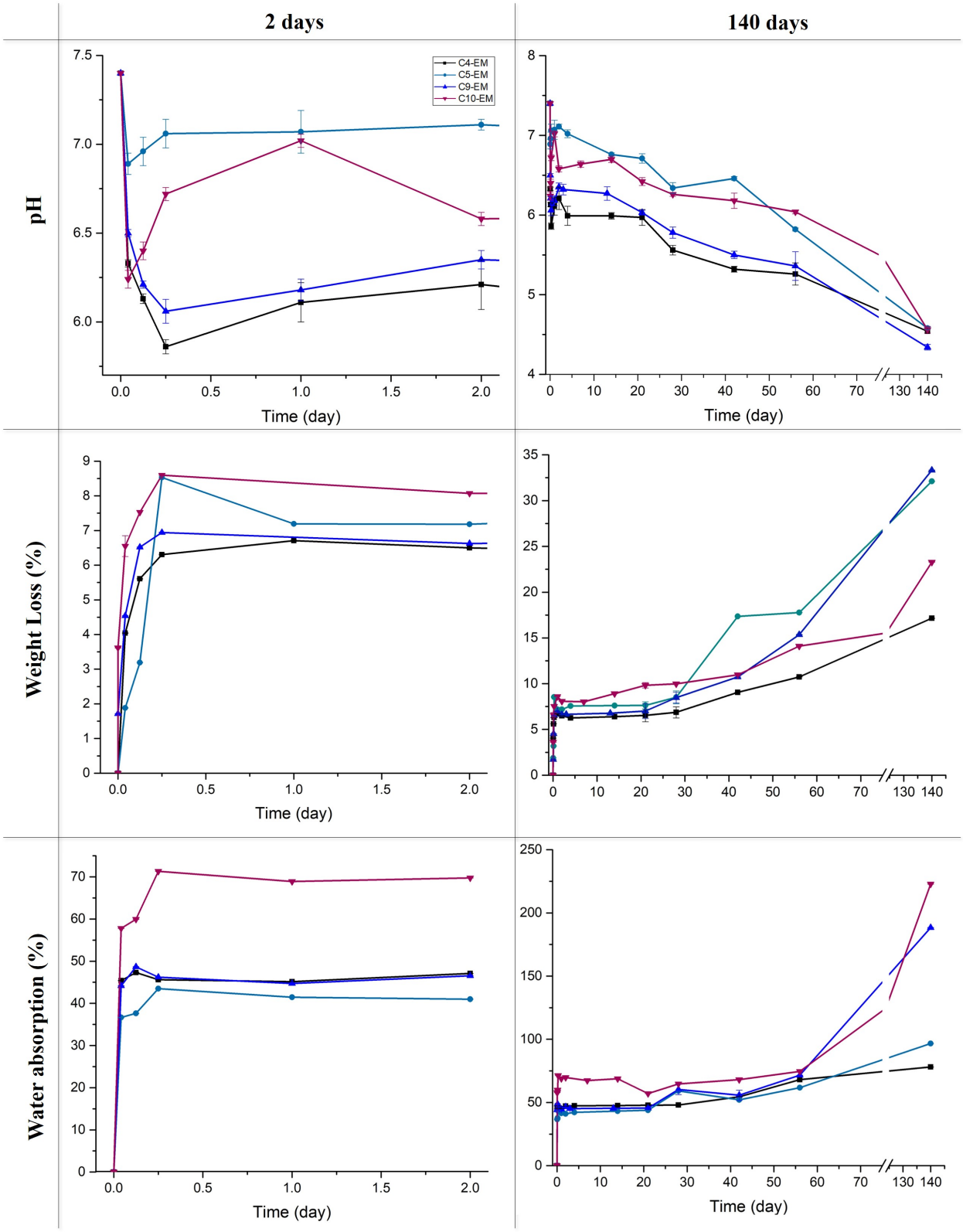

Figure 5.34: pH, weight loss and water absorption measurements on the multi-layered scaffolds of composition **C4** (PCL-PGS(1:1), **C5** (PCL-PGS(1:1)-5wt%BGs), **C9** (PCL-PGS(1:1)-5wt% [45-75μm]-BGs) and **C10** (PCL-PGS(1:1)-10wt% [45-75μm]-BGs) in PBS

Influence of the electrospun scaffold Similar tests were conducted on the 3D scaffold on a shorter period of time (13 days). Those tests were performed in collaboration with a research student: Bridie Catchpole, and helped us understand the influence of the EM on the degradation properties. Results of the research are detailed in Appendix A.
Results, on the 3D printed scaffold showed, that the PCL scaffolds absorbed the least water (16 ± 4.1 %) and did not lose a significant amount of weight over 13 days. This values were explained by the high hydrophobicity of PCL. The pH of the PBS solution varied between 6.85 and 7.2. Concerning the polymer blends, results on the water absorption measurements in the C4 composition scaffolds plateaued after only 3 hours at 29.5 ± 5.1 %. C4-EM also plateaued after 3 hours at 47.33 ± 0.05 %. Despite the use of a PCL of higher molecular weight (Mw=90000), and therefore more hydrophobic, the multi-layered scaffold did not seem to exhibit a higher hydrophobicity. Weight loss was 7.7 ± 1.6 % at 13 days while the C4-EM showed a weight loss of 6.4 ± 0.01 % after 14 days.
Concerning the composition containing BGs, percentage water absorption for the C5 composition was highest at 24 hours (79.5 ± 4.1 %) against 41.45 ± 0.05 %. These results contradicted previous observations on the hydrophobicity of the multi-layered patches and suggested that this difference in water absorption is due to the hydrophobicity brought by the EM. For C5, weight loss after 13 days was significantly greater than the PGS and PCL based scaffold at 12.7 ± 1.6 %. At 13 days, pH had gradually decreased to 6.5 with the C4 composition while the C4-EM exhibited similar values with a pH at 6.76 ± 0.02.

5.3.9.2 SEM

To better understand how the degradation in PBS affects the morphology of the fiber, FEG-SEM were performed on the degraded scaffolds. Those scaffolds were degraded in water for 2 and 4 weeks. They were immersed in water and not PBS so that the 3D architectural structure would not be altered by the ions present in the PBS solution as those samples would not require to be rinsed in water to remove potential crystals formed by the phosphate buffer solution. FEG-SEM images (Figure 5.35 and 5.36) showed how the porosity of the samples increased as the immersion time increased. Indeed,

porosity increased on the outside and inner structure of the 3D printed scaffold, while outer porosity appeared on the 3D printed fibres after only 2 weeks in water. Porosity is beneficial for cell growth, flow transport of nutrients, and metabolic waste which will ultimately help cells regenerate. However, the appearance of porosity will lower the mechanical strength. Finally, FEG-SEM allowed to show that the samples retained their 3D architectural structure despite undergoing various degradation processes

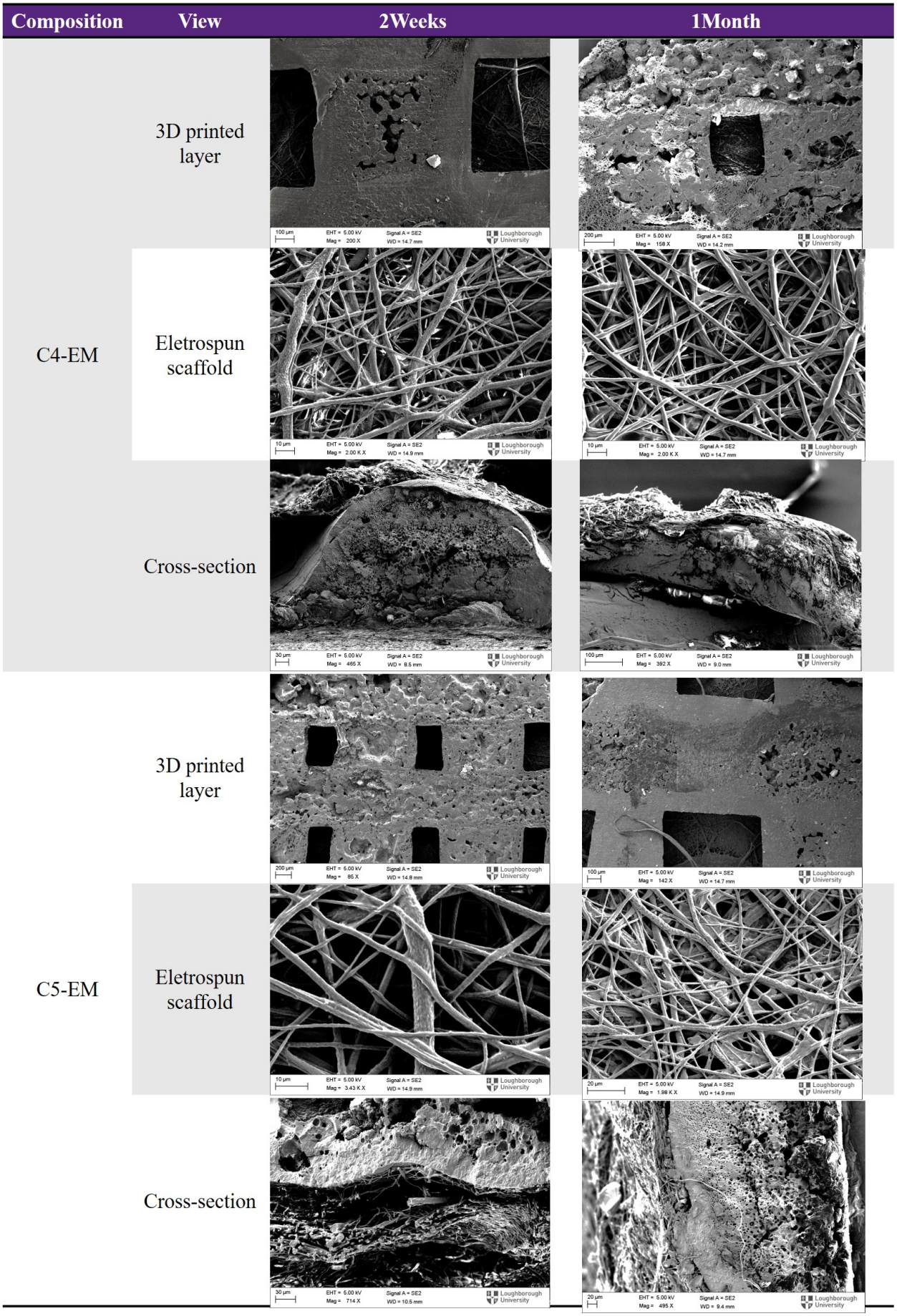

Figure 5.35: FEG-SEM on the degraded scaffolds in deionised water and of composition **C4-EM** and **C5-EM**

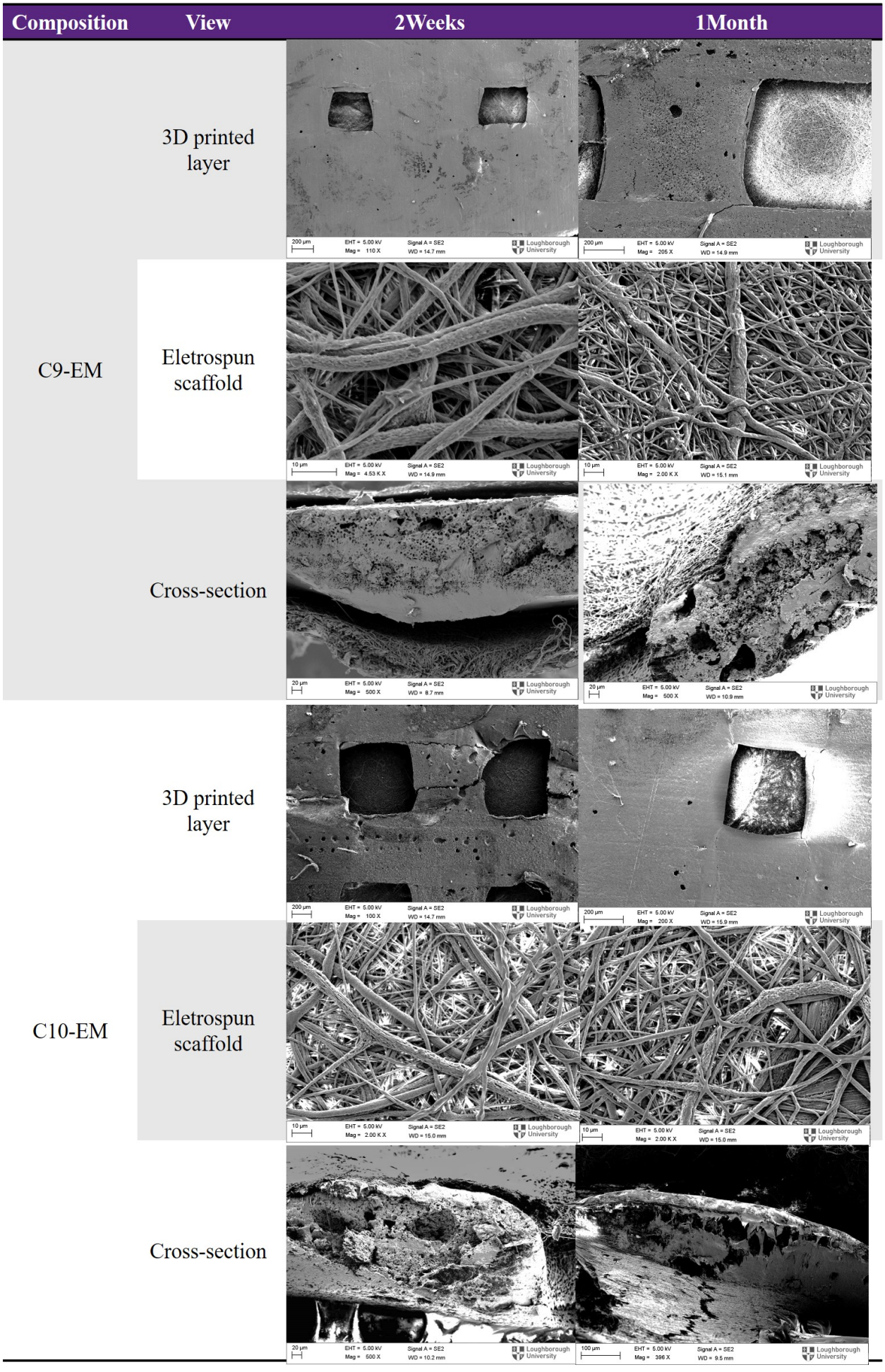

Figure 5.36: FEG-SEM on the degraded scaffolds in deionised water and of composition **C9-EM** and **C10-EM**

5.3.9.3 Mechanical tests

Mechanical tests on the degraded scaffolds were performed after one and two months immersed in PBS and using the compositions C4, C9 and C10. The Young's modulus

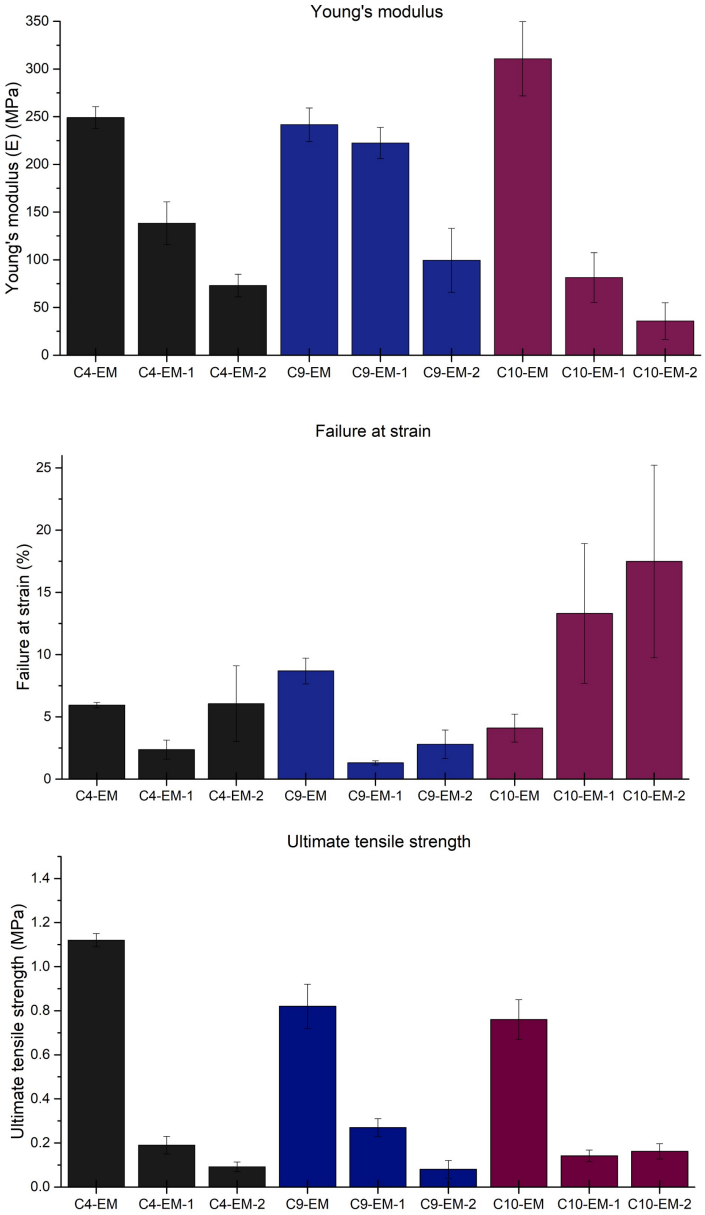

Figure 5.37: Mechanical tests on the compositions **C4-EM** (PCL-PGS(1:1)), **C9-EM** (PCL-PGS(1:1)-5wt% [45-75μm]-BGs) and **C10-EM** (PCL-PGS(1:1)-10wt% [45-75μm]-BGs) before degradation (CX-EM), after 1 (CX-EM-1) and 2 months (CX-EM-2) in PBS

of all composition decreased quite drastically after one and two months with a highest drop of 67% in values (81 $\pm$ 26 MPa for C10-EM-1) for composition C10-EM after 1 month against 45 % (138 $\pm$ 22 MPa) for C4-EM-1. The observed decreased recorded for

C9-EM-1 was not statistically representative. After two months the highest drop in E was also witnessed for C10-EM with a decrease of 86 % (36 ± 19 MPa for C10-EM-2) in value while the values for C4-EM-2 (73 ± 12 MPa) and C9-EM-2 (99 ± 33 MPa) decreased of 71 % and 59 % respectively. The use of a higher amount of larger BGs led to a more rapid decrease of the scaffold stiffness. During the whole degradation process, E values for C9-EM were higher than C4-EM while the C10-EM values showed smaller E after 1 month. Therefore the addition of 10 wt% of BGs led to a faster degradation process. After the dissolution of the BGs the scaffold exhibited a higher porosity that provided an easier access of the aqueous solution of further degraded the scaffold and accelerating the degradation process of PGS through the faster breakdown of ester bonds ultimately leading to the hydrolytic weakening of the material. Another study[400] measured the evolution of PGS-PCL-EM mechanical properties for cardiac patch applications. They have observed a drop in E values after 28 days (from 13.8 ± 6.1 MPa down to 1.4 ± 2.2 MPa). This observation is supported by the UTS measurements while a linear decrease of UTS are observed for all compositions. The highest drop in UTS was observed for the C4-EM composition with a calculated 83 % drop (0.19 ± 0.04 MPa for C4-EM-1) after 1 month while C10-EM-1 and C9-EM-1 observed a drop of respectively 81 % (0.16 ± 0.04 MPa for C10-EM-1) and 67 % (0.27 ± 0.04 MPa for C9-EM-1).

The failure at strain showed interesting results where for C4-EM and C9-EM, a decrease of 60 and 85 % respectively for C4-EM-1 (2.37 ± 0.76 %) and C9-EM-1 (1.31 ± 0.17 %) was observed. This decrease was then followed by a significant increase in the FS values where for C4-EM-1 , FS values went from 2.37 ± 0.76 % to 6.06 ± 3.04 % and for C9-EM-1 , FS values went from 1.31 ± 0.17 % to 2.80 ± 1.15 %. The firstly observed decrease can be attributed to the BGs which might not have been fully dissolved after 2 weeks and therefore led to the formation of alkaline zones with the scaffold weakening the later. Once fully dissolved the scaffold present a better heterogeneity increase the percentage of elongation of the samples. Additionally, PGS undergoes faster degradation than PCL, the ratio of polymer within the blend therefore varies and the scaffold contained an increasing majority of PCL. In this case, the higher porosity of the scaffold resulting from a higher

amount of BGs dissolved led to a faster dissolution of PGS and therefore a higher ratio of PCL with the structure. Finally the high percentage of error witnessed for C10-EM at one and tow month were due to the high brittleness of the samples once degraded were even a delicate manipulation of the sample led to the insertion of heterogeneity with the different patches.

5.3.9.4 Thermal Testing: DSC

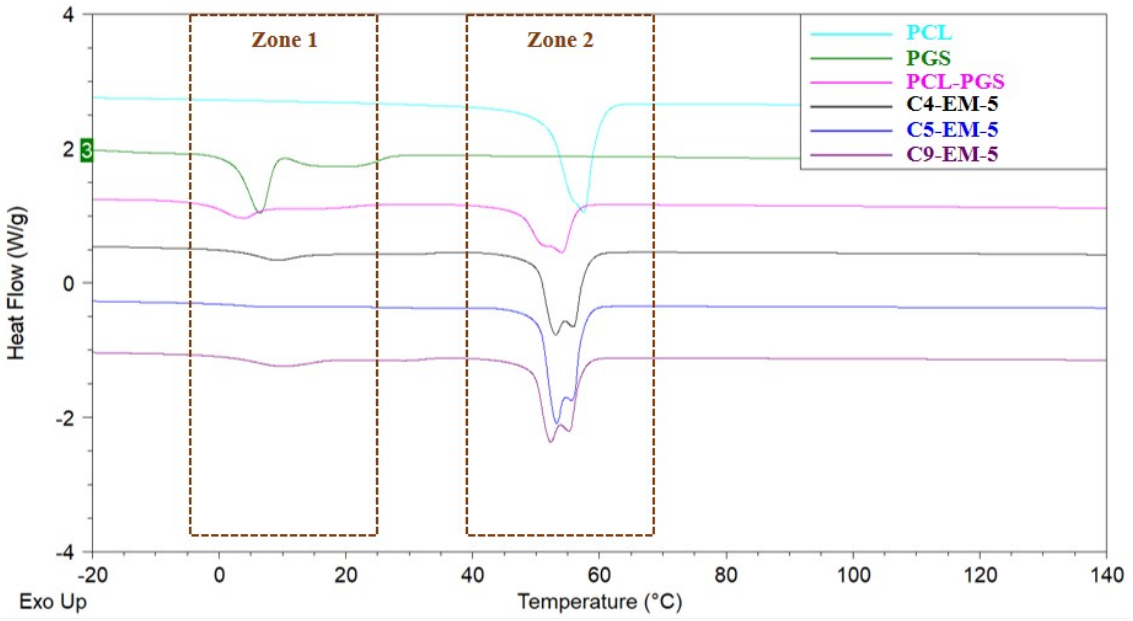

Figure 5.38: DSC measurements on degraded scaffolds after 5 months in PBS with compositions C4-EM, C5-EM and C9-EM compositions

Figure 5.38 can be separated into two zones:

- Zone 1 which is situated around 10°C and gave valuable insight as to whether the tested sample contains PGS
- Zone 2, situated in the vicinity of 50°C corresponded to the Tg of PCL and therefore helped determine if the samples contains any PCL after degradation.

Table 5.5: DSC values for Tg and enthalpy for PCL, PGS, PCL-PGS (1:1) and compositions C4-EM-5, C5-EM-5 and C9-EM-5

Composition	Zone 1			Zone 2		
	Beginning of Tg °C	TgC °C	Enthalpy (J/g)	Beginning of Tg °C	Tg °C	Enthalpy (J/g)
PGS	2.31	6.37	22.25	-	-	-
PCL	-	-	-	51.63	57.43	68.89
PCL-PGS (1:1)	-2.44	3.06	7.29	47.24	53.98	29.79
C4-EM-5	2.47	8.60	5.04	50.09	53.12	45.36
C5-EM-5	0.55	5.91	1.17	50.53	53.23	54.25
C9-EM-5	0.39	9.10	7.98	49.64	52.31	44.48

For each composition and each zone, the values for the temperature and measure enthalpy are listed in Table 5.5. For the thermal tests conducted on the degraded scaffolds after 5 months, PGS has been degrading to various extents in all samples. Compositions C5-EM-5 seemed to be PGS free after 5 months while compositions C4-EM and C9-EM contained a certain remaining amount of PGS. PGS therefore dissolved faster in the composition containing type 1 BGs which are smaller particles. Once those particle were dissolved they left an open porous network for the PBS to infiltrate the scaffolds and to degrade polymers. Smaller size particles would most certainly led to the presence of smaller but more numerous pores which could explain the results on the thermal testing.

Concerning PCL, thermal testing showed us that the polymer was still present in high quantity within the scaffold. Indeed, PCL degradation rate is much slower (from 2 to 4 years).[364] Nonetheless, no significant shifts in the Tg were observed. This can be explained by the degradation process of PCL undergoing a reduction of the average molecular weight due to the scission of hydrolytic chain. This would suggests that PCL is undergoing bulk degradation processes.[365]

5.3.10 *In vitro* viability and toxicity cell studies

The normalised results obtained for day 1, 3 and 7 are presented in Figure 5.39. Details of the values obtained are presented in Appendix B.

All of the three compositions presented viability results above 70% demonstrating satisfactory biocompatibility with the fibroblast cells. Percentages of viability were above that

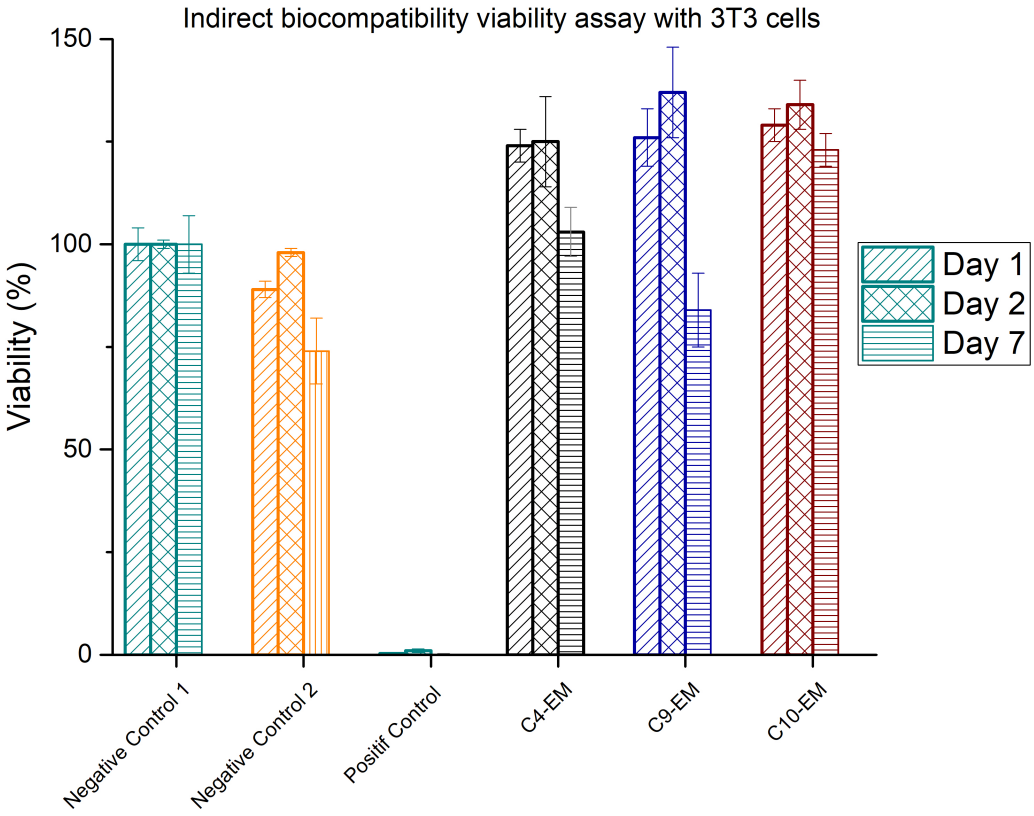

Figure 5.39: Biocompatibility viability assay via indirect contact with 3T3 cells using ethanol sterilisation

of the control for day one and two.

For day 1, results showed a high survival rate of 124 % ± 4, 126% ± 7 and 129% ± 4 respectively for compositions C4-EM, C9-EM and C10-EM. The highest value of viability was observed for all compositions at day 2 with a survival rate of 125% ± 11, 137% ± 11, 134% ± 6 respectively for compositions C4-EM, C9-EM and C10-EM.

All three scaffolds present a drop at day 7. Composition C9-EM presented the highest decrease in viability with 84% ± 9 at day 7. Whilst compositions C4-EM and C10-EM presented percentage of viability of 103% ± 6 and 123% ± 4 respectively. C10-EM demonstrated the smallest drop in cell viability at day 7 and, on overall, sustained high cell viability of a longer period.

These observations can be explained when considering the pH profile (Figure 5.34) matching the release profile of the BGs and degradation of PGS. PGS degradation lead to an acidic environment which is deleterious for the cells. The addition of alkaline BGs helped

counteract this acidity and ensuring a suitable environment for cell proliferations.

Viability results demonstrated the positive effect of the addition of BGs in the 3D constructs since most cell survival rate were above that of the reference (C4-EM) which did not contain any BGs. Cell survival dropped under that of reference at day 7 for C9-EM. This can be explained by the open porous network left after the BGs dissolution which increase the PGS degradation rate as supported by pH measurements and thermal data. The addition of 10 wt% of BGs in C10-EM helped sustaining a suitable environment for cell proliferation for longer as shown by the cell viability percentage over 7 day.

5.3.10.1 Effect of the sterilisation method

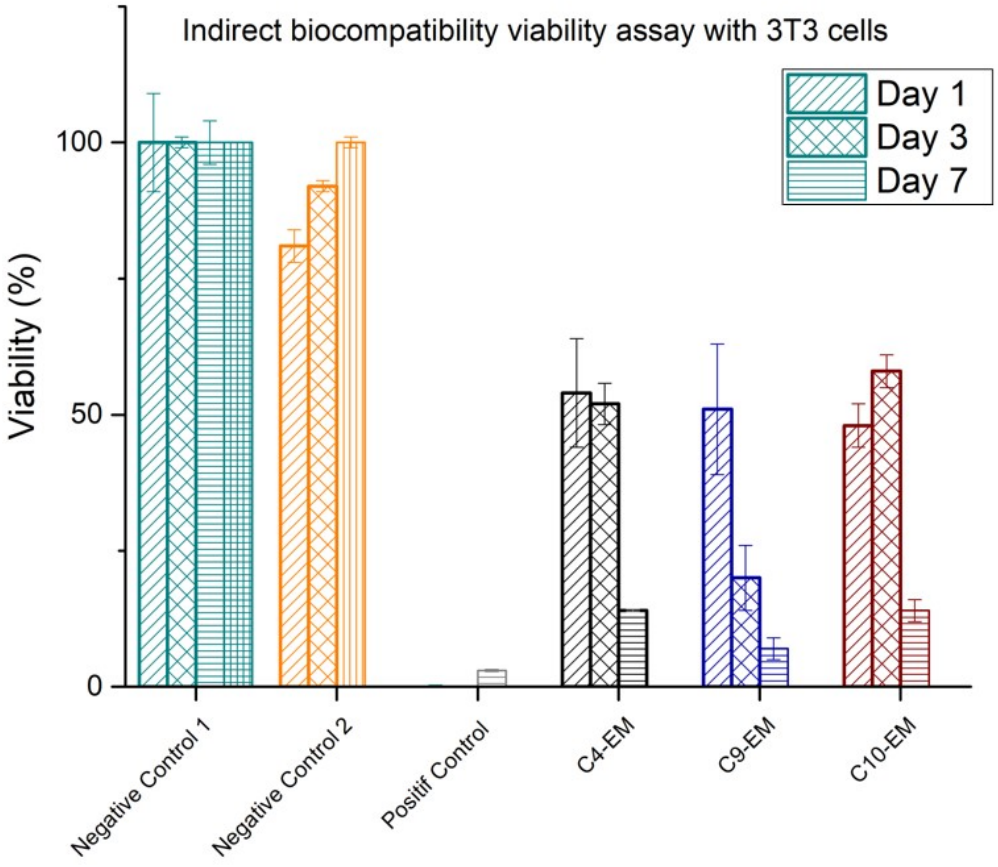

Figure 5.40: Results: Biocompatibility viability assay via indirect contact with 3T3 cells

Figure 5.40 presents the normalised results obtained for day 1, 3 and 7 with scaffolds sterilised using UV. Results showed that cell viability never exceed 50% therefore rendering the scaffolds not biocompatible. These results are in disagreement with what has

previously been observed using ethanol sterilisations. Figure 5.41 shows a comparison for both sterilisation techniques and points out the substantial difference induced by the sterilisation method.

Similar results have been observed in other studies.[461–463] However, explanations for such

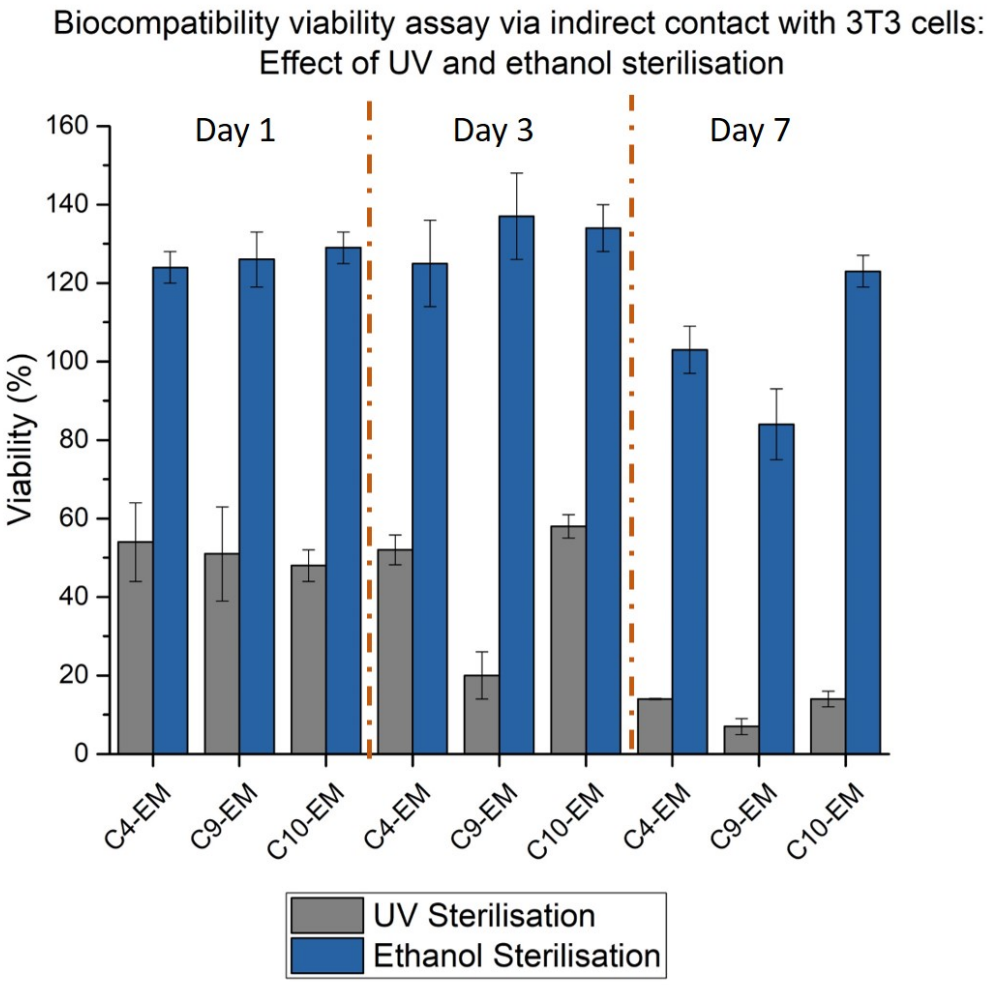

Figure 5.41: Biocompatibility viability assay via indirect contact with 3T3 cells: Comparison between UV and Ethanol Sterilisation

differences in biocompatibility differ. Tallawi *et al.*[462] argues that the increase of biocompatibility when using ethanol sterilisation is due to the apparition of pores following the leaching of unreacted toxic monomers, whereas Liverani *et al.*[463] and Vogt *et al.*[461] debate that this difference is due to pore formation following the complete dissolution of PGS from the blend supported by FTIR measurements.

Studies state that immersion in 70% ethanol does not affect the physical properties of the

PGS film or PGS/polymer blend.[461–463] Nevertheless, further tests should be considered to study the effect of ethanol sterilisation on the scaffolds. Indeed, mechanical properties and degradation properties are crucial for cardiac tissue regeneration applications. Therefore, additional mechanical and degradations tests should be performed. FTIR and DSC data measurements should also be performed on the ethanol sterilised scaffolds to determine whether, in this study, ethanol dissolves the polymer or the monomer. Finally, FEG-SEM could be used to observe the pore formation mentioned in different studies.[461–463]

Cell viability using ethanol sterilisation showed highly satisfactory results demonstrating the beneficial use of BGs in the various 3D constructs. The use of 10 wt% of BGs present the longest sustained viability ensuring cell survival rate above 120% over 7 days. This is due to the BGs counteracting the acidic degradation of PGS ensuring a suited environment for cell proliferation. These viability study present satisfactory first results. Indeed, 3T3 fibroblast cells have been used for this study and are commonly used to obtain preliminary viability data on biomaterials. However, for the purpose of cardiac tissue regeneration, further studies should be performed using cells belonging to myoblast cell line (cell found in muscle tissue such as cardiac tissue eg. C2C12).[462]

Further optimisations could then be undertaken in order to manufacture an electrospun mat mimicking environmental conditions able to differentiate stem cells into cardiomyocytes into the cardiac lineage cells. Stem cell-derived cardiomyocytes requires complex signalling pathway and growth factor in additions with environmental conditions to derive into cardiac lineage cells.[488–491] Finally, effect of sterilisation techniques on the scaffolds chemical and physical properties should be studied furthermore.

5.4 Conclusion

Through this work, the design, fabrication and characterisation of scaffolds meeting various requirements for tissue engineering have been demonstrated.[455] Electrospinning and 3D printing have been combined to manufacture biocompatible patches of PCL-PGS blends containing bioactive glasses. To achieve mechanical properties suitable for the myocardium, 3D printing, more precisely fused method deposition, was used to enable the

manufacture of 3D scaffolds exhibiting tunable mechanical properties dependent on the polymer blend ratio and amounts of 45-S5 bioglasses.

The scaffolds exhibited multiscale three-dimensional porosity that is known to be beneficial for cell growth and infiltration, the transport of nutrients and metabolic waste (not demonstrated in this work). In addition, the use of PGS and bioactive glasses allowed control over degradation and mechanical properties. The strategy used for the fabrication of the hybrid scaffolds has proved repeatable and effective in achieving excellent adhesion between the 3D-printed layer, which provided mechanical support to the whole structure. In addition, the electrospun mat acted as a biomimetic layer. The presence of the PCL-PGS electrospun network enhanced the stiffness of the scaffolds and gave a 2.5-fold increase of the Young's modulus. The addition of the bioactive glasses, although it affected the mechanical response of the scaffolds only slightly (a 30% increase in elastic modulus for samples with 10 wt% BGs), impacted the material degradation in vitro and balanced the acidic character of PGS. The addition of BGs had beneficial effects and helped regulate the pH therefore helping provide a suitable environment for cell growth and proliferation. After 3 months of in vitro degradation tests, the pH of the PBS medium, where the scaffolds were incubated, dropped to 5.3 (from 7.4) when no BGs were used; while it only reached values of 6.0 for scaffolds containing 10 wt% BGs. This had a positive effect on the growth of fibroblasts, whose viability was sustained longer in vitro for scaffolds with 10 wt% BGs. Cell viability showed that the addition of BGs was beneficial in order to provide a suitable environment for cells. All compositions have been shown to favour cell proliferations. It was, also, shown that BGs increased the degradation rate of PCL-PGS scaffolds. This is explained by the open porosity of the scaffold, which is greater once the BGs are dissolved.

The manufactured scaffold are promising devices for cardiac tissue engineering which could be further optimised in the future. Through this work, the design of a scaffold meeting numerous requirements for cardiac tissue regeneration has been achieved.[455] The manufactured cardiac patches are biocompatible with a controllable degradation depending on the composition. They also provide a suitable chemistry for cell proliferation (adhesion

and differentiation to be tested in a further steps) and exhibit three-dimensional porosity (intra and surface) that increases with the immersion time which is beneficial for cell growth, flow transport of nutrients and metabolic waste. Finally, mechanical properties showed high values of more than 200% of the myocardium which will be beneficial for a healthy recovery of the heart scarred tissue.

Chapter 6

Conclusion

Bioactive glasses (BGs) are biologically active materials, inducing a beneficial response from the host body once implanted.[18,94] They are ideal candidates for various applications[27] such as dentistry[19], bone[12,13] or cardiac tissue regeneration[17]. The versatility and biological properties of such materials have been demonstrated in a plethora of research papers.[9,15,16,18,94] The objective of this work was to use modelling and experimental methods to better understand the behaviour of BGs for tissue engineering applications. The work comprised the study of the atomistic structure of fluoridated phosphate-based glasses (F-PBGs) for dentistry applications[401], and the development of 45S5 silicates-based glasses(Si-BGs)-polymer composite scaffolds for cardiac tissue engineering.

Recently, the role played by fluoride ions on the bioactivity of F-PBGs has been debated in the literature and previous studies have concluded opposite results.[210,225] The objective of this work was to provide a new insight into the physical chemistry of F-PBGs, driving forward research. In order to provide a clear answer, classical molecular dynamics (MD) simulations were used to accurately describe the atomistic structure of F-PBGs. To improve the modelling of FPBGs, the following objectives were achieved:

- development of an accurate force field to describe the atomistic structure of F-PBGs by integrating, for the first time, the polarisability of both the oxygen and fluoride atoms;

- providing novel and interesting insights into the influence of fluorine on phosphate-based glasses. MD simulations revealed the presence of soluble ionic-rich clusters formed of fluorine and calcium ions regions and poorly soluble network-rich regions;
- concluding that the effect of the bioactivity and presence of clusters ultimately decreased the bioactivity of the glasses. The ionic-rich regions dissolve at a higher rate than the network-rich regions, leading to an uneven fluoro-apatite layer formation.

This study did not include experimental data on the atomistic structure of F-PBGs, as their fabrication was not feasible during the project. The experimental part was therefore oriented toward commercially available silicate-based glasses for cardiac tissue engineering, using 3D printing and electrospinning.

45S5 silicate-based glasses have shown promising interactions with soft tissues such scarred cardiac myocardium.[17] The use of 45S5 glasses, within a polymeric matrix, has been reported in cardiac tissue applications but it has not been addressed extensively to date.[291,294,305,400] The experimental part of this project consisted in designing patches containing 45S5 glasses for tissue regeneration. To provide new experimental insight on the use of BGs for soft tissue engineering and engineer innovative bioresorbable and biocompatible cardiac patches, the following objectives were achieved:

- development of polymer-BGs composite formulations for 3D printing and electrospinning and engineering patches using 3D printing (solvent based-extrusion) and electrospinning techniques;
- development of mechanically suitable cardiac patches;
- manufacturing of cardiac patches presenting tunable degradation properties and demonstrating satisfactory cell growth and proliferation properties.

This work presented a new and interesting insight on the very promising use of bioactive glasses as a biomaterial for soft and hard tissue engineering. Through this project, modelling and experimental data have helped us better understand the use of bioactive glasses for biomedical applications including personalised treatments for patients.

Chapter 7

Future work

The formation of cluster has a significant role in the assessment of the bioactivity. Further modelling studies could focus on:

- the minimum energy pathway leading to the formation of clusters observed in F-PBGs. This calculation will shed light on the energetic transitions occurring within the chemical structure of the glass;
- studying other ions with therapeutic effects such as silver, copper and cobalt which have known angiogenesis and antibacterial properties.[46,60,123–125]

Future experimental work should focus on optimising mechanical properties during degradation as well as cardiac cell biocompatibility. These would represent the final steps in order to obtain an efficient and specific treatment for patient suffering from myocardial infarction. This work should include:

- testing various thicknesses of patches and PGS curing times to obtain an optimum composition;
- further *in vivo* tests with cardiomyocytes, or endogenous cardiac stem cell if the patches can induce differentiation into cardiomyocytes;
- studying the influence of the sterilisation techniques.

Bibliography

[1] G. K. McKee. Development of total prosthetic replacement of the hip. *Clinical Orthopaedics and Related Research*, 72:85–103, 1970.

[2] Joan Walker and M. Von Britzke. Physiotherapy following total hip replacement: The Mckee-Farrar prosthesis. *South African Journal of Physiotherapy*, 25(1):6–7, 1969.

[3] John Charnley. Surgery of the hip joint. Present and Future developments. *British Medical Journal*, 1(5176):821–826, 1960.

[4] Larry L. Hench and June Wilson. Introduction. In *Clinical Perfomance of Skeletal Prostheses*, volume 40, pages 1–10. Springer Netherlands, 2004.

[5] P A Ring. Total hip replacement. *Proceedings of the Royal Society of Medicine*, 60(3):281–4, 1967.

[6] L. L. Hench. Biomaterials. *Science*, 208(4446):826–831, 1980.

[7] Larry L. Hench and Ian Thompson. Twenty-first century challenges for biomaterials. *Journal of the Royal Society Interface*, 7(4):379–391, 2010.

[8] A Weinstein and Los Angeles. Orthopedic Implants-A Clinical and Metallurgic Analysis. *Journal of Biomedical Materials Research*, 325(4):297–325, 1973.

[9] Larry L. Hench. The story of Bioglass®. *Journal of Materials Science: Materials in Medicine*, 17(11):967–978, 2006.

[10] L. L. Hench, R. J. Splinter, W. C. Allen, and T. K. Greenlee. Bonding mechanisms at the interface of ceramic prosthetic materials. *Journal of Biomedical Materials Research*, 5(6):117–141, 1971.

[11] Julian R. Jones. Reprint of: Review of bioactive glass: From Hench to hybrids. *Acta Biomaterialia*, 23(S):S53–S82, 2015.

[12] Motohiro Uo, Morimichi Mizuno, Yoshinori Kuboki, Akio Makishima, and Fumio Watari. Properties and cytotoxicity of water soluble Na2O-CaO-P2O5 glasses. *Biomaterials*, 19(24):2277–2284, 1998.

[13] E. Gentleman, M. M. Stevens, R. G. Hill, and D. S. Brauer. Surface properties and ion release from fluoride-containing bioactive glasses promote osteoblast differentiation and mineralization in vitro. *Acta Biomaterialia*, 9(3):5771–5779, 2013.

[14] Valentina Miguez-pacheco and David Greenspan. Bioactive glasses in soft tissue repair. *American Ceramic Society Bulletin*, 94(6):27–31, 2015.

[15] Nilay J. Lakhkar, In Ho Lee, Hae Won Kim, Vehid Salih, Ivan B. Wall, and Jonathan C. Knowles. Bone formation controlled by biologically relevant inorganic ions: Role and controlled delivery from phosphate-based glasses. *Advanced Drug Delivery Reviews*, 65(4):405–420, 2013.

[16] I. Ahmed, M. Lewis, I. Olsen, and J. C. Knowles. Phosphate glasses for tissue engineering: Part 1. Processing and characterisation of a ternary-based P2O5-CaO-Na2O glass system. *Biomaterials*, 25(3):491–499, 2004.

[17] Aldo R. Boccaccini, Melek Erol, Wendelin J. Stark, Dirk Mohn, Zhongkui Hong, and João F. Mano. Polymer/bioactive glass nanocomposites for biomedical applications: A review. *Composites Science and Technology*, 70(13):1764–1776, 2010.

[18] Delia S. Brauer. Bioactive Glasses-Structure and Properties. *Angewandte Chemie International Edition*, 54(14):4160–4181, 2015.

[19] Larry L. Hench. Chronology of Bioactive Glass Development and Clinical Applications. *New Journal of Glass and Ceramics*, 03(02):67–73, 2013.

[20] Carlos Bergmann and Aisha Stumpf. Dental Ceramics. In *Dental Ceramics: Microstructure, Properties and Degradation*, Topics in Mining, Metallurgy and Materials Engineering, page 9. Springer Berlin Heidelberg, Berlin, Heidelberg, 2013.

[21] Klaus von der Mark and Jung Park. Engineering biocompatible implant surfaces: Part II: Cellular recognition of biomaterial surfaces: Lessons from cell–matrix interactions. *Progress in Materials Science*, 58(3):327–381, 2013.

[22] George M. Whitesides and Amy P. Wong. The Intersection of Biology and Materials Science. *MRS Bulletin*, 31(1):19–27, 2006.

[23] Erich. Wintermantel and S.W. Ha. Medizintechnik mit biokompatiblen Werkstoffen und Verfahren. pages 1–3. Springer, 2002.

[24] Larry L. Hench. Bioceramics. *Journal of the American Ceramic Society*, 81(7):1705–1728, 2005.

[25] Md Towhidul Islam, Reda M. Felfel, Ensanya A. Abou Neel, David M. Grant, Ifty Ahmed, and Kazi M.Zakir Hossain. Bioactive calcium phosphate–based glasses and ceramics and their biomedical applications: A review. *Journal of Tissue Engineering*, 8(1):1–16, 2017.

[26] V. Salih, K. Franks, M. James, G. W. Hastings, J. C. Knowles, and I. Olsen. Development of soluble glasses for biomedical use part II: The biological response of human osteoblast cell lines to phosphate-based soluble glasses. *Journal of Materials Science: Materials in Medicine*, 11(10):615–620, 2000.

[27] Ensanya A. Abou Neel, David M. Pickup, Sabeel P. Valappil, Robert J. Newport, and Jonathan C. Knowles. Bioactive functional materials: A perspective on phosphate-based glasses. *Journal of Materials Chemistry*, 19(6):690–701, 2009.

[28] Ensanya Ali Abou Neel, Toshihide Mizoguchi, Michio Ito, Malak Bitar, Vehid Salih, and Jonathan Campbell Knowles. In vitro bioactivity and gene expression by cells cultured on titanium dioxide doped phosphate-based glasses. *Biomaterials*, 28(19):2967–2977, 2007.

[29] E.A. AbouNeel, A.M. Young, S.N. Nazhat, and J.C. Knowles. A Facile Synthesis Route to Prepare Microtubes from Phosphate Glass Fibres. *Advanced Materials*, 19(19):2856–2862, 2007.

[30] Joana C. Guedes, Jeong Hui Park, Nilay J. Lakhkar, Hae Won Kim, Jonathan C. Knowles, and Ivan B. Wall. TiO2-doped phosphate glass microcarriers: A stable bioactive substrate for expansion of adherent mammalian cells. *Journal of Biomaterials Applications*, 28(1):3–11, 2013.

[31] G. Nunzi Conti, A. Chiasera, L. Ghisa, S. Berneschi, M. Brenci, Y. Dumeige, S. Pelli, S. Sebastiani, P. Feron, M. Ferrari, and G. C. Righini. Spectroscopic and lasing properties of Er3+-doped glass microspheres. *Journal of Non-Crystalline Solids*, 352(23-25):2360–2363, 2006.

[32] I. Ahmed, C. A. Collins, M. P. Lewis, I. Olsen, and J. C. Knowles. Processing, characterisation and biocompatibility of iron-phosphate glass fibres for tissue engineering. *Biomaterials*, 25(16):3223–3232, 2004.

[33] Malak Bitar, Vehid Salih, Jonathan C. Knowles, and Mark P. Lewis. Iron-phosphate glass fiber scaffolds for the hard-soft interface regeneration: The effect of fiber diameter and flow culture condition on cell survival and differentiation. *Journal of Biomedical Materials Research - Part A*, 87(4):1017–1026, 2008.

[34] R. Shah, A. C.M. Sinanan, J. C. Knowles, N. P. Hunt, and M. P. Lewis. Craniofacial muscle engineering using a 3-dimensional phosphate glass fibre construct. *Biomaterials*, 26(13):1497–1505, 2005.

[35] E. A. Abou Neel, I. Ahmed, J. Pratten, S. N. Nazhat, and J. C. Knowles. Charac-

terisation of antibacterial copper releasing degradable phosphate glass fibres. *Biomaterials*, 26(15):2247–2254, 2005.

[36] A. Kiani, N. J. Lakhkar, V. Salih, M. E. Smith, J. V. Hanna, R. J. Newport, D. M. Pickup, and J. C. Knowles. Titanium-containing bioactive phosphate glasses. *Philosophical Transactions of the Royal Society A: Mathematical, Physical and Engineering Sciences*, 370(1963):1352–1375, 2012.

[37] N. J. Lakhkar, E. A. Abou Neel, V. Salih, and J. C. Knowles. Strontium oxide doped quaternary glasses: Effect on structure, degradation and cytocompatibility. *Journal of Materials Science: Materials in Medicine*, 20(6):1339–1346, 2009.

[38] Sabeel P. Valappil, Jonathan C. Knowles, and Michael Wilson. Effect of silver-doped phosphate-based glasses on bacterial biofilm growth. *Applied and Environmental Microbiology*, 74(16):5228–5230, 2008.

[39] Siddhartha Shrivastava, Tanmay Bera, Arnab Roy, Gajendra Singh, P. Ramachandrarao, and Debabrata Dash. Characterization of enhanced antibacterial effects of novel silver nanoparticles. *Nanotechnology*, 18(22):225103–225112, 2007.

[40] Xiaohai Yang, Wenjuan Yang, Qing Wang, Huimin Li, Kemin Wang, Liu Yang, and Wei Liu. Atomic force microscopy investigation of the characteristic effects of silver ions on Escherichia coli and Staphylococcus epidermidis. *Talanta*, 81(4-5):1508–1512, 2010.

[41] Ensanya Ali Abou Neel, Wojciech Chrzanowski, and Jonathan Campbell Knowles. Effect of increasing titanium dioxide content on bulk and surface properties of phosphate-based glasses. *Acta Biomaterialia*, 4(3):523–534, 2008.

[42] Shinichi Maeno, Yasuo Niki, Hideo Matsumoto, Hideo Morioka, Taku Yatabe, Atsushi Funayama, Yoshiaki Toyama, Tetsushi Taguchi, and Junzo Tanaka. The effect of calcium ion concentration on osteoblast viability, proliferation and differentiation in monolayer and 3D culture. *Biomaterials*, 26(23):4847–4855, 2005.

[43] Eileen Gentleman, Yann C. Fredholm, Gavin Jell, Nasrin Lotfibakhshaiesh, Matthew D. O'Donnell, Robert G. Hill, and Molly M. Stevens. The effects of strontium-substituted bioactive glasses on osteoblasts and osteoclasts in vitro. *Biomaterials*, 31(14):3949–3956, 2010.

[44] Masayoshi Yamaguchi. Role of zinc in bone formation and bone resorption. *The Journal of Trace Elements in Experimental Medicine*, 11(2-3):119–135, 1998.

[45] John D.B. Featherstone. the Science and Practice of Caries Prevention. *The Journal of the American Dental Association*, 131(7):887–899, 2000.

[46] Alexander Hoppe, Nusret S. Güldal, and Aldo R. Boccaccini. A review of the biological response to ionic dissolution products from bioactive glasses and glass-ceramics. *Biomaterials*, 32(11):2757–2774, 2011.

[47] Mudera V. Abou Neel E, Aljabo A, Strange A, Ibrahim S, Coathup M, Young A, Bozec L. Demineralization-remineralization dynamics in teeth and bone. *International Journal of Nanomedicine*, 11(1):4743–4763, 2016.

[48] C. Van Loveren. The Antimicrobial Action of Fluoride and its Role in Caries Inhibition. *Journal of Dental Research*, 69(S2):676–681, 1990.

[49] Robert E Marquis. Antimicrobial actions of fluoride for oral bacteria. *Canadian journal of microbiology*, 41(41):955–964, 1995.

[50] Elisa Fiume, Jacopo Barberi, Enrica Verné, and Francesco Baino. Bioactive glasses: From parent 45S5 Composition to Scaffold-Assisted Tissue-Healing Therapies. *Journal of Functional Biomaterials*, 9(1):24–57, 2018.

[51] Francesco Baino and Chiara Vitale-Brovarone. Three-dimensional glass-derived scaffolds for bone tissue engineering: Current trends and forecasts for the future. *Journal of Biomedical Materials Research - Part A*, 97(4):514–535, 2011.

[52] Lutz-Christian Gerhardt and Aldo R. Boccaccini. Bioactive Glass and Glass-Ceramic Scaffolds for Bone Tissue Engineering. *Materials*, 3(7):3867–3910, 2010.

[53] Qiang Fu, Eduardo Saiz, Mohamed N. Rahaman, and Antoni P. Tomsia. Bioactive glass scaffolds for bone tissue engineering: State of the art and future perspectives. *Materials Science and Engineering C*, 31(7):1245–1256, 2011.

[54] Gurbinder Kaur, Om P. Pandey, Kulvir Singh, Dan Homa, Brian Scott, and Gary Pickrell. A review of bioactive glasses: Their structure, properties, fabrication and apatite formation. *Journal of Biomedical Materials Research - Part A*, 102(1):254–274, 2014.

[55] Francesco Baino, Giorgia Novajra, Valentina Miguez-Pacheco, Aldo R. Boccaccini, and Chiara Vitale-Brovarone. Bioactive glasses: Special applications outside the skeletal system. *Journal of Non-Crystalline Solids*, 432(Part A):15–30, 2016.

[56] Alejandro A. Gorustovich, Judith A. Roether, and Aldo R. Boccaccini. Effect of Bioactive Glasses on Angiogenesis: A Review of In vitro and In vivo Evidences. *Tissue Engineering Part B: Reviews*, 16(2):199–207, 2010.

[57] Aitor Aguirre, Arlyng González, Melba Navarro, Óscar Castaño, Josep A. Planell, and Elisabeth Engel. Control of microenvironmental cues with a smart biomaterial composite promotes endothelial progenitor cell angiogenesis. *European Cells and Materials*, 24:90–106, 2012.

[58] Alexander Hoppe, Viviana Mouriño, and Aldo R. Boccaccini. Therapeutic inorganic ions in bioactive glasses to enhance bone formation and beyond. *Biomaterials Science*, 1(3):254–256, 2013.

[59] Michael J. Cross and Lena Claesson-Welsh. FGF and VEGF function in angiogenesis: Signalling pathways, biological responses and therapeutic inhibition. *Trends in Pharmacological Sciences*, 22(4):201–207, 2001.

[60] Richard M. Day. Bioactive Glass Stimulates the Secretion of Angiogenic Growth Factors and Angiogenesis In Vitro. *Tissue Engineering*, 11(5-6):768–777, 2005.

[61] Lutz Christian Gerhardt, Kate L. Widdows, Melek M. Erol, Charles W. Burch, José A. Sanz-Herrera, Ignacio Ochoa, Rolf Stämpfli, Iman S. Roqan, Simon Gabe,

Tahera Ansari, and Aldo R. Boccaccini. The pro-angiogenic properties of multifunctional bioactive glass composite scaffolds. *Biomaterials*, 32(17):4096–4108, 2011.

[62] Peter Rhee, Carlos Brown, Matthew Martin, Ali Salim, Dave Plurad, Donald Green, Lowell Chambers, Demetrios Demetriades, George Velmahos, and Hassan Alam. Quikclot use in trauma for hemorrhage control: Case series of 103 documented uses. *Journal of Trauma - Injury, Infection and Critical Care*, 64(4):1093–1099, 2008.

[63] Paolo A. Muraro, Roland Martin, Giovanni Luigi Mancardi, Richard Nicholas, Maria Pia Sormani, and Riccardo Saccardi. Autologous haematopoietic stem cell transplantation for treatment of multiple sclerosis. *Nature Reviews Neurology*, 13(7):391–405, 2017.

[64] T. Peltola, M. Jokinen, H. Rahiala, E. Levänen, J. B. Rosenholm, I. Kangasniemi, and A. Yli-Urpo. Calcium phosphate formation on porous sol-gel-derived SiO2 and CaO-P2O5-SiO2 substrates in vitro. *Journal of Biomedical Materials Research*, 44(1):12–21, 1999.

[65] A A Majeed and R A Al Naimi. Role of Hydroxyapatite in Healing of Experimentally Induced Cutaneous Wound in Rabbits. *Al-Anbar Journal of Veterinary Sciences*, 5(1):74–81, 2012.

[66] Kenichiro Kawai, Barrett J. Larson, Hisako Ishise, Antoine Lyonel Carre, Soh Nishimoto, Michael Longaker, and H. Peter Lorenz. Calcium-based nanoparticles accelerate skin wound healing. *PLoS ONE*, 6(11), 2011.

[67] Xiaojun Yu and Ravi V. Bellamkonda. Tissue-Engineered Scaffolds Are Effective Alternatives to Autografts for Bridging Peripheral Nerve Gaps. *Tissue Engineering*, 9(3):421–430, 2003.

[68] S Bunting, L D I Silvio, S Deb, and S Hall. Article in Press Bioresorbable Glass Fibres Facilitate Peripheral Nerve Regeneration. *Journal of Hand Surgery*, 30(3):242–247, 2005.

[69] Masoumeh Foroutan Koudehi, Abbas Ali Imani Fooladi, Kourosh Mansoori, Zahra Jamalpoor, Afsaneh Amiri, and Mohammad Reza Nourani. Preparation and evaluation of novel nano-bioglass/gelatin conduit for peripheral nerve regeneration. *Journal of Materials Science: Materials in Medicine*, 25(2):363–373, 2014.

[70] X. F. Zhang, S. Kehoe, S. K. Adhi, T. G. Ajithkumar, S. Moane, H. O'Shea, and D. Boyd. Composition-structure-property (Zn2+and Ca2+ion release) evaluation of Si-Na-Ca-Zn-Ce glasses: Potential components for nerve guidance conduits. *Materials Science and Engineering C*, 31(3):669–676, 2011.

[71] A Walan. Clinical experience with omeprazole: assessment of efficacy and safety. *Journal of gastroenterology and hepatology*, 4(Suppl 2):27–33, 1989.

[72] Ai Niu Ma, Nian Gong, Jin Miao Lu, Jin Lu Huang, Bin Hao, Yang Guo, Jipin Zhong, Yuhong Xu, Jiang Chang, and Yong Xiang Wang. Local protective effects of oral 45S5 bioactive glass on gastric ulcers in experimental animals. *Journal of Materials Science: Materials in Medicine*, 24(3):803–809, 2013.

[73] B Creamer, R G Shorter, and J Bamforth. The turnover and shedding of epithelial cells. I. The turnover in the gastro-intestinal tract. *Gut*, 2(2):110–116, 1961.

[74] Syed Raza Moosvi and Richard M. Day. Bioactive glass modulation of intestinal epithelial cell restitution. *Acta Biomaterialia*, 5(1):76–83, 2009.

[75] Larry L. Hench and David Greenspan. Interactions between bioactive glass and collagen: A review and new perspectives. *Journal of the Australian Ceramic Society*, 49(2):1–40, 2013.

[76] Michasam B Raredon, Kseniya Gavrilov, Tai Yi, and Zhen W Zhuang. In Vivo Implantation. *Science*, 329:2008–2011, 2010.

[77] C. F. Andrade, A. P. Wong, T. K. Waddell, S. Keshavjee, and M. Liu. Cell-based tissue engineering for lung regeneration. *AJP: Lung Cellular and Molecular Physiology*, 292(2):L510–L518, 2006.

[78] Y. M. Lin, A. R. Boccaccini, J. M. Polak, A. E. Bishop, and V. Maquet. Biocompatibility of poly-DL-lactic acid (PDLLA) for lung tissue engineering. *Journal of Biomaterials Applications*, 21(2):109–118, 2006.

[79] Mark J. Mondrinos, Sirma Koutzaki, Eugean Jiwanmall, Mengyan Li, Jean-Pierre Dechadarevian, Peter I. Lelkes, and Christine M. Finck. Engineering Three-Dimensional Pulmonary Tissue Constructs. *Tissue Engineering*, 12(4):717–728, 2006.

[80] Karen L. Christman and Randall J. Lee. Biomaterials for the Treatment of Myocardial Infarction. *Journal of the American College of Cardiology*, 48(5):907–913, 2006.

[81] Molamma P. Prabhakaran, J. Venugopal, Dan Kai, and Seeram Ramakrishna. Biomimetic material strategies for cardiac tissue engineering. *Materials Science and Engineering C*, 31(3):503–513, 2011.

[82] Qizhi Chen, Liyu Jin, Wayne D Cook, Dirk Mohn, Ebba L Lagerqvist, David A Elliott, John M Haynes, Nicholas Boyd, Wendelin J Stark, Colin W Pouton, Edouard G Stanley, and Andrew G Elefanty. Elastomeric nanocomposites as cell delivery vehicles and cardiac support devices. *Soft Matter*, 6(19):4715–4726, 2010.

[83] Marwa Tallawi, Elisabetta Rosellini, Niccoletta Barbani, Maria Grazia Cascone, Ranjana Rai, Guillaume Saint-Pierre, and Aldo R. Boccaccini. Strategies for the chemical and biological functionalization of scaffolds for cardiac tissue engineering: a review. *Journal of The Royal Society Interface*, 12(108):20150254, 2015.

[84] Christian Frantz, Kathleen M Stewart, and Valerie M Weaver. The extracellular matrix at a glance. *Journal of Cell Science*, 123(24):4195–4200, 2010.

[85] Nancy E. Lane. Epidemiology, etiology, and diagnosis of osteoporosis. *American Journal of Obstetrics and Gynecology*, 194(2 SUPPL.):S3–S11, 2006.

[86] Larry L. Hench. Biomaterials: A forecast for the future. *Biomaterials*, 19(16):1419–1423, 1998.

[87] F. Barrère, T. A. Mahmood, K. de Groot, and C. A. van Blitterswijk. Advanced biomaterials for skeletal tissue regeneration: Instructive and smart functions. *Materials Science and Engineering R: Reports*, 59(1-6):38–71, feb 2008.

[88] Lucy A Bosworth and Sandra Downes. Physicochemical characterisation of degrading polycaprolactone scaffolds. *Polymer Degradation and Stability*, 95(12):2269–2276, 2010.

[89] S D Bruck. Biostability of materials and implants. *Journal of long-term effects of medical implants*, 1(1):89–106, 1991.

[90] Larry L. Hench and Julia M. Polak. Third-generation biomedical materials. *Science*, 295(5557):1014–1017, 2002.

[91] Roger J. Narayan. The next generation of biomaterial development. *Philosophical Transactions of the Royal Society A: Mathematical, Physical and Engineering Sciences*, 368(1917):1831–1837, 2010.

[92] C.A.C. Zavaglia and M.H. Prado da Silva. Feature Article: Biomaterials. In *Reference Module in Materials Science and Materials Engineering*. Elsevier, 2015.

[93] Jk Christie, A Pedone, Mc Menziani, and A Tilocca. Fluorine Environment in Bioactive Glasses: ab Initio Molecular Dynamics Simulations. *Journal of Physical Chemistry B*, 115(9):2038–2045, 2011.

[94] Jonathan C. Knowles. Phosphate-based glasses for biomedical applications. *Journal of Materials Chemistry*, 13(10):2395–2401, 2003.

[95] W. H. Zachariasen. The atomic arrangement in glass. *Journal of the American Chemical Society*, 54(10):3841–3851, 1932.

[96] V. FitzGerald, D.M. Pickup, D. Greenspan, G. Sarkar, J.J. Fitzgerald, K.M. Wetherall, R.M. Moss, J.R. Jones, and R.J. Newport. A Neutron and X-Ray Diffraction Study of Bioglass® with Reverse Monte Carlo Modelling. *Advanced Functional Materials*, 17(18):3746–3753, 2007.

[97] R. Hill. An alternative view of the degradation of bioglass. *Journal of Materials Science Letters*, 15(13):1122–1125, 1996.

[98] Zdeněk Strnad. Role of the glass phase in bioactive glass-ceramics. *Biomaterials*, 13(5):317–321, 1992.

[99] Mattias Edén. The split network analysis for exploring composition-structure correlations in multi-component glasses: I. Rationalizing bioactivity-composition trends of bioglasses. *Journal of Non-Crystalline Solids*, 357(6):1595–1602, 2011.

[100] Matthew D. O'Donnell. Predicting bioactive glass properties from the molecular chemical composition: Glass transition temperature. *Acta Biomaterialia*, 7(5):2264–2269, 2011.

[101] James E. Shelby. Density of vitreous silica. In *Journal of Non-Crystalline Solids*, volume 349, pages 331–336, 2004.

[102] Julian R. Jones and Alexis G. Clare. *Bio-Glasses: An Introduction*. John Wiley and Sons, 2012.

[103] Werner Stöber, Arthur Fink, and Ernst Bohn. Controlled growth of monodisperse silica spheres in the micron size range. *Journal of Colloid and Interface Science*, 26(1):62–69, 1968.

[104] Julian R. Jones. New trends in bioactive scaffolds: The importance of nanostructure. *Journal of the European Ceramic Society*, 29(7):1275–1281, 2009.

[105] Leonid Lichtenstein, Christin Büchner, Bing Yang, Shamil Shaikhutdinov, Markus Heyde, Marek Sierka, Radosåaw Wåodarczyk, Joachim Sauer, and Hans Joachim Freund. The atomic structure of a metal-supported vitreous thin silica film. *Angewandte Chemie - International Edition*, 51(2):404–407, 2012.

[106] D. E. Clark, M. F. Dilmore, E. C. Ethridge, and L. L. Hench. Aqueous Corrosion of Soda-Silica and Soda-Lime-Silica Glass. *Journal of the American Ceramic Society*, 59(1-2):62–65, 1976.

[107] Marc Bohner and Jacques Lemaitre. Can bioactivity be tested in vitro with SBF solution? *Biomaterials*, 30(12):2175–2179, 2009.

[108] Antonio Tilocca and Alastair N. Cormack. Modelling the Water Bioglass Interface by Ab Initio Molecular Dynamics Simulations. *ACS Applied Materials & Interfaces*, 1(6):1324–1333, 2009.

[109] Antonio Tilocca and Alastair N. Cormack. Surface signatures of bioactivity: MD simulations of 45S and 65S silicate glasses. *Langmuir*, 26(1):545–551, 2010.

[110] R. A. Martin, H. Twyman, D. Qiu, J. C. Knowles, and R. J. Newport. A study of the formation of amorphous calcium phosphate and hydroxyapatite on melt quenched Bioglass® using surface sensitive shallow angle X-ray diffraction. *Journal of Materials Science: Materials in Medicine*, 20(4):883–888, 2009.

[111] J C Elliott. General chemistry of the calcium orthophosphates. *Studies in Inorganic Chemistry*, 18(C):1–62, 1994.

[112] R. Z. LeGeros, O. R. Trautz, E. Klein, and J. P. LeGeros. Two types of carbonate substitution in the apatite structure. *Experientia*, 25(1):5–7, 1969.

[113] Max M. Villa, Liping Wang, Jianping Huang, David W. Rowe, and Mei Wei. Bone tissue engineering with a collagen-hydroxyapatite scaffold and culture expanded bone marrow stromal cells. *Journal of Biomedical Materials Research - Part B Applied Biomaterials*, 103(2):243–253, 2015.

[114] Robert John Newport, Laura J. Skipper, Daniela Carta, David M. Pickup, Frank E. Sowrey, Mark E. Smith, Priya Saravanapavan, and Larry L. Hench. The use of advanced diffraction methods in the study of the structure of a bioactive calcia: Silica sol-gel glass. In *Journal of Materials Science: Materials in Medicine*, volume 17, pages 1003–1010. Kluwer Academic Publishers, 2006.

[115] Roger F. Brown, Delbert E. Day, Thomas E. Day, Steve Jung, Mohamed N. Rahaman, and Qiang Fu. Growth and differentiation of osteoblastic cells on 13-93 bioactive glass fibers and scaffolds. *Acta Biomaterialia*, 4(2):387–396, 2008.

[116] Leena Hupa, Kaj H. Karlsson, Mikko Hupa, and Hannu T. Aro. Comparison of bioactive glasses in vitro and in vivo. *Glass Technology: European Journal of Glass Science and Technology Part A*, 51(2):89–92, 2010.

[117] M. D. O'Donnell, S. J. Watts, R. G. Hill, and R. V. Law. The effect of phosphate content on the bioactivity of soda-lime- phosphosilicate glasses. *Journal of Materials Science: Materials in Medicine*, 20(8):1611–1618, 2009.

[118] Mohammed Mneimne, Robert G. Hill, Andrew J. Bushby, and Delia S. Brauer. High phosphate content significantly increases apatite formation of fluoride-containing bioactive glasses. *Acta Biomaterialia*, 7(4):1827–1834, 2011.

[119] M. D. O'Donnell and R. G. Hill. Influence of strontium and the importance of glass chemistry and structure when designing bioactive glasses for bone regeneration. *Acta Biomaterialia*, 6(7):2382–2385, 2010.

[120] Yann C Fredholm, Natalia Karpukhina, Delia S Brauer, Julian R Jones, Robert V Law, and Robert G Hill. Influence of strontium for calcium substitution in bioactive glasses on degradation, ion release and apatite formation. *Journal of the Royal Society, Interface / the Royal Society*, 9(70):880–9, 2012.

[121] Delia S. Brauer, Natalia Karpukhina, Matthew D. O'Donnell, Robert V. Law, and Robert G. Hill. Fluoride-containing bioactive glasses: Effect of glass design and structure on degradation, pH and apatite formation in simulated body fluid. *Acta Biomaterialia*, 6(8):3275–3282, 2010.

[122] T. Kokubo, H. Kushitani, S. Sakka, T. Kitsugi, and T. Yamamuro. Solutions able to reproduce in vivo surface-structure changes in bioactive glass-ceramic A-W3. *Journal of Biomedical Materials Research*, 24(6):721–734, 1990.

[123] Saeid Kargozar, Francesco Baino, Sepideh Hamzehlou, Robert G Hill, and Masoud Mozafari. Bioactive Glasses: Sprouting Angiogenesis in Tissue Engineering. *Trends in Biotechnology*, 36(4):430–444, 2018.

[124] Charles J. Malemud. Matrix Metalloproteinases and Synovial Joint Pathology. In *Progress in Molecular Biology and Translational Science*, volume 148, pages 305–325. Academic Press, 2017.

[125] Rainer Detsch, Patricia Stoor, Alina Grünewald, Judith A. Roether, Nina C. Lindfors, and Aldo R. Boccaccini. Increase in VEGF secretion from human fibroblast cells by bioactive glass S53P4 to stimulate angiogenesis in bone. *Journal of Biomedical Materials Research - Part A*, 102(11):4055–4061, 2014.

[126] Elias Nunes Martins, Martinho De Almeida E Silva, Paulo Sávio Lopes, and Adair José Regazzi. Desvios nas estimativas de componentes de variância obtidos pelo método da máxima verossimilhança restrita. *Revista Brasileira de Zootecnia*, 26(5):935–941, 1997.

[127] Chiara Giacomelli, Maria Letizia Trincavelli, Cristina Satriano, Örjan Hansson, Diego La Mendola, Enrico Rizzarelli, and Claudia Martini. Copper (II) ions modulate Angiogenin activity in human endothelial cells. *International Journal of Biochemistry and Cell Biology*, 60:185–196, 2015.

[128] Emanuela Urso and Michele Maffia. Behind the Link between Copper and Angiogenesis: Established Mechanisms and an Overview on the Role of Vascular Copper Transport Systems. *Journal of Vascular Research*, 52(3):172–196, 2015.

[129] Damiano Cosimo Rigiracciolo, Andrea Scarpelli, Rosamaria Lappano, Assunta Pisano, Maria Francesca Santolla, Paola De Marco, Francesca Cirillo, Anna Rita Cappello, Vincenza Dolce, Antonino Belfiore, Marcello Maggiolini, and Ernestina Marianna De Francesco. Copper activates HIF-1/GPER/VEGF signalling in cancer cells. *Oncotarget*, 6(33), 2015.

[130] Gregor Bührer, Ulrike Rottensteiner, Alexander Hoppe, Rainer Detsch, Diana Dafinova, Tobias Fey, Peter Greil, Christian Weis, Justus P. Beier, Aldo R. Boccacini, Raymund E. Horch, and Andreas Arkudas. Evaluation of in vivo angiogenetic ef-

fects of copper doped bioactive glass scaffolds in the AV loop model. *Biomedical Glasses*, 2(1):111–117, 2016.

[131] Shichang Zhao, Le Li, Hui Wang, Yadong Zhang, Xiangguo Cheng, Nai Zhou, Mohamed N. Rahaman, Zhongtang Liu, Wenhai Huang, and Changqing Zhang. Wound dressings composed of copper-doped borate bioactive glass microfibers stimulate angiogenesis and heal full-thickness skin defects in a rodent model. *Biomaterials*, 53:379–391, 2015.

[132] Atefeh Shamosi, Mehdi Farokhi, Jafar Ai, and Esmaeel Sharifi. Induction of spontaneous neo-angiogenesis and tube formation in human endometrial stem cells by bioglass. *Journal of Medical Hypotheses and Ideas*, 9(2):94–98, 2015.

[133] Wanyin Zhai, Hongxu Lu, Lei Chen, Xiaoting Lin, Yan Huang, Kerong Dai, Kawazoe Naoki, Guoping Chen, and Jiang Chang. Silicate bioceramics induce angiogenesis during bone regeneration. *Acta Biomaterialia*, 8(1):341–349, 2012.

[134] Mani Diba, Ourania Menti Goudouri, Felipe Tapia, and Aldo R. Boccaccini. Magnesium-containing bioactive polycrystalline silicate-based ceramics and glass-ceramics for biomedical applications. *Current Opinion in Solid State and Materials Science*, 18(3):147–167, 2014.

[135] Daniela Bernardini, Anna Nasulewic, Andrzej Mazur, and J. A. Maier. Magnesium and microvascular endothelial cells: a role in inflammation and angiogenesis. *Frontiers in bioscience : a journal and virtual library.*, 10:1177–1182, 2005.

[136] Saeid Kargozar, Nasrin Lotfibakhshaiesh, Jafar Ai, Masoud Mozafari, Peiman Brouki Milan, Sepideh Hamzehlou, Mahmood Barati, Francesco Baino, Robert G. Hill, and Mohammad Taghi Joghataei. Strontium- and cobalt-substituted bioactive glasses seeded with human umbilical cord perivascular cells to promote bone regeneration via enhanced osteogenic and angiogenic activities. *Acta Biomaterialia*, 58:502–514, 2017.

[137] In Ho Lee, Hye Sun Yu, Nilay J Lakhkar, Hae Won Kim, Myoung Seon Gong, Jonathan C Knowles, and Ivan B Wall. Development, characterisation and biocompatibility testing of a cobalt-containing titanium phosphate-based glass for engineering of vascularized hard tissues. *Materials Science and Engineering C*, 33(4):2104–2112, 2013.

[138] Aiah A. El-Rashidy, Judith A. Roether, Leila Harhaus, Ulrich Kneser, and Aldo R. Boccaccini. Regenerating bone with bioactive glass scaffolds: A review of in vivo studies in bone defect models. *Acta Biomaterialia*, 62:1–28, 2017.

[139] Atchariya Chansomwong, Peter L. Douglas, Eric Croiset, Kourosh Zanganeh, Ahmed Shafeen, and Luis Ricardez-Sandoval. Control of an oxy-fuel capture and purification unit for coal-based power plants. *Energy Procedia*, 63(3):476–483, 2014.

[140] T. Livingston, P. Ducheyne, and J. Garino. In vivo evaluation of a bioactive scaffold for bone tissue engineering. *Journal of Biomedical Materials Research*, 62(1):1–13, 2002.

[141] Lei Zhang, Xiurong Ke, Lingzhi Lin, Jun Xiao, Xianyan Yang, Juncheng Wang, Guojing Yang, Sanzhong Xu, Zhongru Gou, and Zhanjun Shi. Systematic evaluation of the osteogenic capacity of low-melting bioactive glass-reinforced 45S5 Bioglass porous scaffolds in rabbit femoral defects. *Biomedical Materials (Bristol)*, 12(3):035010, 2017.

[142] Xin Liu, Mohamed N Rahaman, and Qiang Fu. Bone regeneration in strong porous bioactive glass (13-93) scaffolds with an oriented microstructure implanted in rat calvarial defects. *Acta Biomaterialia*, 9(1):4889–4898, 2013.

[143] Wai Ching Liu, Irina S Robu, Rikin Patel, Ming C Leu, Mariano Velez, and Tien Min Gabriel Chu. The effects of 3D bioactive glass scaffolds and BMP-2 on bone formation in rat femoral critical size defects and adjacent bones. *Biomedical Materials (Bristol)*, 9(4):045013, 2014.

[144] Xin Liu, Mohamed N Rahaman, Yongxing Liu, B. Sonny Bal, and Lynda F Bonewald. Enhanced bone regeneration in rat calvarial defects implanted with surface-modified and BMP-loaded bioactive glass (13-93) scaffolds. *Acta Biomaterialia*, 9(7):7506–7517, 2013.

[145] Yinan Lin, Wei Xiao, Xin Liu, B. Sonny Bal, Lynda F Bonewald, and Mohamed N Rahaman. Long-term bone regeneration, mineralization and angiogenesis in rat calvarial defects implanted with strong porous bioactive glass (13-93) scaffolds. *Journal of Non-Crystalline Solids*, 432(Part A):120–129, 2016.

[146] Wei Xiao, Mohsen Asle Zaeem, B. Sonny Bal, and Mohamed N Rahaman. Creation of bioactive glass (13–93) scaffolds for structural bone repair using a combined finite element modeling and rapid prototyping approach. *Materials Science and Engineering C*, 68:651–662, 2016.

[147] G Poologasundarampillai, D Wang, S Li, J Nakamura, R Bradley, P D Lee, M M Stevens, D. S. McPhail, T Kasuga, and J R Jones. Cotton-wool-like bioactive glasses for bone regeneration. *Acta Biomaterialia*, 10(8):3733–3746, 2014.

[148] Franziska Döhler, Daniel Groh, Shotaro Chiba, Jörg Bierlich, Jens Kobelke, and Delia S. Brauer. Bioactive glasses with improved processing. Part 2. Viscosity and fibre drawing. *Journal of Non-Crystalline Solids*, 432(Part A):130–136, 2016.

[149] Loredana Moimas, Matteo Biasotto, Roberto Di Lenarda, Alessandro Olivo, and Chiara Schmid. Rabbit pilot study on the resorbability of three-dimensional bioactive glass fibre scaffolds. *Acta Biomaterialia*, 2(2):191–199, 2006.

[150] Blanca San Miguel, Rytis Kriauciunas, Samuele Tosatti, Martin Ehrbar, Chafik Ghayor, Marcus Textor, and Franz E. Weber. Enhanced osteoblastic activity and bone regeneration using surface-modified porous bioactive glass scaffolds. *Journal of Biomedical Materials Research - Part A*, 94(4):1023–1033, 2010.

[151] D. C. Clupper, J. E. Gough, M. M. Hall, A. G. Clare, W. C. LaCourse, and L. L. Hench. In vitro bioactivity of S520 glass fibers and initial assessment of osteoblast

attachment. *Journal of Biomedical Materials Research - Part A*, 67(1):285–294, 2003.

[152] Yong-keun Lee and Seong-ho Choi. Novel Calcium Phosphate Glass for Hard-Tissue Regeneration Synthesis of calcium phosphate glass. *Journal of Korean Academy of Periodontology*, 38(2):273–298, 2008.

[153] Lianxiang Bi, Steve Jung, Delbert Day, Katie Neidig, Vladimir Dusevich, David Eick, and Lynda Bonewald. Evaluation of bone regeneration, angiogenesis, and hydroxyapatite conversion in critical-sized rat calvarial defects implanted with bioactive glass scaffolds. *Journal of Biomedical Materials Research - Part A*, 100 A(12):3267–3275, 2012.

[154] Lianxiang Bi, Brett Zobell, Xin Liu, Mohamed N Rahaman, and Lynda F Bonewald. Healing of critical-size segmental defects in rat femora using strong porous bioactive glass scaffolds. *Materials Science and Engineering C*, 42:816–824, 2014.

[155] Yifei Gu, Wenhai Huang, Mohamed N. Rahaman, and Delbert E. Day. Bone regeneration in rat calvarial defects implanted with fibrous scaffolds composed of a mixture of silicate and borate bioactive glasses. *Acta Biomaterialia*, 9(11):9126–9136, 2013.

[156] Hui Wang, Shichang Zhao, Wei Xiao, Xu Cui, Wenhai Huang, Mohamed N. Rahaman, Changqing Zhang, and Deping Wang. Three-dimensional zinc incorporated borosilicate bioactive glass scaffolds for rodent critical-sized calvarial defects repair and regeneration. *Colloids and Surfaces B: Biointerfaces*, 130:149–156, 2015.

[157] H. Aguiar, P. González, and J. Serra. Bioactive glass structure and solubility. In Woodhead Publishing Series, editor, *Bioactive Glasses*, chapter 2, pages 37–61. Elsevier, second edi edition, 2018.

[158] Lorenzo Drago, Christian Vassena, Simone Fenu, Elena De Vecchi, Valentina Signori, Raffaele De Francesco, and Carlo Luca Romanò. In vitro antibiofilm activity of bioactive glass S53P4. *Future Microbiology*, 9(5):593–601, 2014.

[159] Shujun Ran, Zhiyan He, and Jingping Liang. Survival of Enterococcus faecalis during alkaline stress: Changes in morphology, ultrastructure, physiochemical properties of the cell wall and specific gene transcripts. *Archives of Oral Biology*, 58(11):1667–1676, 2013.

[160] Di Zhang, Outi Leppäranta, Eveliina Munukka, Heimo Ylänen, Matti K. Viljanen, Erkki Eerola, Mikko Hupa, and Leena Hupa. Antibacterial effects and dissolution behavior of six bioactive glasses. *Journal of Biomedical Materials Research - Part A*, 93(2):475–483, 2010.

[161] Saima Begum, William E Johnson, Tony Worthington, and Richard A Martin. The influence of pH and fluid dynamics on the antibacterial efficacy of 45S5 Bioglass. *Biomedical Materials (Bristol)*, 11(1):015006, 2016.

[162] N. C. Lindfors. Bioactive glass S53P4 as a bone graft substitute in the treatment of osteomyelitis. *Bioactive Glasses: Materials, Properties and Applications*, 47(2):209–216, 2011.

[163] Lorenzo Drago, Delia Romanò, Elena De Vecchi, Christian Vassena, Nicola Logoluso, Roberto Mattina, and Carlo Luca Romanò. Bioactive glass bag-S53P4 for the adjunctive treatment of chronic osteomyelitis of the long bones: An in vitro and prospective clinical study. *BMC Infectious Diseases*, 13(1):584–592, 2013.

[164] J. McAndrew, C. Efrimescu, E. Sheehan, and D. Niall. Through the looking glass; Bioactive glass S53P4 (BonAlive®) in the treatment of chronic osteomyelitis. *Irish Journal of Medical Science*, 182(3):509–511, 2013.

[165] C. L. Romanò, N. Logoluso, E. Meani, D. Romanò, E. De Vecchi, C. Vassena, and L. Drago. A comparative study of the use of bioactive glass S53P4 and antibiotic-loaded calcium-based bone substitutes in the treatment of chronic osteomyelitis: A retrospective comparative study. *Bone and Joint Journal*, 96 B(6):845–850, 2014.

[166] I Allan, H Newman, and M Wilson. Antibacterial activity of particulate Bioglass® against supra- and subgingival bacteria. *Biomaterials*, 22(12):1683–1687, 2001.

[167] P Stoor, E Söderling, and J I Salonen. Antibacterial effects of a bioactive glass paste on oral microorganisms. *Acta odontologica Scandinavica*, 56(3):161–5, 1998.

[168] Matthias Zehnder, Tuomas Waltimo, Beatrice Sener, and Eva Söderling. Dentin enhances the effectiveness of bioactive glass S53P4 against a strain of Enterococcus faecalis. *Oral Surgery, Oral Medicine, Oral Pathology, Oral Radiology and Endodontology*, 101(4):530–535, 2006.

[169] T. Waltimo, T. J. Brunner, M. Vollenweider, W. J. Stark, and M. Zehnder. Antimicrobial effect of nanometric bioactive glass 45S5. *Journal of Dental Research*, 86(8):754–757, 2007.

[170] Lorenzo Drago, Elena De Vecchi, Monica Bortolin, Marco Toscano, Roberto Mattina, and Carlo Luca Romanò. Antimicrobial activity and resistance selection of different bioglass S53P4 formulations against multidrug resistant strains. *Future Microbiology*, 10(8):1293–1299, 2015.

[171] Lorenzo Drago, Marco Toscano, and Marta Bottagisio. Recent evidence on bioactive glass antimicrobial and antibiofilm activity: A mini-review. *Materials*, 11(2):326–337, 2018.

[172] Ilaria Cacciotti. Bivalent cationic ions doped bioactive glasses: the influence of magnesium, zinc, strontium and copper on the physical and biological properties. *Journal of Materials Science*, 52(15):8812–8831, 2017.

[173] Frank F. Sene, José R. Martinelli, and Emico Okuno. Synthesis and characterization of phosphate glass microspheres for radiotherapy applications. *Journal of Non-Crystalline Solids*, 354(42-44):4887–4893, 2008.

[174] Jamieson K. Christie, Richard I. Ainsworth, Devis Di Tommaso, and Nora H. de Leeuw. Nanoscale chains control the solubility of phosphate glasses for biomedical applications. *Journal of Physical Chemistry B*, 117(36):10652–10657, 2013.

[175] A. Dietzel. Die kationenfeldstärken und ihre beziehungen zu entglasungsvorgängen,

zur verbindungsbildung und schmelzpunkten von silikaten. *Z. Elektrochem. Angew. Phys. Chem.*, 48(1):9–23, 1942.

[176] Uwe Hoppe. A structural model for phosphate glasses. *Journal of Non-Crystalline Solids*, 195(1-2):138–147, 1996.

[177] R.K. Brow, R.J. Kirkpatrick, and G.L. Turner. The short range structure of sodium phosphate glasses I. MAS NMR studies. *Journal of Non-Crystalline Solids*, 116(1):39–45, 1990.

[178] R. James Kirkpatrick and Richard K. Brow. Nuclear magnetic resonance investigation of the structures of phosphate and phosphate-containing glasses: A review. *Solid State Nuclear Magnetic Resonance*, 5(1):9–21, 1995.

[179] B. C. Bunker, G. W. Arnold, and J. A. Wilder. Phosphate glass dissolution in aqueous solutions. *Journal of Non-Crystalline Solids*, 64(3):291–316, 1984.

[180] K. Franks, I. Abrahams, and J. C. Knowles. Development of soluble glasses for biomedical use part I: In vitro solubility measurement. *Journal of Materials Science: Materials in Medicine*, 11(10):609–614, 2000.

[181] Juliano Pelim Pessan, Nahla Saleh Al-Ibrahim, Marília Afonso Rabelo Buzalaf, and Kyriacos Jack Toumba. Slow-release fluoride devices: a literature review. *Journal of Applied Oral Science*, 16(4):238–244, 2008.

[182] John Hicks, Franklin Garcia-Godoy, and Catherine Flaitz. Biological factors in dental caries enamel structure and the caries process in the dynamic process of demineralization and remineralization (part 2). *Journal of Clinical Pediatric Dentistry*, 28(2):119–124, 2005.

[183] Julian R. Jones. Review of bioactive glass: From Hench to hybrids. *Acta Biomaterialia*, 23(S):53–82, 2015.

[184] D. G. Gillam, J. Y. Tang, N. J. Mordan, and H. N. Newman. The effects of a

novel Bioglass® dentifrice on dentine sensitivity: A scanning electron microscopy investigation. *Journal of Oral Rehabilitation*, 29(4):305–313, 2002.

[185] J Aaseth, M Shimshi, J L Gabrilove, and G S Birketvedt. Fluoride: A Toxic or Therapeutic Agent in the Treatment of Osteoporosis? *Journal of Trace Elements in Experimental Medicine*, 17(2):83–92, 2004.

[186] Charles Y.C. Pak, Joseph E. Zerwekh, and Peter Antich. Anabolic effects of fluoride on bone. *Trends in Endocrinology and Metabolism*, 6(7):229–234, 1995.

[187] Delia S. Brauer, Natalia Karpukhina, Robert V. Law, and Robert G. Hill. Structure of fluoride-containing bioactive glasses. *Journal of Materials Chemistry*, 19(31):5629–5636, 2009.

[188] D. S. Brauer, A. Al-Noaman, R. G. Hill, and H. Doweidar. Density-structure correlations in fluoride-containing bioactive glasses. *Materials Chemistry and Physics*, 130(1-2):121–125, 2011.

[189] Alfonso Pedone, Thibault Charpentier, and Maria Cristina Menziani. The structure of fluoride-containing bioactive glasses: New insights from first-principles calculations and solid state NMR spectroscopy. *Journal of Materials Chemistry*, 22(25):12599–12608, 2012.

[190] G. Lusvardi, G. Malavasi, M. Cortada, L. Menabue, M. C. Menziani, A. Pedone, and U. Segre. Elucidation of the structural role of fluorine in potentially bioactive glasses by experimental and computational investigation. *Journal of Physical Chemistry B*, 112(40):12730–12739, 2008.

[191] Andrei A Bunaciu, Elena gabriela Udriştioiu, and Hassan Y. Aboul-Enein. X-Ray Diffraction: Instrumentation and Applications. *Critical Reviews in Analytical Chemistry*, 45(4):289–299, 2015.

[192] G. El-Damrawi, H. Doweidar, H. Kamal, and A. Hassan. Characterization of Some Bioactive Glasses and Glass-ceramics Prepared by a Hydrothermal Method. *Silicon*, 10(2):395–402, 2018.

[193] H. Kamal and A. M. Hezma. Structure and Physical Properties of Borosilicate as Potential Bioactive Glasses. *Silicon*, 10(3):851–858, 2018.

[194] J. M. Gomez-Vega, E. Saiz, and A. P. Tomsia. Glass-based coatings for titanium implant alloys. *Journal of Biomedical Materials Research*, 46(4):549–559, 1999.

[195] Mohamed N. Rahaman, Delbert E. Day, B. Sonny Bal, Qiang Fu, Steven B. Jung, Lynda F. Bonewald, and Antoni P. Tomsia. Bioactive glass in tissue engineering. *Acta Biomaterialia*, 7(6):2355–2373, 2011.

[196] V. Aina, G. Malavasi, A. Fiorio Pla, L. Munaron, and C. Morterra. Zinc-containing bioactive glasses: Surface reactivity and behaviour towards endothelial cells. *Acta Biomaterialia*, 5(4):1211–1222, 2009.

[197] Xanthippi Chatzistavrou, Olga Tsigkou, Harsh D. Amin, Konstantinos M. Paraskevopoulos, Vehid Salih, and Aldo R. Boccaccini. Sol-gel based fabrication and characterization of new bioactive glass-ceramic composites for dental applications. *Journal of the European Ceramic Society*, 32(12):3051–3061, 2012.

[198] Catherine Berthomieu and Rainer Hienerwadel. Fourier transform infrared (FTIR) spectroscopy. *Photosynthesis Research*, 101(2-3):157–170, 2009.

[199] E. I. Kamitsos. Infrared Spectroscopy of Glasses. In Mario Affatigato, editor, *Modern Glass Characterization*, pages 32–73. The American Ceramic Society and John Wiley & Sons, 2015.

[200] J. Serra, P. González, S. Liste, C. Serra, S. Chiussi, B. León, M. Pérez-Amor, H. O. Ylänen, and M. Hupa. FTIR and XPS studies of bioactive silica based glasses. *Journal of Non-Crystalline Solids*, 332(1-3):20–27, 2003.

[201] P. Y. Shih, S. W. Yung, and T. S. Chin. FTIR and XPS studies of P2O5-Na2O-CuO glasses. *Journal of Non-Crystalline Solids*, 244(2):211–222, 1999.

[202] Yashar Rezaei, Fathollah Moztarzadeh, Sima Shahabi, and Mohammadreza Tahriri. Synthesis, characterization, and in vitro bioactivity of sol-gel-derived SiO2-CaO-

P2O5-MgO-SrO bioactive glass. *Synthesis and Reactivity in Inorganic, Metal-Organic and Nano-Metal Chemistry*, 44(5):692–701, 2014.

[203] Furqan A. Shah, Delia S. Brauer, Nikita Desai, Robert G. Hill, and Karin A. Hing. Fluoride-containing bioactive glasses and Bioglass 45S5 form apatite in low pH cell culture medium. *Materials Letters*, 119:96–99, 2014.

[204] Ron Darbeau. Nuclear magnetic resonance (NMR) spectroscopy: A review and a look at its use as a probative tool in deamination chemistry. *Applied Spectroscopy Reviews*, 41(4):401–425, 2006.

[205] K.J.D. Mackenzie and M.E. Smith. Multinuclear Solid-State NMR of Inorganic Materials. In *Pergamon Materials Series*, volume 6, pages 201–265. Pergamon, 1st editio edition, 2002.

[206] Kurt Moedritzer. A review of: "Phosphorus-31 NMR - Principles and Applications.". *Synthesis and Reactivity in Inorganic and Metal-Organic Chemistry*, 15(4):551–552, 1985.

[207] Tatyana Polenova, Rupal Gupta, and Amir Goldbourt. Magic angle spinning NMR spectroscopy: A versatile technique for structural and dynamic analysis of solid-phase systems. *Analytical Chemistry*, 87(11):5458–5469, 2015.

[208] David M Pickup, Richard J Speight, Jonathan C Knowles, Mark E Smith, and Robert J Newport. Sol-gel synthesis and structural characterisation of binary TiO2-P2O5 glasses. *Materials Research Bulletin*, 43(2):333–342, 2008.

[209] Anjiang Tang, Tadanori Hashimoto, Tetsuya Nishida, Hiroyuki Nasu, and Kanichi Kamiya. Structure Study of Binary Titanophosphate Glasses Prepared by Sol-Gel and Melting Methods. *Journal of the Ceramic Society of Japan*, 112(1309):496–501, 2004.

[210] Yaqoot Shaharyar, Eric Wein, Jung-Ju Kim, Randall E Youngman, Francisco Munoz, Hae-Won Kim, Antonio Tilocca, and Ashutosh Goel. Structure-solubility

relationships in fluoride-containing phosphate based bioactive glasses. *Journal of Materials Chemistry B*, 3(48):9360–9373, 2015.

[211] Delia S. Brauer, Natalia Karpukhina, Daphne Seah, Robert V. Law, and Robert G. Hill. Fluoride-Containing Bioactive Glasses. *Advanced Materials Research*, 39-40:299–304, 2008.

[212] M. W.G. Lockyer, D Holland, and R Dupree. NMR investigation of the structure of some bioactive and related glasses. *Journal of Non-Crystalline Solids*, 188(3):207–219, 1995.

[213] Delia S. Brauer, Mohammed Mneimne, and Robert G. Hill. Fluoride-containing bioactive glasses: Fluoride loss during melting and ion release in tris buffer solution. *Journal of Non-Crystalline Solids*, 357(18):3328–3333, 2011.

[214] Jamieson K. Christie, Richard I. Ainsworth, Sergio E. Ruiz Hernandez, and Nora H. de Leeuw. Structures and properties of phosphate-based bioactive glasses from computer simulation: a review. *J. Mater. Chem. B*, 5(27):5297–5306, 2017.

[215] Junko Yano and Vittal K. Yachandra. X-ray absorption spectroscopy. *Photosynthesis Research*, 102(2):241–254, 2009.

[216] Delia S Brauer, Natalia Karpukhina, Robert V Law, and Robert G Hill. Structure of fluoride-containing bioactive glasses. *Journal of Materials Chemistry*, 19(31):5629–5636, 2009.

[217] R. J. Kirkpatrick. A multinuclear MAS NMR study of the short-range structure of fluorophosphate glass. *Journal of Materials Research*, 7(7):1892–1899, 1992.

[218] James York-Winegar, Tristan Harper, Carrie Brennan, Justin Oelgoetz, and Andriy Kovalskiy. Structure of SnF2-SnO-P2O5 glasses. In *Physics Procedia*, volume 44, pages 159–165, 2013.

[219] Daan Frenkel and Berend Smit. Molecular Dynamics Simulations. In *Understanding Molecular Simulation*, pages 63–107. Elsevier, 2002.

[220] P. K. Hung, L. T. Vinh, D. M. Nghiep, and P. N. Nguyen. Computer simulation of liquid Al2O3. In Clarendon Press, editor, *Journal of Physics Condensed Matter*, volume 18, pages 9309–9322. Oxford : Clarendon Press, 2006.

[221] Antonio Tilocca, Nora H. de Leeuw, and Alastair N. Cormack. Shell-model molecular dynamics calculations of modified silicate glasses. *Physical Review B*, 73(10):104209–104223, 2006.

[222] Richard I. Ainsworth, Devis Di Tommaso, Jamieson K. Christie, and Nora H. de Leeuw. Polarizable force field development and molecular dynamics study of phosphate-based glasses. *The Journal of Chemical Physics*, 137(23):234502, 2012.

[223] Antonio Tilocca, Alastair N. Cormack, and Nora H. de Leeuw. The structure of bioactive silicate glasses: New insight from molecular dynamics simulations. *Chemistry of Materials*, 19(1):95–103, 2007.

[224] Dominik Marx and Jürg Hutter. Ab initio molecular dynamics: Theory and implementation. *Modern methods and algorithms of quantum chemistry*, 3:329–477, 2000.

[225] Jamieson K. Christie, Richard I. Ainsworth, and Nora H. de Leeuw. Ab initio molecular dynamics simulations of structural changes associated with the incorporation of fluorine in bioactive phosphate glasses. *Biomaterials*, 35(24):6164–6171, 2014.

[226] Antonio Tilocca. Structure and dynamics of bioactive phosphosilicate glasses and melts from ab initio molecular dynamics simulations. *Physical Review B - Condensed Matter and Materials Physics*, 76(22):224202–224215, 2007.

[227] Antonio Tilocca. Short- and medium-range structure of multicomponent bioactive glasses and melts: An assessment of the performances of shell-model and rigid-ion potentials. *Journal of Chemical Physics*, 129(8):084504–084513, 2008.

[228] Emilia Tang, Devis Di Tommaso, and Nora H. De Leeuw. An ab initio molecular dynamics study of bioactive phosphate glasses. *Advanced Engineering Materials*, 12(7):331–338, 2010.

[229] Antonio Tilocca. Cooling rate and size effects on the medium-range structure of multicomponent oxide glasses simulated by molecular dynamics. *Journal of Chemical Physics*, 139(11):11450, 2013.

[230] M. Bauchy. Structural, vibrational, and thermal properties of densified silicates: Insights from molecular dynamics. *Journal of Chemical Physics*, 137(4):15733, 2012.

[231] Sergio E. Ruiz Hernandez, Richard I. Ainsworth, and Nora H. de Leeuw. Molecular dynamics simulations of bio-active phosphate-based glass surfaces. *Journal of Non-Crystalline Solids*, 451:131–137, 2016.

[232] P. P. Ewald. Die Berechnung optischer und elektrostatischer Gitterpotentiale. *Annalen der Physik*, 369(3):253–287, 1921.

[233] Julian D. Gale. GULP: A computer program for the symmetry-adapted simulation of solids. *Journal of the Chemical Society, Faraday Transactions*, 93(4):629–637, 1997.

[234] R. A. Jackson and C. R.A. Catlow. Computer Simulation Studies of Zeolite Structure. *Molecular Simulation*, 1(4):207–224, 1988.

[235] John W. Perram, Henrik G. Petersen, and Simon W. De Leeuw. An algorithm for the simulation of condensed matter which grows as the power of the number of particles. *Molecular Physics*, 65(4):875–893, 1988.

[236] E. W. Kellermann. Theory of the Vibrations of the Sodium Chloride Lattice. *Philosophical Transactions of the Royal Society A: Mathematical, Physical and Engineering Sciences*, 238(798):513–548, 1940.

[237] W. G. Stirling. Neutron inelastic scattering study of the lattice dynamics of strontium titanate: Harmonic models. *Journal of Physics C: Solid State Physics*, 5(19):2711–2730, 1972.

[238] X. W. Sun, Y. D. Chu, Z. J. Liu, T. Song, P. Guo, and Q. F. Chen. Shell and

breathing shell model calculations for isothermal bulk modulus in MgO at high pressures and temperatures. *Materials Chemistry and Physics*, 116(1):34–40, 2009.

[239] M. J.L. Sangster. Interionic potentials and force constant models for rocksalt structure crystals. *Journal of Physics and Chemistry of Solids*, 34(2):355–363, 1973.

[240] Etsuko Sugawara and Hiroshi Nikaido. Properties of AdeABC and AdeIJK efflux systems of Acinetobacter baumannii compared with those of the AcrAB-TolC system of Escherichia coli. *Antimicrobial agents and chemotherapy*, 58(12):7250–7257, 2014.

[241] J. E. Jones. On the Determination of Molecular Fields. II. From the Equation of State of a Gas. *Proceedings of the Royal Society A: Mathematical, Physical and Engineering Sciences*, 106(738):463–477, 1924.

[242] M Born and J E Mayer. Zur Dittertheorie der Ionenkristalle. *Zeit. Phys.*, 75(1):1–18, 1986.

[243] Philipp M Morse. Diatomic Molecules According to the Wave Mechanics. II. Vibrational Levels. *Physical Review*, 34(1):57–64, 1929.

[244] N. A. Sinitsyn, Q. Niu, and A. H. MacDonald. Coordinate shift in the semiclassical Boltzmann equation and the anomalous Hall effect. *Physical Review B - Condensed Matter and Materials Physics*, 73(7):264–283, 2006.

[245] Maurice L. Huggins and Joseph E. Mayer. Interatomic Distances in Crystals of the Alkali Halides. *The Journal of Chemical Physics*, 1(9):643–646, 1933.

[246] Felcy Fabiola, Richard Bertram, Andrei Korostelev, and Michael S Chapman. An improved hydrogen bond potential: impact on medium resolution protein structures. *Protein science : a publication of the Protein Society*, 11(6):1415–1423, 2002.

[247] Soren Toxvaerd and Jeppe C. Dyre. Communication: Shifted forces in molecular dynamics. *Journal of Chemical Physics*, 134(8):81102–81107, 2011.

[248] C. M. Freeman, J. M. Newsam, S. M. Levine, and C. R. A. Catlow. Inorganic crystal structure prediction using simplified potentials and experimental unit cells: application to the polymorphs of titanium dioxide. *Journal of Materials Chemistry*, 3(5):531, 1993.

[249] J. D. Gale, C. R.A. Catlow, and W. C. MacKrodt. Periodic ab initio determination of interatomic potentials for alumina. *Modelling and Simulation in Materials Science and Engineering*, 1(1):73–81, 1992.

[250] B. J. Alder and T. E. Wainwright. Studies in Molecular Dynamics. I. General Method. *The Journal of Chemical Physics*, 31(2):459–466, 1959.

[251] I. Štich. Correlations in the motion of atoms in liquid silicon. *Physical Review A*, 44(2):1401–1404, 1991.

[252] Loup Verlet. Computer "experiments" on classical fluids. I. Thermodynamical properties of Lennard-Jones molecules. *Physical Review*, 159(1):98–103, 1967.

[253] Max Born and Hun Kuang. Dynamical Theory of Crystal Lattices. In *Oxford University Press*, page 431. Oxford University Press, 1962.

[254] Martin Oliver. *Introduction to Molecular Dynamics Simulations: Applications in Hard and Soft Condensed Matter Physics*. InTech, 2012.

[255] Klaas Douwe B. Dijkstra, Jens Kipping, and Nicolas Mézière. Sixty new dragonfly and damselfly species from Africa (Odonata). *Odonatologica*, 44(4):447–678, 2015.

[256] Anders M.N. Niklasson, C J Tymczak, and Matt Challacombe. Time-reversible born-oppenheimer molecular dynamics. *Physical Review Letters*, 97(12):123001–123005, 2006.

[257] W. Smith and T. R. Forester. DL-POLY-2.0: A general-purpose parallel molecular dynamics simulation package. *Journal of Molecular Graphics*, 14(3):136–141, 1996.

[258] Antonio Tilocca, Alastair N. Cormack, and Nora H. de Leeuw. The structure of bioactive silicate glasses: New insight from molecular dynamics simulations. *Chemistry of Materials*, 19(1):95–103, 2007.

[259] Antonio Tilocca, Alastair N. Cormack, and Nora H. de Leeuw. The formation of nanoscale structures in soluble phosphosilicate glasses for biomedical applications: MD simulations. *Faraday Discussions*, 136:45–55, 2007.

[260] Aboli A. Rane and Karen L. Christman. Biomaterials for the treatment of myocardial infarction: A 5-year update. *Journal of the American College of Cardiology*, 58(25):2615–2629, 2011.

[261] American College of Cardiology. How the Heart Works, 2008.

[262] Jan Kajstura, Narasimman Gurusamy, Barbara Ogórek, Polina Goichberg, Carlos Clavo-Rondon, Toru Hosoda, Domenico D'Amario, Silvana Bardelli, Antonio P. Beltrami, Daniela Cesselli, Rossana Bussani, Federica Del Monte, Federico Quaini, Marcello Rota, Carlo A. Beltrami, Bruce A. Buchholz, Annarosa Leri, and Piero Anversa. Myocyte turnover in the aging human heart. *Circulation Research*, 107(11):1374–1386, 2010.

[263] Marieke Rienks, Anna Pia Papageorgiou, Nikolaos G. Frangogiannis, and Stephane Heymans. Myocardial extracellular matrix: An ever-changing and diverse entity. *Circulation Research*, 114(5):872–888, 2014.

[264] Maria Kitsara, Onnik Agbulut, Dimitrios Kontziampasis, Yong Chen, and Philippe Menasché. Fibers for hearts: A critical review on electrospinning for cardiac tissue engineering. *Acta Biomaterialia*, 48:20–40, 2017.

[265] Qi Zhi Chen, Alexander Bismarck, Ulrich Hansen, Sarah Junaid, Michael Q. Tran, Siân E. Harding, Nadire N. Ali, and Aldo R. Boccaccini. Characterisation of a soft elastomer poly(glycerol sebacate) designed to match the mechanical properties of myocardial tissue. *Biomaterials*, 29(1):47–57, 2008.

[266] A. J. Engler, C. Carag-Krieger, C. P. Johnson, M. Raab, H.-Y. Tang, D. W. Speicher, J. W. Sanger, J. M. Sanger, and D. E. Discher. Embryonic cardiomyocytes beat best on a matrix with heart-like elasticity: scar-like rigidity inhibits beating. *Journal of Cell Science*, 121(22):3794–3802, 2008.

[267] Rajiv R. Chaturvedi, Todd Herron, Robert Simmons, Darryl Shore, Pankaj Kumar, Babulal Sethia, Felix Chua, Efstathios Vassiliadis, and Jonathan C. Kentish. Passive stiffness of myocardium from congenital heart disease and implications for diastole. *Circulation*, 121(8):979–988, 2010.

[268] Olaf Bergmann, Ratan D. Bhardwaj, Samuel Bernard, Sofia Zdunek, Fanie Barnabé-Heide, Stuart Walsh, Joel Zupicich, Kanar Alkass, Bruce A. Buchholz, Henrik Druid, Stefan Jovinge, and Jonas Frisén. Evidence for cardiomyocyte renewal in humans. *Science*, 324(5923):98–102, 2009.

[269] Gordana Vunjak-Novakovic, Nina Tandon, Amandine Godier, Robert Maidhof, Anna Marsano, Timothy P. Martens, and Milica Radisic. Challenges in Cardiac Tissue Engineering. *Tissue Engineering Part B: Reviews*, 16(2):169–187, 2010.

[270] M. Shin, O. Ishii, T. Sueda, and J. P. Vacanti. Contractile cardiac grafts using a novel nanofibrous mesh. *Biomaterials*, 25(17):3717–3723, 2004.

[271] M. Arnal-Pastor, J. C., M. Monlen, and A. Valls- Lluch. Biomaterials for Cardiac Tissue Engineering. In *Regenerative Medicine and Tissue Engineering*, volume 030301, pages 275–323. InTechOpen, 2013.

[272] Michael H. Kwon, Marisa Cevasco, Jan D. Schmitto, and Frederick Y. Chen. Ventricular restraint therapy for heart failure: A review, summary of state of the art, and future directions. *Journal of Thoracic and Cardiovascular Surgery*, 144(4):771–777.e1, 2012.

[273] Yoshiharu Enomoto, Joseph H. Gorman, Sina L. Moainie, Benjamin M. Jackson, Landi M. Parish, Theodore Plappert, Ahmad Zeeshan, Martin G. St. John-Sutton, and Robert C. Gorman. Early ventricular restraint after myocardial infarction:

Extent of the wrap determines the outcome of remodeling. *Annals of Thoracic Surgery*, 79(3):881–887, 2005.

[274] James A. Magovern, Leah Teekell-Taylor, Sunil Mankad, Uday Dasika, Walter McGregor, Robert W.W. Biederman, June Yamrozik, and Dennis R. Trumble. Effect of a flexible ventricular restraint device on cardiac remodeling after acute myocardial infarction. *ASAIO Journal*, 52(2):196–200, 2006.

[275] Douglas L. Mann, Veli K. Topkara, and Srikanth Kondareddy. Modulation of left ventricular dilation remodeling with epicardial restraint devices in postmyocardial infarction heart failure. *Current Heart Failure Reports*, 6(4):229–235, 2009.

[276] A. A. Kocher, M. D. Schuster, M. J. Szabolcs, S. Takuma, D. Burkhoff, J. Wang, S. Homma, N. M. Edwards, and S. Itescu. Neovascularization of ischemic myocardium by human bone-marrow-derived angioblasts prevents cardiomyocyte apoptosis, reduces remodeling and improves cardiac function. *Nature Medicine*, 7(4):430–436, 2001.

[277] Harald C. Ott, Thomas S. Matthiesen, Saik Kia Goh, Lauren D. Black, Stefan M. Kren, Theoden I. Netoff, and Doris A. Taylor. Perfusion-decellularized matrix: Using nature's platform to engineer a bioartificial heart. *Nature Medicine*, 14(2):213–221, 2008.

[278] Eva Korup, Dorthe Dalsgaard, Ole Nyvad, Thomas Møller Jensen, Egon Toft, and Jens Berning. Comparison of degrees of left ventricular dilation within three hours and up to six days after onset of first acute myocardial infarction. *American Journal of Cardiology*, 80(4):449–453, 1997.

[279] Harlan F. Weisman, David E. Bush, John A. Mannisi, and Bernadine Healy Bulkley. Global cardiac remodeling after acute myocardial infarction: A study in the rat model. *Journal of the American College of Cardiology*, 5(6):1355–1362, 1985.

[280] J. S. Hochman and B. H. Bulkley. Expansion of acute myocardial infarction: An experimental study. *Circulation*, 65(7 I):1446–1450, 1982.

[281] Anirudha Singh and Jennifer Elisseeff. Biomaterials for stem cell differentiation. *Journal of Materials Chemistry*, 20(40):8832–8847, 2010.

[282] Nandan L. Nerurkar, Dawn M. Elliott, and Robert L. Mauck. Mechanics of oriented electrospun nanofibrous scaffolds for annulus fibrosus tissue engineering. *Journal of Orthopaedic Research*, 25(8):1018–1028, 2007.

[283] Nathaniel S Hwang, Shyni Varghese, and Jennifer Elisseeff. Controlled differentiation of stem cells. *Advanced drug delivery reviews*, 60(2):199–214, 2008.

[284] Jay J. Lunden, Samuel E. Georgian, and Erik E. Cordes. Aragonite saturation states at cold-water coral reefs structured by Lophelia pertusa in the northern Gulf of Mexico. *Limnology and Oceanography*, 58(1):354–362, 2013.

[285] K. Matsubayashi. Improved Left Ventricular Aneurysm Repair With Bioengineered Vascular Smooth Muscle Grafts. *Circulation*, 108(90101):219II—-225, 2003.

[286] Tao Wang, Xue Jun Jiang, Qi Zhu Tang, Xiao Yan Li, Tao Lin, De Qun Wu, Xian Zheng Zhang, and Emmy Okello. Bone marrow stem cells implantation with α-cyclodextrin/MPEG-PCL-MPEG hydrogel improves cardiac function after myocardial infarction. *Acta Biomaterialia*, 5(8):2939–2944, 2009.

[287] Mukesh K. Gupta, Joel M. Walthall, Raghav Venkataraman, Spencer W. Crowder, Dae Kwang Jung, Shann S. Yu, Tromondae K. Feaster, Xintong Wang, Todd D. Giorgio, Charles C. Hong, Franz J. Baudenbacher, Antonis K. Hatzopoulos, and Hak Joon Sung. Combinatorial polymer electrospun matrices promote physiologically-relevant cardiomyogenic stem cell differentiation. *PLoS ONE*, 6(12):e28935, 2011.

[288] Yasuo Miyagi, Faquan Zeng, Xi Ping Huang, Warren D. Foltz, Jun Wu, Anton Mihic, Terrence M. Yau, Richard D. Weisel, and Ren Ke Li. Surgical ventricular restoration with a cell- and cytokine-seeded biodegradable scaffold. *Biomaterials*, 31(30):7684–7694, 2010.

[289] Tsukasa Ozawa, Donald A.G. Mickle, Richard D. Weisel, Nobuya Koyama, Harvey Wong, Sumiko Ozawa, and Ren Ke Li. Histologic changes of nonbiodegradable and biodegradable biomaterials used to repair right ventricular heart defects in rats. *Journal of Thoracic and Cardiovascular Surgery*, 124(6):1157–1164, 2002.

[290] Christina Theisen, Susanne Fuchs-Winkelmann, Karola Knappstein, Turgay Efe, Jan Schmitt, Juergen R.J. Paletta, and Markus D Schofer. Influence of nanofibers on growth and gene expression of human tendon derived fibroblast. *BioMedical Engineering Online*, 9:9, 2010.

[291] Valentina Miguez-Pacheco, Larry L. Hench, and Aldo R. Boccaccini. Bioactive glasses beyond bone and teeth: Emerging applications in contact with soft tissues. *Acta Biomaterialia*, 13:1–15, 2015.

[292] Qi Zhi Chen, Julian M W Quinn, George A. Thouas, Xian Zhou, and Paul A. Komesaroff. Bone-like elastomer-toughened scaffolds with degradability kinetics matching healing rates of injured bone. *Advanced Engineering Materials*, 12(11):642–648, 2010.

[293] Bing Xu, Yuan Li, Xiya Fang, George A. Thouas, Wayne D. Cook, Donald F. Newgreen, and Qizhi Chen. Mechanically tissue-like elastomeric polymers and their potential as a vehicle to deliver functional cardiomyocytes. *Journal of the Mechanical Behavior of Biomedical Materials*, 28:354–365, 2013.

[294] Aldo R. Boccaccini, Melek Erol, Wendelin J. Stark, Dirk Mohn, Zhongkui Hong, and João F. Mano. Polymer/bioactive glass nanocomposites for biomedical applications: A review. *Composites Science and Technology*, 70(13):1764–1776, 2010.

[295] Eun Jung Lee and Pamela Hitscherich. Cardiac Tissue Engineering. In *Tissue Engineering for Artificial Organs: Regenerative Medicine, Smart Diagnostics and Personalized Medicine*, volume 2-2, pages 413–443. NIH Public Access, 2016.

[296] Wolfram Hubertus Zimmermann, Ivan Melnychenko, and Thomas Eschenhagen. En-

gineered heart tissue for regeneration of diseased hearts. *Biomaterials*, 25(9):1639–1647, 2004.

[297] R. K. Li and R. D. Weisel. *Cardiac regeneration and repair: Biomaterials and tissue engineering*. Woodhead Publishing, 2014.

[298] Dan Li and Younan Xia. Electrospinning of nanofibers: Reinventing the wheel? *Advanced Materials*, 16(14):1151–1170, 2004.

[299] Mohammad Taufik and Prashant K. Jain. Role of build orientation in layered manufacturing: a review. *International Journal of Manufacturing Technology and Management*, 27(1/2/3):47, 2013.

[300] Jianyi Zhang. Engineered Tissue Patch for Cardiac Cell Therapy. *Current Treatment Options in Cardiovascular Medicine*, 17(8):399–408, 2015.

[301] H. Fong, I. Chun, and D. H. Reneker. Beaded nanofibers formed during electrospinning. *Polymer*, 40(16):4585–4592, 1999.

[302] James N. Smith, Richard C. Flagan, and J. L. Beauchamp. Droplet evaporation and discharge dynamics in electrospray ionization. *Journal of Physical Chemistry A*, 106(42):9957–9967, 2002.

[303] Xiaoming Li, Rongrong Cui, Lianwen Sun, Katerina E. Aifantis, Yubo Fan, Qingling Feng, Fuzhai Cui, and Fumio Watari. 3D-printed biopolymers for tissue engineering application. *International Journal of Polymer Science*, 2014:1–13, 2014.

[304] Halime Kenar, Gamze T. Kose, Mehmet Toner, David L. Kaplan, and Vasif Hasirci. A 3D aligned microfibrous myocardial tissue construct cultured under transient perfusion. *Biomaterials*, 32(23):5320–5329, 2011.

[305] Shilpa Sant, Chang Mo Hwang, Sang Hoon Lee, and Ali Khademhosseini. Hybrid PGS-PCL microfibrous scaffolds with improved mechanical and biological properties. *Journal of Tissue Engineering and Regenerative Medicine*, 5(4):283–291, 2011.

[306] Yadong Tang, Li Liu, Junjun Li, Leqian Yu, Francesco Paolo Ulloa Severino, Li Wang, Jian Shi, Xiaolong Tu, Vincent Torre, and Yong Chen. Effective motor neuron differentiation of hiPSCs on a patch made of crosslinked monolayer gelatin nanofibers. *Journal of Materials Chemistry B*, 4(19):3305–3312, 2016.

[307] Susmita Bose, Sahar Vahabzadeh, and Amit Bandyopadhyay. Bone tissue engineering using 3D printing. *Materials Today*, 16(12):496–504, 2013.

[308] Nick A. Sears, Dhruv R. Seshadri, Prachi S. Dhavalikar, and Elizabeth Cosgriff-Hernandez. A Review of Three-Dimensional Printing in Tissue Engineering. *Tissue Engineering Part B: Reviews*, 22(4):298–310, 2016.

[309] R. Gmeiner, U. Deisinger, J. Schonherr, B. Lechner, R. Detsch, A. R. Boccaccini, and J. Stampfl. Additive manufacturing of bioactive glasses and silicate bioceramics. *Journal of Ceramic Science and Technology*, 6(2):75–86, 2015.

[310] Bobak Mosadegh, Guanglei Xiong, Simon Dunham, and James K Min. Current progress in 3D printing for cardiovascular tissue engineering. *Biomedical Materials*, 10(3):034002, 2015.

[311] Milica Radisic, Jos Malda, Eric Epping, Wenliang Geng, Robert Langer, and Gordana Vunjak-Novakovic. Oxygen gradients correlate with cell density and cell viability in engineered cardiac tissue. *Biotechnology and Bioengineering*, 93(2):332–343, 2006.

[312] W. Y. Yeong, N. Sudarmadji, H. Y. Yu, C. K. Chua, K. F. Leong, S. S. Venkatraman, Y. C.F. Boey, and L. P. Tan. Porous polycaprolactone scaffold for cardiac tissue engineering fabricated by selective laser sintering. *Acta Biomaterialia*, 6(6):2028–2034, 2010.

[313] Roberto Gaetani, Peter A. Doevendans, Corina H G Metz, Jacqueline Alblas, Elisa Messina, Alessandro Giacomello, and Joost P G Sluijter. Cardiac tissue engineering using tissue printing technology and human cardiac progenitor cells. *Biomaterials*, 33(6):1782–1790, 2012.

[314] Vahid Serpooshan, Morteza Mahmoudi, Daniel A Hu, James B Hu, and Sean M Wu. Bioengineering cardiac constructs using 3D printing. *Journal of 3D Printing in Medicine*, 1(2):123–139, 2017.

[315] Scott A. Sell, Michael J. McClure, Koyal Garg, Patricia S. Wolfe, and Gary L. Bowlin. Electrospinning of collagen/biopolymers for regenerative medicine and cardiovascular tissue engineering. *Advanced Drug Delivery Reviews*, 61(12):1007–1019, 2009.

[316] M. N. Giraud, Erick Ayuni, Stéphane Cook, Matthias Siepe, Thierry P. Carrel, and Hendrik T. Tevaearai. Hydrogel-based engineered skeletal muscle grafts normalize heart function early after myocardial infarction. *Artificial Organs*, 32(9):692–700, 2008.

[317] T. Dvir, A. Kedem, E. Ruvinov, O. Levy, I. Freeman, N. Landa, R. Holbova, M. S. Feinberg, S. Dror, Y. Etzion, J. Leor, and S. Cohen. Prevascularization of cardiac patch on the omentum improves its therapeutic outcome. *Proceedings of the National Academy of Sciences*, 106(35):14990–14995, 2009.

[318] Jamil A. Matthews, Gary E. Wnek, David G. Simpson, and Gary L. Bowlin. Electrospinning of collagen nanofibers. *Biomacromolecules*, 3(2):232–238, 2002.

[319] S. Z. Yow, C. H. Quek, Evelyn K F Yim, C. T. Lim, and K. W. Leong. Collagen-based fibrous scaffold for spatial organization of encapsulated and seeded human mesenchymal stem cells. *Biomaterials*, 30(6):1133–1142, 2009.

[320] Antonella Lisi, Enrica Briganti, Mario Ledda, Paola Losi, Settimio Grimaldi, Rodolfo Marchese, and Giorgio Soldani. A combined synthetic-fibrin scaffold supports growth and cardiomyogenic commitment of human placental derived stem cells. *PLoS ONE*, 7(4):34284–34296, 2012.

[321] Marie Noëlle Giraud, Remy Flueckiger, Stéphane Cook, Erick Ayuni, Matthias Siepe, Thierry Carrel, and Hendrik Tevaearai. Long-term evaluation of myoblast

seeded patches implanted on infarcted rat hearts. *Artificial Organs*, 34(6):184–192, 2010.

[322] Chang Yang Gong, Shuai Shi, Peng Wei Dong, Bing Kan, Ma Ling Gou, Xian Huo Wang, Xing Yi Li, Feng Luo, Xia Zhao, Yu Quan Wei, and Zhi Yong Qian. Synthesis and characterization of PEG-PCL-PEG thermosensitive hydrogel. *International Journal of Pharmaceutics*, 365(1-2):89–99, 2009.

[323] John J. Stankus, Jianjun Guan, and William R. Wagner. Fabrication of biodegradable elastomeric scaffolds with sub-micron morphologies. *Journal of Biomedical Materials Research - Part A*, 70(4):603–614, 2004.

[324] Todd C. McDevitt, Kimberly A. Woodhouse, Stephen D. Hauschka, Charles E. Murry, and Patrick S. Stayton. Spatially organized layers of cardiomyocytes on biodegradable polyurethane films for myocardial repair. *Journal of Biomedical Materials Research - Part A*, 66(3):586–595, 2003.

[325] Rajeswari Ravichandran, Jayarama Reddy Venugopal, Subramanian Sundarrajan, Shayanti Mukherjee, and Seeram Ramakrishna. Poly(Glycerol Sebacate)/Gelatin Core/Shell Fibrous Structure for Regeneration of Myocardial Infarction. *Tissue Engineering Part A*, 17(9-10):1363–1373, 2011.

[326] Yadong Wang, Guillermo A. Ameer, Barbara J. Sheppard, and Robert Langer. A tough biodegradable elastomer. *Nature Biotechnology*, 20(6):602–606, 2002.

[327] M. Vert, S. M. Li, G. Spenlehauer, and P. Guerin. Bioresorbability and biocompatibility of aliphatic polyesters. *Journal of Materials Science: Materials in Medicine*, 3(6):432–446, 1992.

[328] Dietmar Hutmacher. A review of material properties of biodegradable and bioresorbable polymers and devices for GTR and GBR applications. *The International journal of oral and maxillofacial implant*, 11(5):667–78, 1996.

[329] Jessica M. Kemppainen and Scott J. Hollister. Tailoring the mechanical properties

of 3D-designed poly(glycerol sebacate) scaffolds for cartilage applications. *Journal of Biomedical Materials Research - Part A*, 94(1):9–18, 2010.

[330] Shuling Liang, Wayne D. Cook, and Qizhi Chen. Physical characterization of poly(glycerol sebacate)/Bioglass ® composites. *Polymer International*, 61(1):17–22, 2012.

[331] Cathryn A. Sundback, Jeffery Y. Shyu, Yadong Wang, William C. Faquin, Robert S. Langer, Joseph P. Vacanti, and Tessa A. Hadlock. Biocompatibility analysis of poly(glycerol sebacate) as a nerve guide material. *Biomaterials*, 26(27):5454–5464, 2005.

[332] Matthew Trese, Caio V Regatieri, and Michael J Young. Advances in retinal tissue engineering. *Materials*, 5(1):108–120, 2012.

[333] Delara Motlagh, Jian Yang, Karen Y. Lui, Antonio R. Webb, and Guillermo A. Ameer. Hemocompatibility evaluation of poly(glycerol-sebacate) in vitro for vascular tissue engineering. *Biomaterials*, 27(24):4315–4324, 2006.

[334] Aaron M. Wieland, Cathryn A. Sundback, Allison Hart, Katherine Kulig, Peter T. Masiakos, and Christopher J. Hartnick. Poly(glycerol sebacate)-engineered plugs to repair chronic tympanic membrane perforations in a chinchilla model. *Otolaryngology - Head and Neck Surgery*, 143(1):127–133, 2010.

[335] Bo Yang, Wei Lv, and Ying Deng. Drug loaded poly(glycerol sebacate) as a local drug delivery system for the treatment of periodontal disease. *RSC Advances*, 7(59):37426–37435, 2017.

[336] Ranjana Rai, Marwa Tallawi, Alexandra Grigore, and Aldo R. Boccaccini. Synthesis, properties and biomedical applications of poly(glycerol sebacate) (PGS): A review. *Progress in Polymer Science*, 37(8):1051–1078, 2012.

[337] Qizhi Chen, Shuling Liang, and George A. Thouas. Synthesis and characterisation of poly(glycerol sebacate)-co-lactic acid as surgical sealants. *Soft Matter*, 7(14):6484, 2011.

[338] Tara A. Hartley, John M. Violanti, Anna Mnatsakanova, Michael E. Andrew, and Cecil M. Burchfiel. Military experience and levels of stress and coping in police officers. *International journal of emergency mental health*, 15(4):229–239, 2013.

[339] Milica Radisic, Hyoungshin Park, Timothy P. Martens, Johanna E. Salazar-Lazaro, Wenliang Geng, Yadong Wang, Robert Langer, Lisa E. Freed, and Gordana Vunjak-Novakovic. Pre-treatment of synthetic elastomeric scaffolds by cardiac fibroblasts improves engineered heart tissue. *Journal of Biomedical Materials Research - Part A*, 86(3):713–724, 2008.

[340] Monique Crane and D. Boga. A commentary: Rethinking approaches to resilience and mental health training. Technical Report 1, Boston: Department of Materials Science and Engineering, Massachusetts Institute of Technology, 2017.

[341] S. Yamaguchi. Analysis of stress-strain curves at fast and slow velocities of loading in vitro in the transverse section of the rat incisor periodontal ligament following the administration of β-aminopropionitrile. *Archives of Oral Biology*, 37(6):439–444, 1992.

[342] Achim Göpferich. Mechanisms of polymer degradation and erosion. *The Biomaterials: Silver Jubilee Compendium*, 17(2):117–128, 2006.

[343] Qi Zhi Chen, Hikaru Ishii, George A. Thouas, Alexander R. Lyon, Jamie S. Wright, Jonny J. Blaker, Wojciech Chrzanowski, Aldo R. Boccaccini, Nadire N. Ali, Jonathan C. Knowles, and Siân E. Harding. An elastomeric patch derived from poly(glycerol sebacate) for delivery of embryonic stem cells to the heart. *Biomaterials*, 31(14):3885–3893, 2010.

[344] Per Brøbech Mortensen and Niels Gregersen. The biological origin of ketotic dicarboxylic aciduria. *Biochimica et Biophysica Acta (BBA) - Lipids and Lipid Metabolism*, 666(3):394–404, 1981.

[345] J. Tam and R. L. Anger. The development of polyanhydrides for drug delivery applications. *Journal of Biomaterials Science, Polymer Edition*, 3(4):316–357, 1992.

[346] A V Grego and G Mingrone. Dicarboxylic acids, an alternate fuel substrate in parenteral nutrition: an update. *Clinical Nutrition*, 14(3):143–148, 1995.

[347] Yuan Li, Wayne D. Cook, Cornelis Moorhoff, Wen Chao Huang, and Qi Zhi Chen. Synthesis, characterization and properties of biocompatible poly(glycerol sebacate) pre-polymer and gel. *Polymer International*, 62(4):534–547, 2013.

[348] Zhi Jie Sun, Lan Wu, Wei Huang, Chang Chen, Yan Chen, Xi Li Lu, Xiao Lan Zhang, Bao Feng Yang, and De Li Dong. Glycolic acid modulates the mechanical property and degradation of poly(glycerol, sebacate, glycolic acid). *Journal of Biomedical Materials Research - Part A*, 92(1):332–339, 2010.

[349] George C. Engelmayr, Mingyu Cheng, Christopher J. Bettinger, Jeffrey T. Borenstein, Robert Langer, and Lisa E. Freed. Accordion-like honeycombs for tissue engineering of cardiac anisotropy. *Nature Materials*, 7(12):1003–1010, 2008.

[350] You-Xiong Wang, John L. Robertson, William B. Spillman, Jr., and Richard O. Claus. Effects of the Chemical Structure and the Surface Properties of Polymeric Biomaterials on Their Biocompatibility. *Pharmaceutical Research*, 21(8):1362–1373, 2004.

[351] Cathryn A. Sundback, Jeffery Y. Shyu, Yadong Wang, William C. Faquin, Robert S. Langer, Joseph P. Vacanti, and Tessa A. Hadlock. Biocompatibility analysis of poly(glycerol sebacate) as a nerve guide material. *Biomaterials*, 26(27):5454–5464, 2005.

[352] Loraine L.Y. Chiu, Milica Radisic, and Gordana Vunjak-Novakovic. Bioactive Scaffolds for Engineering Vascularized Cardiac Tissues. *Macromolecular Bioscience*, 10(11):1286–1301, 2010.

[353] Milica Radisic, Hyoungshin Park, Fen Chen, Johanna E. Salazar-Lazzaro, Yadong Wang, Robert Dennis, Robert Langer, Lisa E. Freed, and Gordana Vunjak-Novakovic. Biomimetic Approach to Cardiac Tissue Engineering: Oxygen Carriers and Channeled Scaffolds. *Tissue Engineering*, 12(8):2077–2091, 2006.

[354] Xiaochu Ding, Yen Lin Wu, Jin Gao, Albin Wells, Kee Won Lee, and Yadong Wang. Tyramine functionalization of poly(glycerol sebacate) increases the elasticity of the polymer. *Journal of Materials Chemistry B*, 5(30):6097–6109, 2017.

[355] Jue Hu, Dan Kai, Hongye Ye, Lingling Tian, Xin Ding, Seeram Ramakrishna, and Xian Jun Loh. Electrospinning of poly(glycerol sebacate)-based nanofibers for nerve tissue engineering. *Materials Science and Engineering C*, 70:1089–1094, 2017.

[356] Ranjana Rai, Marwa Tallawi, Niccoletta Barbani, Caterina Frati, Denise Madeddu, Stefano Cavalli, Gallia Graiani, Federico Quaini, Judith A. Roether, Dirk W. Schubert, Elisabetta Rosellini, and Aldo R. Boccaccini. Biomimetic poly(glycerol sebacate) (PGS) membranes for cardiac patch application. *Materials Science and Engineering C*, 33(7):3677–3687, 2013.

[357] Virna L. Sales, George C. Engelmayr, John A. Johnson, Jin Gao, Yadong Wang, Michael S. Sacks, and John E. Mayer. Protein precoating of elastomeric tissue-engineering scaffolds increased cellularity, enhanced extracellular matrix protein production, and differentially regulated the phenotypes of circulating endothelial progenitor cells. *Circulation*, 116(11 Suppl. 1):I–55–I–63, 2007.

[358] Mohammed Abedalwafa, Fujun Wang, Lu Wang, and Chaojing Li. Biodegradable poly-epsilon-caprolactone (PCL) for tissue engineering applications: A review. *Reviews on Advanced Materials Science*, 34(2):123–140, 2013.

[359] Christopher X. F. Lam, Dietmar W. Hutmacher, Jan-Thorsten Schantz, Maria Ann Woodruff, and Swee Hin Teoh. Evaluation of polycaprolactone scaffold degradation for 6 months in vitro and in vivo. *Journal of Biomedical Materials Research Part A*, 90A(3):906–919, 2009.

[360] Lindsay N Woodard and Melissa A Grunlan. Hydrolytic Degradation and Erosion of Polyester Biomaterials. *ACS Macro Letters*, 7(8):976–982, 2018.

[361] Maria Ann Woodruff and Dietmar Werner Hutmacher. The return of a forgot-

ten polymer - Polycaprolactone in the 21st century. *Progress in Polymer Science (Oxford)*, 35(10):1217–1256, 2010.

[362] Marianne Labet and Wim Thielemans. Synthesis of polycaprolactone: a review. *Chemical Society Reviews*, 38(12):3484, 2009.

[363] Michel Vert. Degradable and bioresorbable polymers in surgery and in pharmacology: Beliefs and facts. In *Journal of Materials Science: Materials in Medicine*, volume 20, pages 437–446, 2009.

[364] Pathiraja A Gunatillake, Raju Adhikari, and N. Gadegaard. Biodegradable synthetic polymers for tissue engineering. *European Cells and Materials*, 5:1–16, 2003.

[365] Sandra Sánchez-González, Nazely Diban, and Ane Urtiaga. Hydrolytic degradation and mechanical stability of poly(ϵ-Caprolactone)/reduced graphene oxide membranes as scaffolds for in vitro neural tissue regeneration. *Membranes*, 8(1):12–26, 2018.

[366] R. B. Sorensen, T. L. Jones, G. S. Campbell, and M. Montes-Helu. Heat pulse needles to measure pecan tree transpiration. *Applied Engineering in Agriculture*, 15(6):651–657, 1999.

[367] Alok Rai, Sudipta Senapati, Shyam K. Saraf, and Pralay Maiti. Biodegradable poly(caprolactone) as a controlled drug delivery vehicle of vancomycin for the treatment of MRSA infection. *Journal of Materials Chemistry B*, 4(30):5151–5160, 2016.

[368] Debasish Mondal, May Griffith, and Subbu S Venkatraman. Polycaprolactone-based biomaterials for tissue engineering and drug delivery: Current scenario and challenges. *International Journal of Polymeric Materials and Polymeric Biomaterials*, 65(5):255–265, 2016.

[369] J.E. Bergsma, F.R. Rozema, R.R.M. Bos, G Boering, and W.C. de Bruijn. Late degradation tissue response to poly(l-lactide) bone plates and screws. *The Biomaterials: Silver Jubilee Compendium*, 16:101–107, 1995.

[370] Lu Wang, Mohammed Abedalwafa, Fujun Wang, and Chaojing Li. Biodegradable Poly-Epsilon-Caprolactone (Pcl) for Tissue Engineering Applications: a Review. *Rev. Adv. Mater. Sci*, 34:123–140, 2013.

[371] Hongfan Sun, Lin Mei, Cunxian Song, Xiumin Cui, and Pengyan Wang. The in vivo degradation, absorption and excretion of PCL-based implant. *Biomaterials*, 27(9):1735–1740, 2006.

[372] Tatiana Patricio, Antonio Gloria, and Paulo Bartolo. Mechanical and biological behaviour of PCL and PCL/PLA scaffolds for tissue engineering applications. *Chemical Engineering Transactions*, 32:1645–1650, 2013.

[373] K. Kyriakidou, G. Lucarini, A. Zizzi, E. Salvolini, M. Mattioli Belmonte, F. Mollica, A. Gloria, and L. Ambrosio. Dynamic co-seeding of osteoblast and endothelial cells on 3D polycaprolactone scaffolds for enhanced bone tissue engineering. *Journal of Bioactive and Compatible Polymers*, 23(3):227–243, 2008.

[374] Michel Vert. Polymeric biomaterials: Strategies of the past vs. strategies of the future. *Progress in Polymer Science (Oxford)*, 32(8-9):755–761, 2007.

[375] P. Menei, A. Croué, V. Daniel, A. Pouplard-Barthelaix, and J. P. Benoit. Fate and biocompatibility of three types of microspheres implanted into the brain. *Journal of Biomedical Materials Research*, 28(9):1079–1085, 1994.

[376] Christopher X.F. Lam, Dietmar W. Hutmacher, Jan Thorsten Schantz, Maria Ann Woodruff, and Swee Hin Teoh. Evaluation of polycaprolactone scaffold degradation for 6 months in vitro and in vivo. *Journal of biomedical materials research. Part A*, 90(3):906–919, 2009.

[377] Christopher XF Lam, Swee Hin Teoh, and Dietmar W Hutmacher. Comparison of the degradation of polycaprolactone and polycaprolactone-(β-tricalcium phosphate) scaffolds in alkaline medium. *Polymer International*, 56(6):718–728, 2007.

[378] A A Sawyer, S J Song, E Susanto, P Chuan, C. X.F. Lam, M A Woodruff, D W Hutmacher, and S M Cool. The stimulation of healing within a rat calvarial defect by

mPCL-TCP/collagen scaffolds loaded with rhBMP-2. *Biomaterials*, 30(13):2479–2488, 2009.

[379] Jan-Thorsten Schantz, Dietmar Werner Hutmacher, Christopher Xu Fu Lam, Maik Brinkmann, Kit Mui Wong, Thiam Chye Lim, Ning Chou, Robert Erling Guldberg, and Swee Hin Teoh. Repair of Calvarial Defects with Customised Tissue-Engineered Bone Grafts II. Evaluation of Cellular Efficiency and Efficacy in Vivo. *Tissue Engineering*, 9(supplement 1):127–139, 2003.

[380] Dietmar W Hutmacher. Regenerative medicine will impact, but not replace, the medical device industry. *Expert Review of Medical Devices*, 3(4):409–412, 2006.

[381] Tim Desmet, Rino Morent, Nathalie De Geyter, Christophe Leys, Etienne Schacht, and Peter Dubruel. Nonthermal plasma technology as a versatile strategy for polymeric biomaterials surface modification: A review. *Biomacromolecules*, 10(9):2351–2378, 2009.

[382] Ziyuan Cheng and Swee Hin Teoh. Surface modification of ultra thin poly (ϵ-caprolactone) films using acrylic acid and collagen. *Biomaterials*, 25(11):1991–2001, 2004.

[383] Yan Peng Jiao and Fu Zhai Cui. Surface modification of polyester biomaterials for tissue engineering. *Biomedical Materials*, 2(4):R24–R37, 2007.

[384] Nicole E. Zander, Joshua A. Orlicki, Adam M. Rawlett, and Thomas P. Beebe. Surface-modified nanofibrous biomaterial bridge for the enhancement and control of neurite outgrowth. *Biointerphases*, 5(4):149–158, 2010.

[385] Xiao Zhu, Sin Chian Kerm, Mary Bee Eng Chan-Park, and Teile Lee Seng. Effect of argon-plasma treatment on proliferation of human-skin-derived fibroblast on chitosan membrane in vitro. *Journal of Biomedical Materials Research - Part A*, 73(3):264–274, 2005.

[386] J. Venugopal, Sharon Low, Aw Tar Choon, A. Bharath Kumar, and S. Ramakrishna.

Electrospun-modified nanofibrous scaffolds for the mineralization of osteoblast cells. *Journal of Biomedical Materials Research - Part A*, 85(2):408–417, 2008.

[387] Jim Jia, Yuan Yuan Duan, Jian Yu, and Jian Wei Lu. Preparation and immobilization of soluble eggshell membrane protein on the electrospun nanofibers to enhance cell adhesion and growth. *Journal of Biomedical Materials Research - Part A*, 86(2):364–373, 2008.

[388] Molamma P Prabhakaran, J Venugopal, Casey K Chan, and S Ramakrishna. Surface modified electrospun nanofibrous scaffolds for nerve tissue engineering. *Nanotechnology*, 19(45):455102, 2008.

[389] F. J. Xu, Z. H. Wang, and W. T. Yang. Surface functionalization of polycaprolactone films via surface-initiated atom transfer radical polymerization for covalently coupling cell-adhesive biomolecules. *Biomaterials*, 31(12):3139–3147, 2010.

[390] Lizzie Y. Santiago, Richard W. Nowak, J. Peter Rubin, and Kacey G. Marra. Peptide-surface modification of poly(caprolactone) with laminin-derived sequences for adipose-derived stem cell applications. *Biomaterials*, 27(15):2962–2969, 2006.

[391] Wolfram Hubertus Zimmermann. Tissue engineering: Polymers flex their muscles. *Nature Materials*, 7(12):932–933, 2008.

[392] Lisa E. Freed, George C. Engelmayr, Jeffrey T. Borenstein, Franklin T. Moutos, and Farshid Guilak. Advanced material strategies for tissue engineering scaffolds. *Advanced Materials*, 21(32-33):3410–3418, 2009.

[393] Dan Kai, Molamma P. Prabhakaran, Guorui Jin, and Seeram Ramakrishna. Guided orientation of cardiomyocytes on electrospun aligned nanofibers for cardiac tissue engineering. *Journal of Biomedical Materials Research - Part B Applied Biomaterials*, 98 B(2):379–386, 2011.

[394] Mahshid Kharaziha, Mehdi Nikkhah, Su Ryon Shin, Nasim Annabi, Nafiseh Masoumi, Akhilesh K. Gaharwar, Gulden Camci-Unal, and Ali Khademhosseini.

PGS:Gelatin nanofibrous scaffolds with tunable mechanical and structural properties for engineering cardiac tissKharaziha, M., Nikkhah, M., Shin, S. R., Annabi, N., Masoumi, N., Gaharwar, A. K., ... Khademhosseini, A. (2013). PGS:Gelatin nanofibrous scaffol. *Biomaterials*, 34(27):6355–6366, 2013.

[395] Marwa Tallawi, David C. Zebrowski, Ranjana Rai, Judith A. Roether, Dirk W. Schubert, Miroslawa El Fray, Felix B. Engel, Katerina E. Aifantis, and Aldo R. Boccaccini. Poly(Glycerol Sebacate)/Poly(Butylene Succinate-Butylene Dilinoleate) Fibrous Scaffolds for Cardiac Tissue Engineering. *Tissue Engineering Part C: Methods*, 21(6):585–596, 2015.

[396] Osamu Ishii, Michael Shin, Taijiro Sueda, and Joseph P. Vacanti. In vitro tissue engineering of a cardiac graft using a degradable scaffold with an extracellular matrix-like topography. *Journal of Thoracic and Cardiovascular Surgery*, 130(5):1358–1363, 2005.

[397] Shaun Eshraghi and Suman Das. Mechanical and microstructural properties of polycaprolactone scaffolds with one-dimensional, two-dimensional, and three-dimensional orthogonally oriented porous architectures produced by selective laser sintering. *Acta Biomaterialia*, 6(7):2467–2476, 2010.

[398] J. Venugopal, Y. Z. Zhang, and S. Ramakrishna. Fabrication of modified and functionalized polycaprolactone nanofibre scaffolds for vascular tissue engineering. *Nanotechnology*, 16(10):2138–2142, 2005.

[399] Sepideh Heydarkhan-Hagvall, Katja Schenke-Layland, Andrew P. Dhanasopon, Fady Rofail, Hunter Smith, Benjamin M. Wu, Richard Shemin, Ramin E. Beygui, and William R. MacLellan. Three-dimensional electrospun ECM-based hybrid scaffolds for cardiovascular tissue engineering. *Biomaterials*, 29(19):2907–2914, 2008.

[400] Ranjana Rai, Marwa Tallawi, Caterina Frati, Angela Falco, Andrea Gervasi, Federico Quaini, Judith A. Roether, Tobias Hochburger, Dirk W. Schubert, Lothar Seik, Niccoletta Barbani, Luigi Lazzeri, Elisabetta Rosellini, and Aldo R. Boccaccini.

Bioactive Electrospun Fibers of Poly(glycerol sebacate) and Poly(ϵ-caprolactone) for Cardiac Patch Application. *Advanced Healthcare Materials*, 4(13):2012–2025, 2015.

[401] Adja B.R. Touré, Elisa Mele, and Jamieson K. Christie. Atomic-scale clustering inhibits the bioactivity of fluoridated phosphate glasses. *Biomedical Glasses*, 5(1):76–84, 2019.

[402] Max Born and Elisabeth Bormann. Zur Gittertheorie der Zinkblende. *Annalen der Physik*, 367(11):218–246, 1920.

[403] M. J.L. Sangster and R. M. Atwood. Interionic potentials for alkali halides. II. Completely crystal independent specification of Born-Mayer potentials. *Journal of Physics C: Solid State Physics*, 11(8):1541–1555, 1978.

[404] M. J. Sangster, R. M. Atwood, and U. Schroder. Interionic potentials for alkali halides. I. Crystal independent shell parameters and fitted Born-Mayer potentials. *Journal of Physics C: Solid State Physics*, 11(8):1523–1540, 1978.

[405] David Jason Binks. *Computational Modelling of Zinc Oxide and Related Oxide Ceramics*. PhD thesis, University of Surrey, 1994.

[406] C. R.A. Catlow, K. M. Diller, and M. J. Norgett. Interionic potentials for alkali halides. *Journal of Physics C: Solid State Physics*, 10(9):1395–1412, 1977.

[407] Rebecca A. Bird and Mark S.D. Read. Derivation of enhanced potentials for cerium brannerite and the calculation of lattice and intrinsic defect properties. *Nuclear Instruments and Methods in Physics Research, Section B: Beam Interactions with Materials and Atoms*, 393:63–67, 2017.

[408] C. R A Catlow, M. J. Norgett, and T. A. Ross. Ion transport and interatomic potentials in the alkaline-earth-fluoride crystals. *Journal of Physics C: Solid State Physics*, 10(10):1627–1640, 1977.

[409] Stephen D. Bond and Benedict J. Leimkuhler. Molecular dynamics and the accuracy of numerically computed averages. *Acta Numerica*, 16:1–65, 2007.

[410] Donald Mkhonto and Nora H. de Leeuw. A computer modelling study of the effect of water on the surface structure and morphology of fluorapatite: introducing a Ca10(PO4)6F2 potential model. *Journal of Materials Chemistry*, 12(9):2633–2642, 2002.

[411] W. T. Lee, M. T. Dove, and E. K H Salje. Surface relaxations in hydroxyapatite. *Journal of Physics Condensed Matter*, 12(48):9829–9841, 2000.

[412] a Pavese, M Catti, S C Parker, and a Wall. Modelling of the thermal dependence of structural and elastic properties of calcite, CaCO3. *Physics and Chemistry of Minerals*, 23(2):89–93, 1996.

[413] C R A Catlow, M J Norgetts, and T Ross. Ion transport and interatomic potentials in the alkaline-earth-fluoride crystals Ion transport and interatomic potentials in the alkaline -earth- fluoride crystals. *J. Phys. J. Phys. C: Solid State Phys*, 10(10):1627–1640, 1977.

[414] M. J. Sanders, M. Leslie, and C. R. A. Catlow. Interatomic potentials for SiO2. *Journal of the Chemical Society, Chemical Communications*, 4(19):1271–1274, 1984.

[415] Marina G. Taylor, Stewart F. Parker, Kenneth Simkiss, and Philip C. H. Mitchell. Bone mineral: evidence for hydroxy groups by inelastic neutron scattering. *Physical Chemistry Chemical Physics*, 3(8):1514–1517, 2001.

[416] H. S. Gutowsky, D. W. McCall, and C. P. Slichter. Nuclear Magnetic Resonance Multiplets in Liquids. *The Journal of Chemical Physics*, 21(2):279–292, 1953.

[417] David M. Pickup, Paul Guerry, Robert M. Moss, Jonathan C. Knowles, Mark E. Smith, and Robert J. Newport. New sol–gel synthesis of a (CaO)0.3(Na2O)0.2(P2O5)0.5 bioresorbable glass and its structural characterisation. *Journal of Materials Chemistry*, 17(45):4777, 2007.

[418] D. S. Brauer, M. N. Anjum, M. Mneimne, R. M. Wilson, H. Doweidar, and R. G. Hill. Fluoride-containing bioactive glass-ceramics. *Journal of Non-Crystalline Solids*, 358(12-13):1438–1442, 2012.

[419] Robert G. Hill and Delia S. Brauer. Predicting the bioactivity of glasses using the network connectivity or split network models. *Journal of Non-Crystalline Solids*, 357(24):3884–3887, 2011.

[420] G. Venkateswara Rao and H. D. Shashikala. Structural, optical and mechanical properties of ternary CaO-CaF2-P2O5 glasses. *Journal of Advanced Ceramics*, 3(2):109–116, 2014.

[421] U Hoppe, G Walter, R Kranold, and D Stachel. Structural specifics of phosphate glasses probed by diffraction methods: a review. *Journal of Non-Crystalline Solids*, 263-264:29–47, 2000.

[422] A. Tilocca. Structural models of bioactive glasses from molecular dynamics simulations. *Proceedings of the Royal Society A: Mathematical, Physical and Engineering Sciences*, 465(2104):1003–1027, 2009.

[423] Robert N Mead and Gavin Mountjoy. A Molecular Dynamics Study of the Atomic Structure of (CaO) x (SiO 2) 1- x Glasses. *The Journal of Physical Chemistry B*, 110(29):14273–14278, 2006.

[424] Jamieson K. Christie and Antonio Tilocca. Integrating biological activity into radioisotope vectors: molecular dynamics models of yttrium-doped bioactive glasses. *Journal of Materials Chemistry*, 22(24):12023, 2012.

[425] Jamieson K. Christie and Antonio Tilocca. Aluminosilicate glasses as yttrium vectors for in situ radiotherapy: Understanding composition-durability effects through molecular dynamics simulations. *Chemistry of Materials*, 22(12):3725–3734, 2010.

[426] Antonio Tilocca, Alastair N. Cormack, and Nora H. de Leeuw. The structure of bioactive silicate glasses: New insight from molecular dynamics simulations. *Chemistry of Materials*, 19(1):95–103, 2007.

[427] HANNES JÓNSSON, GREG MILLS, and KARSTEN W. JACOBSEN. Nudged elastic band method for finding minimum energy paths of transitions. In *Classical and Quantum Dynamics in Condensed Phase Simulations*, pages 385–404, 1998.

[428] R. A. Marcus. On the analytical mechanics of chemical reactions. Classical mechanics of linear collisions. *The Journal of Chemical Physics*, 45(12):4500–4504, 1966.

[429] George H. Vineyard. Frequency factors and isotope effects in solid state rate processes. *Journal of Physics and Chemistry of Solids*, 3(1-2):121–127, 1957.

[430] Lawrence R. Pratt. A statistical method for identifying transition states in high dimensional problems. *The Journal of Chemical Physics*, 85(9):5045–5048, 1986.

[431] Lewis A. Reis, Loraine L.Y. Chiu, Nicole Feric, Lara Fu, and Milica Radisic. Biomaterials in myocardial tissue engineering. *Journal of Tissue Engineering and Regenerative Medicine*, 10(1):11–28, 2016.

[432] Patrizia Camelliti, Thomas K. Borg, and Peter Kohl. Structural and functional characterisation of cardiac fibroblasts. *Cardiovascular Research*, 65(1):40–51, 2005.

[433] Giedrius Gaudesius, Michele Miragoli, Stuart P. Thomas, and Stephan Rohr. Coupling of cardiac electrical activity over extended distances by fibroblasts of cardiac origin. *Circulation Research*, 93(5):421–428, 2003.

[434] Karen E. Porter and Neil A. Turner. Cardiac fibroblasts: At the heart of myocardial remodeling. *Pharmacology and Therapeutics*, 123(2):255–278, 2009.

[435] Genzou Takemura and Hisayoshi Fujiwara. Role of apoptosis in remodeling after myocardial infarction. *Pharmacology and Therapeutics*, 104(1):1–16, 2004.

[436] K Reiss, J M Capasso, H E Huang, L G Meggs, P Li, and P Anversa. ANG II receptors, c-myc, and c-jun in myocytes after myocardial infarction and ventricular failure. *The American journal of physiology*, 264(3):H760–9, 1993.

[437] L B Tan and A S Hall. Cardiac remodelling. *British heart journal*, 72(4):315–316, 1994.

[438] A.J. Tipton J.C. Middleton. Synthetic biodegradable polymers as medical devices. *Med Plast Biomater*, 1998.

[439] Bruce Parsons, Danuta Szczesna, Jiaju Zhao, Glen Van Slooten, W. Glenn L. Kerrick, John A. Putkey, and James D. Potter. The effect of pH on the Ca2+ affinity of the Ca2+ regulatory sites of skeletal and cardiac troponin C in skinned muscle fibres. *Journal of Muscle Research and Cell Motility*, 18(5):599–609, 1997.

[440] Guido Macchiarelli, O. Ohtani, S. A. Nottola, T. Stallone, A. Camboni, I. M. Prado, and P. M. Motta. A micro-anatomical model of the distribution of myocardial endomysial collagen. *Histology and Histopathology*, 17(3):699–706, 2002.

[441] Adèle J. Pope, Gregory B. Sands, Bruce H. Smaill, and Ian J. LeGrice. Three-dimensional transmural organization of perimysial collagen in the heart. *AJP: Heart and Circulatory Physiology*, 295(3):H1243–H1252, 2008.

[442] Lisa E. Freed, George C. Engelmayr, Jeffrey T. Borenstein, Franklin T. Moutos, and Farshid Guilak. Advanced material strategies for tissue engineering scaffolds. *Advanced Materials*, 21(32-33):3410–3418, 2009.

[443] Sherif F. Nagueh, Gopi Shah, Yiming Wu, Guillermo Torre-Amione, Nicholas M P King, Sunshine Lahmers, Christian C. Witt, Katy Becker, Siegfried Labeit, and Henk L. Granzier. Altered titin expression, myocardial stiffness, and left ventricular function in patients with dilated cardiomyopathy. *Circulation*, 110(2):155–162, 2004.

[444] Sara M Weis, Jeffrey L Emery, K David Becker, Daniel J McBride, Jeffrey H Omens, and Andrew D McCulloch. Myocardial mechanics and collagen structure in the osteogenesis imperfecta murine (oim). *Circulation Research*, 87(8):663–669, 2000.

[445] Catherine Coirault, Jane-Lyse Samuel, Denis Chemla, Jean-Claude Pourny, Francine Lambert, Francoise Marotte, and Yves Lecarpentier. Increased compliance

in diaphragm muscle of the cardiomyopathic Syrian hamster. *Journal of Applied Physiology*, 85(5):1762–1769, 1998.

[446] Jeffrey H. Omens. Stress and strain as regulators of myocardial growth. *Progress in Biophysics and Molecular Biology*, 69(2-3):559–572, 1998.

[447] R. Verheggen, W. J. Schulte-Baumann, G. Hahm, J. Lang, S. Freudenthaler, Th Schaake, and E. Markakis. A new technique of dural closure - Experience with a vicryl mesh. *Acta Neurochirurgica*, 139(11):1074–1079, 1997.

[448] Hideyuki Takaoka, Giovanni Esposito, Lan Mao, Hiroyuki Suga, and Howard A. Rockman. Heart size-independent analysis of myocardial function in murine pressure overload hypertrophy. *American Journal of Physiology-Heart and Circulatory Physiology*, 282(6):H2190–H2197, 2015.

[449] Samuel T. Wall, Joseph C. Walker, Kevin E. Healy, Mark B. Ratcliffe, and Julius M. Guccione. Theoretical impact of the injection of material into the myocardium: A finite element model simulation. *Circulation*, 114(24):2627–2635, 2006.

[450] Masato Morita, Chad E. Eckert, Kanji Matsuzaki, Mio Noma, Liam P. Ryan, Jason A. Burdick, Benjamin M. Jackson, Joseph H. Gorman, Michael S. Sacks, and Robert C. Gorman. Modification of infarct material properties limits adverse ventricular remodeling. *Annals of Thoracic Surgery*, 92(2):617–624, 2011.

[451] Jonathan F. Wenk, Parastou Eslami, Zhihong Zhang, Chun Xu, Ellen Kuhl, Joseph H. Gorman, J. Daniel Robb, Mark B. Ratcliffe, Robert C. Gorman, and Julius M. Guccione. A novel method for quantifying the in-vivo mechanical effect of material injected into a myocardial infarction. *Annals of Thoracic Surgery*, 92(3):935–941, 2011.

[452] Gregory M. Fomovsky and Jeffrey W. Holmes. Evolution of scar structure, mechanics, and ventricular function after myocardial infarction in the rat. *American Journal of Physiology-Heart and Circulatory Physiology*, 298(1):H221–H228, 2009.

[453] Athanasios Makrodimopoulos. Remarks on some properties of conic yield restrictions in limit analysis. *International Journal for Numerical Methods in Biomedical Engineering*, 26(1):807–827, 2010.

[454] Dimitri Mojsejenko, Jeremy R. McGarvey, Shauna M. Dorsey, Joseph H. Gorman, Jason A. Burdick, James J. Pilla, Robert C. Gorman, and Jonathan F. Wenk. Estimating passive mechanical properties in a myocardial infarction using MRI and finite element simulations. *Biomechanics and Modeling in Mechanobiology*, 14(3):633–647, 2015.

[455] Adja B. R. Touré, Elisa Mele, and Jamieson K. Christie. Multi-layer Scaffolds of Poly(caprolactone), Poly(glycerol sebacate) and Bioactive Glasses Manufactured by Combined 3D Printing and Electrospinning. *Nanomaterials*, 10(4):626, 2020.

[456] Anthony E. Armenàkas. *Advanced Mechanics of Materials and Applied Elasticity*. Prentice Hall, 2018.

[457] C. Miehe, S. Göktepe, and J. Méndez Diez. Finite viscoplasticity of amorphous glassy polymers in the logarithmic strain space. *International Journal of Solids and Structures*, 46(1):181–202, 2009.

[458] Souheng Wu. Secondary relaxation, brittle–ductile transition temperature, and chain structure. *Journal of Applied Polymer Science*, 46(4):619–624, 1992.

[459] J. Richeton, G. Schlatter, K. S. Vecchio, Y. Rémond, and S. Ahzi. A unified model for stiffness modulus of amorphous polymers across transition temperatures and strain rates. *Polymer*, 46(19):8194–8201, 2005.

[460] A. D. Mulliken and M. C. Boyce. Mechanics of the rate-dependent elastic-plastic deformation of glassy polymers from low to high strain rates. *International Journal of Solids and Structures*, 43(5):1331–1356, 2006.

[461] Lena Vogt, Laura Ramos Rivera, Liliana Liverani, Agnieszka Piegat, Miroslawa El Fray, and Aldo R. Boccaccini. Poly(ϵ-caprolactone)/poly(glycerol sebacate) elec-

trospun scaffolds for cardiac tissue engineering using benign solvents. *Materials Science and Engineering C*, 103:109712–109725, 2019.

[462] M. Tallawi, D. Dippold, R. Rai, D. D'Atri, J. A. Roether, D. W. Schubert, E. Rosellini, F. B. Engel, and A. R. Boccaccini. Novel PGS/PCL electrospun fiber mats with patterned topographical features for cardiac patch applications. *Materials Science and Engineering C*, 69:569–576, 2016.

[463] Liliana Liverani, Agnieszka Piegat, Agata Niemczyk, Miroslawa El Fray, and Aldo R. Boccaccini. Electrospun fibers of poly(butylene succinate–co–dilinoleic succinate) and its blend with poly(glycerol sebacate) for soft tissue engineering applications. *European Polymer Journal*, 81:295–306, 2016.

[464] Lucila Navarro, Diana Elena Mogosanu, Thijs de Jong, Astrid D. Bakker, David Schaubroeck, Julio Luna, Ignacio Rintoul, Jan Vanfleteren, and Peter Dubruel. Poly(polyol sebacate) Elastomers as Coatings for Metallic Coronary Stents. *Macromolecular Bioscience*, 16(11):1678–1692, 2016.

[465] D. Bellucci, V. Cannillo, and A. Sola. An overview of the effects of thermal processing on bioactive glasses. *Science of Sintering*, 42(3):307–320, 2010.

[466] Todd R. Zeitler and A. N. Cormack. Interaction of water with bioactive glass surfaces. *Journal of Crystal Growth*, 294(1):96–102, 2006.

[467] Jonathan Massera, Susanne Fagerlund, Leena Hupa, and Mikko Hupa. Crystallization mechanism of the bioactive glasses, 45S5 and S53P4. *Journal of the American Ceramic Society*, 95(2):607–613, 2012.

[468] Aldo R. Boccaccini, Qizhi Chen, Leila Lefebvre, Laurent Gremillard, and Jérôme Chevalier. Sintering, crystallisation and biodegradation behaviour of Bioglass®-derived glass-ceramics. *Faraday Discussions*, 136:27–44, 2007.

[469] P. Li, Q. Yang, F. Zhang, and T. Kokubo. The effect of residual glassy phase in a bioactive glass-ceramic on the formation of its surface apatite layer in vitro. *Journal of Materials Science: Materials in Medicine*, 3(6):452–456, 1992.

[470] Jennifer N Duggan, Michael J Bozack, and Christopher B Roberts. The synthesis and arrested oxidation of amorphous cobalt nanoparticles using DMSO as a functional solvent. *Journal of Nanoparticle Research*, 15(11):2089–2105, 2013.

[471] Jennifer N Duggan and Christopher B Roberts. Aggregation and precipitation of gold nanoparticle clusters in carbon dioxide-gas-expanded liquid dimethyl sulfoxide. *Journal of Physical Chemistry C*, 118(26):14595–14605, 2014.

[472] N A David. The Pharmacology of Dimethyl Sulfoxide. *Annual Review of Pharmacology*, 12(1):353–374, 1972.

[473] Xiaohong Pan, Thomas Julian, and Larry Augsburger. Increasing the dissolution rate of a low-solubility drug through a crystalline-amorphous transition: A case study with indomethicin. *Drug Development and Industrial Pharmacy*, 34(2):221–231, 2008.

[474] Csaba Mártha, Levente Kürti, Gabriella Farkas, Orsolya Jójárt-Laczkovich, Balázs Szalontai, Erik Glässer, Mária A. Deli, and Piroska Szabó-Révész. Effects of polymers on the crystallinity of nanonized meloxicam during a co-grinding process. *European Polymer Journal*, 49(9):2426–2432, 2013.

[475] Geoff Smith, Amjad Hussain, Nadeem Irfan Bukhari, and Irina Ermolina. Quantification of residual crystallinity in ball milled commercially sourced lactose monohydrate by thermo-analytical techniques and terahertz spectroscopy. *European Journal of Pharmaceutics and Biopharmaceutics*, 92:180–191, 2015.

[476] K. A. Akinade, R. M. Campbell, and David A.C. Compton. The use of a simultaneous TGA/DSC/FT-IR system as a problem-solving tool. *Journal of Materials Science*, 29(14):3802–3812, 1994.

[477] Tamara Elzein, Mohamad Nasser-Eddine, Christelle Delaite, Sophie Bistac, and Philippe Dumas. FTIR study of polycaprolactone chain organization at interfaces. *Journal of Colloid and Interface Science*, 273(2):381–387, 2004.

[478] C. Schild, A. Wokaun, and A. Baiker. On the mechanism of CO and CO2 hydrogenation reactions on zirconia-supported catalysts: a diffuse reflectance FTIR study. Part II. Surface species on copper/zirconia catalysts: implications for methanoi synthesis selectivity. *Journal of Molecular Catalysis*, 63(2):243–254, 1990.

[479] Wei Wu, Robert A. Allen, and Yadong Wang. Fast-degrading elastomer enables rapid remodeling of a cell-free synthetic graft into a neoartery. *Nature Medicine*, 18(7):1148–1153, 2012.

[480] O. Hakimi, P. A. Mouthuy, N. Zargar, E. Lostis, M. Morrey, and A. Carr. A layered electrospun and woven surgical scaffold to enhance endogenous tendon repair. *Acta Biomaterialia*, 26:124–135, 2015.

[481] Sung Jin Kim, Da Hyun Jang, Won Ho Park, and Byung Moo Min. Fabrication and characterization of 3-dimensional PLGA nanofiber/microfiber composite scaffolds. *Polymer*, 51(6):1320–1327, 2010.

[482] Izabella Rajzer. Fabrication of bioactive polycaprolactone/hydroxyapatite scaffolds with final bilayer nano-/micro-fibrous structures for tissue engineering application. *Journal of Materials Science*, 49(16):5799–5807, 2014.

[483] Ali Mohammadkhah, Laura M. Marquardt, Shelly E. Sakiyama-Elbert, Delbert E. Day, and Amy B. Harkins. Fabrication and characterization of poly-(ϵ)-caprolactone and bioactive glass composites for tissue engineering applications. *Materials Science and Engineering C*, 49:632–639, 2015.

[484] Nisha Shankhwar, Manishekhar Kumar, Biman B. Mandal, and A. Srinivasan. Novel polyvinyl alcohol-bioglass 45S5 based composite nanofibrous membranes as bone scaffolds. *Materials Science and Engineering C*, 69:1167–1174, 2016.

[485] Jing Chen, Yuzhang Du, Wenxiu Que, Yonglei Xing, and Bo Lei. Content-dependent biomineralization activity and mechanical properties based on polydimethylsiloxane-bioactive glass-poly(caprolactone) hybrids monoliths for bone tissue regeneration. *RSC Advances*, 5(75):61309–61317, 2015.

[486] D. Kurniawan, F. M. Nor, H. Y. Lee, and J. Y. Lim. Elastic properties of polycaprolactone at small strains are significantly affected by strain rate and temperature. *Proceedings of the Institution of Mechanical Engineers, Part H: Journal of Engineering in Medicine*, 225(10):1015–1020, 2011.

[487] Milica Radisic, Hyoungshin Park, Timothy P. Martens, Johanna E. Salazar-Lazaro, Wenliang Geng, Yadong Wang, Robert Langer, Lisa E. Freed, and Gordana Vunjak-Novakovic. Pre-treatment of synthetic elastomeric scaffolds by cardiac fibroblasts improves engineered heart tissue. *Journal of Biomedical Materials Research - Part A*, 86(3):713–724, 2008.

[488] Kashif Khan, Karina Gasbarrino, Ibtisam Mahmoud, Georges Makhoul, Bin Yu, Line Dufresne, Stella S. Daskalopoulou, Adel Schwertani, and Renzo Cecere. Bioactive scaffolds in stem-cell-based therapies for cardiac repair: Protocol for a meta-analysis of randomized controlled preclinical trials in animal myocardial infarction models 11 Medical and Health Sciences 1102 Cardiorespiratory Medicine and Haemato. *Systematic Reviews*, 7(1):225–232, 2018.

[489] Junjie Jiang, Pengcheng Han, Qiangzhe Zhang, Jianmin Zhao, and Yue Ma. Cardiac differentiation of human pluripotent stem cells. *Journal of Cellular and Molecular Medicine*, 16(8):1663–1668, 2012.

[490] Nicholas D. Evans, Eileen Gentleman, and Julia M. Polak. Scaffolds for stem cells. *Materials Today*, 9(12):26–33, 2006.

[491] Fatemeh Sadat Hosseini, Fatemeh Soleimanifar, Abdolreza Ardeshirylajimi, Saeid Vakilian, Majid Mossahebi-Mohammadi, Seyed Ehsan Enderami, Arash Khojasteh, and Shohreh Zare Karizi. In vitro osteogenic differentiation of stem cells with different sources on composite scaffold containing natural bioceramic and polycaprolactone. *Artificial cells, nanomedicine, and biotechnology*, 47(1):300–307, 2019.

Appendix A

Degradation studies on the scaffolds without electrospun mat

In this work, a collaboration with Bridie Catchpole was conducted. The degradation behaviour of the compositions C1, C4 and C5 was studied. The solutions were prepared and 3D printed following the protocole decribed in chapter 4. The water absorption, weight loss and pH were monitored at the following time points: 3 hours, 6 hours, 1 day, 4 days, 8 days and 13 days,where samples (n=5) were removed from solution. Mechanical tests were also perfomed on 8 samples of each compositions after 12 days at 40°C.

To determine the percentage water absorption of the three different scaffolds were incubated in PBS, the wet weight was measured following 3 hours, 6 hours, 1 day, 4 days, 8 days and 13 days. This was then compared to the weight of the sample once it had been left to dry out overnight. Figure A.1 displays the mean percentage water absorption of each sample (n=5) at each time point. For the PCL scaffolds, there was no significant water absorption in the first 8 days, with absorption values of 9.5 – 11.2%. At 13 days the percentage water absorption increased to 16% ± 4.1, with a significance of 0.02.

This contrasted with the PCL-PGS composite scaffolds where water absorption was higher after only 3 hours (29.5% ± 5.1). This value then remains at a similar level for up to 13 days.

In the C5 (PCL-PGS-5%) BG samples, water absorption was also observed in the first

3 hours (43.9% ± 4). This observation was followed by a further increase observed at 6 hours (70.4% ± 2.9), with peak water absorption at 24 hours (79.5% ± 4.1). A significant decrease in water absorption was observed at 4 days (50.1% ± 5.7) compared to at 24 hours. Water absorption then remained at a similar level for the duration of the experiment.

It could also be noted that the water absorption of the samples containing BG was greater than in the other samples at comparable time points. The scaffolds of composition C4 also absorbed significantly more water than the PCL scaffolds at all time points.

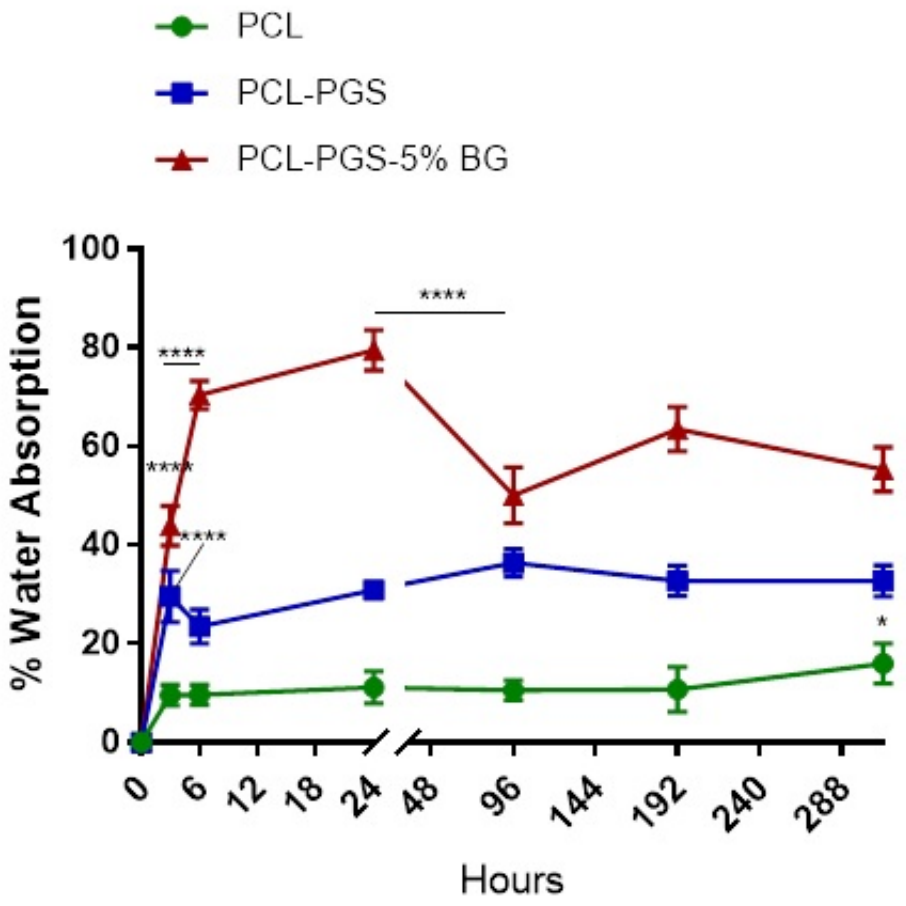

Figure A.1: Percentage water absorption for the compositions **C1** (PCL), **C4** (PCL-PGS) and **C5** (PCL-PGS-5%wt BG) scaffolds over a 13 day period in PBS. Wet weight was measured at 3 hours, 6 hours, 1 day, 4 days, 8 days and 13 days for each scaffold (n=5). The mean and SEM are plotted as line graphs (n=5)

The weight loss of the samples following incubation in PBS was investigated to characterise their degradation. The scaffolds were dried out overnight and weighed once dry, this

measurement was then compared to the initial dry weights to obtain a percentage weight loss figure. The mean percentage weight loss (n=5) for each scaffold following incubation in PBS for 3 hours, 6 hours, 1 day, 4 days, 8 days and 13 days is displayed in Figure A.2.

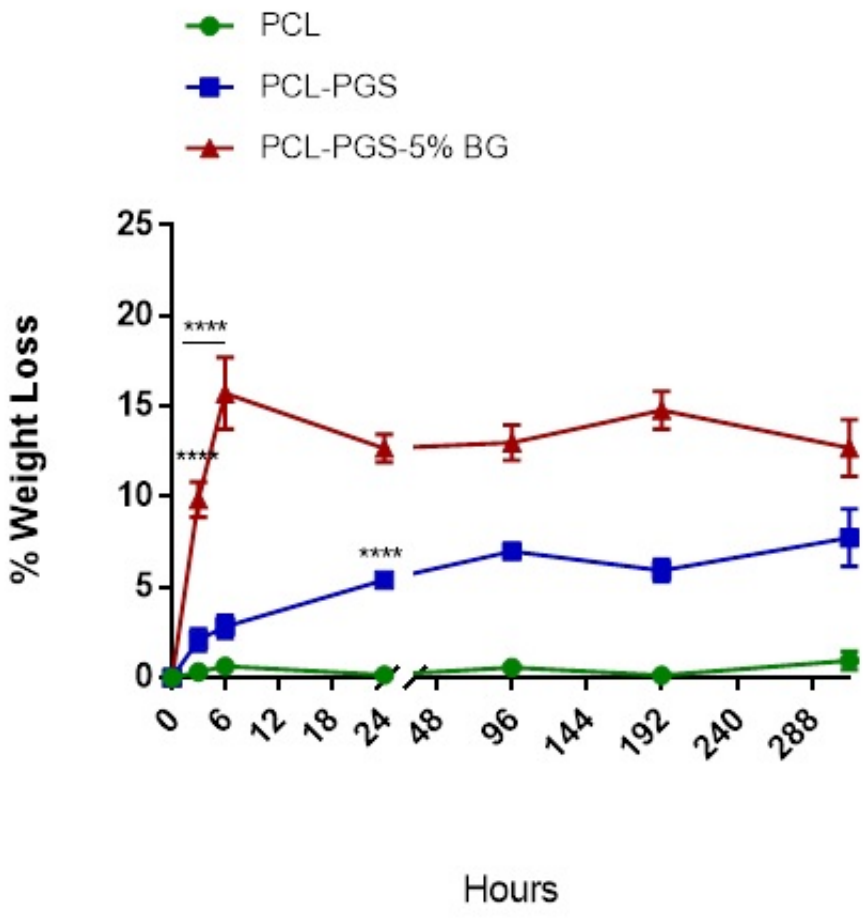

Figure A.2: Percentage weight loss for the compositions **C1** (PCL), **C4** (PCL-PGS) and **C5** (PCL-PGS-5%wt BG) scaffolds over a 13 day period in PBS. Wet weight was measured at 3 hours, 6 hours, 1 day, 4 days, 8 days and 13 days for each scaffold (n=5). The mean and SEM are plotted as line graphs (n=5)

The scaffolds of composition C1 did not undergo significant weight loss during the degradation study, with only 0.9% ± 0.5 weight loss at day 13. For the PCL-PGS scaffolds, a significant weight loss of 5.4% ± 0.5 was observed at day 1, there is then no further significant increase in weight loss up to day 13 (7.7% ± 1.6). The scaffolds containing BG lost on average 9.8% ± 1 of their weight within the first 3 hours. This figure then increased to 15.7% ± 2 at 6 hours. The weight loss then plateaued at a similar level for the duration of the experiment.

The PCL and PCL-PGS scaffolds displayed a similar weight loss profile to each other up to 24 hours, at which point the weight loss of the composite was significantly greater. The PCL-PGS-5% BG samples exhibited significantly greater weight loss than the other scaffold types at all time points.

To determine the pH of the degradation products of the three different scaffold types, the degradation solution was tested following the removal of the samples for weighing at each of the time points 3 hours, 6 hours, 1 day, 4 days, 8 days and 13 days. The mean pH of the solution is depicted in Figure A.3 (n=2).

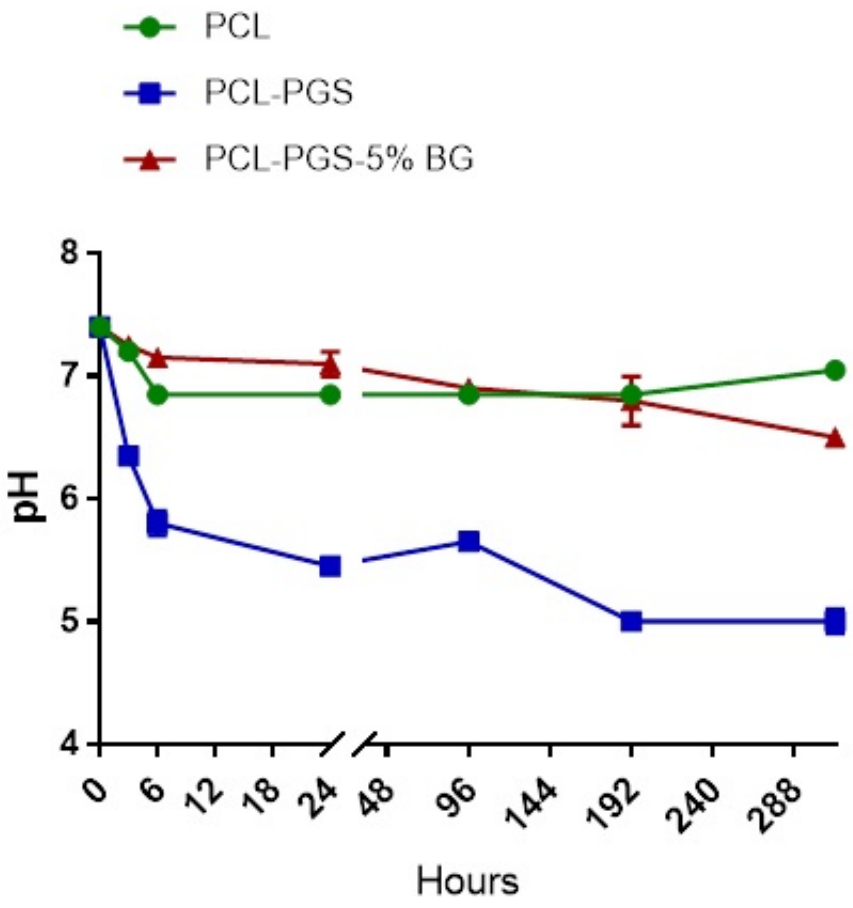

Figure A.3: pH for the compositions **C1** (PCL), **C4** (PCL-PGS) and **C5** (PCL-PGS-5%wt BG) scaffolds over a 13 day period in PBS. Wet weight was measured at 3 hours, 6 hours, 1 day, 4 days, 8 days and 13 days for each scaffold (n=5). The mean and SEM are plotted as line graphs (n=5)

A decrease in pH below physiological level was detected in all three sample solutions at 3

hours. The samples containing BG displayed a steady decrease in pH, to 6.5 at 13 days. The pH of the PCL degradation solution plateaued at 6.9 from 6 hours to 8 days, with a slight increase seen at 13 days (pH 7.1) The PCL-PGS scaffold displayed the largest pH drop (6.4) at the first time point. The pH then continued to decrease over 24 hours (5.5), remaining at a similar level at 4 days. A further large decrease in pH was observed at 8 days (5).

Following 12 days in the PBS degradation solution, the mechanical properties of the PCL, PCL-PGS and PCL-PGS-5% BG scaffolds were tested (Figure A.4.). The Young's modulus was measured to determine the stiffness of each of the scaffold materials. Results found that the Young's modulus of the PCL samples was greater than the modulus of the samples containing PGS and BG, with a value of 919.3MPa ± 40.1. There was no statistical significance between the Young's modulus of PCL-PGS and PCL-PGS-5% BG at 12 days degradation with mean values of 220.8MPa ± 10.4 and 242.1MPa ± 17 respectively. The PCL samples also possessed a higher failure at strain than the other two scaffolds, with an elongation at break of 6.2% ± 0.4. This was similar to the failure strain of the BG-containing samples (5.5% ± 0.2). Both the PCL and PCL-PGS-5% BG samples have statistically greater elongation at break than the PCL-PGS scaffolds (3.5% ± 0.3).

The ultimate tensile strength (UTS) was again higher for the PCL samples (4.2MPa ± 0.3) than the other scaffolds. As with the Young's modulus, there was no significant difference between the UTS of the PCL-PGS and PCL-PGS-5% BG samples (0.9Mpa ± 0.1 and 1.2 MPa ± 0.1).

The results of this study focusing on the 3D printed scaffolds highlighted preliminary potential advantages of combining BG with a PCL-PGS copolymer. BGs were shown to influence greatly the degradation rate and water absorption of the copolymer, in addition to counteracting the acidity caused by PGS degradation. The addition of BG also increases the ductility of PCL-PGS scaffolds.

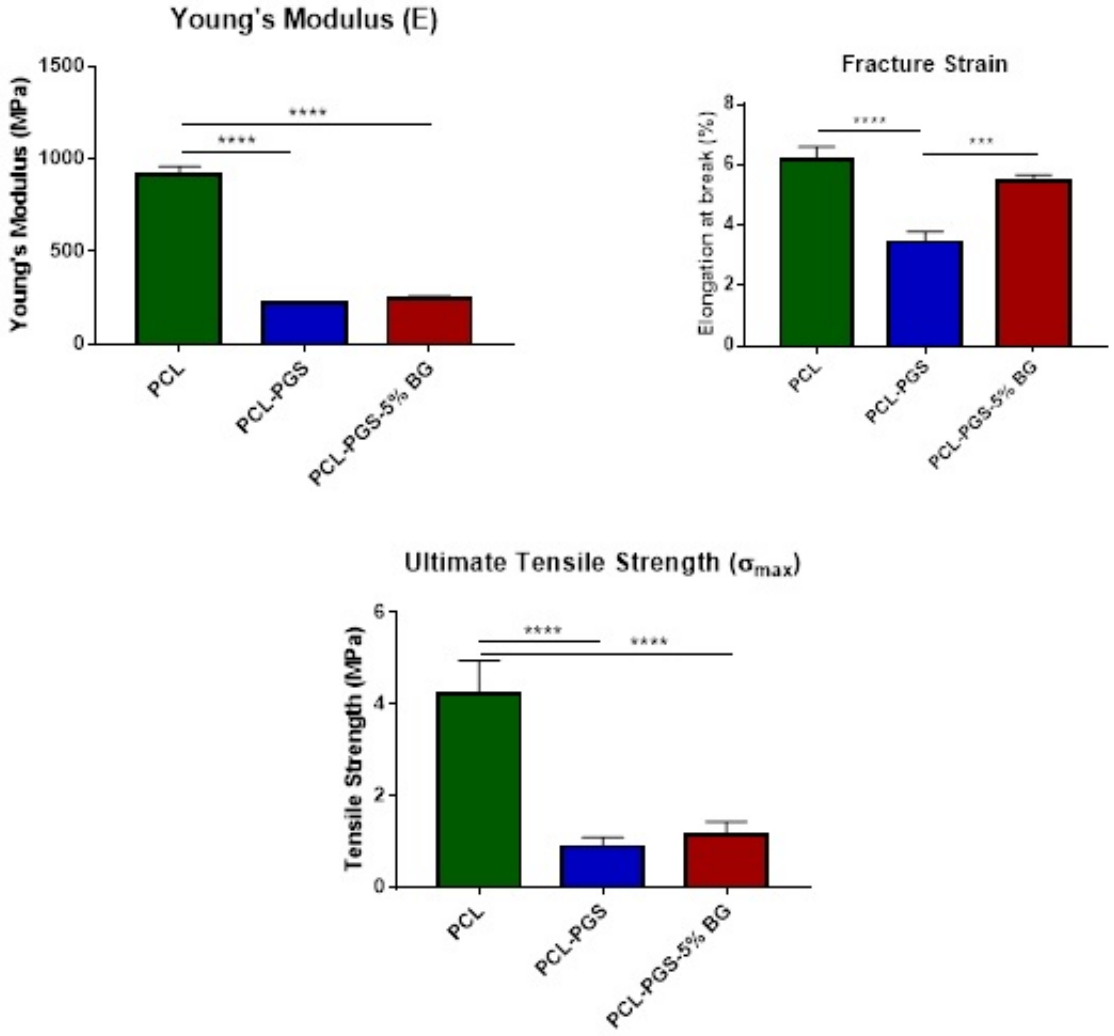

Figure A.4: Young's modulus, failure at strain and ultimate tensile strength of the compositions **C1** (PCL), **C4** (PCL-PGS) and **C5** (PCL-PGS-5%wt BG) scaffolds over a 13 day period in PBS. Measurements were taken following a 12 day incubation in PBS; mean and SEM values are displayed as bar charts (n=8)

Appendix B

Biocompatibility Assay via indirect method using 3T3 fibroblast cells

B.1 Fluorescence Protocol and Parameters

Viability was assessed through fluorescence measurements using PrestoBlue Cell Viability tests. This reagent uses colourimetric/Fluorometric growth factors in order to evaluate the viability and proliferation of a various range of cell types. Indeed, as cells proliferate and grow, their metabolic activity leads to a chemical reduction of their surrounding environment. PrestoBLue contains a non-toxic chemical reagent called resazurin that when exposed to the reducing environment of viable cell converts to resofurin which is an red fluorescent dye. This REDOX reaction allows the metabolism and hence viability to be monitored by way of change of colour and fluorescence. To measure the fluorescence activity, a plate reader was used in combination with the Tecan i-control software. Measurements were performed using the following parameters:

- Linear Shaking: 5 s
- Linear Shaking Amplitude: 1 mm
- Mode : Fluorescence top reading
- Excitation wavelength :560 nm

- Emission wavelength : 590 nm
- Excitation bandwidth : 9 nm
- Emission bandwidth : 20 nm
- Gain : 75%
- Room temperature

In the following section is presented the detail of the fluorescence measurements for each triplicate along with the associated standard error. Samples within each triplicates present some divergence in values which points towards a certain heterogeneity between different construct which could represent a point of optimisation. Values obtained for UV sterilised scaffolds are presented in Table B.1 while the ones obtained for Ethanol sterilised scaffold in Table B.2.

Table B.1: Viability results for the multi-layered scaffolds using an indirect assay method and UV light sterilisation

Sample	Day 1					Day 3					Day 7				
	Fluorescence	Viability per triplicates	Standard Error per triplicates	Average viability	Standard Error	Fluorescence	Viability per triplicates	Standard Error per triplicates	Average viability	Standard Error	Fluorescence	Viability per triplicates	Standard Error per triplicates	Average viability	Standard Error
Negative Control 1	14246	100%	9%	-	-	46501	100%	1%	-	-	17663	100%	4%	-	-
Negative Control 2	11506	81%	3%	-	-	42918	92%	1%	-	-	17840	101%	1%	-	-
Positive Control	-551	-4%	0,3%	-	-	-188	0%	0,1%	-	-	491	3%	0,2%	-	-
C4-EM	9184	64%	3%			26892	58%	4%			2558	14%	2%		
C4-EM	9020	63%	4%	54%	10%	25284	54%	5%	52%	3.8%	2583	15%	1%	14%	0.6
C4-EM	4721	33%	4%			20924	45%	1%			2246	13%	2%		
C9-EM	3845	27%	2%			5119	11%	1%			738	4%	0,3%		
C9-EM	9653	68%	12%	51%	12%	14273	31%	2%	20%	6%	1857	11%	1%	7%	2%
C9-EM	8409	59%	5%			9130	20%	2%			1148	6%	0,4%		
C10-EM	7672	54%	2%			29325	63%	3%			2867	16%	1%		
C10-EM	5681	40%	3%	48%	4%	25934	56%	3%	58%	3%	1919	11%	2%	14%	2%
C10-EM	7088	50%	4%			25211	54%	1%			2425	14%	1%		

Table B.2: Viability results for the multi-layered scaffolds using an indirect assay method and Ethanol sterilisation

Sample	Day 1					Day 3					Day 7				
	Fluorescence	Viability per triplicates	Standard Error per triplicates	Average viability	Standard Error	Fluorescence	Viability per triplicates	Standard Error per triplicates	Average viability	Standard Error	Fluorescence	Viability per triplicates	Standard Error per triplicates	Average viability	Standard Error
Nehative Control 1	26875	100%	4%	-	-	36181	100%	9%	-	-	26445	100%	7%	-	-
Negative Control 2	24026	89%	2%	-	-	35335	98%	4%	-	-	19580	74%	8%	-	-
Positive Control	-393	-1%	0,3%	-	-	491	1%	0,4%	-	-	-199	-1%	0,3%	-	-
C4-EM	31762	118%	4%			43256	120%	6%			24184	91%	10%		
C4-EM	32658	122%	3%	124%	4%	39814	110%	1%	125%	11%	27196	103%	5%	103%	6%
C4-EM	35310	131%	5%			52761	146%	5%			30084	114%	6%		
C9-EM	32090	119%	4%			44263	122%	11%			18275	69%	6,7%		
C9-EM	37832	141%	5%	126%	7%	57435	159%	2%	137%	11%	26282	99%	6%	84%	9%
C9-EM	32012	119%	3%			47329	131%	6%			22316	84%	11,7%		
C10-EM	33795	126%	17%			52313	145%	8%			34359	130%	4%		
C10-EM	36960	138%	10%	129%	4%	48580	134%	3%	134%	6%	32555	123%	7%	123%	4%
C10-EM	33546	125%	17%			44641	123%	5%			30694	116%	11%		